# Cosmology from Cosmic Shear

A thesis submitted to the University of Manchester
for the degree of Doctor of Philosophy
in the Faculty of Engineering and Physical Sciences

2016

By
Niall MacCrann
School of Physics and Astronomy

# Contents

This thesis contains 46616 words in the main text, 343 words in headers and 4323 in captions, calculated using TeXcount[1].

[1] http://app.uio.no/ifi/texcount/

# List of Tables



# List of Figures

# The University of Manchester

ABSTRACT OF THESIS submitted by Niall MacCrann

for the Degree of Doctor of Philosophy and entitled

"Cosmology From Cosmic Shear", March 2016.

The observed accelerated expansion of the Universe presents a confounding challenge to our understanding of fundamental physics on cosmic scales, contradicting our experience of the attractive nature of gravity. Despite the accumulating evidence from independent analyses of various observational probes over the last two decades, no satisfactory theoretical explanation for this phenomenon has arisen, allowing the placeholder name 'dark energy' to stubbornly linger. I start by describing the concordance model of modern cosmology, and some of the compelling observational evidence that supports it. In the rest of this thesis I explore how we can use *weak gravitational lensing*, the subtle distortion of galaxy shapes by the Universe's matter field, to constrain and test cosmological models.

Having introduced the theoretical basis of weak lensing, I introduce various systematic effects that make unbiased estimation and interpretation of weak lensing signals so difficult. I do so in the context the Dark Energy Survey (DES), which will provide a significant increase in the volume of weak lensing data available, and thus places stricter requirements on systematic uncertainties than previous datasets. Weak lensing is sensitive to a wide range of systematics, including those arising from incomplete understanding of the instrument and data reduction, and theoretical uncertainties in modelling the signal.

I demonstrate improvements in the treatment of various systematic effects by implementation on current data. Firstly, I analyse CFHTLenS data, exploring the tension between this low redshift constraint on the amplitude of matter fluctuations, and the *Planck* CMB results. I outline further improvements in my analysis of early DES data, presenting cosmological results and comparing to other probes of cosmology. Finally I investigate the theoretically uncertain, systematics-ridden small scales of cosmic shear.

# Declaration

No portion of the work referred to in this thesis has been submitted in support of an application for another degree or qualification of this or any other university or other institution of learning.

# Copyright

# Acknowledgements

I'm immeasurably grateful to Sarah Bridle, whose advice is cosmologically useful whether or not it concerns cosmology. I could not have hoped for a wiser or kinder supervisor.

I've had the privilege of working with some extremely bright people from UCL, Manchester and the Dark Energy Survey, and the pleasure of becoming friends with many more. Thanks in particular to Joe Zuntz, whose door has always been open to my frequent, frequently annoying questions.

Thanks to Cathal, Chris, David, Francesca, Indy, John, Kris, Mihai, Sophie and Simon, for making me feel so welcome when I moved to Manchester. I won't forget it. Thanks in particular to David for teaching me the meaning of respect.

Thanks to Autechre for putting me in robot-mode, recommended listening for mind-numbing introduction writing.

And last but not least, thanks to Agnes, Cormac and Dónal for your love and support.

*Our legs dangled. And along came a dawn fisherman, a cosmic porter, in just a little tub with a front shelter and struggling outboard. On his second passing he agreed with our waving and pointing and decided to take us to the other side. We boarded and set off into the rising headwind on which gulls were hanging, still above the boat. Low in the water we passed in silence, feeling the magic tones of night flatten into morning. An infinity of spectra danced on the wind tipped waves as mirages on an endless plane. Holographic light, sheathed and squinting out from soft metal leapt in untraceable parcels, reflecting the bouncing energy within every colour, surface and sound, so that all senses became one. At the eastern shore Alejandro dropped us at the Chinese Gardens, asking only for a photo.*

Thom Henshall, *The Commentary*

# Supporting Publications

**MacCrann N.**, Zuntz J., Bridle S., Jain B., Becker M. R., 2015, *Cosmic discordance: are Planck CMB and CFHTLenS weak lensing measurements out of tune?*, MNRAS, 451, 2877

The DES Collaboration et al., Corresponding authors: **MacCrann, N.**, Zuntz, J., 2015, *Cosmology from Cosmic Shear with DES Science Verification Data*, preprint, (`arXiv:1507.05552`)

Jarvis, M. and Sheldon, E. and Zuntz, J. and Kacprzak, T. and Bridle, S. L. and Amara, A. and Armstrong, R. and Becker, M. R. and Bernstein, G. M. and Bonnett, C. and Chang, C. and Das, R. and Dietrich, J. P. and Drlica-Wagner, A. and Eifler, T. F. and Gangkofner, C. and Gruen, D. and Hirsch, M. and Huff, E. M. and Jain, B. and Kent, S. and Kirk, D. and **MacCrann, N.**, et al., 2015, *The DES Science Verification Weak Lensing Shear Catalogs*, preprint, (`arXiv:1507.05603`)

# Chapter 1

# Introduction

Apparently we live in an 'almost perfect Universe'[1]. A variety of observational probes, with the *Planck*[2] satellite's exquisite measurements of the Cosmic Microwave Background at the forefront, indicate that we live in a universe whose large-scale properties can be described by a six-parameter model known as ΛCDM. So what is there to do? Do we care about improving the precision to which we know the Universe's mean density from 1% to 0.5%? Personally I do not. What motivates me, and I assume most cosmologists, is that although we have an extremely successful description of the Universe, this is not the same as a successful *explanation*. The 'Λ' in ΛCDM implies the presence of 'dark energy', a placeholder term for whatever is causing the accelerated expansion of the Universe. We know what dark energy does, but is it a substance, or does it point to a problem with our theories of gravity? If it is a substance, what is it made of? In the science chapters of this thesis, the mentions of dark energy are not as frequent as one might expect from this stated motivation. This is because weak lensing, the cosmological probe which I have worked on primarily, is only now reaching the maturity required to produce competitive constraints on models of dark energy; my efforts have mostly been attempts to overcome systematic effects

[1] `http://www.esa.int/Our_Activities/Space_Science/Planck/Planck_reveals_an_almost_perfect_Universe`

[2] `http://www.esa.int/Planck`

in weak lensing analyses.

In this chapter, I start (§1.1-1.4), by describing the 'concordance model' of cosmology including the geometry, expansion history and growth of structure of the Universe. Amongst the countless books, review articles and of course other theses' introductions on the topic, my description will likely stand out like a piece of dried grass in a hay-stack. However, it is reasonably concise, up-to-date in terms of including observational results from the last few years, and should provide a non-cosmologist at least some of the context required to understand the rest of the thesis. In §1.5, I describe some of the cosmological probes which provide compelling evidence for the concordance cosmological model. In §1.6, I discuss one of these probes, weak lensing, in more detail. I start by overviewing weak lensing theory in §1.6.1-1.6.5, and describe the use of cosmic shear as a cosmological probe in §1.6.6. Much of this thesis involves the Dark Energy Survey, which I describe briefly in §1.7. I conclude this chapter in §1.8 with a brief preview of the rest of the thesis.

## 1.1 The Cosmological Principle and the Expanding Universe

I start with the *cosmological principle*, that when viewed on sufficiently large scales, the Universe looks the same to all observers, independent of their location. This implies that the Univserse we observe should be isotropic and homogeneous. The most exquisite example of the Universe's observed isotropy is the Cosmic Microwave Background radiation (CMB). This is 2.7K, close-to-blackbody radiation which is observed to be isotropic to one part in $10^5$.

A caveat to the expectation of homogeneity is that a Universe that evolves with time will not appear homogeneous; observations of a more distant region of the Universe will appear less evolved than observations of a closer region, since the

light received originates from an earlier time in the case of the more distant region. This caveat became necessary to preserve the cosmological principle with Edwin Hubble's 1929 observations of Cepheid variable stars (Hubble 1929). Hubble used three of the observable properties of Cepheids to arrive at a startling result. Cepheids are pulsating stars with a tight relationship between pulsation period and luminosity, hence their distance can be inferred from from their observed period and flux. Hubble also used measurements by V. M. Slipher (e.g. Slipher 1917) of the redshift, $z$, of these objects, which is the fractional increase in the wavelength of the observed radiation, $\lambda_o$, relative to the wavelength at emission, $\lambda_e$

$$z = \frac{\lambda_o - \lambda_e}{\lambda_e}. \tag{1.1}$$

Hubble's startling result was that Cepheids at a greater distance from earth had a greater redshift. In a static Universe (i.e. one which did not evolve with time), the implication would be that this observed redshift is Doppler shift due to the emitting objects' velocities relative to the Earth. The Doppler redshift $z_{\text{Doppler}}$ would be given by

$$z_{\text{Doppler}} = v/c \tag{1.2}$$

where $v$ is the speed of the Cepheid relative to Hubble. The greater Doppler shift of further away Cepheids would imply that they had higher velocity relative to the Earth, a violation of homogeneity. However, in an expanding universe, the observed redshift of light can be ascribed to the expansion that has occurred since emission of that light. The light from more distant objects, which was emitted at earlier times, will experience more expansion, and will therefore appear more redshifted. This is known as *cosmological redshift*. Hence Hubble's observations were not inconsistent with an expanding homogeneous universe, only with a static homogeneous universe.

Hubble's observations implied a linear relation between the objects' distance,

$d$, and redshift, $z$, which we now call Hubble's law,

$$z = \frac{H_0}{c} d \tag{1.3}$$

where $H_0$ is the *Hubble constant*. $H_0$ is the present day value of the *Hubble parameter* $H(t)$. $H_0$ is often written in terms of the order unity *dimensionless Hubble parameter*, $h$, via

$$H_0 = 100\, h\, \mathrm{km\, s^{-1}\, Mpc^{-1}}. \tag{1.4}$$

## 1.2 The Geometry and Contents of the Universe and ΛCDM

On sufficiently large scales (i.e. those where we can assume homogeneity), the Universe's evolution can be described as the dynamics of various cosmological fluids under gravity. In General Relativity (GR) (Einstein 1915), the action of gravity is encoded in the geometry of spacetime, described by the metric tensor of that spacetime. For a homogeneous, expanding universe, the most general metric is the Friedmann-Lemaitre-Robertson-Walker (FLRW) metric

$$ds^2 = -c^2 dt^2 + a^2(t)[d\chi^2 + D_A(\chi)^2(d\theta^2 + \sin^2(\theta) d\phi^2)]. \tag{1.5}$$

Here $\chi$ is the *comoving radial distance*. If the light we observe from an object was emitted at time $t$, then that object is at a comoving radial distance

$$\chi(t) = \int_t^{t_0} \frac{c dt}{a(t)} \tag{1.6}$$

where $t_0$ is the time now. $a(t)$ is the *scale factor*, which is conventionally normalised to one at the present time. The nature of $a(t)$ can be intuited by considering a spacelike ($dt = 0$) interval at different times - the displacement element

$ds$ is scaled by $a(t)$. Hence $a(t)$ relates 'comoving' distances, $\chi$ i.e. those in a coordinate system where the Universe is not expanding, to physical distances, $d$, via $d(t) = a(t)\chi$.

$D_A(\chi)$ is the *comoving angular diameter distance*, which depends on the Universe's global curvature, $K$, via

$$D_A(\chi) = \begin{cases} \sqrt{K}\sin(\sqrt{K}\chi) & \text{if } K > 0 \\ \chi & \text{if } K = 0 \\ K^{-\frac{1}{2}}\sinh(\sqrt{-K}\chi) & \text{if } K < 0. \end{cases} \tag{1.7}$$

$D_A(\chi)$ relates $l$, an object's comoving size, to $\theta(\chi)$, its observed angular size at comoving distance $\chi$, via $\theta(\chi) = l/D_A(\chi)$.

It will also be useful to define the luminosity distance, $D_L$, which relates an object's flux, $f$, to its luminosity, $L$ via

$$D_L(\chi) = \sqrt{\frac{L}{4\pi f}} = (1+z)D_A(\chi). \tag{1.8}$$

The full definition of the Hubble parameter is

$$H(a) = \frac{\dot{a}}{a}. \tag{1.9}$$

The scale factor is related to the cosmological redshift via

$$a(t) = \frac{1}{1+z}. \tag{1.10}$$

The comoving radial distance can be recast as an integral over $z$ using equations 1.9 & 1.10

$$\chi(z) = \int_0^z \frac{cdz'}{H(z')}. \tag{1.11}$$

Einstein's field equations relate the local curvature of spacetime to the stress-

energy tensor, which in the case of the Universe, is determined by the properties of the cosmological fluids it contains. Solving Einstein's equations in the FLRW metric results in Friedmann's equations, which govern the Universe's expansion

$$\left(\frac{\dot{a}}{a}\right)^2 = H^2 = \frac{8\pi G}{3}\rho - \frac{Kc^2}{a^2} + \frac{\Lambda c^2}{3} \tag{1.12}$$

$$\frac{\ddot{a}}{a} = -\frac{4\pi G}{c^2}(\rho + 3p) + \frac{\Lambda c^2}{3} \tag{1.13}$$

where $\rho$ and $p$ are the energy density and pressure of the Universe, and $\Lambda$ is a constant, known as the *cosmological constant*. It was originally included by Einstein to allow for a static Universe solution to the Einstein equations. The Friedman equations can be simplified by redefining $\rho$ and $p$ to absorb the cosmological constant terms

$$\rho \to \rho + \frac{\Lambda c^2}{8\pi G} \tag{1.14}$$

$$p \to p - \frac{\Lambda c^4}{8\pi G}. \tag{1.15}$$

yielding

$$\left(\frac{\dot{a}}{a}\right)^2 = H^2 = \frac{8\pi G}{3}\rho - \frac{Kc^2}{a^2} \tag{1.16}$$

$$\frac{\ddot{a}}{a} = -\frac{4\pi G}{c^2}(\rho + 3p). \tag{1.17}$$

From equation 1.17, it is clear that the sign of the Universe's acceleration, $\ddot{a}$ depends on the balance between the energy density and pressure of its contents. It is instructive to consider a universe containing a cosmological fluid with equation of state

$$p = w\rho c^2 \tag{1.18}$$

where $w$ is some constant. Then the value of $w$ determines whether this universe's expansion accelerates or decelerates. For $w < -\frac{1}{3}$, from equation 1.17, this

universe's expansion accelerates.

For an adiabatically expanding universe, we can use the first law of thermodynamics to derive the fluid equation. The work done on the external pressure $p$ by a volume element $V$ is $pdV$. If this volume element contains energy $U = \rho c^2 V$, then we have:

$$dU = d(\rho c^2 V) = -pdV$$
$$\rho c^2 dV + V c^2 d\rho = -pdV$$

Noting that $V \propto a^3$, and substituting equation 1.18, we find

$$\frac{d\rho}{da} = -3\left(\frac{p + \rho c^2}{a}\right) \tag{1.19}$$
$$\frac{d\rho}{da} = -3\frac{\rho c^2(1+w)}{a}. \tag{1.20}$$

The cosmological fluids that we require to model the Universe's expansion history in the standard cosmological model are

- **Baryonic Matter.** Cosmologists use the term 'baryonic matter' to refer to ordinary matter, the massive particles such as protons, neutrons, electrons (but not neutrinos) that we are familiar with from particle physics. It may be because the baryons (protons and neutrons) dominate the mass content of ordinary matter, that cosmologists refer to this component as 'baryonic matter', although that may be giving us too much credit. Baryonic matter can interact with photons, hence we can 'see' it. Matter, which clumps into structures separated by vast voids, can be assumed to be pressureless in it's large scale behaviour i.e. $w = 0$. Substituting this into equation 1.20, we find that the baryon density, $\rho_b \propto a^{-3}$.

- **Cold Dark Matter (CDM).** There is compelling observational evidence for *dark matter*, another form of matter which either interacts with photons

too weakly for us to detect at present, or not at all. In particular, as early as the 1930s, observations by Oort (1932) of the dynamics of Milky Way stars suggested the presence of far more mass than suggested by the visible content of the Milky Way, while Zwicky (1937) came to similar conclusions from the dynamics of galaxies within the Coma cluster. This was put onto a firm footing with studies of galactic rotation curves (Rubin 1983). Meanwhile, the value of the baryonic matter density inferred from both Big Bang Nucleosynthesis (BBN) and CMB observations is $\approx 6$ times smaller than the total matter density favoured by a wide range of cosmological probes, with dark matter assumed to make up the difference. Further evidence comes from systems such as the Bullet cluster, the spectacular remains of the merging of two clusters, which shows an offset between the gas inferred from X-ray observations and the total mass distribution inferred from gravitational lensing (Clowe et al. 2006).

The 'cold' in CDM describes dark matter that can be treated as non-relativistic and pressureless since matter-radiation equality (the epoch in the early universe at which the matter and radiation densities were equal). Gravity is ambivalent about whether matter is baryonic or dark, so we can consider a total matter density $\rho_m = \rho_c + \rho_b$, which evolves as $\rho_m \propto a^{-3}$.

- **Radiation.** This is the contribution to the energy density from photons, which have $w = 1/3$. Equation 1.20 implies that the radiation density, $\rho_r$, scales as $\rho_r \propto a^{-4}$. The contribution of radiation to the total energy density today is negligible but it was dominant in the early universe (at much smaller $a$).

- **Dark Energy.** The substitution in equation 1.15 implies that the cosmological constant, $\Lambda$ can also be considered a cosmological fluid, with $w = -1$. As befitting a cosmological constant, it has constant energy density $\rho_\Lambda$. From equation 1.17, in a universe dominated by $\Lambda$ the scale factor

$a(t)$ increases exponentially i.e. there is accelerated expansion. More generally we consider the possibility that $w \neq -1$ and refer to this componenet as *dark energy*.

It's convenient to define the *critical density*, $\rho_{\rm crit}$

$$\rho_{\rm crit} = \frac{3H^2}{8\pi G}, \tag{1.21}$$

which from equation 1.16, is the total energy density for which the curvature $K$ is zero. For each energy density component $i$, we define $\Omega_i \equiv \rho_i/\rho_{\rm crit}$. Then we can write the total energy density as

$$\rho = \rho_{\rm crit}\Omega = \rho_{\rm crit}(\Omega_m + \Omega_r + \Omega_\Lambda). \tag{1.22}$$

The global curvature, K, is then positive for $\Omega > 1$, flat ($K = 0$) for $\Omega = 1$, and negative for $\Omega < 1$. We can additionally define $\Omega_k = 1 - \Omega$. By convention, the $\rho_i$ and $\Omega_i$ refer to their present day (i.e. $t = 0$, $a = 1$) value, and $\rho_i(t)$, $\Omega_i(t)$ to their value at some other time $t$. When I differentiate between the baryonic and dark components of $\Omega_m$, I'll refer to them as $\Omega_b$ and $\Omega_c$ respectively (the 'C' stands for 'cold' dark matter).

In the absence of a cosmological constant ($\Lambda = 0$), a universe with positive curvature will eventually stop expanding, and contract into a 'Big-Crunch'; this is known as a 'closed' universe. One with negative curvature is known as an 'open' universe and will expand forever. Observations indicate that our universe is very close to flat, although the apparent presence of a cosmological constant, or dark energy, suggests the Universe is destined to expand forever anyway.

These are the components of the Universe that are required to model the expansion history of the Universe inferred from observations, as I'll outline in §1.5. They make up the components of the current 'vanilla' cosmological model, the ΛCDM model, a Universe with a cosmological constant and cold (non-relativistic

since matter-radiation equality) dark matter, as well as baryonic matter and radiation. Current observations constrain the curvature to be very close to zero (e.g. Planck Collaboration et al. 2015a); unless otherwise specified, I will take the term ΛCDM to mean a flat (i.e. zero curvature) ΛCDM model.

## 1.3 Beyond ΛCDM

Although ΛCDM successfully models a wide range of cosmological observations, the 'Λ' in particular lacks a theoretical explanation that would take it from a phenomenon inferred from observations, to a tenet of fundamental physics. There are numerous theories which try to explain the observed acceleration of the universe without a cosmological constant, including those which modify GR. All of these must satisfy the requirement of being able to produce a Universe that looks very similar to one with a cosmological constant. A somewhat agnostic approach to probing dark energy with observational cosmology is to look for deviations from a cosmological constant. Evidence of deviation from ΛCDM would be a spectacular finding[3] and so many current and and upcoming projects are at least partly designed to be sensitive to these deviations.

The most popular way of parameterising the deviation from a cosmological constant $\Lambda$ is to allow the dark energy equation of state parameter, $w$, to vary, either to a constant, $\neq -1$ value, or additionally with some time-dependence via (Chevallier & Polarski 2001; Linder 2003)

$$w(a) = w_0 + w_a(1 - a), \tag{1.23}$$

where $w_0$ is the the value today ($a = 1$). This parameterisation was used by the report of the Dark Energy Task Force (DETF, Albrecht et al. 2006), which was set up to to advise the US Department of Energy, NASA, and the US National

[3]This kind of statement is what makes performing 'blind' analyses so important.

Science Foundation on approaches to studying dark energy, and has played a significant role in shaping the current and future landscape of observational cosmology. The DETF defined a 'figure of merit' to allow quantitative comparison of the sensitivity of different observational approaches to the properties of dark energy[4], defined as "the reciprocal of the area of the error ellipse enclosing the 95% confidence limit in the $w_0 - w_a$ plane". Hence a larger figure of merit implies tighter constraints on $w_0$ and $w_a$.

Another extension of ΛCDM that is of interest to the fundamental physics world as well as cosmologists is the inclusion of massive neutrinos. The ΛCDM model assumes neutrinos are massless and therefore fully relativistic, and just add to the radiation density. Since the observed oscillations of solar neutrinos (Fukuda et al. 1998) imply they do in fact have non-zero mass, including massive neutrinos is an obvious extension of ΛCDM to explore.

## 1.4 The Growth of Structure

In 1.5.1, I explain how density fluctuations in the hot plasma of the early Universe resulted in sound waves that are imprinted onto the CMB power spectrum. In the inflationary picture, these density fluctuations are the result of quantum fluctuations that are rapidly expanded to very non-quantum spatial scales by the Universe's rapid expansion, and thus captured. The overdensity, $\delta(\mathbf{x}, t)$ is defined

$$\delta(\mathbf{x}, t) \equiv \frac{\rho(\mathbf{x}, t) - \bar{\rho}(t)}{\bar{\rho}(t)}, \tag{1.24}$$

where $\bar{\rho}(t)$ is the mean density at time $t$. It's more convenient to consider the density fluctuations in Fourier space, defining

$$\tilde{\delta}(\mathbf{k}) = \int d^3\mathbf{x}\delta(\mathbf{x})e^{i\mathbf{k}.\mathbf{x}}. \tag{1.25}$$

[4]to the parameterisation in equation 1.23 anyway...

**k** is the wavenumber, with small $k$ implying large scales in real-space, and large $k$ implying small scales in real-space. In the case of isotropic, Gaussian density fluctuations, the statistics of the density fluctuations can be completely described by the power spectrum, $P_i(k)$, defined as

$$\langle\tilde{\delta}(\mathbf{k})\tilde{\delta}(\mathbf{k'})\rangle \equiv (2\pi)^3\delta_D^3(\mathbf{k}-\mathbf{k'})P_i(k). \tag{1.26}$$

Inflation generically predicts a dimensionless power spectrum for initial fluctuations in the gravitational potential, $\Delta^2_{\Phi,i}(k)$ which is close to scale invariant

$$\Delta^2_{\Phi,i}(k) \propto k^3 P_{\Phi,i}(k) \propto k^{n_s-1} \tag{1.27}$$

where $n_s$ is the scalar spectral index, with $n_s = 1$ meaning scale invariance. The latest results from the *Planck* satellite (Planck Collaboration et al. 2015a) find $n_s = 0.9655 \pm 0.0062$ i.e. a close to, but significantly not, scale invariant power spectrum. Using Poisson's equation to relate potential fluctuations to density fluctuations implies an initial power spectrum of density fluctuations

$$P_i(k) = A_s k^{n_s}. \tag{1.28}$$

These density fluctuations provide the seeds for structure growth, and hence the formation of galaxies, in the low redshift Universe. For a non-relativistic fluid, once can show (see e.g. Padmanabhan 1993) that small ($\delta \ll 1$) dark matter perturbations, $\delta$, have the following behaviour

$$\ddot{\delta} + 2H\dot{\delta} - 4\pi G\rho_m\delta = 0. \tag{1.29}$$

The term in $\delta$ leads to a growing solution, which for the flat, $\Lambda = 0$ case (a good

approximation except at late times when $\Omega_\Lambda$ becomes important) is given by

$$\delta \propto 1 + \frac{3\rho_r}{2\rho_m} = 1 + \frac{3a}{2a_{eq}}, \tag{1.30}$$

where $\rho_r$ and $\rho_m$ are the energy densities of the radiation and the non-relativistic matter whose perturbations are under consideration, and I have defined $a_{eq}$, the scale factor at matter radiation equality, i.e. when $\rho_r = \rho_m$. The $\dot{\delta}$ terms leads to a decaying solution which can be ignored at times much later than the origin of the perturbations. For $a \ll a_{eq}$ the rapid expansion due to radiation domination means matter density perturbations are effectively frozen, while $\delta \propto a$ for $a \gg a_{eq}$.

This treatment assumes Newtonian dynamics, which is only valid on scales smaller than the horizon, $R_H$, the distance light can have travelled since the Big Bang, which is of order $c/H$. Relativistic perturbation theory (see e.g. Padmanabhan 1993) predicts that the superhorizon modes evolve as

$$\delta(a) \propto \begin{cases} a^2 & \text{for } a < a_{eq} \\ a & \text{for } a > a_{eq} \end{cases}. \tag{1.31}$$

During radiation domination the horizon grows as $a^2$, while after $a_{eq}$, during matter domination, it grows as $a$. So the general picture is that during radiation domination, density perturbations with physical scale $a\lambda$ start growing according to equation 1.31 until they 'enter' the horizon at $a_{\rm enter}$ i.e. the horizon grows sufficiently such that

$$a_{\rm enter}\lambda < \frac{c}{H(a_{\rm enter})}. \tag{1.32}$$

If this occurs during radiation domination i.e. if $a_{\rm enter} < a_{eq}$, then the perturbation's growth is suppressed according to equation 1.30. Well after radiation domination (for $a \gg a_{eq}$), the growth resumes again as $\delta \propto a$. This behaviour is known as the *Mészáros effect*, after Meszaros (1974).

One can define a scale $k_0$, which corresponds to the particle horizon at matter-

radiation equality. In the idealised situation of an instantaneous change between a radiation dominated and matter dominated universe, $k_0$ would mark the threshold above which scales are suppressed during radiation domination. For $k \ll k_0$ i.e. scales which are still larger than the horizon (super-horizon) at matter domination, we expect the power spectrum of linear matter density perturbations, the *linear matter power spectrum*, $P_\delta^{\rm lin}(k)$ to be proportional to the primordial power spectrum, since the super-horizon modes all experience the same growth. On scales much smaller than $k_0$ ($k \gg k_0$), there is $\sim k^{-4}$ suppression of power due to modes entering the horizon, and being frozen by the rapid expansion during radiation domination (see e.g. Peacock 2003). The large and small scale behaviour that emerges is

$$P_\delta^{\rm lin}(k) \propto \begin{cases} P_i(k) \propto k^{n_s} & \text{for } k \ll k_0 \\ P_i(k) k^{-4} \propto k^{n_s - 4} & \text{for } k \gg k_0 \end{cases}. \tag{1.33}$$

Thus $k_0$ approximately sets the peak position of the linear matter power spectrum, which is plotted as the solid line in Figure 3.3. For late times, $t \gg t_{eq}$, the redshift evolution of linear density perturbations is often parameterised in terms of the *linear growth factor*, $G(z)$ defined via

$$\delta(\mathbf{x}, z) = \delta(\mathbf{x}, z_i) \times \frac{G(z)}{G(z_i)} \tag{1.34}$$

where $z_i$ is some arbitrary early redshift. The linear matter power spectrum can then be be related to the power spectrum at $z = 0$ via

$$P(k, z) = \left(\frac{G(z)}{G(0)}\right)^2 P(k, 0). \tag{1.35}$$

While for a particular cosmological model, the amplitude of the matter power spectrum at a given redshift can be related to the primordial power spectrum amplitude, $A_s$, a less model-dependent parameterisation for low-redshift cosmo-

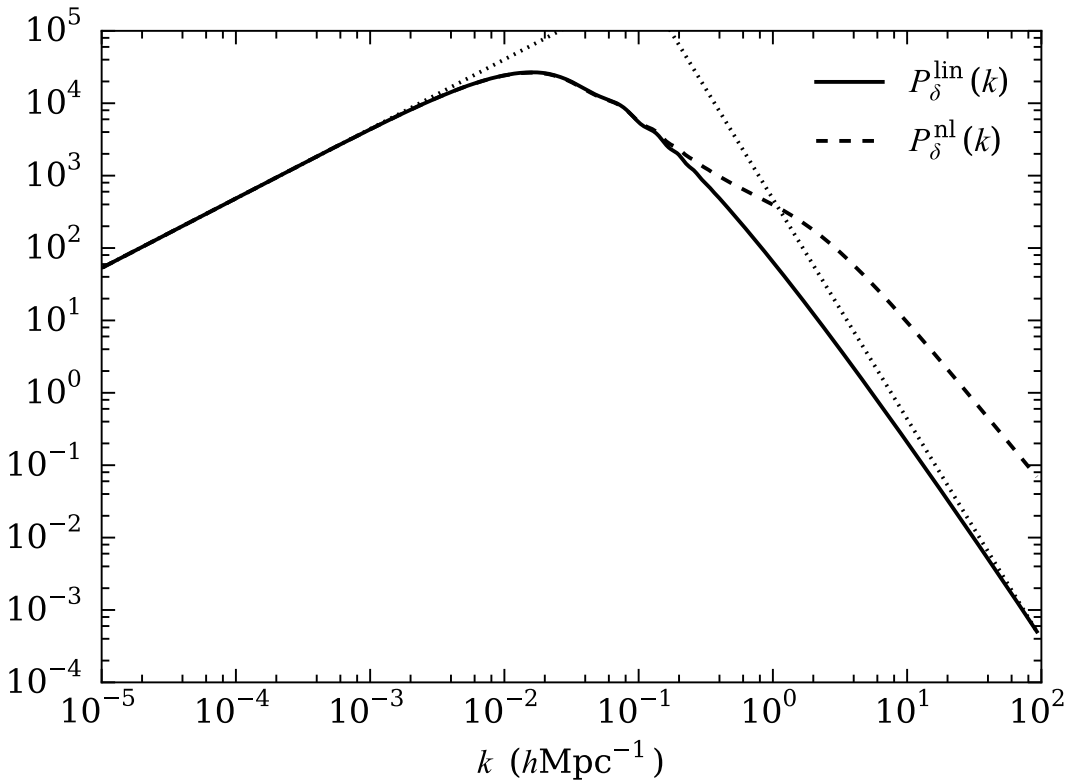


Figure 1.1: The $z = 0$ matter power spectra. The solid line is the linear matter power spectrum, calculated using CAMB (Lewis et al. 2000). The dashed line is the nonlinear matter power spectrum, using the Takahashi et al. (2012) version of HALOFIT (Smith et al. 2003). The dotted lines are the power laws from equation 1.33.

logical probes is $\sigma_R(z)$. $\sigma_R(z)$ is the linear theory rms mass density in $Rh^{-1}$Mpc spheres at redshift $z$, given by

$$\sigma_R^2(z) = \int_0^\infty \frac{k^2 dk}{2\pi} P_\delta^{\rm lin}(k,z)\tilde{W}^2(k,R) \tag{1.36}$$

where $\tilde{W}$ is the Fourier transform of a spherical top hat window function,

$$\tilde{W}(k,R) = \frac{3}{k^3R^3}\left[\sin(kR) - kR\cos(kR)\right]. \tag{1.37}$$

By convention $\sigma_8 \equiv \sigma_8(z = 0)$.

How does dark energy affect the growth of linear structure at late times? This can be qualitatively answered with reference to the evolution equation for

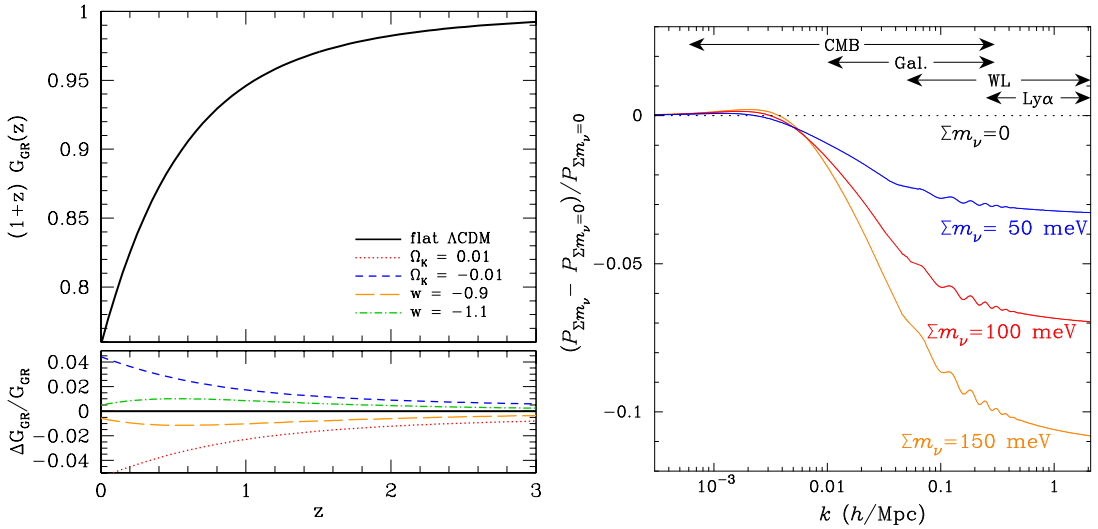


Figure 1.2: These plots show the effect on the linear density perturbations of two extensions to ΛCDM. The left panel, taken from Weinberg et al. (2013), shows the ΛCDM (i.e. $w = -1$) growth factor as a function of redshift in the upper panel, and the fractional differences induced by having $w = -0.9$ (orange, long dashed line) or $w = -1.1$ (green dot-dashed line). The right panel, taken from Abazajian et al. (2015), shows the fractional change in the linear matter power spectrum of due to the presence of massive neutrinos, for different values of the sum of the neutrino masses $\sum m_\nu$ (which are labelled on the plot).

the density perturbations, equation 1.29. Compared to an EdS universe ($\Omega_m = 1$), the accelerated expansion due to $\Lambda$ will increase $H(t)$, and decrease $\rho_m(t)$, hence the decaying mode solution is increased, and the growing mode solution is decreased i.e. dark energy suppresses the growth of structure compared to the EdS case. The amount of suppression depends on the dark energy equation of state parameter, $w$, as shown in the left panel of Figure 1.2, which compares the growth factor as a function of redshift for different values of $w$.

Massive neutrinos, one of the most promising extensions to ΛCDM, have a marked effect on the growth of the density perturbations at low redshift. The right panel of Figure 1.2 shows the $z = 0$ linear matter power spectrum for different values of the sum of the neutrino masses, $\sum m_\nu$, compared to the $\sum m_\nu = 0$ case. In fact, Figure 1.2 isolates the effect of the neutrino mass on the shape of the matter power spectrum by normalising the matter power spectra at large scales.

In the early universe (before $z_{\rm nr} \sim 2000 m_\nu / 1\,{\rm eV}$ (Abazajian et al. 2015)), neutrinos behave relativistically, free-streaming out of matter overdensities, and therefore reducing the amount of clustering on scales smaller than the free-streaming length.

### 1.4.1 Nonlinear growth of structure

As matter perturbations grew in the Universe, structures such as halos stabilised, and the linear treatment above, which requires $\delta \ll 1$, no longer holds on small scales. Power is transferred from large to small scales (since e.g. halos are more likely to form in large scale overdensities), so Fourier modes no longer evolve independently. While perturbation theory has had some success on mildly nonlinear scales, and analytic models such as the halo model (Seljak 2000; Peacock & Smith 2000) are surprisingly successful on highly nonlinear scales, suites of N-body simulations are the most successful method of obtaining reliable, cosmology dependent predictions of the nonlinear matter power spectrum across a wide range of scales. The most notable efforts include Peacock & Dodds (1996), Smith et al. (2003) and Takahashi et al. (2012) (the dashed line in Figure 3.3), who calibrated a fitting formula to (increasingly high resolution) suites of N-body simulations to allow prediction of $P(k, z)$ at different points in cosmological parameter space. The current state-of-the-art in nonlinear matter power spectrum prediction is the FrankenEmu[5] emulator based on the Extended Coyote Universe Simulations (Heitmann et al. 2014). As I shall discuss in §5, none of these approaches account for the effect of non-gravitational physics on the matter clustering.

[5] http://www.hep.anl.gov/cosmology/CosmicEmu/emu.html

## 1.5 Observational Probes of Cosmology

Observational probes of cosmology have come a long way from Hubble's Cepheid variables. Cosmologically sensitive phenomena observed throughout the electromagnetic spectrum are exploited for cosmological inference, from the microwaves of the 2.7 K CMB, to X-ray emission from the $\sim 10^8$ K intracluster medium. There are even prospects for observing the Universe using non-electromagnetic means, for example using neutrinos (e.g. IceCube Collaboration (2013)), and the spectacular recent detection of gravitational waves (Abbott et al. 2016).

I focus here on a few of the most successful cosmological probes, both in terms of their historical impact, and their current constraining power on the standard cosmological model and its 1-2 parameter extensions, rather than giving a comprehensive overview of observational cosmology. Before getting into details, a general point to make is that it is the presence of multiple, very different cosmological probes that make the evidence for a close-to-ΛCDM universe so convincing.

### 1.5.1 The cosmic microwave background

I've already mentioned the temperature of the CMB as evidence for the isotropy of the Universe. This isotropy suggests that regions that are causally disconnected today were once causally connected. In the standard cosmological model, this is achieved by having a period of extremely rapid expansion in the early universe, known as inflation (Guth 1981; Linde 1982; Albrecht & Steinhardt 1982). The early universe was a hot soup consisting of mostly photons, electrons and protons until 'recombination', 378,000 years after the Big Bang when sufficient expansion and cooling had occurred for protons and electrons to form hydrogen atoms. This allowed photons to decouple from matter and travel freely, which we observe today as the CMB. The epoch of photon decoupling defines a surface in space, the *surface of last scattering*, from which the light we're receiving now was emitted at

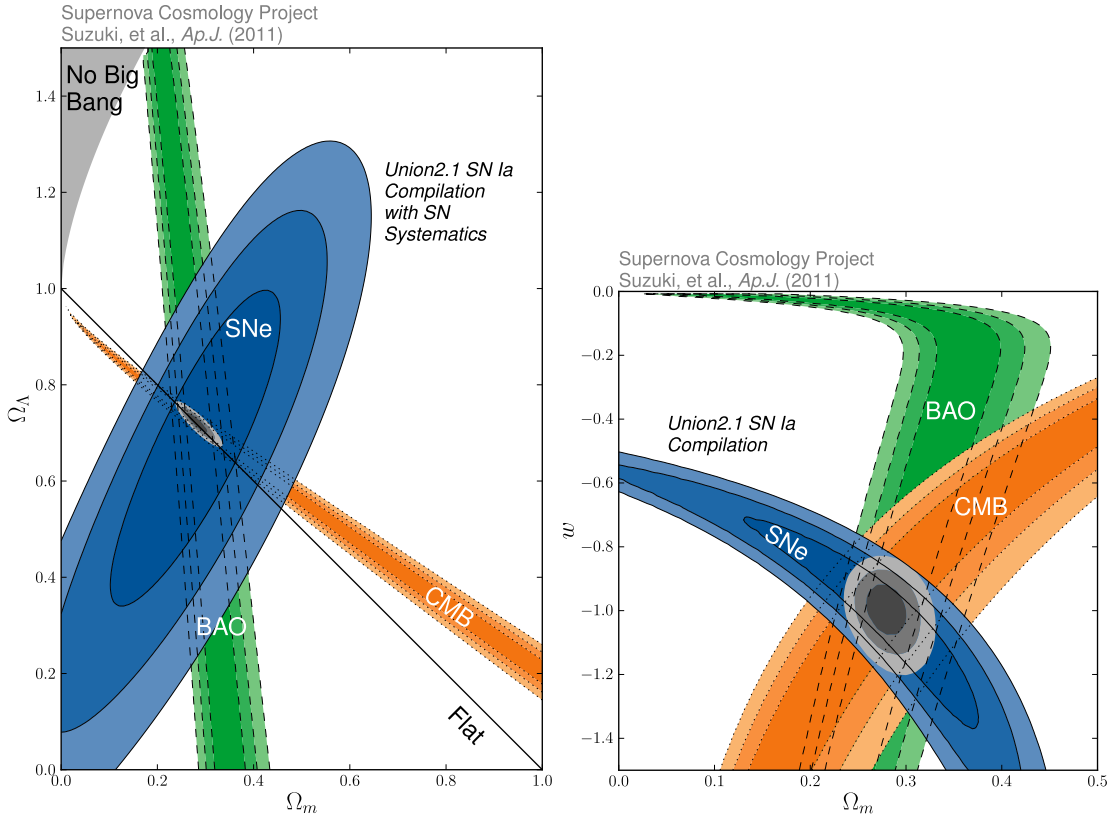


Figure 1.3: Taken from Amanullah et al. (2010), both plots show the consistency and complementarity (i.e. the different degeneracy directions) of CMB, BAO and SNe Ia data. The blue contour labelled 'SNe' uses SN Ia data from Amanullah et al. (2010) and the Union2 compilation (Kowalski et al. 2008); the orange contour labelled 'CMB' uses the seven-year WMAP data (Komatsu et al. 2011); the green contour labelled 'BAO' uses the BAO measurements of Percival et al. (2010) (from SDSS and 2dFGRS data). The left panel shows that each probe has a large degeneracy in $\Omega_\mathrm{m}$ and $\Omega_\Lambda$ when flatness is not assumed, but that the combination of the probes breaks this degeneracy, and favours $\Omega_K \approx 0$. Similarly in the right panel (where $\Omega_K$ is not set to zero), each probe individually has strong degeneracy between $\Omega_\mathrm{m}$ and $w$, which is broken by combining the probes.

photon decoupling. The primary *anisotropies* in the CMB temperature, although small, contain a wealth of information about the inhomogeneities of the Universe at the epoch of photon decoupling. The anisotropies were discovered by the COBE satellite (Smoot et al. 1992), and since then two further satellite missions, WMAP (Bennett et al. 2003, 2013) and *Planck* have measured the anisotropies with increasing precision, placing the CMB at the forefront of modern cosmology.

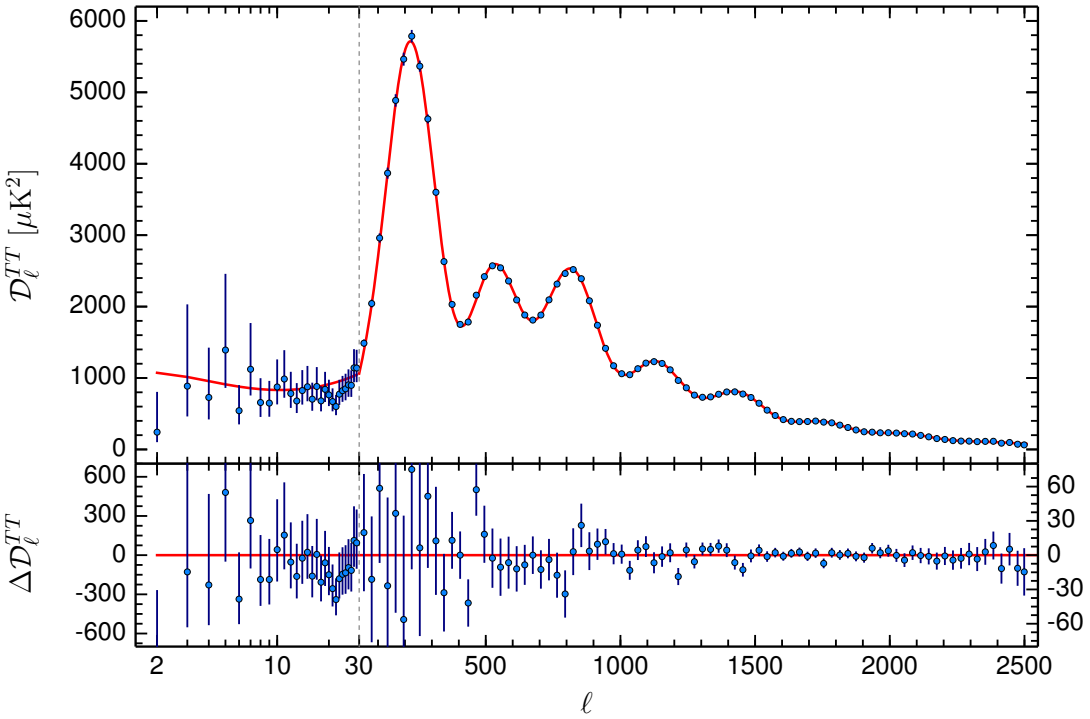


Figure 1.4: The CMB temperature power spectrum measured by the *Planck* satellite, and presented in Planck Collaboration et al. (2015e). The red line shows the best-fit ΛCDMmodel prediction from Planck Collaboration et al. (2015a), using the 'TT+lowP' dataset. The lower panel shows the residuals between the data and this model.

The temperature fluctuation in direction $\hat{\boldsymbol{n}}$, $\Theta(\hat{\boldsymbol{n}})$ can be decomposed in spherical harmonics as

$$\Theta(\hat{\boldsymbol{n}}) = \frac{T(\hat{\boldsymbol{n}}) - \bar{T}}{\bar{T}} = \sum_{lm} \Theta_{lm} Y_{lm}(\hat{\boldsymbol{n}}). \tag{1.38}$$

Assuming statistical isotropy, the temperature fluctuations can be described by the power spectrum $C_l$, given by

$$\langle \Theta_{lm} \Theta^*_{l'm'} \rangle = \delta_{ll'} \delta_{mm'} C_l. \tag{1.39}$$

The *Planck* temperature power spectrum presented in Planck Collaboration et al. (2015e) is shown in Figure 1.4. The peaks are known as the acoustic peaks, since they arise from sound waves in the hot plasma of photons, baryons, and electrons before recombination. Before recombination, photons and baryons are tightly

coupled through interactions of free electrons. Acoustic oscillations, or sound waves, arise from the competing effects of gravity and radiation pressure - the potential wells resulting from density fluctuations attract baryons, causing an overdensity in the coupled photons, and an increase in the repulsive radiation pressure.

The first (largest scale) peak corresponds to the largest physical mode of the sound waves, with characteristic physical scale set by the *sound horizon*, $r_s$ at last scattering, $r_* = r_s(z_*)$. This is the maximum distance travelled by sound waves up to last-scattering

$$r_* = \int_0^{t_*} dt \frac{c_s(t)}{a(t)} = \int_{z_*}^{\infty} \frac{c_s(z)}{H(z)} dz \tag{1.40}$$

where $c_s(z)$ is the sound speed. The observed angular scale, $\theta$, of the first peak is then given by

$$\theta \sim r_*/D_A(z_*) \tag{1.41}$$

where $z_*$ ($t_*$) is the redshift (time) of last-scattering. The main cosmological analysis of the *Planck* 2015 data is performed in Planck Collaboration et al. (2015a) (PCP15 henceforth). They quote constraints from various different combinations of CMB temperature and polarisation data. Unless specified otherwise, I will quote the 'TT + lowP' constraints (see PCP15 for a description of this and the other *Planck* dataset combinations). The angular scale of the first acoustic peak is constrained to better than 1% precision by PCP15. While $r_*$ depends primarily on $\Omega_m h^2$ and $\Omega_b h^2$, $D_A(z_*)$ depends on the $z < z_*$ expansion history, which depends on both $\Omega_\Lambda$ and $\Omega_K$. Different combinations of $\Omega_\Lambda$, $\Omega_K$, $\Omega_m$ and $h$ can produce very similar primary CMB anisotropies, this is referred to as "geometrical degeneracy" (Bond et al. 1997; Zaldarriaga et al. 1997; Efstathiou & Bond 1999). A consequence of this is the strong degeneracy between $\Omega_\mathrm{m}$ and $\Omega_\Lambda$ shown in Figure 1.3, especially when flatness is not enforced. Information from low redshift can break these degeneracies. For CMB data alone, some degener-

acy breaking comes from the *secondary anisotropies* in the CMB temperature, caused by interactions between CMB photons and matter along the line of sight, for example the integrated Sachs-Wolfe (ISW) effect, and gravitational lensing of the CMB (CMB lensing henceforth). Using only CMB data, PCP15 find

$$\Omega_K = -0.052^{+0.032}_{-0.018} \tag{1.42}$$

and with CMB lensing,

$$\Omega_K = -0.0053^{0.0089}_{-0.0075}. \tag{1.43}$$

While the acoustic peak positions are sensitive to some combination of $h$, $\Omega_b$ and $\Omega_c$, measuring the relative heights of the acoustic peaks helps to disentangle $\Omega_b h^2$ and $\Omega_c h^2$, which are measured to 1.5% and 3% precision by Planck temperature data alone, assuming ΛCDM. Furthermore, the underlying shape and amplitude of the power spectrum constrains the primordial power spectrum, with $n_s$ and $A_s$ (see equation 1.28) constrained to 1% and 5% accuracy in ΛCDM by PCP15.

The primary CMB anisotropies provide a snap-shot of the high-redshift Universe, and as such provide little information on dark energy, whose effect only becomes significant at low redshift. However, they do play a crucial role in constraining dark energy, because the constraints I've outlined break degeneracies suffered by the low-redshift probes I discuss next. Similar to the case of curvature, when the secondary anisotropies, and in particular CMB lensing are included, dark energy can be constrained by CMB data alone.

### 1.5.2 Type 1a supernovae

I've already introduced an example of a standard candle - the Cepheid variable stars used by Hubble to estimate $H_0$. Cepheids have a known period-luminosity relation, so that a measurement of their period serves as a proxy luminosity, $L$ measurement. When combined with a measurement of the flux, the luminosity

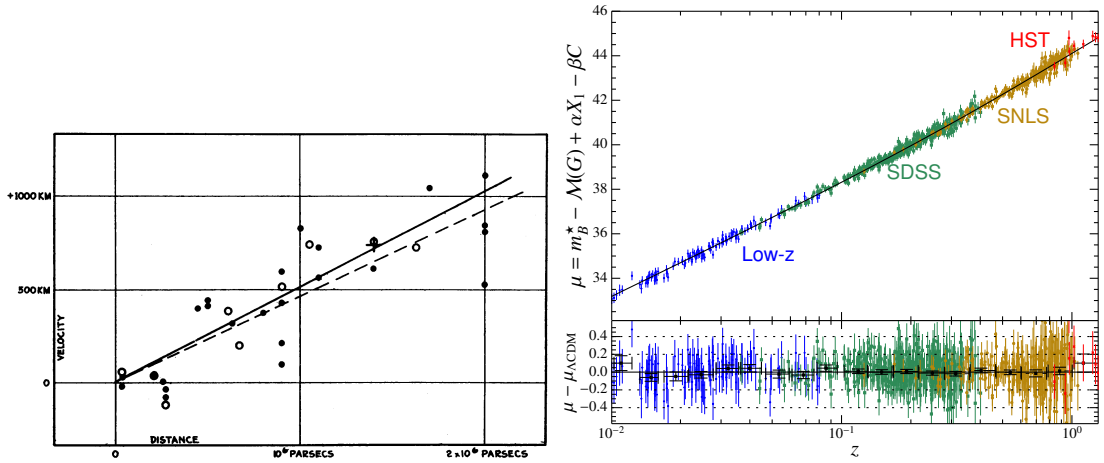


Figure 1.5: The original and modern day Hubble diagrams. The left panel is from Hubble (1929), and shows the recession velocity of 'extra-galactic nebulae' as a function of their distance from Earth. The right panel, from Betoule et al. (2014), is referred to as a Hubble diagram. It shows the 'distance modulus' (related to the apparent magnitude) of 740 Type Ia supernovae, as a function of their redshift. The increase in the gradient at high redshift provides evidence for the accelerated expansion of the Universe.

distance, $d_L$, to the Cepheid can be estimated via

$$f = \frac{L}{4\pi d_L^2}. \tag{1.44}$$

With an estimate of the redshift, $H_0$ can be estimated via equation 1.3. Hubble's original plot is shown in the left panel of Figure 1.5, and shows the expected linear trend between distance and recession velocity, although various systematic errors meant that the gradient is around an order of magnitude larger than the value of $H_0$ favoured today. One of these systematics was the Cepheids' *peculiar motions*, their local velocity relative to the 'Hubble flow', that is, the flow of particles of the idealised cosmological fluids described in §1.2 due to the Universe's expansion. This peculiar motion means the observed redshift contains some Doppler redshift, as well as cosmological redshift. Galaxy peculiar velocities tend to be less than a few thousand km/s, which corresponds to a Doppler redshift of $\sim 10^{-3}$. A way of reducing the importance of peculiar motions therefore, is to find a standard

candle at higher redshift ($\gg 10^{-3}$), which leads me to Type Ia supernovae (SN Ia or SNe Ia henceforth).

SNe Ia are often referred to as 'standardisable' candles. In particular, it is assumed that SNe Ia of the same colour, galactic environment, and whose light curves have the same shape, have the same luminosity, independent of redshift i.e. there exists a mapping from these observable quantities to luminosity. Compared to using Cepheid stars alone, a much improved estimate of $H_0$ can be obtained by calibrating the mapping between the observable properties of SNe Ia and their luminosity, using SNe Ias which are sufficiently local that Cepheid variables in their host galaxies can be observed. Riess et al. (2011) use this technique to estimate $H_0 = 73.8 \pm 2.4\,\mathrm{km\,s^{-1}\,Mpc^{-1}}$ (see Efstathiou 2014a for a reanalysis of the Riess et al. 2011 data, which reported $H_0 = 70.6 \pm 3.3\,\mathrm{km\,s^{-1}\,Mpc^{-1}}$).

The right panel of Figure 1.5, taken from Betoule et al. (2014) is commonly called a Hubble diagram, although it is somewhat different from Hubble's most famous plot. On the y-axis is the 'distance modulus' for each SN Ia, which is a standardized apparent magnitude, corrected for the variation in color, environment and light curve. The apparent magnitude is proportional to the logarithm of the luminosity distance $d_L$, so although the axes are different to Hubble's original plot, we again expect a straight line at low redshift where Hubble's law (equation 1.3) is valid. Inferring $H_0$ directly from this plot requires the calibration of the SN luminosities using Cepheids.

However, the greatest achievement of SN Ia cosmology does not require this calibration. While Hubble's constant cannot be measured directly using SNe Ia, deviations from Hubble's law at high redshift, caused by acceleration or deceleration of the Universe can; these show up as the deviations from a straight line in Figure 1.5[6]. The ratio of the observed flux of a low redshift SN Ia to a high redshift one tells us the about the ratio of the distances to the two redshifts. It

[6]For a constantly expanding Universe $a\dot{a}$ = constant, so $H(z) \propto a^2 \propto (1+z)^2$. From equations 1.11 & 1.8, $d_l \propto z$.

is this ratio that is sensitive to the acceleration of the Universe.

To characterise this acceleration, the *deceleration parameter*, $q(t)$ is defined

$$q(t) = -\frac{a\ddot{a}}{\dot{a}^2}. \tag{1.45}$$

Using the distance-redshift relation inferred from (10 and 42 respectively) SNe Ia, Riess et al. (1998) and Perlmutter et al. (1999) both found significant evidence for $q_0 < 0$ i.e. an accelerating universe. While SNe Ia provided convincing evidence for an accelerating Universe, that did not directly necessarily imply the presence of a cosmological constant, since negative curvature can also produce accelerated expansion. The evidence for acceleration from SN Ia was much complemented by the first measurements of the first acoustic peak in the CMB that followed soon after (de Bernardis et al. 2000; Hanany et al. 2000), which indicated that $\Omega \approx 1$, implying a non-zero cosmological constant as at least partly responsible for the acceleration.

The Betoule et al. (2014) analysis of the 740 SN Ias plotted in Figure 1.5 achieved a constraint on the matter density, $\Omega_m = 0.295 \pm 0.034$, assuming $\Lambda$CDM. SNe Ia constraints are a powerful addition to the CMB, in particular breaking degeneracies when deviations from a cosmological constant are allowed, as demonstrated in the right panel of Figure 1.3. PCP15 use a subset of the same sample in Betoule et al. (2014), and achieve a factor of 5 improvement in the constraint on $w_0$, through the addition of the SNe data, compared to CMB data alone (not including CMB lensing).

### 1.5.3 The baryon acoustic oscillations

The sound horizon, which is imprinted on the CMB as the first acoustic peak, it also imprinted on the low redshift galaxy distribution. This effect is known as the *baryon acoustic oscillations (BAO)*. At photon-decoupling, overdensities in baryonic matter remain after the photons diffuse away, with the sound horizon

at last scattering, $r_*$, as the characteristic separation between overdensities. The CMB provides tight constraints on the sound horizon at recombination for a given expansion history (PCP15 find $r_* = 144.61 \pm 0.49\,\mathrm{Mpc}$). The characteristic physical scale, $r_s(z)$ can be identified in the distribution of matter (e.g. galaxies) at low redshift, and acts as standard ruler, indicating the amount of expansion the Universe has undergone since recombination. The large size of the feature makes it insensitive to nonlinear structure growth at low redshift. Dark matter, which is much more abundant than baryonic matter, did not couple with photons in the early universe, and so the acoustic peak in the dark matter clustering only arises through its gravitational interaction with baryonic matter, and so the amplitude of the acoustic peak at low-redshift is much lower than it would be if matter was baryon-dominated. Furthermore, the large physical size of the BAO peak means observations of extremely large cosmic volumes are required to reduce the effect of cosmic variance. Nevertheless, in 2005 significant detections of the BAO acoustic peak were reported by Cole et al. (2005) from the 2dF Galaxy Redshift Survey (Colless et al. 2001), and by Eisenstein et al. (2005) from the Sloan Digital Sky Survey (SDSS), two galaxy redshift surveys which were large enough (1,800 and 3,816 square degrees respectively at that time), and made sufficiently numerous redshift measurements (221,414 and 46,748 respectively at that time), for a significant detection to be possible.

The galaxy clustering is measured in both the line-of-sight direction, and transverse to the line-of-sight. In the line-of-sight direction, the acoustic scale is a characteristic redshift difference sensitive to $H(z)r_s(z)$. The transverse measurement constrains the angle $r_s(z)/D_A(z)$. These can be combined, and BAO constraints reported (e.g. Eisenstein et al. 2005; Planck Collaboration et al. 2015a) in terms of the distance ratio

$$d(z) = \frac{r_{\mathrm{drag}}}{D_V(z)} \tag{1.46}$$

where

$$D_V(z) = \left[ D_A^2(z) \frac{cz}{H(z)} \right]^{\frac{1}{3}}, \tag{1.47}$$

$r_{\rm drag} = r_s(z_{\rm drag})$ and $z_{\rm drag}$ is the redshift at which baryons decoupled from photons[7].

The best current BAO constraints come from Baryonic Oscillation Spectroscopic Survey of SDSS-III (BOSS) (e.g. Anderson et al. (2014); Ross et al. (2015)), a $\sim 10,000$ square degree survey with $\sim 1.5$ million galaxy redshifts. Anderson et al. (2014) measure $D_V$ to 2% accuracy at $z = 0.32$ and 1% accuracy at $z = 0.57$. BAO and the CMB are highly complementary probes, since they probe the same standard ruler, $r_s(z)$, at very different redshifts. This is shown in Figure 1.3, where both probes have strong degeneracies in $\Omega_{\rm m}$, $\Omega_\Lambda$ and $\Omega_K$, which are broken by their combination. PCP15 use BAO data from Beutler et al. (2011); Ross et al. (2015); Anderson et al. (2014) as one of their primary external datasets, and achieve a factor of 10(5) improvement in the constraint on $\Omega_K(w_0)$, through the addition of the BAO data, compared to CMB data alone (not including CMB lensing). The left panel of Figure 1.6 shows the good agreement of the distance ratio measured at a range of redshifts, compared to that predicted from the PCP15 best-fit ΛCDM model.

The BAO feature has also recently been detected in the Lyman-$\alpha$ forest at high redshift ($z \approx 2.3$), using the absorption spectra of BOSS quasars (Busca et al. 2013; Slosar et al. 2013; Font-Ribera et al. 2014; Delubac et al. 2015).

### 1.5.4 Probes of the growth of structure

The three observational probes I've mentioned are primarily 'homogeneous Universe' probes, in that they probe the expansion history of the Universe, rather than the growth of density perturbations in the Universe[8]. Figure 1.2 demon-

[7] Not actually the same as when photons decoupled from baryons! See e.g. Eisenstein & Hu (1998).

[8] The growth of perturbations does affect the CMB secondary anisotropies, and produces extra scatter in the SNe Hubble diagram through peculiar motions and gravitational lensing.

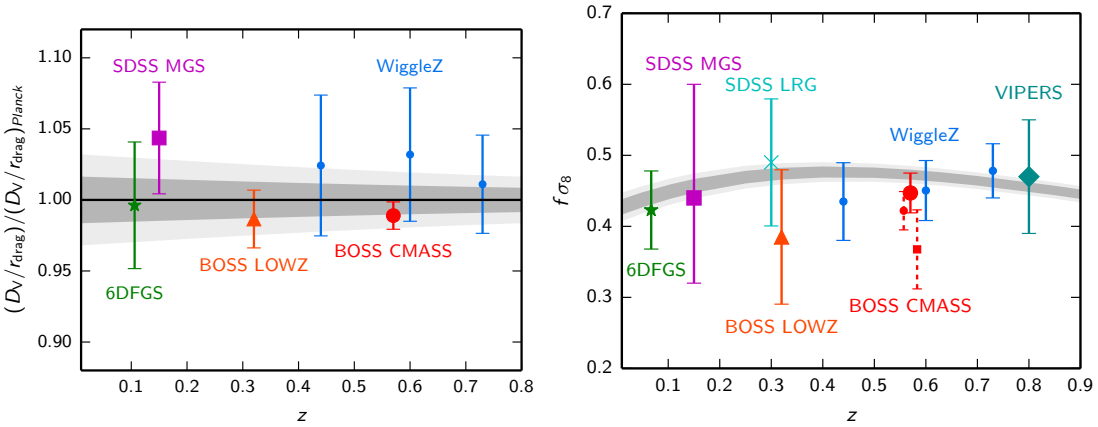


Figure 1.6: The ΛCDM model at high and low redshift: both figures, taken from PCP15, compare a low redshift measurement with the prediction from the Planck CMB best-fit ΛCDMmodel. Left panel: Constrains on the BAO distance ratio, divided by the Planck ΛCDMprediction, as measured by Beutler et al. (2011) (green star), Ross et al. (2015), (purple square), Anderson et al. (2014) (red triangle and circle), Kazin et al. (2014) (blue circles). Right panel: Constraints on the RSD parameter $f\sigma_8$, with $1\sigma$ uncertainties, as measured by Beutler et al. (2012) (green star), Howlett et al. (2015) (purple square), Oka et al. (2014) (cyan cross), Chuang et al. (2013) (red triangle), Samushia et al. (2014) (large red circle), Blake et al. (2012) (blue circles), Beutler et al. (2014c) (small red circle), Chuang et al. (2013) (small square). The three red data points at $z \sim 0.57$ all use BOSS CMASS data, and so are not independent.

strates that the redshift dependence of the growth of matter perturbations, parameterised by the linear growth factor $G(z)$ has clear dependence on the dark energy. Measuring the amplitude of the linear matter power spectrum as a function of redshift would allow us to constrain $G(z)$, and therefore e.g. $w_0$ and $w_a$, while also measuring its scale dependence would provide constraints on the neutrino masses. Unfortunately, we cannot directly observe the dark matter-dominated density perturbations, but must use instead a tracer of the density field, such as galaxies or galaxy clusters. Galaxies and clusters, as discrete, gravitationally bound objects, are biased tracers of the density field, likely only residing only in dark matter halos above some mass threshold. Under the simple assumption of linear *galaxy bias*, the galaxy power spectrum is

$$P_g(k, z) = b_g^2(z) P_\delta(k, z), \tag{1.48}$$

where $b_g(z)$ is the unknown galaxy bias. Therefore $b_g$, which depends on galaxy-formation physics as well as cosmology, is fully degenerate with the growth factor.

Redshift-space distortions (RSD) can be used to break this degeneracy. Galaxy clustering can be measured perpendicular to the line-of-sight, and along the line-of-sight using redshift information. Peculiar velocities produce anisotropy, known as redshift space distortions, since they perturb the observed redshifts from the cosmological redshift. Kaiser (1987); Hamilton (1998) show on linear scales, the galaxy power spectrum is

$$P_g(k,\mu) = P_\delta(k)(b_g(z) + \mu^2 f(z)) \tag{1.49}$$

where f(z) is the logarithmic growth rate

$$f = \frac{d\ln G}{da} \tag{1.50}$$

and $\mu$ is the cosine of the angle of wavevector $\mathbf{k}$ to the line-of-sight. RSD primarily constrain the parameter combination $f(z)\sigma_8(z)$, and constraints on these parameters from a range of surveys show reasonable agreement with the ΛCDM model currently favoured by PCP15, as shown in the right panel of Figure 1.6. A challenge for RSD is modelling the growth of structure and galaxy bias on nonlinear scales, where much of the signal comes from (see e.g. Bianchi et al. 2012; Okumura et al. 2012; Reid et al. 2014; White et al. 2015).

Cluster abundance studies attempt to measure the growth of structure in a different way. Nonlinear structures grow from matter overdensities into halos, and the halo mass function, the volume density of halos of a given mass, is a cosmologically sensitive quantity. The cosmology dependence can be calculated using N-body simulations (e.g. Tinker et al. 2008). Galaxy clusters form in the largest halos, and if a mapping can be found from the observable properties of galaxy clusters to the halo mass, then counts of galaxy clusters can be converted to

counts of halos of a given mass. The observable properties used include 'richness', the number of galaxies of a particular type within a given radius (see e.g Rozo et al. 2010); the X-ray luminosity or temperature (see e.g. Mantz et al. 2015); and the tSZ signal (see e.g. Planck Collaboration et al. 2015d). Finding the mapping from cluster observable to halo mass is the main challenge for cluster abundance cosmology, with weak lensing being a promising tool for calibrating this mapping (see Mantz et al. 2015; Hoekstra et al. 2015). Allen et al. (2011) provide a useful review of galaxy cluster cosmology.

Compared to galaxies, the relation between the Lyman-$\alpha$ absorption power spectra and the matter power spectrum can be more easily theoretically modelled (see e.g. Weinberg et al. 2003), and the Ly$\alpha$ signal from BOSS quasars has recently been used by Palanque-Delabrouille et al. 2015 to achieve impressive constraints on neutrino mass, $\sum m_\nu < 0.12$eV (95%), when combining with Planck CMB data.

In the next section I describe weak gravitational lensing, a probe of the matter perturbations that does not require the use of biased tracers of the density field[9].

## 1.6 Weak Lensing

Gravitational lensing is the distortion of light from the distant universe by the gravitational influence of intervening structure. Behind massive clusters, the light we receive from galaxies can be distorted into long arcs, and even multiple images; this is the *strong lensing* regime. However, most galaxies experience only $\sim 1\%$ distortions in their size and shape, the regime known as *weak lensing*. The great selling point of gravitational lensing, strong or weak, is that it is sensitive to the total (dark and baryonic) matter distribution, hence this distribution can be characterised without requiring a visible tracer like galaxies or clusters. This makes it a potentially very powerful probe of the growth of structure. In this

[9]Except perhaps to mitigate systematic effects such as intrinsic alignments, see §2.2.

section, I give a brief overview of general weak lensing theory (§1.6.1-1.6.5), and cosmic shear cosmology (§1.6.6).

### 1.6.1 Small gravitational deflections of light

Light from the observable universe travels to us along geodesics, which means its path is influenced by any changes in the gravitational potential, $\Phi$, due to density perturbations, $\delta$, that it comes across. These changes in $\Phi$ determine a mapping from unlensed 'source plane' quantities, to the observed 'image plane' quantities. For example, a source with unlensed angular position on the sky $(\theta_1^S, \theta_2^S)$ will be observed at position $(\theta_1^I, \theta_2^I)$. The observed position depends on the accumulation of the deflections along the line of sight, and can be written (Bartelmann & Schneider 2001; Weinberg et al. 2013), for a source at distance $\chi_s$

$$\theta_i^I = \theta_s^S + 2\int_0^{\chi_s} d\chi \frac{D_A(\chi_s - \chi)}{D_A(\chi)D_A(\chi_s)} \frac{\partial\Phi(\chi, \theta_i(\chi))}{\partial\theta_i} \tag{1.51}$$

where $\theta_i$ denotes the sky coordinates along the light path. Several approximations are implicit in this expression: (i) the perturbations of the gravitational potential are non-relativistic, so that their time derivatives can be neglected; (ii) the deflections are small enough to be treated in the flat-sky limit (see e.g. Castro et al. 2005 for a full-sky treatment); (iii) the perturbations are small enough that we need only consider the first derivative of $\Phi$ i.e. work to first order in perturbation theory (see e.g. Krause & Hirata 2010 for the limitations of this approximation).

It's convenient then to define the lensing potential $\phi$

$$\phi(\chi_s, \theta_i) = -2\int_0^{\chi_s} d\chi \frac{D_A(\chi_s - \chi)}{D_A(\chi)D_A(\chi_s)} \Phi(\chi, \theta_i(\chi)). \tag{1.52}$$

By making the *Born approximation*, in which the derivative in 1.51 is evaluated along the path of an undeflected light ray i.e. at $\theta_i^I$, equation 1.51 can be simplified

to

$$\theta_i^I = \theta_i^S - \frac{\partial\phi(\chi_s, \theta_i^I)}{\partial\theta_i^I}. \tag{1.53}$$

The Born approximation is another example of working to first order in the perturbations of the gravitational potential (since the deflection angle depends on the derivative of $\Phi$, changes in this derivative on the scale of the deflection angle will depend on second derivatives of $\Phi$).

### 1.6.2 The convergence and the shear

If we could observe the deflection angle $\theta_i^I - \theta_i^S$ we could probe the perturbations in the gravitational potential along the line of sight. However, since we can never know $\theta_i^S$, the 'unlensed' direction from which a light ray originated, the deflection angle is not an observable quantity. To get to observable quantities, we need to move beyond the first derivative of the lensing potential, to second derivatives of the lensing potential i.e. first derivatives of the deflection angle

$$\frac{\partial\theta_i^S}{\partial\theta_i^I} = \delta_{ij} + \frac{\partial^2\phi}{\partial\theta_i\partial\theta_j} = \begin{pmatrix} 1-\kappa-\gamma_1 & -\gamma_2 \\ -\gamma_2 & 1-\kappa+\gamma_1 \end{pmatrix} = A_{ij}, \tag{1.54}$$

where $\delta_{ij}$ is the identity matrix and $A_{ij}$ is the lensing Jacobian matrix. In the weak lensing regime, $A_{ij}$ defines the mapping from source to image plane. The decomposition of $A_{ij}$ into terms containing $\kappa$, $\gamma_1$ and $\gamma_2$ is useful since these quantities have characteristic effects on a source galaxy image.

The *convergence*, $\kappa$ causes magnification, for $\kappa > 0$, an increase in size and therefore flux, since surface brightness is conserved by Liouville's theorem. From equation 1.54, we have

$$\kappa(\theta) = -\frac{1}{2}\left(\frac{\partial\phi^2}{\partial\theta_x^2} + \frac{\partial\phi^2}{\partial\theta_y^2}\right) = -\frac{1}{2}\bigtriangledown_\theta^2\,\phi. \tag{1.55}$$

Substituting in for $\phi$, and using $\bigtriangledown_\theta^2 = D_A^2(\chi)\bigtriangledown_x^2$, where $x, y$ denote comoving

distance coordinates transverse to the line of sight, the convergence can be related to the gravitational potential via

$$\kappa(\theta, \chi_s) = \int_0^{\chi_s} d\chi \frac{D_A(\chi_s - \chi) D_A(\chi)}{D_A(\chi_s)} \bigtriangledown_x^2 \Phi(\chi_s, \theta). \tag{1.56}$$

We can use the Poisson equation to relate the gravitational potential $\Phi$ to the matter overdensity $\delta$:

$$\bigtriangledown_x^2 \Phi(\chi_s, \theta) = 4\pi G a^2 \rho(\chi_s, \theta) = 4\pi G a^2 \rho_m(\chi)(1 + \delta(\chi_s, \theta)) \tag{1.57}$$

where the factors of $a$ arise because the derivatives are with respect to comoving coordinates. The first term adds a constant background value to $\kappa$, which can be ignored, since it does not contribute to correlations in the convergence field. Substituting for $\rho_m(\chi)$, we have

$$\bigtriangledown_x^2 \Phi(\chi_s, \theta) = \frac{3H_0^2 \Omega_m}{2a} \delta(\chi_s, \theta). \tag{1.58}$$

The convergence can then be written

$$\kappa(\theta, \chi_s) = \frac{3H_0^2 \Omega_m}{2a} \int_0^{\chi_s} d\chi \frac{D_A(\chi_s - \chi) D_A(\chi)}{D_A(\chi_s)} \delta(\chi_s, \theta). \tag{1.59}$$

So the convergence is a weighted projection of the matter overdensity along the line of sight.

$\gamma_1$ and $\gamma_2$ are the components of the *shear*. Positive $\gamma_1$ stretches the galaxy image along the $\theta_x$ axis, and squeezes it along the $\theta_y$ axis, while $\gamma_2$ acts equivalently in a coordinate frame rotated anticlockwise by 45°. In terms of the lensing

potential,

$$\gamma_1 = -\frac{1}{2}\left(\frac{\partial^2\phi}{\partial\theta_x^2} - \frac{\partial^2\phi}{\partial\theta_y^2}\right), \tag{1.60}$$

$$\gamma_2 = -\left(\frac{\partial^2\phi}{\partial\theta_x\partial\theta_y}\right). \tag{1.61}$$

The rotational symmetry of the shear can be nicely captured by defining the complex shear

$$\gamma = |\gamma|\, e^{2i\alpha} = \gamma_1 + i\gamma_2. \tag{1.62}$$

where $\alpha$ is the position angle, the angle of the direction of maximum stretching, with respect to the $x$-axis. Under a rotation of the coordinate system by an angle $\beta$, the shear transforms as

$$\gamma \to e^{2i\beta}\gamma, \tag{1.63}$$

$$\gamma_1 \to \cos(2\beta)\gamma_1 + \sin(2\beta)\gamma_2, \tag{1.64}$$

$$\gamma_2 \to -\sin(2\beta)\gamma_1 + \cos(2\beta)\gamma_2. \tag{1.65}$$

Neither the convergence (which magnifies galaxy images), or the shear (which stretches and squeezes galaxy images) are directly observable, since again, for a given galaxy, we do not know what it would have looked like in the absence of convergence or shear. If all galaxies had the same known unlensed size or the same known unlensed brightness, then every galaxy would give a direct measurement of the convergence. If all galaxies were originally circular (in the plane of the sky), then the observed shape of every galaxy would give a direct measurement of the shear. Of these two unrealistic scenarios, it turns out the latter is closer to being true! Galaxies are round on average, and the shear is generally considered much easier to estimate than the convergence. For the rest of this thesis, it is the shear which I concentrate on.

### 1.6.3 The ellipticity and the shear

The shear on a galaxy image is manifested as a small change in the complex galaxy ellipticity, $\epsilon$, which I define as[10]

$$\epsilon = \frac{a-b}{a+b} e^{2i\alpha} \tag{1.66}$$

where $a$ and $b$ are the semi-major and semi-minor axes, and $\alpha$ is the position angle. In the presence of a shear, $\gamma$, and a convergence, $\kappa$, the lensed ellipticity $\epsilon^{\rm obs}$ is

$$\epsilon^{\rm obs} = \frac{\epsilon^{\rm I} + g}{1 + g^* \epsilon^{\rm I}}, \tag{1.67}$$

where $g$ is the reduced shear,

$$g = \frac{\gamma}{1-\kappa}, \tag{1.68}$$

and $\epsilon^{\rm I}$ is the *intrinsic* i.e. unlensed galaxy ellipticity. In the weak lensing limit, $\kappa, |\gamma| \ll 1$, and

$$\epsilon^{\rm obs} \approx \epsilon^{\rm I} + \gamma, \tag{1.69}$$

so for an ensemble of galaxies with randomly oriented intrinsic ellipticities

$$\langle \epsilon^{\rm obs} \rangle \approx \langle \gamma \rangle. \tag{1.70}$$

Therefore in the weak lensing limit the ellipticity, which can be measured, is an unbiased estimator for the shear (which cannot be directly measured). The noise on this shear estimate depends on the standard deviation (per ellipticity component) of the intrinsic ellipticity, $\sigma_\gamma$, known as the *shape noise*. If all galaxies were round, $\sigma_\gamma$ would be zero, and we'd get a noiseless estimate of the shear from each galaxy. If we measure the shapes of $N$ galaxies in a region of sky, the variance on the estimate of the mean shear in that region is $\approx \sigma_\gamma^2/N$ (per shear

[10] Other definitions are also common, see e.g. Bartelmann & Schneider (2001); Bernstein & Jarvis (2002) for a discussion of these.

component).

Galaxies do not in general have well defined semi-major/minor axes, or even elliptical isophotes, so a given galaxy image doesn't have a uniquely defined ellipticity. Whatever way the ellipticity is defined and estimated, the fact that it can be used to estimate the shear after averaging over many galaxies is the important point. I discuss some approaches to estimating the shear in §2.1.

### 1.6.4 Shear two-point statistics: The power spectrum and correlation functions

Equation 1.59 should hint that two-point correlations of the convergence (and as we'll see, the shear) are related to two-point correlations of the density field. It is more convenient to work with the shear in Fourier space, defining

$$\tilde{\gamma}_{1,2}(\mathbf{l}) = \int d^2\boldsymbol{\theta}\, \gamma_{1,2}(\boldsymbol{\theta}) e^{-i\mathbf{l}.\boldsymbol{\theta}}. \tag{1.71}$$

It is also convenient to define rotated shear components, such that one is aligned with the wavevector $\mathbf{l}$, and one is aligned at 45° to $\mathbf{l}$. These rotated components are called the E-mode and B-mode respectively, and are given by

$$\tilde{\gamma}_E(\mathbf{l}) = \cos(2\phi_{\mathbf{l}})\tilde{\gamma}_1(\mathbf{l}) + \sin(2\phi_{\mathbf{l}})\tilde{\gamma}_2(\mathbf{l}) \tag{1.72}$$

$$\tilde{\gamma}_B(\mathbf{l}) = \cos(2\phi_{\mathbf{l}})\tilde{\gamma}_2(\mathbf{l}) - \sin(2\phi_{\mathbf{l}})\tilde{\gamma}_1(\mathbf{l}), \tag{1.73}$$

where $\phi_{\mathbf{l}}$ is the angle made by $\mathbf{l}$ with the $x$-axis. The shear components are related to the lensing potential by equation 1.61. In Fourier space, we can use that $\partial\theta_i \rightarrow -il_i$, such that

$$\tilde{\gamma}_1(\mathbf{l}) = \frac{1}{2}(l_1^2 - l_2^2)\tilde{\phi}(\mathbf{l}),\ \tilde{\gamma}_2(\mathbf{l}) = l_1 l_2 \tilde{\phi}(\mathbf{l}) \tag{1.74}$$

and so

$$\tilde{\gamma}_E(\mathbf{l}) = \frac{1}{2} l^2 \tilde{\phi}(\mathbf{l}) \text{ and } \tilde{\gamma}_B(\mathbf{l}) = 0. \tag{1.75}$$

So then, (under the approximations made in Section 1.6.1) the B-mode shear vanishes. By symmetry arguments, this is perhaps not surprising, since the direction of a positive B-mode component was defined to be at 45° to the direction $\hat{\mathbf{l}}$ of a plane wave mode in the lensing potential, $\phi(\mathbf{l})$, that causes the shear. A non-zero B-mode would suggest that the shear produced in this positive B-mode direction was different to the shear produced in the negative B-mode direction (perpendicular to the positive B-mode direction, at 135° to the plane wave direction).

The E-mode shear power spectrum $C_{EE}(l)$ is defined

$$\langle \tilde{\gamma}_E^*(\mathbf{l}) \tilde{\gamma}_E(\mathbf{l}') \rangle = (2\pi)^2 \delta_D(\mathbf{l} - \mathbf{l}') C_{EE}(l). \tag{1.76}$$

$C_{BB}(l)$ and $C_{EB}$ are defined similarly, with $C_{EB}$ zero by parity arguments (see e.g. Bartelmann & Schneider 2001). $C_{BB}(l)$ is often used as a test of systematic effects in weak lensing data (see e.g. Jarvis et al. 2015), since in the leading order treatment given here the B-mode due to gravitational shear vanishes, but incorrect treatment of instrumental effects can introduce a spurious B-mode. However, a non-zero B-mode can arise from a variety of higher order lensing effects (see e.g. Krause & Hirata 2010; Schneider et al. 2002b), as well as from intrinsic alignments (see Section 2.2). In the following, I drop the 'EE' subscript for brevity, so that $C(l)$ refers to $C_{EE}(l)$. From Equation 1.75,

$$\langle \tilde{\gamma}_E^*(\mathbf{l}) \tilde{\gamma}_E(\mathbf{l}') \rangle = \frac{l^4}{4} \langle \tilde{\phi}^*(\mathbf{l}) \tilde{\phi}(\mathbf{l}') \rangle. \tag{1.77}$$

The calculation of the power spectrum is much simplified by using the Limber approximation (Limber (1954); Kaiser (1992)), which, for a quantity, $a(\mathbf{n}, \chi)$,

defined as a projection over a three-dimensional random field $A(\mathbf{x})$ via

$$a(\mathbf{n},\chi) = \int_0^\chi d\chi' g(\chi') A(\chi'\mathbf{n}), \tag{1.78}$$

gives the angular power spectrum, $C_{aa}(l)$ of $a$

$$C_{aa}(l) = \int_0^\chi d\chi' \frac{g(\chi')^2}{D_A^2(\chi')} P_A\left(\frac{l}{D_A(\chi')}, \chi'\right), \tag{1.79}$$

where $P_A(k,\chi)$ is the three-dimensional power spectrum of the quantity $A(\mathbf{x})$, at radial distance $\chi$, for physical wavevector of magnitude $k$. See e.g. Kaiser (1992); Bartelmann & Schneider (2001) for a derivation and justification of the Limber approximation in the context of weak lensing.

In this context $a(\mathbf{x}) = \phi(\mathbf{x})$, and $A(\mathbf{x}) = \Phi(\mathbf{x})$, and using the expression for $\phi(\mathbf{x})$ from equation 1.52 results in an E-mode power spectrum, for galaxies at radial distance $\chi_s$

$$C(l) = l^4 \int_0^{\chi_s} d\chi \left[\frac{D_A(\chi_s - \chi) D_A(\chi)}{D_A(\chi_s)}\right]^2 P_\Phi(k = l/D_A(\chi), \chi). \tag{1.80}$$

Again using Poisson's equation to relate pertubations in $\Phi$ to density perturbations, we arrive at

$$C_{EE}(l) = \int_0^{\chi_s} d\chi \frac{g^2(\chi,\chi_s)}{D_A^2(\chi)} P_\delta(k = l/D_A(\chi), \chi) \tag{1.81}$$

where $P(k,\chi)$ is the matter power spectrum, and $g(\chi,\chi_s)$ is the *lensing efficiency*, given by

$$g(\chi,\chi_s) = \begin{cases} \frac{3}{2} H_0^2 \Omega_m [1+z(\chi)] D_A(\chi) \frac{D_A(\chi_s - \chi)}{D_A(\chi_s)} & \text{for } \chi < \chi_s \\ 0 \text{ otherwise.} \end{cases} \tag{1.82}$$

In cosmic shear analyses, it is normal to consider the angular power spectrum

of a population of source galaxies, with radial distribution function $N(\chi_s)$. In this case the *lensing kernel*, $W(\chi)$ is an integral over $g(\chi, \chi_s)$

$$W(\chi) = \int d\chi N(\chi_s) g(\chi, \chi_s) \tag{1.83}$$

where the integral is over all $\chi$ (although only need be evaluated over the range of non-zero $N(\chi_s)$), and then the angular power spectrum is

$$C(l) = \int_0^\infty d\chi \frac{W^2(\chi)}{D_A^2(\chi)} P_\delta(k = l/D_A(\chi), \chi). \tag{1.84}$$

We also use the cross-spectrum $C^{ij}(l)$, between the shears of two galaxy populations, $i$ and $j$, with radial distributions $N_i(\chi)$ and $N_j(\chi)$ and lensing kernels $W_i(\chi)$ and $W_j(\chi)$

$$C^{ij}(l) = \int_0^\infty d\chi \frac{W_i(\chi) W_j(\chi)}{D_A^2(\chi)} P_\delta(k = l/D_A(\chi), \chi). \tag{1.85}$$

Splitting of a galaxy sample into multiple bins in redshift, and then measuring both the shear power spectrum of each bin, and all the cross-spectra between the bins, is known as *tomography*.

Since we observe galaxies and obtain shear estimates at positions in real space, it is often easier to estimate real-space two-point statistics of the shear field, rather than the Fourier-space angular power spectrum. There are numerous such real-space statistics (see e.g. Schneider et al. 2002a), but all can be derived from the two-point correlation functions $\xi_{+/-}(\theta)$, defined

$$\xi_{+/-}(\theta) = \langle \gamma_t(\boldsymbol{\theta}_1) \gamma_t(\boldsymbol{\theta}_2) \rangle \pm \langle \gamma_\times(\boldsymbol{\theta}_1) \gamma_\times(\boldsymbol{\theta}_2) \rangle, \;\; |\boldsymbol{\theta}_1 - \boldsymbol{\theta}_2| = \theta. \tag{1.86}$$

Here the subscripts '$t$' and '$\times$' denote components of the shear aligned with, and at 45° to the separation vector $\boldsymbol{\theta}_2 - \boldsymbol{\theta}_1$. The shear two-point correlation functions

can be related to the shear power spectra (in the flat-sky limit) via

$$\xi_{+/-}(\theta) = \int_0^\infty \frac{ldl}{2\pi} J_{0/4}(l\theta) \left[C_{EE}(l) +/- C_{BB}(l)\right] \tag{1.87}$$

where $J_{0/4}$ is the zeroth/fourth order Bessel function of the first kind. The $\xi_{+/-}(\theta)$ are estimated in angular bins, by averaging over pairs of galaxies $ij$ with separation $|\boldsymbol{\theta}_i - \boldsymbol{\theta}_i|$ within that bin, via

$$\hat{\xi}_{+/-}(\theta) = \frac{\sum_{ij} w_i w_j \left[\epsilon_t(\boldsymbol{\theta}_i)\epsilon_t(\boldsymbol{\theta}_j) \pm \epsilon_\times(\boldsymbol{\theta}_i)\epsilon_\times(\boldsymbol{\theta}_j)\right]}{\sum_{ij} w_i w_j} \tag{1.88}$$

where $\epsilon(\boldsymbol{\theta}_i)$ is the ellipticity of galaxy $i$ and $w_i$ is the weight of galaxy $i$ (giving higher signal-to-noise galaxies higher weight can decrease the noise on the estimated signal) and $\hat{\xi}_{+/-}$ denotes $\xi_{+/-}$ averaged over the angular bin.

The two-point correlation functions (in the idealised case of being measured over all scales), contain the same information as the shear power spectra, as is clear from the fact that they can be derived from each other. The choice of which to use is a practical one - my feeling is that while the $\xi_{+/-}(\theta)$ are more straightforward to estimate from real-space data, $C(l)$ is in some sense closer to theory (requiring one integral rather than two to relate it to the matter power spectrum), and has less mixing of physical scales $k$, which can be an advantage if the matter power spectrum prediction is uncertain at small scales.

### 1.6.5 Density tracer×shear correlations

As well as correlating the shear with itself, as in the shear power spectrum, correlating the shear with positions of galaxies, clusters or any other tracer of the density field is a very useful technique. The galaxies which provide the shear estimates are called the *source* or *background* galaxies, and the objects whose positions the shear is correlated with are called the *lenses* or *foreground* galaxies or clusters etc. The signal is only non-zero when the source galaxies are at

higher redshift than the lens galaxies. When galaxy positions are used as the lens sample, this is known as *galaxy-galaxy lensing*. For a population of lens galaxies with radial distribution $N_{\rm lens}(\chi)$, and source galaxies with lensing kernel $W(\chi)$, the angular cross-spectrum between lens galaxy overdensity and source galaxy shear is (again using the Limber approximation)

$$C_{gE}(l) = \int_0^\infty d\chi \frac{N_{\rm lens}(\chi)W(\chi)}{D_A^2(\chi)} P_{g\delta}(k = l/D_A(\chi), \chi), \tag{1.89}$$

where $P_{g\delta}(k, z)$ is the 3-dimensional matter-galaxy cross-spectrum. The most commonly used statistic for probing this cross-correlation is the *tangential shear*, $\gamma_t(\theta)$ of the source galaxies around the lens galaxy positions, averaged in angular bins, which contains mostly the same information as $C_{gE}(l)$ (Hu & Jain 2004). Again, the subscript $t$ denotes the component of the shear aligned with the lens-source separation vector. The tangential shear can be related to $C_{gE}(l)$ via

$$\gamma_t(\theta) = \int \frac{ldl}{2\pi} J_2(l\theta) C_{gE}(l). \tag{1.90}$$

Galaxy-galaxy lensing, or cluster lensing (when cluster positions are used as the lenses), probes the connection between these tracers, and the underlying density field. On large scales it is often assumed that

$$P_{g\delta} = b_g P_\delta, \tag{1.91}$$

where $b_g$ is the galaxy or cluster bias. The large scale galaxy-galaxy lensing signal can be combined with the lens galaxy clustering signal, which has a power spectrum

$$P_{gg} = b_g^2 P_\delta. \tag{1.92}$$

Hence the galaxy bias, which prevents cosmological inference from either probe alone, can in some sense be divided out by combining the two signals, at least in

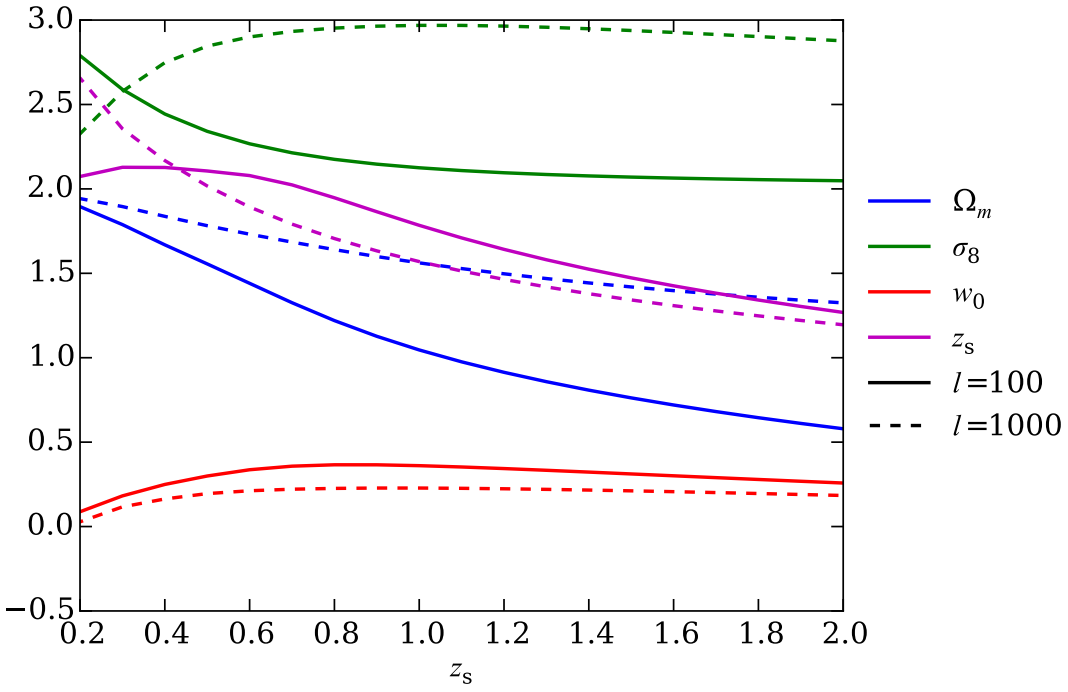


Figure 1.7: The source redshift evolution of the shear power spectrum cosmological parameter degeneracies. For parameter $\Omega \in (\Omega_m, \sigma_8, w_0, z_s)$, I have plotted $\alpha(z_s)$, where $C_{EE}(l)(z_s) \propto \Omega^{\alpha(z_s)}$. If two parameters have similar values of $\alpha$, they are very degenerate. I show these parameters for $l = 100, 1000$, which probe the linear (except at low redshift) and quite nonlinear regimes.

the simple linear bias case leading to equations 1.91 & 1.92. Going beyond linear bias, galaxy-galaxy lensing is a key observable for constraining more complex bias parameterisations, for example HOD modelling (e.g. Guzik & Seljak 2002; Yoo et al. 2006; Yoo & Seljak 2012; Mandelbaum et al. 2013).

Small-scale galaxy-galaxy lensing or cluster-lensing measurements allow characterisation of the halos in which the lens objects reside. For example, cluster-lensing is used to estimate cluster halo masses, as discussed in §1.5.4.

### 1.6.6 Cosmic shear cosmology

The term *cosmic shear* usually refers to measurements of gravitational lensing by the total matter field, using two-point statistics of the shear field such as the

shear power spectrum or shear correlation functions[11]. When I refer to cosmic shear, it can be assumed I'm referring to the two-point signal, unless I specify otherwise. From equation 1.89 the cosmic shear signal is sensitive to the matter power spectrum $P_\delta(k, z)$, the factor $(\Omega_\mathrm{m} H_0^2)^2$ from the lensing kernels, and the curvature, via the distance ratio in the lensing kernels. Hence it is sensitive to both geometry, and growth of structure. This sensitivity to multiple parameters makes it difficult to constrain any single parameter with cosmic shear data alone. Even when flatness is assumed, and $H_0$ fixed, there is a strong degeneracy between $\Omega_\mathrm{m}$ and $\sigma_8$. Using tomography, as well as combining with external data (e.g. $\Omega_\mathrm{m} h^2$ is very well constrained by the CMB), can break some of these degeneracies, as well as generally providing greater constraining power (Hu 1999).

I demonstrate some of these parameter degeneracies in Figure 1.7, which shows the the power law dependencies of the cosmic shear signal on $\Omega_\mathrm{m}$, $\sigma_8$, $w_0$, and the source redshift $z_\mathrm{s}$, as a function of $z_\mathrm{s}$. For each parameter $\Omega$, and source redshift, I find the value of $\alpha$ which satisfies $C_{EE}(l)(z_\mathrm{s}) \propto \Omega^{\alpha(z_\mathrm{s})}$. This is an extension of work by Huterer et al. (2006); Jain & Seljak (1997), who report similar relations for a single source galaxy plane at $z_\mathrm{s} = 1$. Some of the often used cosmic shear rules of thumb are apparent, for example the signal is roughly proportional to $\sigma_8^2$ on linear scales, and $\sigma_8^3$ on nonlinear scales. The fact that the ratios of the various $\alpha$s evolve with source redshift reinforces my earlier statement that tomography helps to break degeneracies.

In addition to breaking degeneracies between cosmological parameters, tomography can also help break degeneracies with systematic effects. Intrinsic alignments in particular have a very different redshift dependence to the cosmic shear signal, and so can be disentangled in a tomographic analysis (see §2.2 and e.g. King & Schneider 2003; Joachimi & Schneider 2010).

Cosmic shear was first detected in 2000 by four groups (Bacon et al. 2000;

[11] Measurements of higher order statistics of the shear field are also sometimes referred to as 'cosmic shear' measurements in the literature.

Kaiser et al. 2000; Van Waerbeke et al. 2000; Wittman et al. 2000) using four different ground-based telescopes. These detections, using $\sim 1$ square degree, were followed by studies using deeper and wider datasets, which reported competitive constraints on cosmological parameters, although many used single-band imaging and did not have reliable redshift information (see Kilbinger 2015 for a discussion of these). Cosmic shear was also detected from space using the Hubble Space Telescope (HST) (Rhodes et al. 2004).

The Canada-France Hawaii Legacy Survey[12] (CFHTLS), which observed over five years from 2004-2009, presented a significant advance on previous weak lensing datasets, providing five optical band imaging across $\sim 150$ square degrees, with a $5\sigma$ point source limiting magnitude of 25.5 in the $i$-band. With this increase in data volume and decrease in statistical errors, robust treatment of systematics errors became much more important, and early results from CFHTLS suffered from e.g. excess variance in the signal between telescope pointings (Kilbinger et al. 2009), and non-zero large-scale B-mode (Fu et al. 2008).

The CFHT lensing survey (CFHTLenS, Erben et al. 2013; Heymans et al. 2012) made significant improvements with a weak-lensing motivated re-analysis of the CFHTLS data; with more robust photometric redshift estimation and validation (Hildebrandt et al. 2012), shape measurement (Miller et al. 2013), and systematics removal (Heymans et al. 2012). CFHTLenS presented cosmological constraints in a series of papers using different shear two-point statistics: Kilbinger et al. (2013) investigated several different real-space statistics without redshift binning; Benjamin et al. (2013) performed a two redshift bin tomographic analysis using real-space correlation functions, with an emphasis on testing the photometric redshift accuracy; Heymans et al. (2013) performed a six-bin tomographic analysis using real-space correlation functions, with an emphasis on the treatment of intrinsic alignments. Meanwhile Kitching et al. (2014) performed a 3D cosmic shear (Heavens 2003; Castro et al. 2005) analysis, which uses a three-

[12] `http://www.cfht.hawaii.edu/Science/CFHLS/`

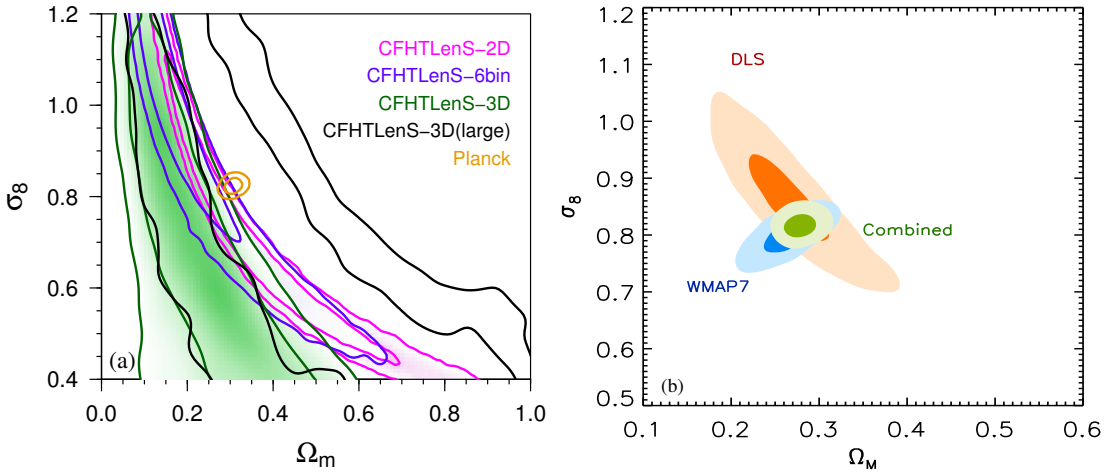


Figure 1.8: Recent cosmic shear cosmological constraints on the total matter density, $\Omega_{\rm m}$, and the $z = 0$ amplitude of matter fluctuations, $\sigma_8$. The left panel (taken from Kilbinger (2015)) shows constraints using CFHTLenS data from Kitching et al. (2014) (green lines; and black lines after applying more conservative cuts to small scales), Kilbinger et al. (2013) (pink lines), and Heymans et al. (2013) (blue lines), as well as *Planck* CMB constraints from Planck Collaboration et al. (2013c) (orange lines). The right panel (taken from Jee et al. (2013)) shows the Jee et al. (2013) constraints from the DLS survey, as well as WMAP7 CMB constraints from Komatsu et al. (2011).

dimensional spherical Bessel/spherical harmonic decomposition of the shear field. Constraints on $\Omega_{\rm m}$ and $\sigma_8$ from Kilbinger et al. (2013), Heymans et al. (2013) and Kitching et al. (2014) are shown in the left panel of Figure 1.8.

Despite the advances made, more recent re-analyses of the CFHTLenS data provide evidence for the need for further improvements in systematics treatments: Choi et al. (2015) find evidence for inaccuracies in the CFHTLenS photometric redshift estimates by cross-correlating with spectroscopic data, while Asgari et al. (2016) find evidence for large scale B-mode power.

Competitive recent constraints were also achieved by Jee et al. (2013, 2015) using the Deep Lens Survey (DLS), a 20 square degree ground based survey with a limiting $5\sigma$ $r$-band magnitude limit of $\sim 27$. The constraints on $\Omega_{\rm m}$ and $\sigma_8$ from the non-tomographic analysis of Jee et al. (2013) are shown in the right panel of Figure 1.8.

Although the small area limits the cosmological information, the $\sim 2$ square

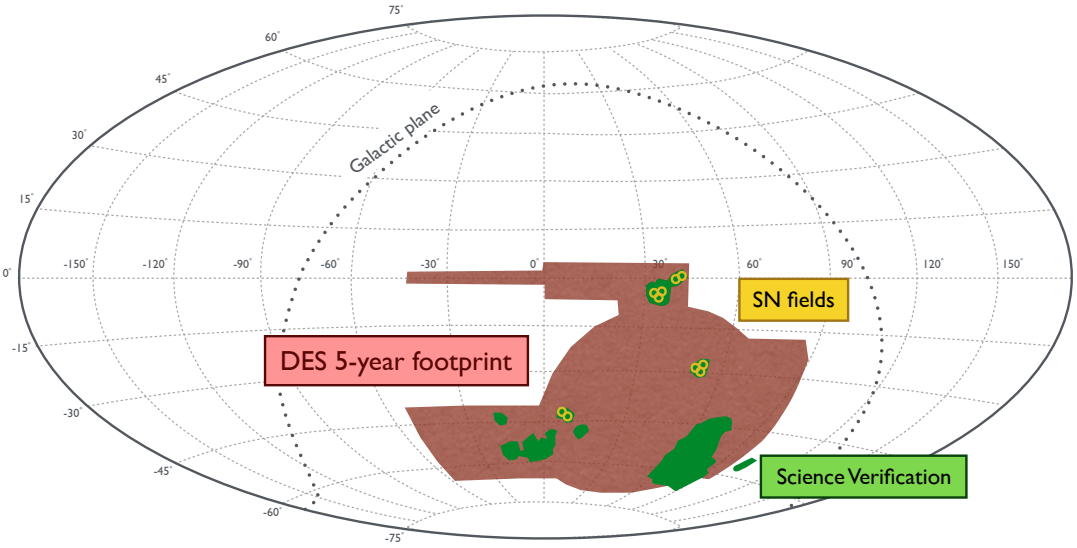


Figure 1.9: The Dark Energy Survey footprint. In brown is the full five-year ($\sim$ 5000 square degrees) footprint. The green patches are the areas covered in the Science Verification (SV) season; the largest contiguous SV region is known as SPT-East or SPT-E. The yellow circles denote the pointings of the supernovae fields. Image credit: Jelena Aleksić.

degree HST Cosmic Evolution Survey (COSMOS, Koekemoer et al. 2007) has provided extremely important weak lensing data. As well as cosmological analyses (e.g. Schrabback et al. 2010), the high quality[13], deep (27.2 ($5\sigma$) in the F814W band) imaging has provided a crucial calibration set for galaxy shape measurement with ground-based data (see e.g. Miller et al. 2013; Jee et al. 2013; Jarvis et al. 2015). Multi-band follow-up observations have produced relatively accurate photometric redshifts (Ilbert et al. 2009) for the COSMOS area, useful for calibration or validation of photometric redshift methods (e.g. Hildebrandt et al. 2012; Bonnett et al. 2015).

## 1.7 The Dark Energy Survey

Chapters 2, 4 & 5 of this thesis all involve the Dark Energy Survey (DES), so I give a brief overview of this project below. DES started its main survey observations in

[13]Compared to ground-based data, due to the absence of atmospheric distortions.

autumn of 2013, and in a five-year program, aims to image 5000 square degrees of the southern sky using the 570 megapixel imager DECam (Flaugher et al. 2015), on the Blanco telescope at the Cerro Tololo Inter-American Observatory in Chile. Imaging is performed in five optical bands spanning 0.40-1.06 $\mu$m ($grizY$) to a $10\sigma$ $i$-band limiting magnitude of $\sim$ 24, with the full depth reached after ten 90s (45s for the $Y$-band) exposures. This comprises the 'wide' survey, which is concurrent with a supernovae survey, involving repeated observations of ten 3 square degree fields with a cadence of around a week. DES aims to use multiple cosmological probes to constrain models of dark energy, including weak lensing, SNe Ia, BAO and galaxy clusters. DES is a "Stage III" experiment by the DETF categorisation scheme, with a significant increase in data volume over "Stage II" experiments like CFHTLS, and providing a precursor to the even more ambitious future "Stage IV"experiments like the Large Synoptic Survey Telescope (LSST)[14], Euclid[15] and the Wide Field InfraRed Survey Telescope (WFIRST)[16].

DES performed Science Verification (SV) observations from November 2012 to February 2013, with the aim of preparing the camera, instrument and data management for the main survey. In SV, we observed $\sim$ 250 square degrees at close to full survey depth, including a contiguous $\sim$ 140 square degree region known as 'SPT-East' or 'SPT-E'. Shape measurements for weak lensing analyses of the SPT-E region were presented in Jarvis et al. (2015), and photometric redshift estimates in Sánchez et al. (2014); Bonnett et al. (2015). I'll often refer to this dataset as 'DES-SV'. The SV regions, as well as the final five-year footprint are shown in Figure 1.9.

[14] `http://www.lsst.org`
[15] `http://sci.esa.int/euclid`
[16] `http://wfirst.gsfc.nasa.gov`

## 1.8 Work in this Thesis

In Chapter 2, I give an overview of some of the main systematic effects which make extracting cosmology from weak lensing difficult, drawing on my experience of working on the Dark Energy Survey. In Chapter 3 (published in similar form as MacCrann et al. (2015)), motivated by the tension between the cosmic shear measurements from CFHTLenS, and *Planck* CMB constraints, I investigate various explanations including more advanced weak lensing systematics treatments, and extensions of ΛCDM. MacCrann et al. (2015) provided me with vital experience and preparation for Chapter 4 (published in similar form as The Dark Energy Survey Collaboration et al. (2015)), in which I perform the cosmic shear analysis of DES Science Verification data, producing the first cosmology constraints from the project. Finally, in Chapter 5, I look in more detail at the small scales in cosmic shear measurements, which are afflicted with theoretical uncertainties in modelling nonlinear matter clustering. I investigate competing small scale systematics, and attempt to model new measurements of the DES SV small scale cosmic shear signal. I make some concluding remarks in Chapter 6.

# Chapter 2

# Cosmic Shear Systematic Barriers

Cosmic shear can probe both the geometry and growth of structure of the Universe, over a wide range of redshifts, making it potentially an extremely powerful probe of dark energy. Unlike most other low-redshift probes of growth, it does not rely on a biased tracer of the matter field, such as galaxies or clusters. However, there does exist a range of other potential sources of systematic biases which will require significantly improved treatments in order to exploit the statistical power of future datasets. These can be roughly divided into two categories. The first is 'data' systematics - those which arise from an incomplete understanding of how photons from galaxies are propagated through the instrument to e.g. shear estimates, for example biases in galaxy shape measurement. There also exist 'theoretical' systematics, which would exist even with perfect understanding of the photon-to-catalog process, and make interpretation of the observed signal difficult, for example disentangling the contribution from galaxies' intrinsic alignments to this observed signal[1]. In this chapter, I aim to give

[1]There's plenty of grey in this binary categorization, for example, shape measurement biases could arise from either a poor PSF model, or a 'theoretical' uncertainty in the intrinsic ellipticity distribution of galaxies.

an overview of some of the major sources of biases in cosmic shear analyses, mostly in the context of the efforts to extract cosmology results from DES Science Verification data. The content of §2.1.5 has minimal changes from Section 8.6.1 of Jarvis et al. (2015), to which I originally contributed this section.

In §1.6 I explained how the shear power spectrum $C(l)$, could be related to the matter power spectrum, $P_\delta(k, z)$ via

$$C(l) = \int d\chi \frac{W^2(\chi, n(z_s))}{D_A^2(\chi)} P_\delta(k = l/D_A(\chi), \chi). \tag{2.1}$$

This is a beautifully simple result, suggesting all we need to do is measure the shears and redshifts of our galaxy sample, compute the shear power spectrum, and this will allow us to probe the matter power spectrum, the distance redshift relation, and extract the cosmological information that they reveal. This chapter is aimed as an overview of some of the challenges in estimating and interpreting the cosmic shear signal.

Firstly, to estimate $C(l)$, we need to estimate the shear of our galaxies. It is often assumed that a galaxy's observed ellipticity is an unbiased estimate of the shear[2], hence the problem becomes one of estimating galaxy ellipticities, commonly referred to as *shape measurement*; I describe some of the challenges associated with measuring the shapes of small, noisy galaxies with uncertain morphologies in §2.1.

The fact we use the observed ellipticity as a proxy for the shear sources the second systematic I consider, which arises if there are non-zero correlations in the intrinsic (i.e. unlensed) ellipticities of the source galaxies, which will contaminate the shear two-point function. This effect is known as *intrinsic alignments*, which I consider in §2.2.

Thirdly, the lensing kernel, $W$ in equation 2.1 requires knowledge of the red-

[2]For the ellipticity as defined in equation 1.66 anyway.

shift distribution, $n(z_s)$ of the source galaxies. Any bias or uncertainty in the estimate of $n(z_s)$ will introduce bias or uncertainty in the interpretation of the signal. I briefly address this in §4.2.4.

Finally, in order to infer the true cosmological parameters, we need to be able to predict from theory the cosmic shear signal for a wide range of cosmological parameters, which requires a theoretical prediction of the matter power spectrum $P_\delta(k)$ for a wide range cosmological parameters. On small scales, where the matter power spectrum is dominated by nonlinear clustering, this theoretical prediction becomes very non-trivial, especially when the effects of astrophysical processes on matter clustering is taken into account. I defer discussion of this topic to Chapter 5.

## 2.1 Shear Estimation

Unbiased shear estimation, from the tiny distortions in the shapes of large numbers of noisy galaxy images, is a problem that has attracted a wide variety of methodologies, from the fields of statistics and computer science as well as astronomy. Community challenges (starting with STEP, Heymans et al. 2006, and most recently GREAT3, Mandelbaum et al. 2014), in which multiple teams attempt to achieve the best results on simulated weak lensing data, have been instrumental in advancing the field, by providing a common testing grounds for different methods and attempting to attract non-astronomer participation. The latter point in particular makes the 'handbooks' for these challenges (e.g. Bridle et al. 2009; Mandelbaum et al. 2014) excellent introductory literature on the problem of shape measurement. I start this chapter with a brief overview of galaxy shape measurement for weak lensing; the aforementioned handbooks are a good place to start for those who require more detail than I provide here.

From equation 1.69, in the weak lensing limit

$$\epsilon \approx \epsilon_I + \gamma \tag{2.2}$$

where $\epsilon$ is the observed (complex) ellipticity, $\epsilon_I$ is the intrinsic ellipticity, and $\gamma$ is the shear. If $\epsilon_I$ can be assumed random, then

$$\langle \epsilon \rangle \approx \langle \gamma \rangle, \tag{2.3}$$

so the ellipticity becomes an unbiased estimate of the shear. Most approaches to shear estimation (for galaxy weak lensing) therefore aim to measure the ellipticity of each galaxy in the sample, which can then be fed into a statistic (e.g. the mean in a certain area of sky, or a two-point correlation function) in which the intrinsic ellipticity averages to zero. While not all methods explicitly return an estimate of the ellipticity, they all effectively use the ellipticity as a proxy for the shear.

Photons from a galaxy whose shear we wish to estimate undergo various distortions on the way to becoming counts in images. First is the small gravitational shear which we wish to measure. Variations in refractive index due to atmospheric turbulence cause a blurring and additional ellipticity in the observed galaxy, known as *seeing*. The telescope produces additional blurring and extra 'shear' due to imperfections in the optics. Further distortions can occur at the focal plane, where the image is pixelised. The response of a point source to these various processes (excluding the initial gravitational distortion) is called the *Point Spread Function (PSF)*. The galaxy image we observe is a convolution of the true (gravitationally sheared) appearance of the galaxy with the PSF. The PSF can be estimated from the observed profile of the stars in that image, since these can be treated as point sources. The PSF at a general point in the image (e.g. at the position of a galaxy) is then interpolated. The galaxies in the image are typically noisy due to sky background and thermal noise in the detector, further

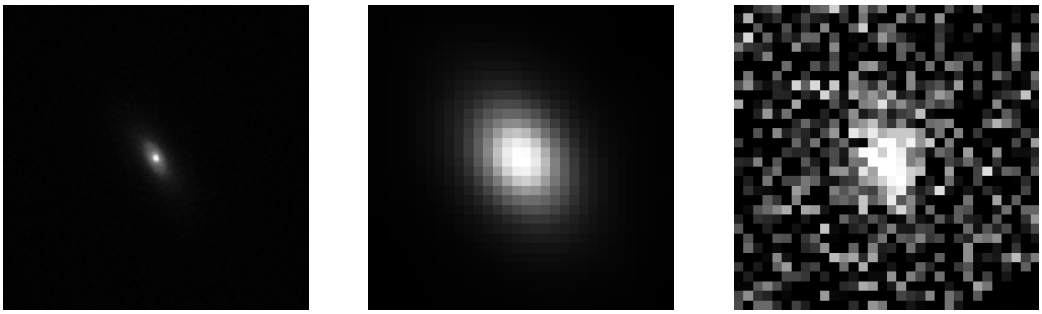

Figure 2.1: Degradation of a typical weak lensing galaxy image. The galaxy as observed in space (left panel) is smeared by the atmosphere and the telescope (middle panel), and pixelised at the focal plane. Additionally there is noise from e.g. sky background and thermal noise in the detector (right panel). The galaxy image is taken from the COSMOS survey (Koekemoer et al. 2007), rendered using the GalSim[3] package.

complicating attempts to recover the original gravitational distortion.

The typical galaxy whose ellipticity we wish to measure has an intrinsic size smaller than the PSF, as for the example in Figure 2.1, and has been gravitationally sheared by an amount a few times smaller than the shear imparted by the atmosphere and optics. Hence accurate deconvolution of the PSF is crucial. The fact that there are always more faint galaxies than bright galaxies, means that the typical galaxy signal-to-noise ratio ($S/N$) will not be much above the minimum $S/N$ for which a useful shape measurement can be made. The intrinsic ellipticity has a standard deviation of $\sim 0.2$ per component, while a typical shear is an order of magnitude smaller. So if we require the recovered shear to be fractionally biased at e.g. the sub-percent level, then the ellipticity has to be fractionally biased at less than one part in $10^3$ (see Huterer et al. 2006; Amara & Réfrégier 2008 for detailed investigations of shape measurement accuracy requirements for cosmic shear). I discuss some of the potential sources of bias in §2.1.2, after outlining some shape measurement methods in §2.1.1.

### 2.1.1 Methods

There are many ways to extract an estimate of the ellipticity from an image such as that in Figure 2.1. The most straightforward is to measure weighted quadrupole moments, defined as

$$Q_{ij} = \frac{\sum(x_i - \bar{x}_i)(x_j - \bar{x}_j)W(\mathbf{x} - \bar{\mathbf{x}})I(\mathbf{x})}{\sum W(\mathbf{x} - \bar{\mathbf{x}})I(\mathbf{x})} \tag{2.4}$$

where $\bar{\mathbf{x}}$ is the galaxy centroid, $I(\mathbf{x})$ is the flux at position $\mathbf{x}$, and the subscripts $i, j$ denote image coordinate components of $\mathbf{x}$. The weighting function, $W$, is chosen to upweight pixels where the galaxy flux is more significant, and downweight the contribution from noise in pixels far from the centroid. For $W(\mathbf{x}) = 1$, the (complex) ellipticity, $\epsilon$, can be estimated from the following combination of quadrupole moments

$$\epsilon = \frac{Q_{xx} - Q_{yy} + 2iQ_{xy}}{Q_{xx} + Q_{yy} + 2\sqrt{Q_{xx}Q_{yy} - Q_{xy}^2}}. \tag{2.5}$$

However, this only estimates the ellipticity of the PSF-convolved galaxy image. The most well-known moments-based method is KSB (Kaiser et al. 1995), which corrects for the PSF perturbatively, using the moments of the PSF. Various improvements have been made on the original KSB methods (e.g. Luppino & Kaiser 1997; Hoekstra et al. 1998; Rhodes et al. 2000; Bacon et al. 2001; Hirata & Seljak 2003), but accurate PSF correction in this framework becomes difficult for realistic PSFs. Various works (Kaiser 2000; Zhang 2008; Bernstein & Armstrong 2014a) have demonstrated that the PSF correction can be accurately performed by using Fourier space moments.

An alternative approach is the *model-fitting* approach, in which it is assumed that a galaxy's light profile can be fit by a parametric model, with parameters $\boldsymbol{\theta}$. This model can be convolved with the PSF, to produce a (pixelised) model galaxy image, $\boldsymbol{M}$ which is then compared with the observed (pixelised) galaxy

image $\boldsymbol{I}$. The probability of the galaxy having parameters $\boldsymbol{\theta}$ is then, using Bayes' theorem,

$$P(\boldsymbol{\theta}|\boldsymbol{I}) \propto P(\boldsymbol{I}|\boldsymbol{\theta})Pr(\boldsymbol{\theta}). \tag{2.6}$$

where $Pr(\boldsymbol{\theta})$ is the prior on the parametric model, and the first term on the right is the likelihood $\mathcal{L}$ which, for Gaussian uncorrelated noise, is given by

$$\log \mathcal{L} = -\frac{\chi^2}{2} = -\frac{1}{2}\sum_i (M_i(\boldsymbol{\theta}) - I_i)^2/\sigma_i^2 \tag{2.7}$$

where $i$ now denotes a pixel index, and $\sigma_i$ is the noise in pixel $i$. Hence we have a standard parameter estimation problem, and standard statistical methods can be applied to explore the posterior of the model parameters, $\boldsymbol{\theta}$. Usually a single estimate of the ellipticity for each galaxy is used, for example Miller et al. (2007) use the mean of the posterior, and Zuntz et al. (2013) use the maximum likelihood estimate (MLE). Commonly used parametric models are sums of elliptical Gaussians (Kuijken 1999; Bridle et al. 2002), and elliptical Sérsic profiles (e.g Miller et al. 2007; Zuntz et al. 2013).

The Sérsic profile (Sérsic 1963) has the intensity at radius $r$, $I(r)$ given by

$$I(r) = I_0 \exp\left(-\left(\frac{r}{\alpha}\right)^{1/n}\right) \tag{2.8}$$

where $I_0$ is the central ($r = 0$) intensity, $\alpha$ is the scale radius, and $n$ is the Sérsic index. A Sérsic profile with $n = 1$ is an exponential model, while $n = 4$ is known as the *de Vaucouleurs* profile (de Vaucouleurs 1953). The $n = 1$ and $n = 4$ models are also known as 'disc' and 'bulge' models, respectively, from their suitability in describing the light profiles of these galaxy components.

In Jarvis et al. (2015), we used two model-fitting methods. IM3SHAPE (Zuntz et al. 2013) used a maximum likelihood 'bulge or disc' procedure i.e. it fits separately a bulge model and a disc model, and picks the result with better likelihood. It uses simulations to correct biases associated with the limitations of

the maximum likelihood estimate and model (see §2.1.2). NGMIX[4] was used in 'disc-only' mode, approximating an exponential profile using sums of Gaussians (Hogg & Lang 2013). It also fits a sum of Gaussians to the PSF, allowing for fast analytic convolution of the model and PSF.

### 2.1.2 Sources of bias

The STEP challenge (Heymans et al. 2006) parameterised biases on the estimated shear as a combination of a multiplicative term $m_i$, and an additive term $c_i$, where the index $i$ now denotes component $i$ of the shear

$$\gamma_i^{\rm obs} = (1 + m_i)\gamma_i^{\rm true} + c_i. \tag{2.9}$$

This parameterisation is now the standard in the shape measurement literature. In the following, I describe some of the main sources of biases which can produce non-zero $m_i$ and $c_i$.

#### Noise bias

Whether using a moments-based or model-fitting approach, a point-estimate of the ellipticity is very likely to be a non-linear function of the pixel values of the galaxy image. For example, in the moments-based approach, Equation 2.5 takes a ratio of linear functions of the pixel values, while the treatment of the PSF may also add nonlinearity. The presence of pixel noise in the estimation of these nonlinear functions leads to bias on the ellipticity estimates, known as *noise bias*. Hirata et al. (2004) derive the noise bias on weighted moments estimates of Gaussian galaxy profiles, including the effect of the PSF. Refregier et al. (2012) derive the dependency of the noise bias on the $S/N$ for maximum likelihood model-fitting methods, and derive analytic results for the case of an elliptical Gaussian galaxy profile. Kacprzak et al. (2012) extend this using more realistic image simulations,

[4] `https://github.com/esheldon/ngmix`

and outline a method for calibrating MLE model-fitting shear estimates using image simulations. They find that noise bias produced multiplicative bias $m \sim 10\%$ and additive bias $\sim 0.3\%$ for $S/N = 20$, $R_{\rm gp}/R_{\rm p} = 1.4$ galaxies, where $R_{\rm gp}/R_{\rm p}$ is the ratio of the PSF-convolved galaxy full-width-at-half-maximum (FWHM) to the PSF FWHM. Noise bias of this level makes it the dominant multiplicative bias for these methods.

Various other approaches to dealing with noise bias have been proposed. Perhaps the most theoretically satisfying, although yet to be proven on real data, is that of Bernstein & Armstrong (2014b), who present Bayesian methods to estimate the shear of an ensemble of source galaxies, rather than assigning individual ellipticity point-estimates. These methods rely on having low-noise galaxy images (from significantly deeper observations than the main survey data) of a representative sample of the source galaxies. In Jarvis et al. (2015) we also used low-noise galaxy images to calibrate the IM3SHAPE pipeline, simulating the effect of noise bias, by adding noise. Specifically, we created the 'GREAT-DES' image simulations, with noise properties and PSF model parameters matched to the DES-SV data. The input galaxies are real images from the COSMOS survey (Koekemoer et al. 2007), rendered using the GALSIM[5] package. The GREAT-DES simulations are described in detail in Section 6.1 of Jarvis et al. (2015). In fact, this approach to calibration should also account for the model bias and selection biases, described below, as long as the calibration simulations are sufficiently realistic. From the GREAT-DES simulations, we derived a fitting function relating the measured galaxy $S/N$ and $R_{\rm gp}/R_{\rm p}$ to the multiplicative and additive biases, $m$ and $c$. This fitting function was then applied to the real data, producing a correction to ellipticity estimates for each galaxy in the sample. Figure 2.2 shows $m$ as a function of $S/N$ and size. As expected, the bias is largest for the smallest, noisiest galaxies.

The NGMIX pipeline took a different approach to the noise-bias, based on a

[5] `https://github.com/GalSim-developers/GalSim/wiki/RealGalaxy%20Data`

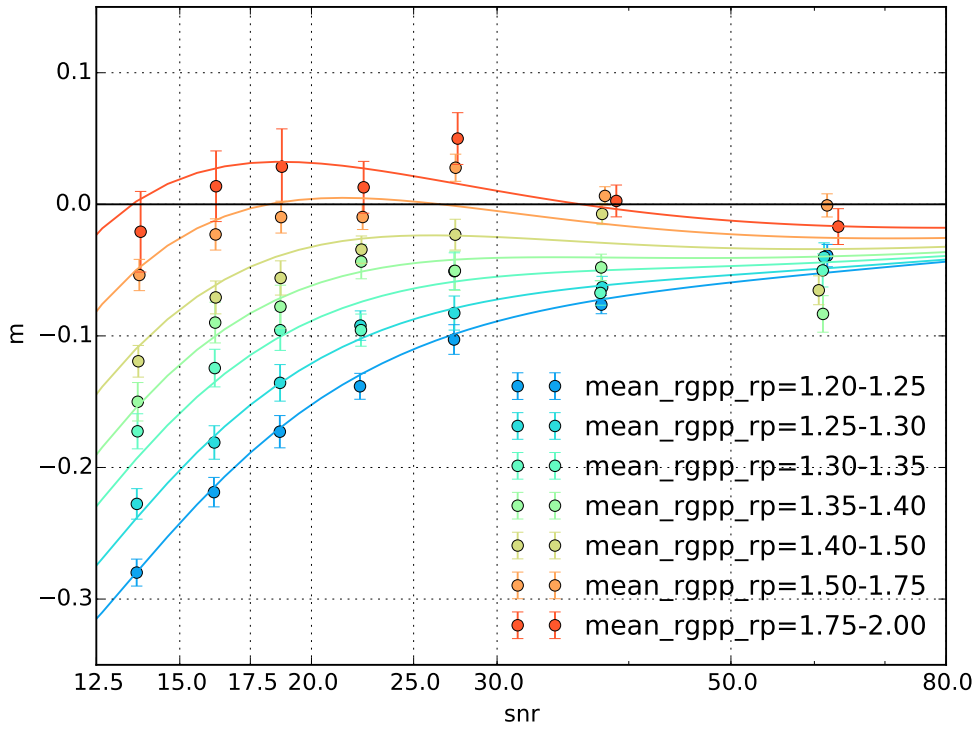


Figure 2.2: The multiplicative shear bias, $m$, on IM3SHAPE maximum likelihood shear estimates, signal-to-noise ('snr'). The galaxies are seperated into multiple size bins, represented by the different coloured lines. The size measure 'mean_rgpp_rp' is the ratio of the observed (i.e. PSF concolved) galaxy full-width-at-half-maximum to the PSF full-width-at-half-maximum. These are estimated from the GREAT-DES simulations. This plot was taken form Jarvis et al. (2015), and was made by Tomasz Kacprzak.

'lensfit'-style method (Miller et al. 2007). Rather than using a maximum likelihood estimate of the model, a Markov Chain Monte Carlo (MCMC) chain is used to explore the full posterior of the model, and the mean of this posterior used as the ellipticity estimate. To reduce the effect of noise bias, a prior on the model parameters is used. The prior has the effect of reducing the sensitivity of the shear estimate because as the $S/N$ tends to zero, the posterior will tend to the prior. This requires a 'sensitivity correction' be applied to each ellipticity estimate, which is also calculated from the posterior as estimated from the MCMC chain.

### Model bias

Model-fitting methods (such as IM3SHAPE and NGMIX) use a limited basis set to fit galaxies with arbitrarily complex morphologies. Some amount of under-fitting is inevitable, which can result in biased shear estimates; this is known as *model-bias* (Lewis 2009; Voigt & Bridle 2010; Bernstein 2010; Melchior et al. 2010). In Kacprzak et al. (2013) we showed that for a 'bulge+disc' model (i.e. simultaneously fitting bulge and disc components), the model bias from fitting to COSMOS galaxies is on average at the 0.5% level. However, for the bulge *or* disc model used by IM3SHAPE in Jarvis et al. (2015), it may be larger. The model-bias is likely to be larger still for the disc-only model used by NGMIX. Since the GREAT-DES simulations that were used to calibrate IM3SHAPE used real galaxy images as input, then model bias should be included in the calibration, assuming that the galaxies in the GREAT-DES simulation are representative of the real data. However, there is some evidence that the bulge-fraction as a function of $S/N$ does not match between the simulations and real data (see Section 6.1 of Jarvis et al. 2015). The few percent errors shown by NGMIX on the GREAT-DES simulations (see Section 8.5 of Jarvis et al. 2015) are likely to be at least partly due to model bias.

### PSF errors

The PSF at galaxy positions is interpolated from the PSF measured at star positions. There is arbitrary freedom in the choice of basis functions for the interpolation. The PSF can be a very non-trivial function, for example, the contributions from the optics will likely have very different characteristics to the more random contributions from the atmosphere. Furthermore, some components of the PSF are likely to be common between the multiple CCDs that make up the focal plane, while some are likely to be isolated to single CCDs. Bilinear polynomial interpolation is popular, while PCA methods (Jarvis & Jain 2004;

Schrabback et al. 2010) have been suggested as a good way of identifying a basis set for features common between exposures (e.g. aspects of the optics, rather than the atmosphere). A poor choice in basis functions can result in overfitting or underfitting the PSF; Rowe (2010) explore possible source of, and diagnostics for both of these effect. Paulin-Henriksson et al. (2008) place requirements on the number of stars required for PSF estimation at a particular point, for simple PSF models, taking into account the limitations of finite pixel size.

In Jarvis et al. (2015), we used the package PSFEx (Bertin 2011), which fits a pixelised image of the PSF at each star, which is then interpolated using a two-dimensional second-order polynomial, separately on each CCD. I present methods for diagnosing how errors in the PSF treatment are propagated to the cosmic shear signal in §2.1.4, and apply them to the DES-SV data.

### Star-galaxy separation

Estimation of weak lensing statistics requires a clean galaxy sample, since the inclusion of any stars will dilute the signal. For PSF estimation a clean stellar sample is required, since the inclusion of galaxies, which are not point-sources, will contaminate what should be a model of the response of point-sources. Henrion et al. (2011) provide a useful review of star-galaxy classification methods, as well as developing a Bayesian framework to tackle the problem.

### Blending

The challenge of unbiased shear estimation from single, isolated galaxies, has proven sufficiently time-consuming that comparatively few advances have been made in accounting for when the target galaxy has a close neighbour, be it a star or another galaxy. Assuming the two (or more) objects in question can be identified as multiple objects, a robust shape measurement method must minimize the effect of light from the neighbour. The zeroth[6] order approach taken in

[6]and currently highest!

weak lensing is masking any pixels associated with neighbouring objects, or in other words, giving them zero weight in the shape measurement process. This approach is likely to be sufficient for neighbours which are close, but do not have significant isophotal overlap with the target object. For objects which do have significant isophotal overlap, which are known as *blended* objects, a given pixel cannot be unambigously assigned to one of the objects, since both objects may contribute significantly to the flux in that pixel. For the DES-SV analyses we removed blended objects, which were identified by SExtractor, the detection and photometry software used on the DES-SV images. For unblended objects with close neighbours, I developed the 'überseg' masking scheme, which masks any pixels closer to a neighbouring object than the target object. This scheme, demonstrated in Figure 2.3, was adopted by both pipelines, since we observed an improvement in the performance on the end-to-end simulations (Section 6.2 of Jarvis et al. 2015), after its implementation. In §5.3, I discuss and quantify the selection bias that arises from excluding blended objects, which was identified by Hartlap et al. (2011).

Blending presents a major challenge for shear estimation from future datasets, particularly for ground-based experiments, where the larger PSF due to the atmosphere increases the amount of blending. The amount of blending also increases with the galaxy number density, so LSST, a deep, ground-based experiment, will be particularly adversely affected. Even if shape measurement methods (for example simultaneously model-fitting multiple objects) are developed that can deal with objects identified as blended, there will still exist many objects in the data which are blended to such an extent that they cannot be identified as two objects. Dawson et al. (2014) call these 'ambiguous blends', and focus only on the effect of blending on the shape noise, which is significant since the variance in total ellipticity of blended pairs of galaxies is greater than the ellipticity variance for single objects. They predict that for the full LSST dataset, with limiting magnitude $i \sim 27$, ambiguous blending results in a $\sim 14\%$ increase in the shape noise.

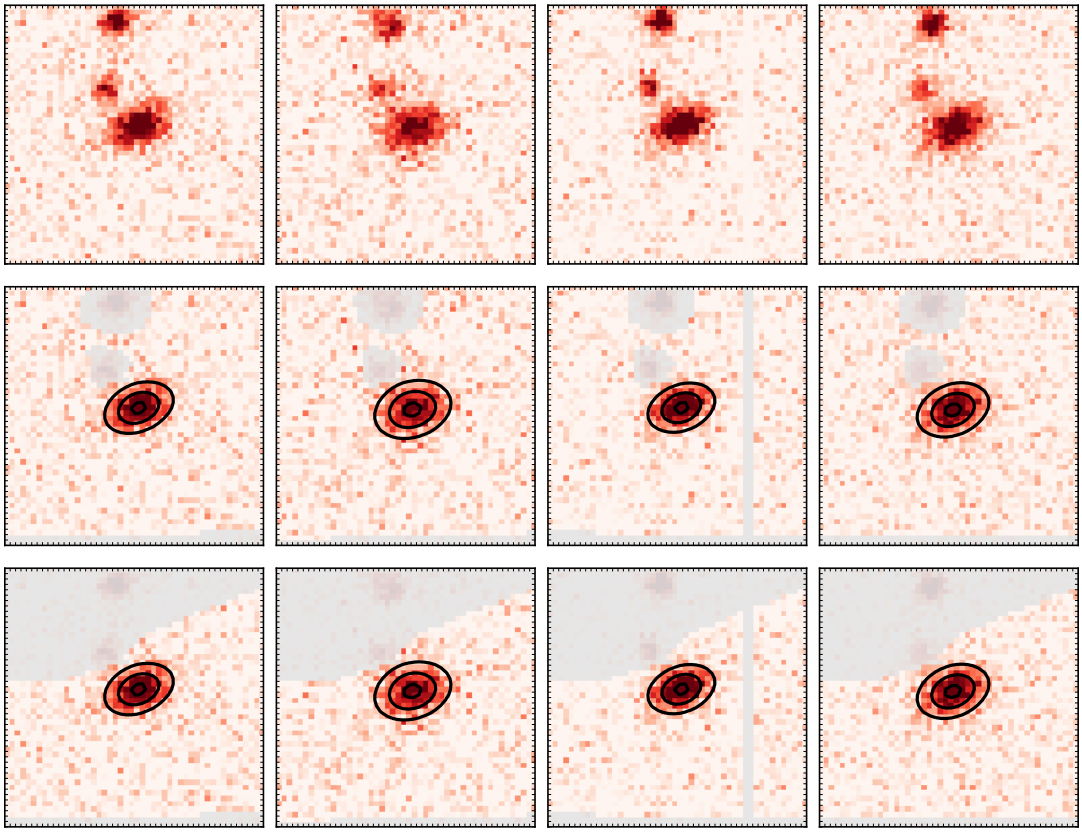

Figure 2.3: The überseg masking scheme. The first row shows four single-epoch observations of a single galaxy in DES-SV. The galaxy has two close neighbours. In order to reduce bias and noise in the shape measurement, we tried two masking schemes. In the second row, masked pixels are those assigned to the neighbouring objects by SExtractor. The third row shows the überseg scheme, with only those pixels closer to the target object than any other object left unmasked. This plot was taken form Jarvis et al. (2015), and was made by Joe Zuntz.

### Selection bias

A common situation is that a shape measurement method will perform well on some selection of the source galaxies e.g. the higher $S/N$ source galaxies. Even in the situation where we have a method which returns an unbiased shape measurement from every galaxy above some $S/N$ threshold, we can still obtain a biased estimate of the ensemble shear, in the case that a *selection bias* has been induced by selecting those particular galaxies.

Selection biases tend to arise because most $S/N$ estimators use some filter, or

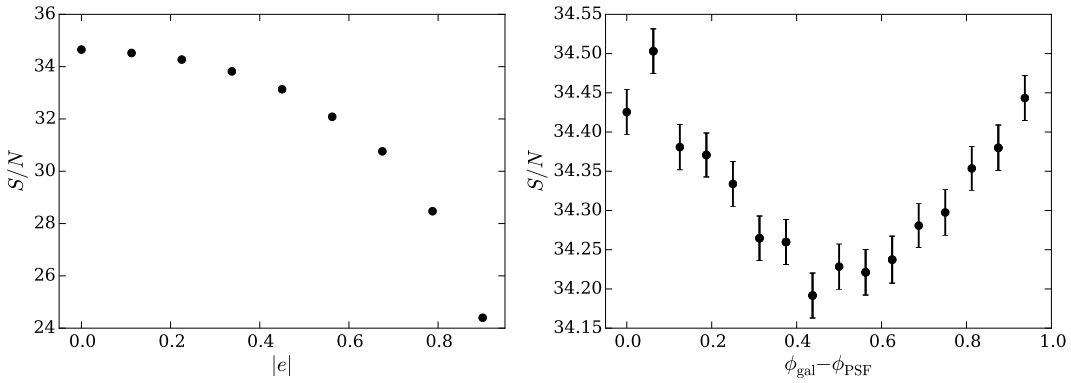


Figure 2.4: Two sources of selection bias. Left panel: The IM3SHAPE $S/N$ as a function of ellipticity, for a galaxy of the same flux, size, noise level, and PSF. Right panel: The IM3SHAPE $S/N$ for a galaxy with ellipticity 0.2, and PSF with ellipticity 0.05, as a function of the misalignment between the galaxy and PSF major axes.

weight function, that will result in a higher $S/N$ estimate the more similar the object is to the filter. For example, the PSF acts as such a filter, and is close to round on average (for DES at least), hence round galaxies are given higher $S/N$ than elliptical ones with the same intrinsic flux and area. The left panel of Figure 2.4 demonstrates this effect on the $S/N$ as returned by IM3SHAPE[7]. For this figure I simulated exponential disc galaxies with different ellipticities, but otherwise equal properties using GALSIM. I ran IM3SHAPE on these images, and plot the $S/N$ returned, which is 30% lower for $|e| = 0.9$ than for $|e| = 0$.

A result of this is that galaxies with intrinsic shape anti-aligned with the shear (and therefore rounder), are given higher $S/N$ than galaxies aligned with the shear. So applying a $S/N$ cut[8], or weighting galaxies by the $S/N$, will produce a galaxy sample with a negative correlation between intrinsic shape and shear. Thus the observed ellipticity (the intrinsic shape plus the shear) is no longer an

[7]IM3SHAPE uses a 'matched-filter' $S/N$, defined

$$S/N = \frac{\sum_p M_p I_p/\sigma_p}{(\sum_p M_p^2/\sigma_p^2)^{1/2}}, \tag{2.10}$$

where the sums are over the pixel indices $p$, $I_p$ is the flux of the data in pixel $p$, $M_p$ is the flux of the best-fit model in pixel $p$, and $\sigma_p$ is the noise of the data in pixel $p$.

[8]This 'cut' may be implicit in the galaxy detection algorithm.

unbiased estimate of the shear. The result is a multiplicative bias - since the higher the shear, the stronger the selection bias. Hirata & Seljak (2003) find this multiplicative bias to be a few percent for a moments-based shear estimator.

Another consequence of this kind of selection bias is an additive bias (a correlation between the inferred shear and the PSF shape) since galaxies aligned with the PSF are given higher $S/N$ than those anti-aligned with the PSF. This effect was identified by Kaiser et al. (2000), and further investigated by Bernstein & Jarvis (2002). In Miller et al. (2013), which provides the shear catalog for CFHTLenS, this effect manifests as a correlation between the weights assigned to source galaxies, and the orientation with respect to the PSF ellipticity, resulting in a non-zero correlation between the estimated shear and the PSF ellipticity when the weights are applied (see Section 8.4 and Figure. 10 of that work). I demonstrate this effect in the right panel of Figure 2.4, which shows the IM3SHAPE $S/N$ as a function of the alignment between the galaxy and PSF major axes. The $S/N$ estimate has a small, but significant bias, depending on the alignment angle, with galaxies aligned with the PSF having higher $S/N$, as expected.

Selection biases can be calibrated using image simulations, by making the same selections on the simulations as are made on the real data, with the usual caveat that the effectiveness of the calibration depends on how realistic the simulations are. This was the approach taken for the IM3SHAPE catalog for DES-SV; the same galaxy size and $S/N$ cuts that were made on the data were applied to the GREAT-DES calibration simulations. NGMIX, The other shape measurement pipeline in Jarvis et al. (2015), took a more analytic approach, defining a 'round' $S/N$ estimator, which involves shearing the fitted galaxy model such that it is round, and calculating the $S/N$ using this model (see Section 7.2 of Jarvis et al. 2015).

### 2.1.3 Diagnostics

There are various tests that can be performed on a shape catalog than can reveal systematic errors, or give us confidence that they are science-ready. These tests should be cosmology independent, since the passing or failure of a test under an assumed cosmology will bias for or against that cosmology. Therefore these tests usually take the form of *null tests*, tests which pass when a null signal is observed. For example, we do not expect gravitational lensing to produce a B-mode signal (at least at the currently achievable level of precision). Most null tests involve correlating the shear signal with some quantity which we do not expect the true shear to be correlated with.

In Jarvis et al. (2015), we performed a suite of these null tests, including demonstrating the shear had zero B-mode. I calculated several of these, some of which were easy to interpret, and others less so. One of the former was looking at the tangential shear around stars. We expect to observe a tangential shear signal around galaxies, since galaxy positions are correlated with the matter field which produces the lensing signal. We might expect at least some of any systematic contributions to the signal to also be present in the tangential shear around stars, while of course any gravitational lensing signal will not be. Figure 2.5 demonstrates the satisfactory null signal.

Another null-test I worked on was examining correlations between the measured galaxy shapes and the PSF shape, which could arise from imperfect deconvolution of the PSF, resulting in a 'leakage' of the PSF ellipticity into the galaxy ellipticity. In §2.1.4, I detail the derivation of the estimator of this leakage coefficient which we used in Jarvis et al. (2015). I also extend this formalism to include correlations between the observed galaxy shapes and PSF model residuals.

Unfortunately, there is no source of absolute calibration for the multiplicative errors that arise from e.g. noise bias. Shape measurement methods should be tested on image simulations, with the degree of belief imparted in the method

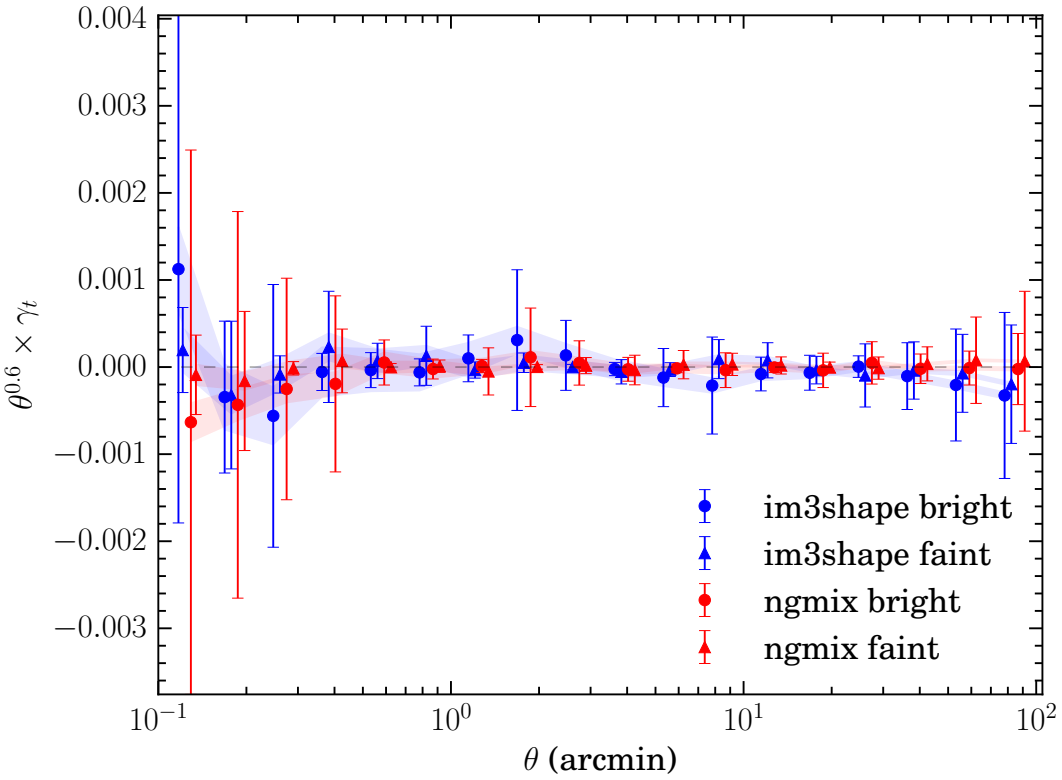


Figure 2.5: Tangential shear around stars for IM3SHAPE (blue) and NGMIX (red). Stars are split into to two bins of i-band magnitude. "bright" means $14 < m_i < 18.3$ and "faint" means $18.3 < m_i < 22$. The faint sample includes stars used for PSF modeling; bright stars are excluded to avoid the brighter-fatter effect (cf. Section 4.1 of Jarvis et al. 2015). Shaded regions represent $1\sigma$ shape noise error, while error bars are from jackknifing the stars. I made this plot for Jarvis et al. (2015).

dependent on how realistic the simulations are believed to be. A method which continues to perform well despite variations in the image simulations is more likely to be a robust one. As precarious as this may sound, shape measurement is not alone in cosmology or fundamental physics (e.g. Aad et al. 2012; Abbott et al. 2016), in requiring realistic simulations for robust inference. For the DES-SV analyses, we did have the advantage of having two significantly independent shape pipelines, so demonstrations of their consistency are encouraging if not definitive. I implemented a powerful test of their consistency, the ratio of their tangential shear signals around LRGs, which I discuss in §2.1.5.

### 2.1.4 Galaxy×PSF and galaxy×PSF-residual correlations

Effective galaxy shape measurement requires effective treatment of the PSF, which can be separated into two steps. Firstly, the PSF at the position of galaxies needs to be accurately estimated from the stars in the image. The result of this process is a PSF model. Any residuals between the PSF model and the true PSF will be propagated to the estimated galaxy ellipticity when the PSF model is 'deconvolved'. Paulin-Henriksson et al. (2008) investigate how PSF model errors are propagated to errors on the shear estimation. They show that for an unweighted quadrupole moments shear estimator, in the case of elliptical Gaussian galaxy and PSF profiles, the bias, $\delta\epsilon$, on the shear due to a PSF model ellipticity residual $q$ is, to first order in $q$

$$\delta\epsilon = -\left(\frac{R_{\rm PSF}}{R_{\rm gal}}\right)^2 q \tag{2.11}$$

where $R_{\rm PSF}$ and $R_{\rm gal}$ are the PSF and galaxy size respectively.

The second step is the deconvolution of the PSF model from the galaxy image; inaccuracy in this step can result in correlation between the PSF model ellipticity and the estimated galaxy ellipticity, sometimes called 'leakage' of the PSF model ellitpicity into the estimated galaxy ellipticity. While many shape measurement methods, e.g. model-fitting methods, do not perform a formal deconvolution, this PSF-leakage can still occur, for example, as a result of noise bias, or because galaxies oriented with the PSF may have higher $S/N$, and therefore be more likely to be detected[9].

With these considerations in mind, I write the observed shape, $\epsilon$, as a sum of the true shear, $\gamma$; an additive term linear in the PSF ellipticity $p$, due to imperfect deconvolution of the PSF; and an additive term linear in the PSF model ellipticity residual, $q$. $q$ can be calculated at the position of stars, by

[9] or pass any quality cuts on $S/N$, or be given a higher weight in the calculation of whatever statistic the shear catalog is being used for.

comparing the prediction of the PSF model to a direct measurement of the star ellipticity (see Section 4.4. of Jarvis et al. (2015)). So

$$\epsilon = \gamma + \alpha p + \beta q \tag{2.12}$$

where $\alpha$ and $\beta$ are constants of proportionality. Note I am only considering here additive biases related to the PSF treatment, and ignore multiplicative bias in equation 2.12. Although the exact effect on $\epsilon$ of errors in the deconvolution or estimation of the PSF will in general be complex and nonlinear, it is reasonable to assume that in the case that these errors are small, we can treat the problem perturbatively, and the first order terms will be those in equation 2.12. The 'true shear', $\gamma$, actually also contains the intrinsic shape and for a finite patch of sky, need not average to zero. It simplifies the algebra considerably to subtract the mean from each variable, $x$, in equation 2.12, defining a zero mean version of each, $x' \equiv x - \bar{x}$. Then for two uncorrelated variables $x$ and $y$, $\langle x'y' \rangle = \bar{x}\bar{y} = 0$. Having subtracted the means, we have

$$\epsilon' = \gamma' + \alpha p' + \beta q'. \tag{2.13}$$

We can estimate the mean $\alpha$ and $\beta$ (which I will continue to refer to as $\alpha$ and $\beta$, but note these coefficients will likely vary with e.g. the galaxy size) by measuring cross-correlations between the observed ellipticity and the PSF model, and also between the observed ellipticity and the PSF ellipticity residual

$$\langle \epsilon' p' \rangle = \langle \gamma' p' \rangle + \alpha \langle p' p' \rangle + \beta \langle p' q' \rangle \tag{2.14}$$

$$\langle \epsilon' q' \rangle = \langle \gamma' q' \rangle + \alpha \langle p' q' \rangle + \beta \langle q' q' \rangle. \tag{2.15}$$

Since $\gamma$ and $p$ are uncorrelated, $\langle \gamma' p' \rangle = 0$, and similarly $\langle \gamma' q' \rangle = 0$. Solving for

$\alpha$ and $\beta$, we get

$$\alpha = \frac{\langle \epsilon' p' \rangle \langle q' q' \rangle - \langle \epsilon' q' \rangle \langle p' q' \rangle}{\langle p' p' \rangle \langle q' q' \rangle - \langle p' q' \rangle^2} \tag{2.16}$$

$$\beta = \frac{\langle \epsilon' q' \rangle \langle p' p' \rangle - \langle \epsilon' p' \rangle \langle p' q' \rangle}{\langle q' q' \rangle \langle p' p' \rangle - \langle p' q' \rangle^2}. \tag{2.17}$$

In the case that the PSF residuals are uncorrelated with the galaxy or PSF model ellipticities, $\langle \epsilon' q' \rangle = \langle p' q' \rangle = 0$, and

$$\alpha = \frac{\langle \epsilon' p' \rangle}{\langle p' p' \rangle} = \frac{\langle \epsilon p \rangle - \bar{\epsilon}\bar{p}}{\langle pp \rangle - \bar{p}^2}, \tag{2.18}$$

which is the expression we used in Jarvis et al. (2015).

In the case that the PSF ellipticity is uncorrelated with the galaxy or PSF residual ellipticity (i.e. the zero leakage case), $\beta$ simplifies to

$$\beta = \frac{\langle \epsilon' q' \rangle}{\langle q' q' \rangle}. \tag{2.19}$$

To estimate these quantities for the DES-SV NGMIX shape catalog, I use the same star catalog as described Section 4.4 of Jarvis et al. (2015) (which contains the stars used for the PSF estimation). I follow Rowe (2010) by using the correlation function $\xi_+(\theta)$, as the two-point statistic denoted by the $\langle\rangle$ in equations 2.14 onwards, which gives estimates of $\alpha$ and $\beta$ for each angular bin in $\xi_+(\theta)$. The left panel of Figure 2.6 shows estimates of these quantities as a function of angular scale, for the NGMIX catalog. I find a best fit $\alpha = -0.004 \pm 0.005$ (consistent with zero, in agreement with Jarvis et al. (2015) where we did not consider $\beta$). I find $\beta = -1.1 \pm 0.23$, which is the same order of magnitude as that from the unweighted moments esimate of Paulin-Henriksson et al. (2008). I assume both are independent of scale.

These constraints mean that firstly, the leakage of PSF model ellipticity into galaxy ellipticity for the NGMIX shape catalog is consistent with zero, and below

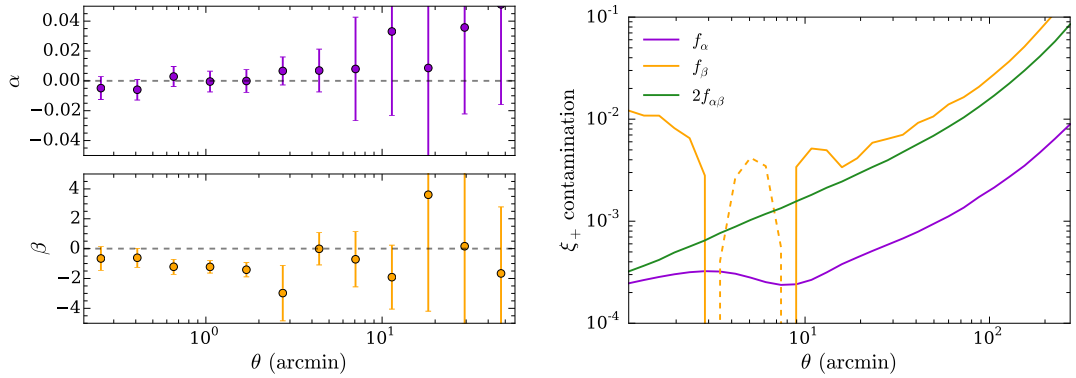


Figure 2.6: Left panel: Estimates of the PSF-leakage coefficient $\alpha$ and PSF ellipticity residual coefficient $\beta$ from the shear-PSF and shear-PSF-residual correlation functions. Right panel: The fractional contamination of the predicted shear-shear correlation function $\xi_+(\theta)$. The lines indicate the upper and lower $1\sigma$ limits, with negative contamination plotted as dashed lines.

the percent level. Note though that PSF correlations can be much larger than the cosmic shear signal, so this low level of leakage is crucial. Secondly, an error in the PSF model ellipticity is propagated to an approximately equal error in the galaxy ellipticity. I use these estimates of $\alpha$ and $\beta$ to estimate the contamination of the predicted shear correlation function, for the NGMIX catalog. The fractional contamination, $f(\theta)$, of $\xi_+^{\gamma\gamma}(\theta)$ is given by

$$f = f_\alpha + 2f_{\alpha\beta} + f_\beta = \frac{\alpha^2\xi_+^{pp} + 2\alpha\beta\xi_+^{pq} + \beta^2\xi_+^{qq}}{\xi_+^{\gamma\gamma}} \tag{2.20}$$

where I have dropped the $\theta$ argument from all terms. $f_\alpha(\theta)$, $2f_{\alpha\beta}(\theta)$ and $f_\beta(\theta)$ are plotted separately in the right panel of Figure 2.6, specifically, the maximum contamination allowed by the $1\sigma$ limits on $\alpha$ and $\beta$. All contamination terms are below 1% for most of the range used in the The Dark Energy Survey Collaboration et al. (2015) cosmology analysis ($2' < \theta < 60'$).

### 2.1.5 Tangential shear ratio

Galaxy-galaxy lensing provides a very clean test of the relative multiplicative bias between the NGMIX and IM3SHAPE catalogs, because the azimuthal symmetry inherent in the tangential shear signal largely cancels most sources of additive systematic error.

For this test, I use the tangential shear signal around Luminous Red Galaxies (LRGs) as determined by redMaGiC (red sequence Matched-filter Galaxies Catalog; Rozo et al. 2015) from the same DES SPT-E data. I use all galaxies that are well-measured by both NGMIX and IM3SHAPE. Regardless of the redshift of the LRGs and the source galaxies, the signal is expected to be the same for both catalogs.

The observed signal $\langle \epsilon_{t,i}(\theta) \rangle$ for each method $i \in \{\text{IM3SHAPE, NGMIX}\}$ can be written as:

$$\langle \epsilon_{t,i}(\theta) \rangle = (1 + m_i) \langle \gamma_t(\theta) \rangle + \langle \eta_i(\theta) \rangle, \tag{2.21}$$

where $\langle \gamma_t \rangle$ is the true underlying signal, $\langle \eta_i \rangle$ is a noise term including both intrinsic shape noise and measurement noise, and $m_i$ is a possible calibration error for each method. We mostly drop the argument $\theta$ in the following for brevity. For the same ensemble of galaxies, the two catalogs have identical values of $\langle \gamma_t \rangle$ and a similar shape noise contribution to $\langle \eta_i \rangle$ (though not identical, since the two methods use different bands). The contribution to $\langle \eta_i \rangle$ from shape measurement noise, however, may be somewhat different.

The red points in Figure 2.7 represent the ratio of measured tangential shear using the two shear catalogs. The weighted mean of the ratio over the range from 1 to 20 arcminutes (the typical scales of interest for weak lensing) is $0.932 \pm 0.018$. We would naively expect this to be an estimate of $(1 + m_{\text{NGMIX}})/(1 + m_{\text{IM3SHAPE}}) \approx 1 + m_{\text{NGMIX}} - m_{\text{IM3SHAPE}}$. However, three corrections are required before any conclusions can be drawn from this result about potential differences in the relative calibration.

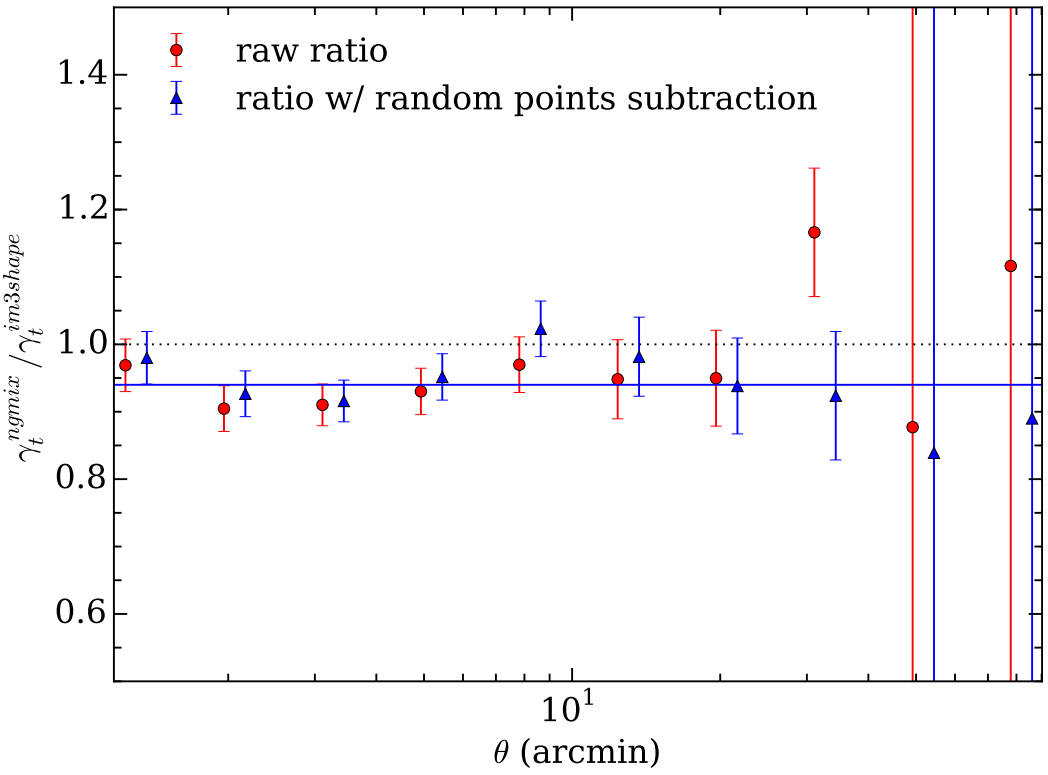


Figure 2.7: The ratios of tangential shear measurements around LRG galaxies from shears measured by NGMIX to those measured by IM3SHAPE. The red circles show the direct ratio and the triangles correspond to the ratio after subtraction of the tangential shear around random points. The weighted mean ratio in the scale range $1 - 20$ arcminutes is $0.954 \pm 0.018$. The blue line shows a prediction of the ratio (0.94) based on the GREAT-DES simulations, which accounts for a selection bias induced by the intersection of the two shape catalogs. This result is in good agreement with the data points. I made this plot for Jarvis et al. (2015)

First, the additive systematics only cancel if the sources are distributed uniformly around the lenses. This is approximately true, but the survey geometry can break the symmetry, especially at large scales. One solution is to subtract off the measured tangential shear around random points, drawn from the same region and with the same masking as the LRGs. No signal is expected around such points, but any additive bias will affect both measurements equally. Thus the difference is a cleaner estimate of the true tangential shear than the uncorrected signal. The blue points in Figure 2.7 show the effect of this subtraction,

and have a mean ratio of $0.954 \pm 0.018$,

Second, the ratio of two noisy quantities with the same mean does not in general have an expectation value equal to 1. If the denominator is a random variable, $X$, with a symmetric probability distribution (e.g. $X \sim \mathcal{N}(\bar{X}, \sigma_X)$), the ratio will be approximately $1 + \sigma_X^2/\bar{X}^2$.

To account for this, I created simulated realizations of the ratio, and compared the measured signal to the mean and variance of these. I generated a ratio realization in the following way:

1. Fit a polynomial, $\log(\langle\epsilon_t\rangle(\theta)) = p(\log(\theta))$ to the measured NGMIX signal, and take this to be the true signal, $\hat{\gamma}_t(\theta)$.

2. For each source in the ensemble, rotate both the NGMIX and IM3SHAPE shear by the same random angle.

3. Re-measure the two tangential shear signals, which now give estimates of the noise, $\langle\eta^r(\theta)\rangle$, as the true signal is removed by the random rotations.

4. Compute the realization ratio as

$$(\hat{\gamma}_t + \langle\eta^r_{\rm NGMIX}\rangle)/(\hat{\gamma}_t + \langle\eta^r_{\rm IM3SHAPE}\rangle). \tag{2.22}$$

I found the mean of these realizations to be consistent with a ratio of 1 on all scales, and so conclude that the high $S/N$ of the tangential shear ensures that the effect of the noise term in the denominator is negligible.

Finally, I find that the act of matching the two catalogs causes a selection bias in the NGMIX catalog for two reasons. First, the IM3SHAPE algorithm tends to fail more often for objects with low Sérsic index ($n < 1$). And second, the cuts we make on the IM3SHAPE measurements of $S/N$ and $R_{gp}/R_p$ mean round galaxies are preferentially selected. These two selection effects, when applied to the NGMIX catalog impart a net bias on the NGMIX shear estimates in the matched

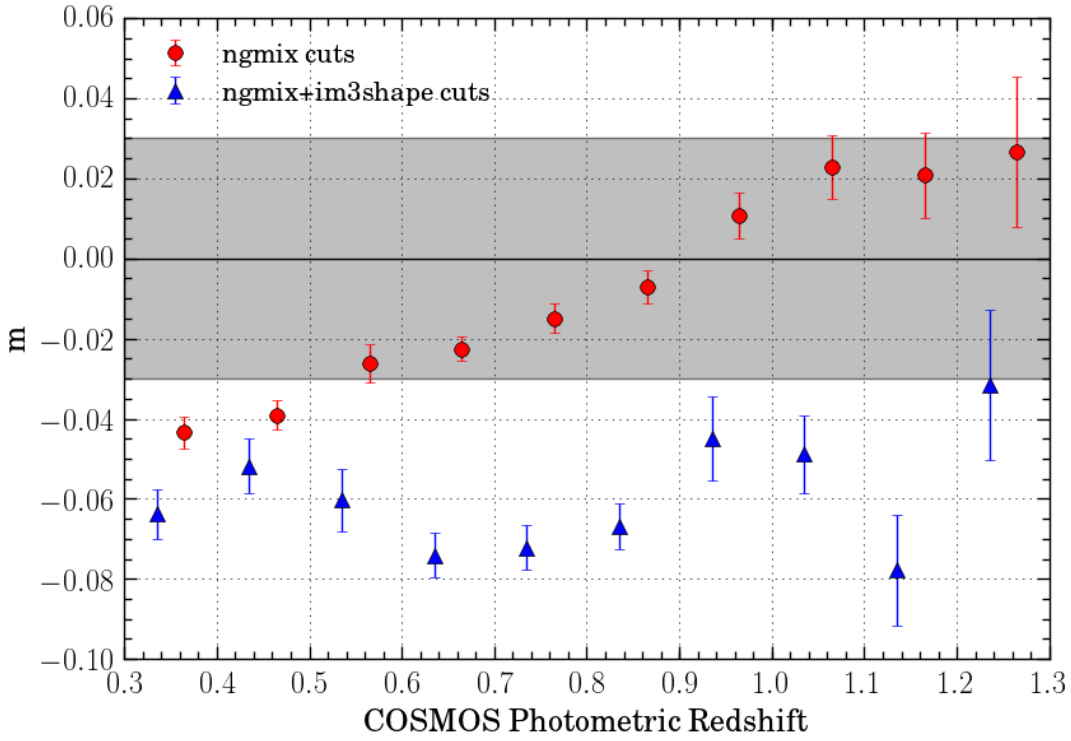


Figure 2.8: Multiplicative bias for NGMIX shear measurements on GREAT-DES simulated data as a function of redshift. The red circles show the bias calculated using all galaxies that pass the NGMIX cuts. The blue triangles show the bias when also including the recommended IM3SHAPE cuts, as we do to obtain the matched catalog used for Figure 2.7. The grey band represents the ±3% requirement for the SV data. This plot is taken from Jarvis et al. (2015), and was made by Simon Samuroff.

catalog that is not present in the full NGMIX catalog. Note that these selections do not bias the IM3SHAPE catalog, since the same selections are applied to the image simulations that are used for calibration.

I quantify the level of this selection bias by performing the same procedure on the GREAT-DES simulations. I compare the mean bias for NGMIX as a function of redshift first using only its own cuts and then also applying the IM3SHAPE cuts. The result is shown in Figure 2.8. The matching induces a mean selection bias of about −3%. Furthermore, the bias increases with redshift. Weighting the bias according to the lens redshift distribution and the lensing efficiency of the source galaxies used in the tangential shear ratio test (and assuming that the lenses do

not evolve with redshift), I find a net selection bias of $-6\%$ for NGMIX in the matched catalog relative to whatever bias might be present in the full NGMIX catalog[10].

The mean ratio of $0.954 \pm 0.018$ is thus consistent with the prediction from GREAT-DES of $-6\%$ selection bias (which would produce a ratio of 0.94). This bias induced by the combination of IM3SHAPE and NGMIX cuts in the matched shape catalogs is shown by the blue line in Figure 2.7. Thus the measurement is not inconsistent with there being no multiplicative bias in either catalog.

## 2.2 Intrinsic Alignments

Because the observed ellipticity is used to estimate the shear, the two-point correlation function of the observed ellipticity is naturally used to estimate the two-point correlation function of the shear. From equation 1.69, we have

$$\langle \epsilon_i \epsilon_j^* \rangle = \langle \gamma_i \gamma_j^* \rangle + \langle \gamma_i \epsilon_j^{\mathrm{I}*} \rangle + \langle \epsilon_i^{\mathrm{I}} \gamma_j^* \rangle + \langle \epsilon_i^{\mathrm{I}} \epsilon_j^{\mathrm{I}*} \rangle, \tag{2.23}$$

where the angle brackets denote an average over all galaxy pairs $i, j$. The first term is the cosmologically sensitive term that we wish to relate to theory. The last term is the 'intrinsic-intrinsic' (II) term, which arises when a pair of galaxies' intrinsic shapes are correlated. It is reasonable to assume that this correlation only arises for physically close galaxy pairs i.e. galaxies close in redshift as well as on the sky. The second and third terms arise from correlations between the gravitational shear of one galaxy in the pair, and the intrinsic shape of the other galaxy, hence these terms are known as the gravitational-intrinsic, or 'GI' contribution (Hirata & Seljak 2004, 2010). The GI contribution occurs for galaxy pairs widely separated in redshift (of which there are many more than pairs close in

[10] I tested for a similar selection bias in the IM3SHAPE catalog due to imposition of the NGMIX cuts. The impact of the matching was found to be negligible, in part because the NGMIX catalog is deeper, so its cuts have very little impact on the IM3SHAPE selection.


Figure 2.9: (yet another) Intrinsic alignments cartoon: The left panel demonstrates the 'II' contribution. The blue solid lines represent the unlensed elliptical isophotes of two galaxies at the same redshift as some overdensity, which due to e.g. tidal forces, point at the overdensity. Thus the two galaxies' intrinsic shapes are correlated, adding to any correlation in their observed shapes due to cosmic shear. The right panel demonstrates the 'GI' contribution. The red solid line demonstrates the unlensed isophotes of a higher redshift galaxy, which is lensed by the overdensity such that the dashed red line is the observed shape.

redshift!). Figure 2.9 attempts to give some physical intuition about how these correlation may arise. A non-zero II term can arise if the tidal field due to a dark matter halo causes physically close galaxies to point towards it, in which case close galaxies pairs point in the same direction. A non-zero GI term can arise due to the lensing of a higher redshift galaxy by the same dark matter halo, resulting in an anti-correlation between the intrinsic shapes of the lower redshift galaxies, and the shear on the high redshift galaxy.

Using this 'G' and 'I' notation, the observed shear power spectrum, $C^{\rm obs}(l)$, is often written

$$C^{\rm obs}(l) = C^{\rm GG}(l) + C^{\rm GI}(l) + C^{\rm II}(l). \tag{2.24}$$

Note that for the cross-spectrum $C_{ij}$ between two different redshift bins $i$ and $j$, $C^{\rm GI}$ has two contributions, $C^{\rm GI}_{ij}$ and $C^{\rm GI}_{ji}$.

Although the study of galaxy alignments is by no means a recent one (e.g. Hawley & Peebles 1975), the first works which explored it in the context of weak lensing (Catelan et al. 2001; Heavens et al. 2000; Croft & Metzler 2000)

appropriately appeared around the same time as the first detections of cosmic shear. Catelan et al. (2001) introduce what is now known as the *linear alignment* model (see also Hirata & Seljak 2004, 2010), which assumes galaxies are oriented with their halos, whose ellipticity is linear in the tidal field. While potentially a good description of elliptical galaxies, Lee & Pen (2001), Catelan et al. (2001) and Mackey et al. (2002) (to name a few) suggest that the orientation of disc galaxies is likely to be determined by the angular momentum of the tidal field, and use the predictions of tidal torque theory (White 1984) to make predictions for the observed alignments of spiral galaxies.

Just as in equation 2.1 the shear power spectrum can be written as an integral over the matter power spectrum, $P_\delta(k, z)$, in the Limber approximation, the GI and II angular power spectra in equation 2.24 can be written as integrals over the three-dimensional intrinsic-intrinsic and matter-intrinsic power spectra $P_{\rm II}(k, z)$ and $P_{\delta{\rm I}}(k, z)$ (e.g. Mackey et al. 2002; Hirata & Seljak 2010)

$$C_{ij}^{II}(l) = \int d\chi N_i(\chi) N_j(\chi) P_{\rm II}(l/\chi, \chi) \tag{2.25}$$

$$C_{ij}^{GI}(l) = \int d\chi W_i(\chi) N_j(\chi) P_{\delta{\rm I}}(l/\chi, \chi) \tag{2.26}$$

where $i$ and $j$ denote redshift bins, $W_i(\chi)$ is the lensing kernel for redshift bin $i$, and $N_i(\chi)$ is the comoving radial distribution of galaxies in redshift bin $i$.

One approach to mitigating the impact of intrinsic alignments, is to model $P_{\rm II}(k, z)$ and $P_{\delta{\rm I}}(k, z)$; I overview some basic intrinsic alignment models, and observational constraints on these models, in §2.2.1.

An alternative approach attempts to use redshift information to minimise any intrinsic alignment contribution to the measurement of the signal, a technique known as 'nulling'. For the 'II' term, with precise redshift information, nulling is straightforward - simply do not include pairs which are physically close (i.e. close in redshift, or equivalently, close in $\chi$) in the shear correlation function. In this case $N_i(\chi)$ and $N_j(\chi)$ in equation 2.25 do not overlap, and $C_{i,j}^{\rm II}(l) = 0$.

For the GI term, things are not so simple, because in general either $W_i(\chi)N_j(\chi)$ or $W_j(\chi)N_i(\chi)$ will be non-zero[11]. Joachimi & Schneider (2010) demonstrate that the different redshift dependencies of the GG, II and GI terms allow robust nulling of both the II and GI contributions, when using many narrow redshift bins. However, with photometric redshift scatter of $\sigma_z = 0.05(1+z)$ (typical for a photometric weak lensing survey), cosmological parameter constraints are degraded by a factor of a few. Since the photometric redshift quality I've been working with in DES is of inferior quality to this, I concentrate on the modeling approach.

One promising approach to mitigating intrinsic alignments involves using cross-correlations with large scale structure, which Joachimi & Bridle (2010) demonstrated could be used to recover most of the statistical constraining power of cosmic shear, even when marginalising over a very flexible intrinsic alignmnet model. By cross-correlating galaxy shapes with tracers of the large-scale-structure (and also using the auto-correlation of those tracers to constrain their bias), the density-intrinsic ellipticity correlation (i.e. $P_{\delta \mathrm{I}}$ in equation 2.26) can be constrained, freeing up the cosmic shear measurements to constrain cosmology.

### 2.2.1 Intrinsic alignment models

The underlying physical source of galaxy shapes and alignments is assumed to be the gravitational potential tidal field, which can both torque and stretch galaxies and their halos. Following Hirata & Seljak (2010), I define the tidal tensor $T_{\mu\nu}$ in terms of second derivatives of the smoothed gravitational potential

$$T_{\mu\nu} = (\bigtriangledown_\mu \bigtriangledown_\nu - \frac{1}{3}\delta_{\mu\nu}\bigtriangledown^2)\mathcal{S}[\Phi], \tag{2.27}$$

where $\bigtriangledown$ is a comoving derivative, and $\mathcal{S}$ is some smoothing function that would e.g. cut off fluctuations on the scales of the galaxy itself. The assumed effect of

[11] except for galaxy pairs at the same redshift, but we're excluding those because of II!

tidal interactions on galaxy shapes is often differentiated for elliptical and spiral galaxies. It is assumed that elliptical galaxies follow the shape of their halos, which due to the aforementioned stretching and torquing, are aligned with the principle axis of the tidal field. I call these 'tidal alignment' models. It is assumed that spiral-galaxies, which are supported by angular momentum, have their symmetry axis aligned with the angular momentum vector of the host halo, which is produced by tidal torquing. Correlations in the angular momentum of halos can be described using tidal torque theory, so I call these models 'tidal torque' models. Kiessling et al. (2015) present a review of popular intrinsic alignment models, including comparison to simulations.

**Tidal alignment**

The most simple tidal alignment model is the linear alignment model (Catelan et al. 2001; Hirata & Seljak 2010), in which it is assumed that the (complex) intrinsic galaxy ellipticity $\epsilon^I$ is linear in the tidal field,

$$\begin{aligned} \epsilon^I &\propto (T_{xx} - T_{yy}) + i(T_{xy} + T_{yx}), \\ \epsilon^I &= -\frac{C_1}{4\pi G}(\bigtriangledown_x^2 - \bigtriangledown_y^2 + 2i \bigtriangledown_x \bigtriangledown_y)\mathcal{S}[\Phi_P], \end{aligned} \tag{2.28}$$

where $C_1$ is a constant of proportionality, and $x$ and $y$ are the coordinates in the plane of the sky; note we do not need to consider the component of the tidal field along the line-of-sight, since this won't affect the projected ellipticity that we observe.

We can use Poisson's equation to relate the potential, $\Phi(\boldsymbol{k})$ to the linear density contrast $\delta_{\rm lin}(\boldsymbol{k})$

$$\Phi(\boldsymbol{k}, z) = -4\pi G\bar{\rho}(z)k^{-2}\delta_{\rm lin}(\boldsymbol{k}, z). \tag{2.29}$$

Hirata & Seljak (2010) assume that the intrinsic shape $\epsilon^{\rm I}$ is 'frozen' in at some

early time during galaxy formation[12], and so it is the primordial potential $\Phi_P(\boldsymbol{k})$ that should be used in equation 2.28, given by

$$\Phi_P(\boldsymbol{k}) = -4\pi G \frac{\bar{\rho}(z)}{D(z)} a^2 k^{-2} \delta_{\rm lin}(\boldsymbol{k}, z) \tag{2.30}$$

where $D(z)$ is the linear growth factor normalised to one at $z = 0$ and $\bar{\rho}$ is the mean matter density of the Universe.

On linear scales, and keeping terms only up to second order in the density fluctuations $\delta$, the (E-mode) intrinsic-intrinsic power spectrum $P_{\rm II}(k, z)$ can be written

$$P_{\rm II}^{\rm LA}(k, z) = \frac{C_1^2 \bar{\rho}^2(z)}{\bar{D}^2} a^4 P_\delta^{\rm lin}(k, z) \tag{2.31}$$

and the density-intrinsic power spectrum

$$P_{\delta I}^{\rm LA}(k, z) = -\frac{C_1 \bar{\rho}(z)}{\bar{D}} a^2 P_\delta^{\rm lin}(k, z) \tag{2.32}$$

where the 'LA' stands for linear alignment, because of the assumption in equation 2.28 that the intrinsic shape is linear in the tidal field. Note there is no theoretical prediction for $C_1$. Bridle & King (2007) used the observed amplitude in measurements by Brown et al. (2002) of alignments of low-redshift (median $z \sim 0.1$) galaxies from the SuperCOSMOS survey (Hambly et al. 2001) to set this normalisation to the value $C_1 = 5 \times 10^{-14} (h^2 M_\odot {\rm Mpc}^{-3})^{-1}$. It is then conventional to define a constant $A$, which is of order unity, to parameterise deviations from this normalisation, such that

$$P_{\rm II}^{\rm LA}(k, z) = A^2 \frac{C_1^2 \bar{\rho}^2(z)}{\bar{D}^2} a^4 P_\delta^{\rm lin}(k, z) \tag{2.33}$$

$$P_{\delta I}^{\rm LA}(k, z) = -A \frac{C_1 \bar{\rho}(z)}{\bar{D}} a^2 P_\delta^{\rm lin}(k, z). \tag{2.34}$$

[12]Perhaps not a very realistic assumption, given the morphology of elliptical galaxies is believed to be heavily influenced by mergers and interactions long after galaxy formation. This assumption mostly effects the redshift dependence of the signal, which in practice is often liberated by an additional nuisance parameter anyway.

The linear alignment (LA) model assumes that the alignment is linear in the tidal field of linear fluctuations, implying that the theory is only valid on linear scales (i.e. $\gtrsim 10\,\mathrm{Mpc}$). To make predictions for nonlinear scales, Bridle & King (2007) proposed replacing the linear matter power spectrum $P_\delta^{\rm lin}(k,z)$ in Equations 2.31 and 2.32, with the nonlinear matter power spectrum, resulting in a model where the alignment is now linear in the tidal field of the nonlinear density fluctuations. This model is known as either the *Nonlinear linear alignment* model or the *Nonlinear alignment* (NLA) model. While the NLA model has proven both popular and successful, it is not a fully consistent description of alignment which is linear in the tidal field, as pointed out by Blazek et al. (2015a), who model all terms that contribute at up to next-to-leading order in perturbation theory (i.e. third order in density field). This model is referred to as the complete tidal alignment (CTA) model in The Dark Energy Survey Collaboration et al. (2015).

**Tidal torque alignment**

Crittenden et al. (2001); Mackey et al. (2002) derive predictions for the intrinsic alignment signal for spiral galaxies, assuming the observed ellipticity is determined principally by the angular momentum direction of its disc

$$e^I \propto (L_x^2 - L_y^2) + 2iL_xL_y \tag{2.35}$$

where, again, $x$ and $y$ denote coordinates in the plane of the sky. Note that a galaxy with angular momentum in the $z$-direction will have its disc in the plane of the sky and hence zero observed ellipticity.

Following White (1984), they assume that the component $i$ of the angular momentum, $L_i$, acquired by a protogalaxy during gravitational collapse is

$$L_i \propto \epsilon_{ijk} T_{jl} I_{kl} \tag{2.36}$$

where $T_{ij}$ is the tidal field tensor, and $I_{ij}$ is the moment of inertia tensor of the protogalaxy. $I_{ij}$ would also likely be influenced by the tidal field, but if it is fully aligned with the tidal field, the $\epsilon_{ijk}$ enforces that no torque is applied. Mackey et al. (2002) make the argument that the large-scale Fourier modes that are responsible for large-scale correlations in the tidal field may not be very correlated with the smaller scale modes which determine the inertia tensor, and proceed by assuming that there is no correlation between the initial moment of inertia tensor and the tidal field. Alternatively, one could assume that some fraction of the inertia tensor is randomly misaligned with the tidal field, and absorb this fraction into the normalisation of the model. Either way, the resulting E-mode intrinsic-intrinsic power spectrum is to leading order quadratic in the matter power spectrum, hence these models are sometimes referred to as *quadratic alignment* models. In the notation of Hirata & Seljak (2010), the leading order result is

$$P_{\rm II}(k,z) = \frac{2C_2^2\bar{\rho}^4 a^8}{D^4}\int \frac{d^3\boldsymbol{k}_1}{(2\pi)^3}[h_E(\hat{\mathbf{k}}_1,\hat{\mathbf{k}}_2)]^2 P_{\delta\delta}^{\rm lin}(k_1,z)P_{\delta\delta}^{\rm lin}(k_2,z) \tag{2.37}$$

where $\mathbf{k}_2 = \mathbf{k} - \mathbf{k}_1$, and $h_E$ is a geometric factor defined $h_E = h_{xx} - h_{yy}$, with

$$h_{\lambda\mu}(\hat{\mathbf{u}},\hat{\mathbf{v}}) = (\hat{u}_\mu\hat{u}_\nu - \frac{1}{3}\delta_{\mu,\nu})(\hat{v}_\lambda\hat{v}_\nu - \frac{1}{3}\delta_{\lambda,\nu}). \tag{2.38}$$

In the limit of Gaussian fluctuations of the tidal field, there is no density-ellipticity correlation in this tidal torque model i.e. $P_{\rm GI} = 0$. However, Hui & Zhang (2002) note that non-Gaussian fluctuations do induce a non-zero density-ellipticity correlation.

### 2.2.2 Observational constraints

Kirk et al. (2015) present a review of intrinsic alignment observations; I give a much shorter summary below. See also Troxel & Ishak (2015); Joachimi et al.

(2015) for useful recent reviews of the topic as a whole. The large samples of Luminous Red Galaxies (LRGs) observed by the SDSS (Eisenstein et al. 2011) and BOSS (Dawson et al. 2013) surveys have proven particularly fruitful for observational constraints on intrinsic alignments. These are pressure-supported, elliptical galaxies, so tidal alignment theories are expected to be a reasonable description of their alignments. The most popular statistic for directly measuring IAs has been based on measuring the correlation between intrinsic galaxy shapes and the positions of galaxies. Assuming the galaxies used for the position sample have linear bias $b_g(z)$, this correlation will have a spatial power spectrum

$$P_{gI}(k,z) = b_g(z)P_{\delta I}(k,z) \tag{2.39}$$

where $P_{\delta I}(k,z)$ is the power spectrum of matter-intrinsic shape correlations, given by Equation 2.34 for the LA model. The observable most commonly used is the projected galaxy position-ellipticity correlation function, $w_{g+}(r_p)$ estimated as a function of physical separation perpendicular to the line of sight (see e.g. Mandelbaum et al. (2011a) for derivation of the theoretical expectation of this estimator). The projection is along the line of sight, such that all pairs with a line-of-sight separation less than some value $\Pi_{max}$ are included in the correlation estimator. The analogous statistic for ellipticity-ellipticity correlations is $w_{++}(r_p)$, the projected ellipticity-ellipticity correlation function, which is generally noisier, due to the extra factor of shape noise, and suffers from contamination by the cosmic shear signal.

Hirata et al. (2007) measured $w_{g+}$ for various galaxy samples from the SDSS and 2SLAQ (Cannon et al. 2006) surveys, finding a $> 3\sigma$ detection for the SDSS LRG sample. Joachimi et al. (2011) used the 800,000-strong SDSS MegaZ-LRG sample to obtain the first detection of intrinsic alignments using photometric redshifts, finding an amplitude $A \sim 5$. They also tested for redshift and luminosity scaling of the signal, finding evidence for the latter. More recently, Singh

et al. (2015) presented measurements of the BOSS 'LOWZ' sample, $\sim$ 160000 red galaxies with spectroscopic redshift and shape measurements in the redshift range $0.16 < z < 0.36$. They extensively study both the luminosity dependence and halo mass dependence of the large-scale IA signal, finding that both can be described by power-laws, and find amplitudes consistent with Joachimi et al. (2011).

While large spectroscopic samples over a wide range in redshift and luminosities exist for early-type, elliptical galaxies, motivated by their suitability for galaxy clustering studies, the available data for direct intrinsic alignment measurements of disc galaxies is much more limited. Arguably the most useful current dataset for disc galaxy alignments is the spectroscopic WiggleZ Survey (Drinkwater et al. 2010) of blue emission line galaxies with median redshift 0.6. Mandelbaum et al. (2011b) combined the WiggleZ spectra with SDSS imaging, and measured null signals in $w_{g+}$ and $w_{++}$. Assuming that these galaxies are representative of those used in a cosmic shear analysis, they propagate their measurement to an upper limit of a few percent contamination of the cosmic shear signal, for a CFHTLS-like survey.

In terms of cosmic shear cosmology, the usefulness of all of these 'direct' intrinsic alignment constraints is limited by the representativeness of the samples in question with respect to the galaxies used in a cosmic shear study. For example, while the best observational constraints are on LRGs, galaxies used for cosmic shear are typically much less luminous, and the majority are early-type, disc dominated rather than ellipticals like LRGs. Mandelbaum et al. (2011b) note that the WiggleZ galaxies also occupy a small region of colour space, rather than spanning the full range of blue galaxies found in weak lensing datasets.

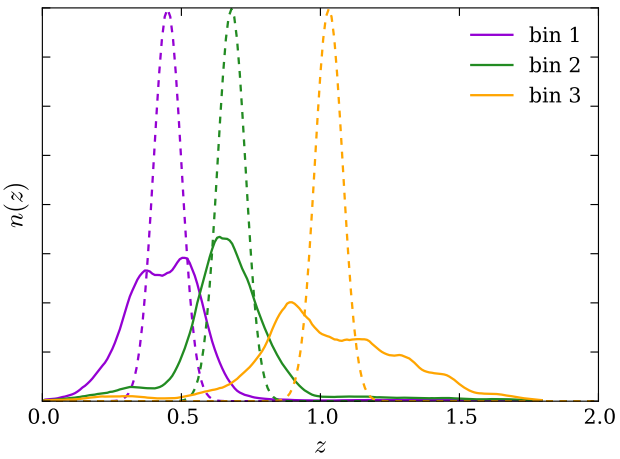


Figure 2.10: Redshift distributions for the intrinsic alignment predictions in Figures 2.11 & 2.12, all normalised such that $\int dz n(z) = 1$. The solid lines are the DES-SV redshift distributions. The dashed lines are Gaussian $n(z)$s with the same means as the DES-SV distributions, but with widths $\sigma = 0.05$.

### 2.2.3 Contamination of cosmic shear

To illustrate the effect of intrinsic alignments on the observed tomographic cosmic shear signal, I show the predictions from the NLA model (with the fiducial amplitude i.e. $A = 1$) and the tidal torque model (using the normalisation from Mackey et al. 2002). I consider two sets of tomographic redshift bins. Firstly, I use the three redshift bins used in the The Dark Energy Survey Collaboration et al. (2015) cosmic shear analysis, which I will call DES-SV. The redshift distributions, which are wide and overlapping due to the limited precision of the photo-$z$ estimates, are shown as the solid lines in Figure 2.10. For comparison, I also consider three redshift bins which have the same mean redshifts as the DES-SV bins, but are Gaussians of width 0.05, and so are much narrower and less overlapping, as shown by the dashed lines in Figure 2.10.

Figure 2.11 demonstrates the contributions from the NLA model to the observed shear power spectrum (the solid line marked 'total'). In the lower set of panels, the case of the narrow, Gaussian redshift bins, the II contribution is the largest contribution in the autocorrelation bin pairings (the diagonal pan-

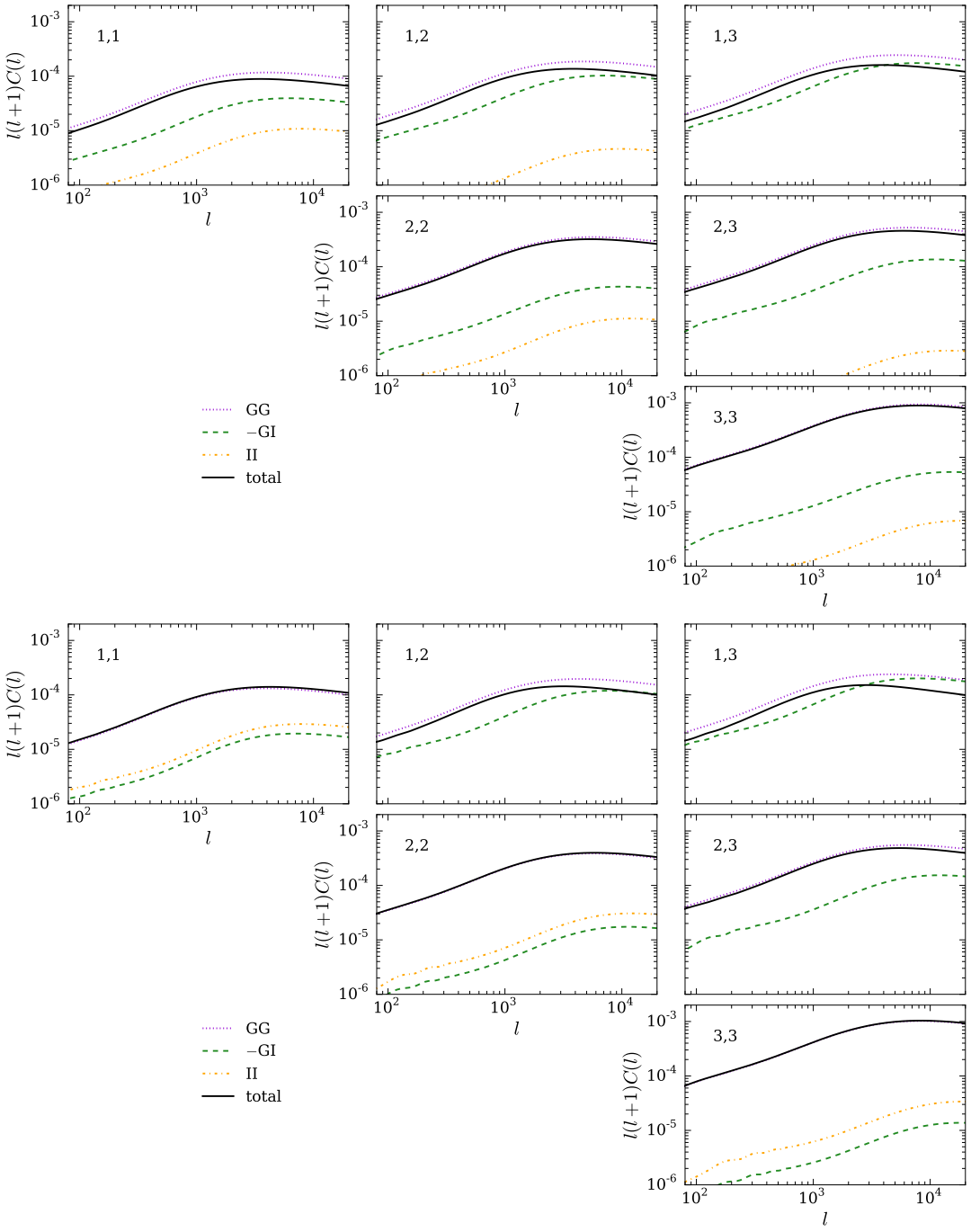


Figure 2.11: Shear power spectra with NLA intrinsic alignments, amplitude $A = 1$, for three redshift bins. The redshift bin combination is labeled in the top-left of each panel. Top panel: DES-SV redshift distributions; wide, overlapping redshift bins subdue the II contribution even in the autocorrelation bin pairings. Bottom panel: Narrow Gaussian ($\sigma = 0.05$) redshift bins with the same means as the DES-SV redshift bins. Now the II term is more significant than GI in the autocorrelations, and negligible in the cross-correlations.

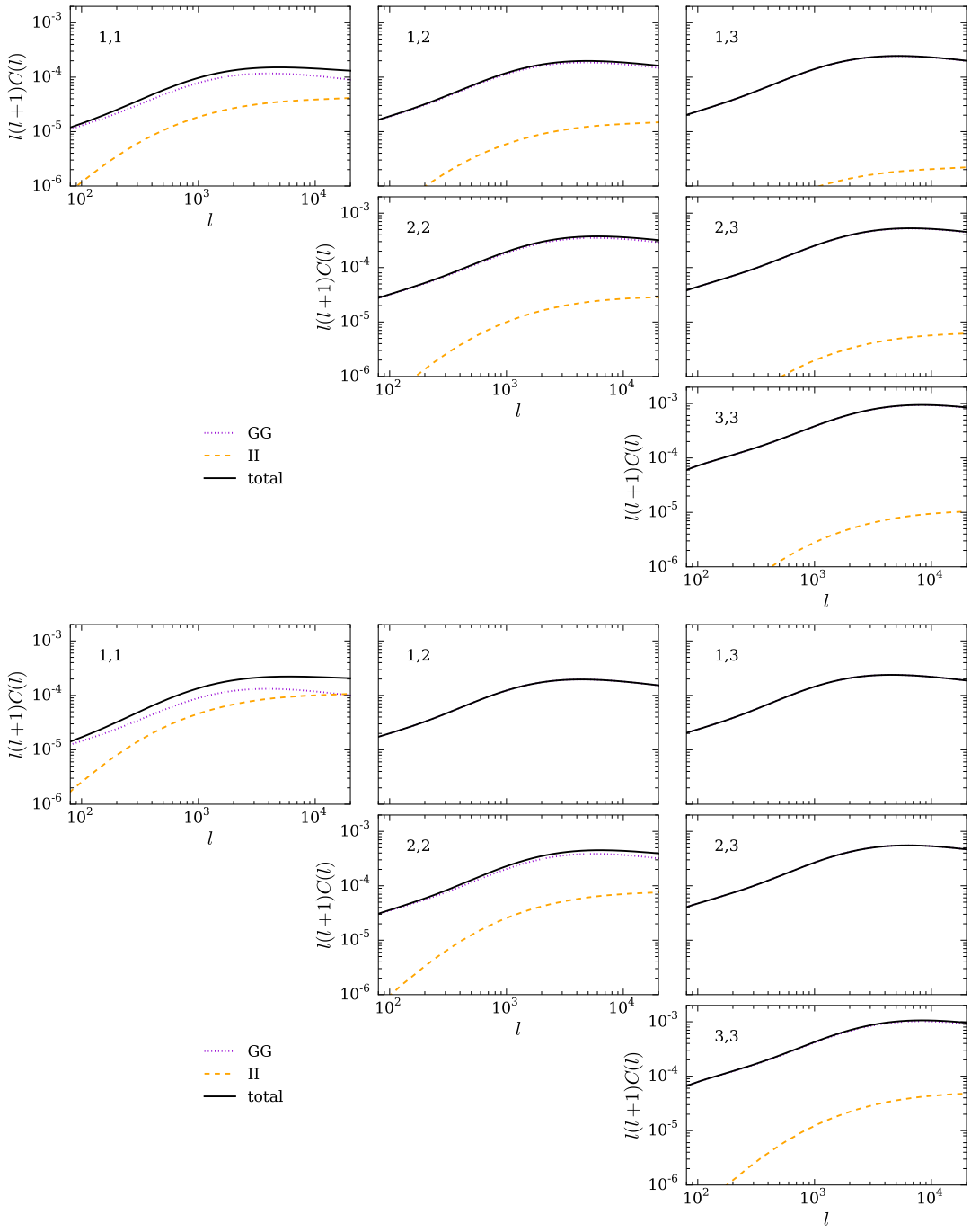


Figure 2.12: Same as Figure 2.11, but with the Mackey et al. (2002) tidal torque intrinsic alignment model. For the wide DES redshift bins in the top panel, the II signal is an order of magnitude below the cosmic shear signal, except in the lowest redshift (1,1) bin pair. With the narrower bins in the bottom panel, the II contribution becomes more significant for all the autocorrelation bin pairs.

els), and negligible in the cross-correlation bin pairings. This is expected, since the II contribution is non-zero only for physically close (i.e. close in redshift) galaxies. Conversely, the GI contribution, which arises from galaxy pairs widely separated in redshift dominates the intrinsic alignment contribution only in the cross-correlation bin pairings. For the DES-SV redshift bins, the width of the bins is such that the II contribution is reduced to below the GI contribution for all bin pairs. The GI contribution is a $> 10\%$ contaminant to the low and middle redshift bin autocorrelations.

Figure 2.12 is the equivalent for the tidal torque model. Again, the II contribution to the auto-correlation bin pairs is diluted by the wide DES-SV redshift bins (upper panels), such that it is below the 10% level for all bin pairs except the lowest redshift autocorrelation (1,1). The fact that the bins overlap somewhat means there is an II contribution in the cross-correlation bin pairs, unlike in the narrow Gaussian case (lower panels), where only the autocorrelation bin pairs are contaminated.

## 2.3 Photometric Redshift Calibration

Current (future) weak lensing datasets use (will use) shear estimates from $\sim 10^7$ ($\sim 10^9$) galaxies. To interpret the measured cosmic shear signal, we need accurate estimates of the redshifts of these galaxies, or at least the redshift distribution, $n(z)$, of the galaxies as an ensemble. As shown in Figure 1.7, the cosmic shear signal scales as $\sim z^{1.7}$, so that 1% error in the source redshift would be as bad as mis-estimating the signal by $\sim 1.7\%$. Huterer et al. (2006) investigate the requirements on redshift accuracy for future weak lensing surveys. They find that for a DES(LSST)-like survey, for a 7(10) redshift bin cosmic shear analysis, the mean redshift of the tomographic bins must be known to better than $\sim$ 0.003 (0.001), to avoid more than a 20% degradation in the constraint on $w_0$. Calibration of intrinsic alignments places further requirements on the redshift

accuracy (Bridle & King 2007).

A redshift estimate that uses (usually multiband) imaging data, rather than a direct spectroscopic redshift (spec-$z$) measurement, is called a *photometric redshift*, often abbreviated to *photo-z*. The simplest way to estimate the $n(z)$ is to histogram the spectroscopic redshifts of a representative sample of the full weak lensing sample. However, getting spectroscopic redshift information for even a small fraction of these galaxies is extremely expensive. The spectroscopic samples used for galaxy clustering studies typically target particular galaxy types, which are generally much brighter than typical weak lensing galaxies. Furthermore, a representative sample for weak lensing needs to have a much lower failure rate than is typical for current spectroscopic samples, since the objects which fail will in general not be randomly sampled from the population, and hence their exclusion will bias the estimate of the total $n(z)$.

More practical photometric redshift methods take advantage of the multiple (5 for the Dark Energy Survey) wide photometric filters in which the sky is observed for optical weak lensing surveys. While a spectroscopic redshift estimate is achieved by identifying spectral features from a high wavelength-resolution measurement of the galaxy spectral energy distribution (SED), a photometric redshift method has only the $\sim 5$ wide-band magnitudes estimates, effectively a very low-resolution SED measurement. This information can be used to ameliorate the requirement for a fully representative training sample in the histogramming method above. Lima et al. (2008) propose reweighting the spectroscopic calibration sample such that it has the same distribution of multiband magnitudes as the weak lensing sample.

'Training' photo-$z$ methods (see e.g. Collister & Lahav 2004 for an early example) take this a step further, by using the small fraction of galaxies in the sample which do have accurate spec-$z$s, to train a machine learning algorithm to find a mapping between the multiband magnitudes[13], and the spec-$z$s. Unlike the

[13]or any other photometric observable

reweighting method, the training methods can therefore assign a photo-$z$ estimate to each galaxy in the weak lensing sample, and in many cases, a probability distribution function for the true redshift of each object, $p(z)$. Training and reweighting methods alike still require extensive spectroscopic calibration/training data, which although need not be truly representative of the full weak lensing sample, must span the space of galaxy properties in the full sample, and sample that space sufficiently densely. Furthermore, the training sample must cover a large enough area of sky such that radial features due to sample variance are not significant. Cunha et al. (2012) estimate a total of 60,000 galaxies in 150 patches of sky (optimistically assuming random completeness), would be sufficient for DES.

I've so far discussed 'empirical' photo-$z$ methods, where no model is used for the galaxy SED. An alternative approach is taken by *template-fitting* methods. These methods use a set of template galaxy SEDs, which provide models with which to fit the data i.e. the $\sim 5$ photometric magnitudes, with the redshift as a free parameter. A maximum-likelihood method (e.g. Bolzonella et al. 2000) will return both the best-fit redshift and the best-fit template, which has the benefit of providing extra information about the galaxy type. More suitable for estimating redshift uncertainties which are crucial for constructing the $n(z)$, are Bayesian methods (e.g. Benítez 2000). As with any model-fitting approach, the success of template-fitting photo-$z$ estimation depends on the quality of the templates; they must accurately cover all the galaxy types and redshifts in the survey, including effects like dust redenning, and AGN, while also not including unrealistic SEDs. Additionally, in a Bayesian approach, some priors on galaxy properties must be assumed; the accuracy of the inferred $p(z)$s will be sensitive to some extent on the accuracy of these priors. Finally, template-fitting methods can be more dependent on the photometric calibration than training methods[14]. Template methods do not require training, and so do not have the same requirements on

[14]Training methods should not be sensitive to calibration errors in the full dataset, as long as the same calibration errors exist in the training data.

a representative training sample, although constructing a realistic template set requires much of the same information. Whatever spectroscopic training data is available can be used to validate or calibrate template fitting methods.

One approach that will complement the aforementioned methods is cross-correlation methods (Newman 2008). Rather than using spectroscopic data as a training set, one instead uses the fact that the positions of the spectroscopic galaxies will be correlated with the positions of other galaxies at the same redshift. So by measuring angular cross-correlations between spectroscopic and imaging data, information about the redshift distributions of the galaxies in the imaging data can be inferred. Choi et al. (2015) used a cross-correlation method to test the CFHTLenS photometric redshift estimates, finding significant biases in the redshift distributions estimated from template-fitting.

### 2.3.1 DES-SV photometric redshifts

The photo-$z$ estimation process for DES-SV is described in Bonnett et al. (2015), who compare the performance of three training methods (ANNz2 (Sadeh et al. 2015), SKYNET (Graff et al. 2014), and TPZ (Carrasco Kind & Brunner 2013)), and one template-fitting method (BPZ (Benítez 2000)). These methods are a subset of the methods tested in Sánchez et al. (2014) (see Figure 2.13). Bonnett et al. (2015) perform various tests, including comparison with blind (i.e. not used for training) spectroscopic data, and comparisons between the methods, with a view to validating the redshift estimates for use in a cosmic shear cosmology analysis. The quality of the training methods was likely limited by the deficit at faint magnitudes in the spectroscopic training sample, as shown in the left panel of Figure 2.14. Meanwhile, the template fitting method BPZ performed relatively poorly, although was improved by a calibration using the BCC-UFIG (Chang et al. 2015) simulations. Apart from BPZ, there was reasonable agreement between the different methods, as shown in the right panel of Figure 2.14.

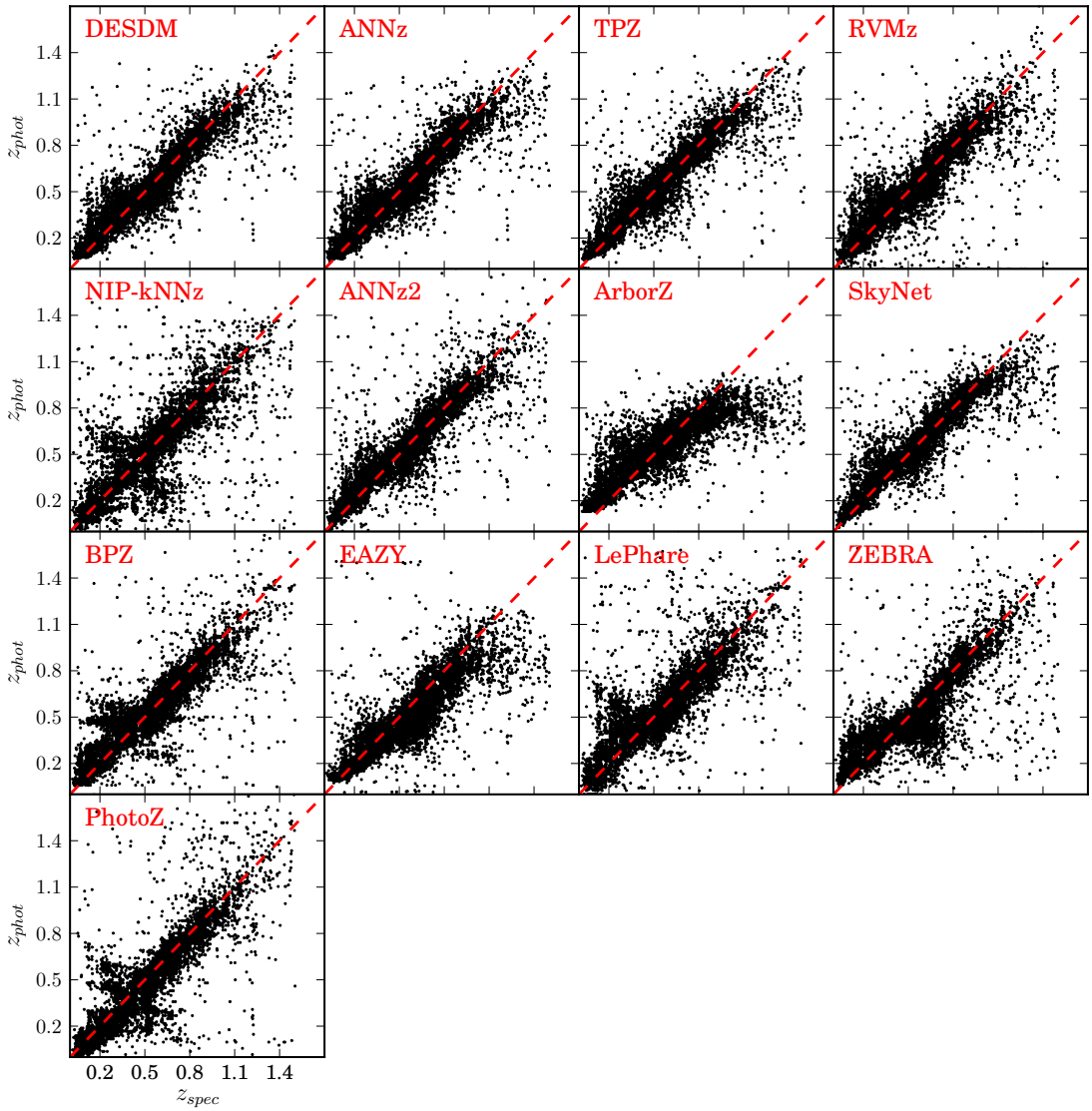


Figure 2.13: Taken from Sánchez et al. (2014), each panel shows photometric redshift estimates (y-axis) of the subset of the DES-SV galaxies which also have spectroscopic redshift measurements, compared to the spectroscopic redshift (x-axis). Each panel is a different method, see Sánchez et al. (2014) for a description of these, and the spectroscopic data used.

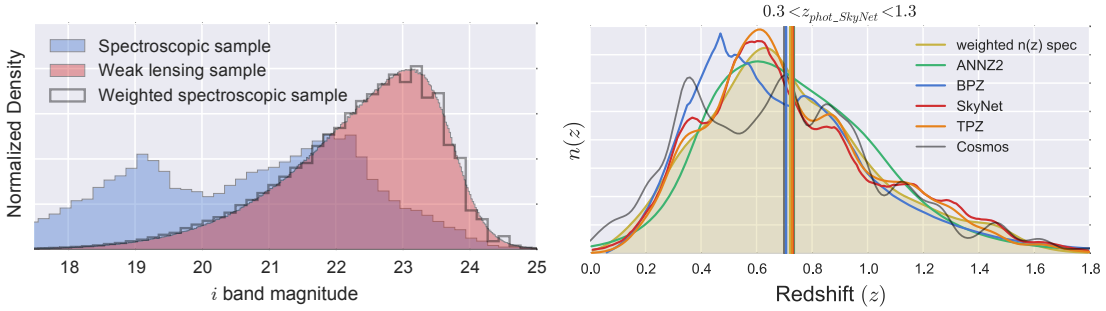


Figure 2.14: The $i$-band magnitude distribution of the spectroscopic sample used as training data for the DES-SV photometric redshift estimates. The blue histogram is the unweighted distribution; the grey lined histogram is the histogram after reweighting to match the NGMIX weak lensing catalog (red histogram). This plot is taken from Bonnett et al. (2015).

# Chapter 3

# Cosmic Discordance: Are *Planck* CMB and CFHTLenS weak lensing measurements out of tune?

*This chapter is largely a reproduction of MacCrann et al. (2015) which I worked on with Joe Zuntz, Sarah Bridle, Bhuvnesh Jain and Matt Becker.*

I examine the level of agreement between low redshift weak lensing data and the CMB using measurements from the CFHTLenS and *Planck*+WMAP polarization. I perform an independent analysis of the CFHTLenS six bin tomography results of Heymans et al. (2013). I extend their systematics treatment and find the cosmological constraints to be relatively robust to the choice of non-linear modeling, extension to the intrinsic alignment model and inclusion of baryons. I find that when marginalised in the $\Omega_m$-$\sigma_8$ plane, the 95% confidence contours of CFHTLenS and *Planck*+WP only just touch, but the discrepancy is less significant in the full 6-dimensional parameter space of $\Lambda$CDM. Allowing a massive active neutrino or tensor

modes does not significantly resolve the tension in the full n-dimensional parameter space. My results differ from some in the literature because I use the full tomographic information in the weak lensing data and marginalize over systematics. I note that adding a sterile neutrino to ΛCDM brings the 2d marginalised contours into greater overlap, mainly due to the extra effective number of neutrino species, which I find to be $0.88 \pm 0.43$ (68%) greater than standard on combining the datasets. I discuss why this is not a completely satisfactory resolution, leaving open the possibility of other new physics or observational systematics as contributing factors. I provide updated cosmology fitting functions for the CFHTLenS constraints and discuss the differences from ones used in the literature.

## 3.1 Introduction

The Cosmic Microwave Background (CMB) radiation has been the most powerful probe of cosmology for more than a decade. The *Planck* satellite (Planck Collaboration et al. 2013a) gives us an unprecedented view of the temperature fluctuations at recombination and the Wilkinson Microwave Anisotropy Probe (WMAP, Bennett et al. 1997, 2003, 2013) has until recently (Planck Collaboration et al. 2015a) provided the most detailed maps of the polarisation fluctuations (Bennett et al. 2013). *Planck* and WMAP polarisation together provide a self-consistent constraint on the 6 parameter ΛCDM cosmological model i.e. a flat universe containing only cold dark matter and baryons, and a cosmological constant, Λ.

At the same time, pressure is mounting on the ΛCDM model from tension between the CMB and low-redshift measurements of matter clumpiness. The primary CMB anisotropies place a constraint on the matter fluctuation amplitude at the time of recombination, which can be extrapolated to the present day for a particular assumed cosmological model. The primary measures of the amplitude

of matter fluctuations at low redshift are weak lensing, galaxy clustering and the abundance of galaxy clusters. Low-redshift observations seem to be finding a lower value for this fluctuation amplitude than expected in ΛCDM (Beutler et al. 2014b; Planck Collaboration et al. 2013e; Vikhlinin et al. 2009). This could be reconciled by new physics which reduces the rate of clustering between recombination and today (Planck Collaboration et al. 2013e; Hamann & Hasenkamp 2013; Battye & Moss 2014; Beutler et al. 2014b; Dvorkin et al. 2014; Archidiacono et al. 2014).

Gravitational lensing is the most direct method for measuring the distribution of matter in the low-redshift universe. The image distortion of distant galaxies in typical patches of sky was first detected in 2000 (Bacon et al. 2000; Kaiser et al. 2000; Van Waerbeke et al. 2000; Wittman et al. 2000) and last year the Canada-France-Hawaii Telescope Lensing Survey (CFHTLenS) provided the tightest constraints on cosmology yet from cosmic shear. This arguably provides one of the most robust and constraining low-redshift measures of cosmology, and is the low-redshift dataset I focus on in this paper.

One way to reduce the matter clustering rate is for some of the matter to travel fast enough to leave the clumps and smear out the fluctuations ("free-streaming"). Active neutrinos are an obvious candidate for this hot dark matter, because we already know they have mass (Beringer et al. 2012) and particle physics experiments allow a mass range that would have a significant impact on cosmology (Lobashev et al. 1999; Weinheimer et al. 1999). They have been invoked at various times to reconcile CMB and low-redshift counts of galaxy clusters.

Even if the active neutrino has the smallest mass allowed by particle physics experiments, an alternative hot dark matter particle might be responsible for smearing out the fluctuations. A sterile neutrino is a promising candidate which would also affect the CMB anisotropies by introducing an additional relativistic species in the early universe.

In this paper I focus in detail on combining the CMB with the CFHTLenS low-redshift dataset to examine whether they alone warrant new physics. In contrast to the earlier papers, I use the full 6 tomographic redshift bins and marginalise over intrinsic alignments, as in Heymans et al. (2013) and described in Section 2. Earlier papers drew conclusions about agreement between datasets by comparing marginalised contours in one or two dimensions. In Section 3 I investigate whether these conclusions hold up in the full multi-dimensional parameter space, and extend the treatment of weak lensing systematics. In Section 4 I investigate the effect of cosmological extensions (massive active neutrinos, a massive sterile neutrino, tensors and running of the spectral index) to the base model. I compare with related work, and discuss other possible explanations for the tension in Section 5.

## 3.2 Datasets and methodology

The *Planck* satellite (Planck Collaboration et al. 2013a) provided high resolution ($\sim$10 arcminutes) temperature maps of the CMB at a range of frequencies between $\sim$25 and $\sim$1000 GHz. These observations allow the estimation of the CMB temperature power spectrum for $2 \leq l \leq 2500$ (Planck Collaboration et al. 2013b). I use the publicly available *Planck* likelihood codes which use this power spectrum, and the corresponding polarisation power spectrum from WMAP9 (Bennett et al. 2013). Throughout, I marginalise over the 14 nuisance parameters which account for astrophysical systematics in the *Planck* likelihood codes. I refer to this combination as *Planck*+WP.

The Canada France Hawaii Lensing Survey (Heymans et al. 2012), hereafter referred to as CFHTLenS, is a 154 square degree multi-filter survey which achieved an effective weighted number density of 11 galaxies per square arcminute with shape and photometric redshift estimates. Kilbinger et al. (2013) performed a 2d cosmic shear analysis of the CFHTLenS data, producing constraints on

the ΛCDM model which they approximated by $\sigma_8(\Omega_m/0.27)^{0.59} = 0.787 \pm 0.032$. Heymans et al. (2013) (HE13 henceforth) performed a tomographic cosmic shear analysis of the CFHTLenS data, dividing the galaxies into six tomographic redshift bins (with photometric redshift estimate between 0.2 and 1.3) and taking into account the effect of galaxy intrinsic alignments using a free parameter for the overall intrinsic alignment amplitude. For each tomographic bin combination, they measured the real space shear-shear correlation functions $\xi_{+,-}(\theta)$ in 5 evenly log-spaced angular bins for $1 \leq \theta \leq 40$ arcmin. In this paper I use the full HE13 correlation functions and covariance matrices (which were obtained from N-body simulated mock surveys), and marginalise over the same model for intrinsic alignments as in HE13.

The analysis in this paper is performed with CosmoSIS, a new cosmological parameter estimation framework (Zuntz et al. 2014 in prep). A parameter estimation problem in CosmoSIS is represented as a sequence of independent modules each performing a specific part of the calculation and passing on their results to later modules. For this work the modules were: CAMB (Lewis et al. 2000), to calculate CMB and linear matter power spectra and expansion histories; HALOFIT for non-linear power; a module based on COSMOCALC[1] to compute cosmic shear and intrinsic alignments power spectra; a custom module to compute the 2-point shear correlation functions $\xi_{\pm}(\theta)$ from $C_\ell$; the commander, lowlike and CAMSpec *Planck* likelihood codes (Planck Collaboration et al. 2013b); and a custom CFHTLenS likelihood code. As a default I use the HALOFIT formulation as implemented by CAMB, which is Takahashi et al. (2012) with modified massive neutrino parameters (although we compare this nonlinear correction to others in Section 3.3.2). I'll refer to this implementation as TA12 from now on. Note that HE13 used the fitting formula of Eisenstein & Hu to get the linear matter power spectrum and the Smith et al. (2003) (SM03 henceforth) version of HALOFIT to perform the non-linear correction.

[1] https://bitbucket.org/beckermr/cosmocalc

I use the following parameter definitions. $\Omega_{\rm m}$ is the total matter density at redshift zero (as a fraction of the critical density at redshift zero). The present-day baryon density is given by $\Omega_b$. $\sigma_8$ is the rms fluctuation in $8h^{-1}$ Mpc spheres at the present day in linear theory. The spectral index of the scalar primordial power spectrum is given by $n_s$. $\tau$ is the optical depth due to reionization. The Hubble constant is written as $h$, in units of 100 (km/s)/Mpc. When I refer to 'base ΛCDM', I mean the same model as the Planck Collaboration et al. (2013c) baseline model - the normal 6 parameter ΛCDM model, assuming 1 massive active neutrino eigenstate, with $m_\nu = 0.06\,\mathrm{eV}$.

## 3.3 Discordance in ΛCDM

I assess the level of agreement between CFHTLenS and *Planck*+WP in the 6 parameter base ΛCDM model, and provide an updated fitting function to the CFHTLenS data.

### 3.3.1 Quantifying the tension

Figure 3.1 shows the *Planck* and CFHTLenS data superposed onto the matter power spectrum (following Tegmark & Zaldarriaga 2002). This can provide a qualitative indication of the level of agreement between the datasets and a given cosmological model. However, note that the conversion of observables to the matter power spectrum is highly dependent on the assumed cosmology . Therefore an apparent disagreement between two datasets can simply be an indication that the wrong model was assumed when converting the data points. In the left panel, one can see that the *Planck* best-fit cosmology goes straight through the *Planck* datapoints, as expected from the good fit of the *Planck* Cls to the best fit theory model. The CFHTLenS datapoints appear to be more often below the theory line, as expected from the lower preferred $\sigma_8$. This was also illustrated in Battye & Moss (2014) using the cosmic shear correlation function.

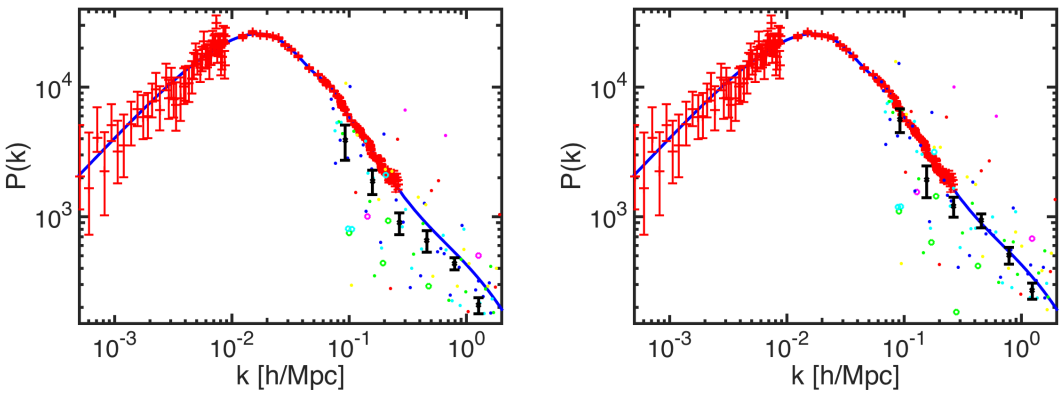


Figure 3.1: The Planck and CFHTLenS data superposed onto the present day matter power spectrum, using the method of Tegmark & Zaldarriaga (2002). Each coloured CFHTLenS point corresponds to an angular correlation function measurement. Cross correlations with tomographic bin 1 are magenta, with bin 2 (and not with bin 1) are red, with bin 3 (and not with bins 1 or 2) are yellow, bin 4 are green, bin 5 are cyan and bin 6 are blue. There are 105 points from CFHTLenS $\xi_+$ which are illustrated by the coloured points. Some of them fall at smaller scales than shown on this plot, and some are negative and shown by an open circle. These have been averaged using the noise covariance matrix to make the black points. Left: For the *Planck* best fit cosmology. Right: For the *Planck* + CFHTLenS ΛCDM best fit cosmology. Note that because of the extrapolation to the matter power spectrum, both the points and the lines move when the cosmology changes. In the range of the CFHTLenS data points the line moves down by about the same amount as the CFHTLenS points move up, on switching the cosmology from *Planck* (left panel) to *Planck* + CFHTLenS (right panel).

In Figure 3.2 I show that the two-dimensional marginalised constraints from *Planck*+WP and CFHTLenS are discrepant in the $\Omega_{\rm m}$-$\sigma_8$ plane: the $2\sigma$ contours only just touch. This is a significantly stronger conclusion than reached in other works, e.g. Leistedt et al. (2014), Beutler et al. (2014b). There are four main reasons for this: (i) I use an improved non-linear HALOFIT treatment (see Section 3.3.5 below) for the lensing constraints. (ii) I use exactly the same cosmological model (i.e. include an active neutrino with mass 0.06 eV) for the CFHTLenS constraints as for the *Planck*+WP constraints, although Figure 4 of Beutler et al. (2014b) suggests that at least for the CFHTLenS constraints, this is less important than (i). (iii) I use a full likelihood analysis of CFHTLenS rather than just a prior in the $\Omega_{\rm m}$-$\sigma_8$ plane; (iv) I follow HE13 by using 6 bin tomographic results

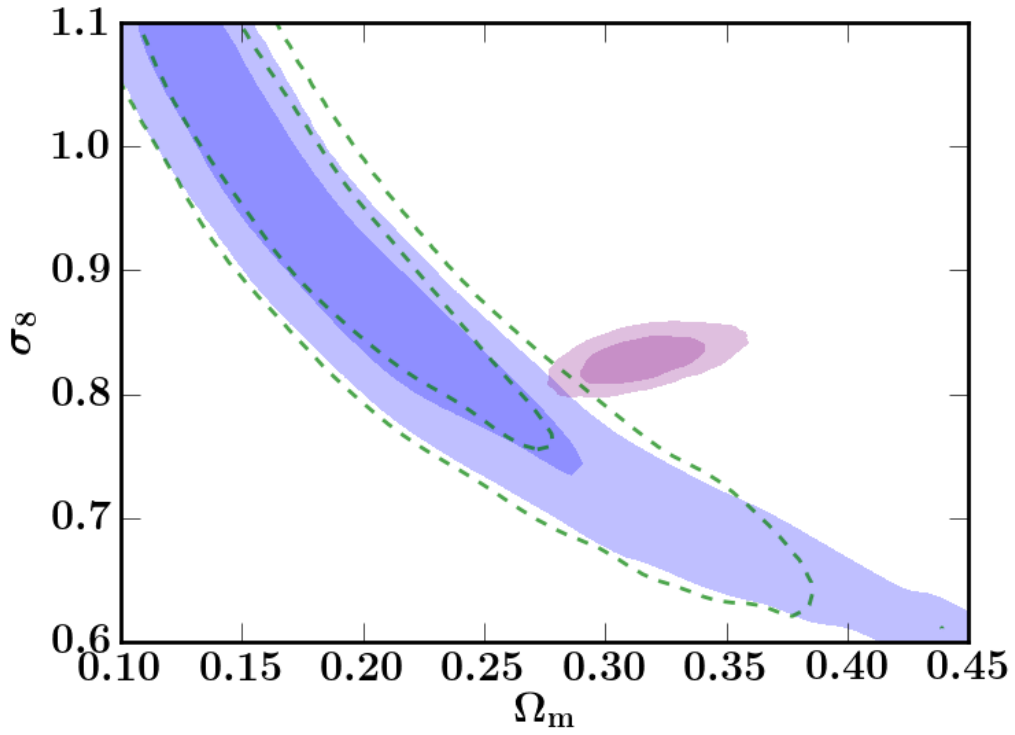


Figure 3.2: Constraints in the clustering amplitude $\sigma_8$ and matter density $\Omega_m$ plane from *Planck*+WP and CFHTLenS, assuming our base cosmological model. Filled blue banana: 1 and $2\sigma$ CFHTLenS only constraints using all $\theta$ bins in $\xi_{+/-}(\theta)$. Dashed green banana: 1 and $2\sigma$ CFHTLenS only constraints excluding small scales (see Section 3.3.2 for cuts on $\theta$). Small, purple contours: The constraints on the base model from *Planck*+WP. Discrepancy between the 2d marginalised *Planck*+WP and CFHTLenS contours is clear at the $\sim 95\%$ level

marginalised over intrinsic alignments (see Figure 4 of HE13 for the effect of this).

However, one might argue that the fact that the 2d marginalised CFHTLenS and *Planck*+WP contours do not overlap is not necessary or sufficient to prove that they are discrepant, since the ΛCDM model has 6 dimensions, so it is the amount of overlap in 6 dimensions that is important.

One way to quantify the discrepancy between two datasets (e.g. *Planck*+WP and CFHTLenS) within a particular $n$-parameter cosmological model is by checking how much the $n$-dimensional posterior distributions overlap. I first calculate the positions of the 68% and 95% surfaces of equal likelihood in the full

n-dimensional parameter space for a given dataset and can then assess whether a given point lies within these confidence intervals. I call these surfaces iso-likelihood surfaces, or 'iso-likes' for brevity. More generally one can identify the percentage iso-like a given point in parameter space lies on, for each dataset.

I find the multi-dimensional iso-likes as follows. I perform fits of the model to the two measurements individually, and obtain a histogram of probability values for each dataset. As in the 1d case, I define the 68% iso-like as the surface of equal likelihood which contains 68% of the probability distribution, or in the case of MCMC samples, 68% of the samples. This allows identification of the probability value of the 68% iso-like for each dataset. More generally, one can use this histogram to read off the percentage iso-like for any point in parameter space, given its probability value.

As an example of a point of interest, I perform a joint fit, and define $\sigma_i(\mathbf{p}_{\rm joint})$ as the percentage iso-like on which the joint-best fit point lies, for dataset $i$ (where $i$ is one of C and P, denoting CFHTLenS and *Planck*+WP respectively). The values of $\sigma_{\rm C}(\mathbf{p}_{\rm joint})$ and $\sigma_{\rm P}(\mathbf{p}_{\rm joint})$ are given in Table 1. The best joint fit is a poor fit to CFHTLenS, lying on the 76% iso-like. The fact that it is an acceptable fit to *Planck*+WP reflects the greater constraining power from *Planck*+WP, which pulls the best fit point close to the best fit to *Planck*+WP alone.

I also wish to know if there are regions of parameter space which are a good fit to both datasets (albeit a slightly worse fit to *Planck*+WP), i.e. the minimum percentage iso-likes which overlap. For this I define $\sigma_{\rm eq}$, the minimum value of $\sigma_{\rm C}$=$\sigma_{\rm P}$. Therefore $\sigma_{\rm eq}$ is the best percentile value for which equal percentage iso-likes of *Planck*+WP and CFHTLenS touch. For base ΛCDM I find $\sigma_{\rm eq} = 54\%$ , (or $\sigma_{\rm eq} = 64\%$ when cutting small scales from the CFHTLenS correlation functions, see Section 3.3.2). This means that the best points, or at least those where the tension is least, are still on at least the 54% (64% ) iso-likes of *both* probes. These $\sigma$ values are collected for this and subsequent sections in Table 3.1.

| Model | Datasets | small scales cut? | $\sigma_C(\mathbf{p}_{\rm joint})$ | $\sigma_P(\mathbf{p}_{\rm joint})$ | $\sigma_{\rm eq}$ |
|---|---|---|---|---|---|
| $\Lambda$CDM (6) | P + C | No | 76% | 23% | 54% |
| $\Lambda$CDM (6) | P + C | Yes | 89% | 11% | 64% |
| $\Lambda$CDM + IA(z) (6+1) | P + C | Yes | 70% | 15% | 52% |
| $\Lambda$CDM + AGN (6+1) | P + C | Yes | 86% | 8% | 52% |
| $m_\nu\Lambda$CDM (6+1) | P + C | Yes | 90% | 1% | 50% |
| $m_{\rm s}^{\rm eff}\Delta N_{\rm eff}\Lambda$CDM (6+2) | P + C | Yes | 60% | 2% | 31% |
| $r\alpha_{run}\Lambda$CDM (6+2) | P + C | Yes | 92% | 8% | 63% |

Table 3.1: Goodness of fit of joint fit to individual datasets, for several extensions to $\Lambda$CDM. 'C' and 'P' denote CFHTLenS and *Planck*+WP respectively. 'small scales cut' refers to removing some of the $\xi_{+/-}(\theta)$ bins used in the CFHTLenS analysis, as described in Section 3.3.2. $\mathbf{p}_{\rm joint}$ denotes the parameters of the best joint fit to the datasets. $\sigma_i$ values are defined at the end of Section 3.3.1. In parentheses after the model names, I also include the number of parameters in the model, not including the *Planck* nuisance parameters.

It's clear that when considering the relative positions of the 68% and 95% confidence intervals as a test of tension or discrepancy, then the number of dimensions under consideration is important - a naive interpretation is that the marginalised 2d picture suggests a greater tension than the 6d case. However this is likely to be largely a geometrical effect - when we marginalise over some parameters, if those parameters are (even weakly) constrained, the surface of equal probability containing e.g. 68% of the probability (the 68% contour in 2d) will be found at a higher probability, making confidence regions tighter. Appendix 3.A illustrates this effect further for the case of two gaussian probability distributions. I believe that while the 2d marginalised picture does still give a useful indication of the tension, the full n-dimensional $\sigma_{eq}$ should also be considered as as an alternative and more conservative assessment.

### 3.3.2 Sensitivity to the choice of nonlinear matter power spectrum

One strength of weak lensing lies in its ability to constrain the total matter power spectrum, $P_\delta(k)$ however, it is most sensitive to scales where nonlinear effects on

$P_\delta(k)$ are significant. This is demonstrated by Figure 3.3, the upper panel of which shows the weighting of $k$ scales in $\xi_+$ for the autocorrelation of the highest redshift CFHTLenS redshift bin. I show $W(\log(\mathrm{k}), \theta)$, where

$$\xi_+(\theta) = \int \mathrm{dlog(k)W(log(k), \theta)P_\delta(k)} \tag{3.1}$$

The 5 lines are the 5 angular bins ($1 \leq \theta \leq 40$ arcmin) used in the HE13 measurement, with larger angles peaking at lower $k$. The lower panel shows the fractional difference between the two HALOFIT versions, SM03 and TA12 and the prediction of the publicly available code FrankenEmu[2], a matter power spectrum emulator based on the Coyote Universe simulations (Heitmann et al. 2014), which I'll refer to as Coyote. Comparing the two panels, it is clear, particularly for smaller angular bins, that the choice of nonlinear correction is important for the $k$-scales being probed.

Beutler et al. (2014b) already noted a $\approx 1\sigma$ shift in the constraint on $\sigma_8$ from using the newer version of HALOFIT. This is not unexpected from the fractional differences in P(k) for different nonlinear prescriptions, shown in Figure 3.3. HE13 suggest the conservative approach of cutting some of the lower $\theta$ bins in $\xi_{+/-}$ as a way of reducing the importance of the nonlinear correction. They boost and decrease the SM03 non-linear correction by $\pm 7\%$, and propose cutting all $\theta$ bins where the predicted $\xi$ changes by more than 10%. For $\xi_+$, this corresponds to $\theta \leq 3$ arcmin for tomographic bin combinations including bins 1 and 2. For $\xi_-$ (which is sensitive to higher $k$ than $\xi_+$ for a given angular scale), this corresponds to $\theta \leq 30$ arcmin for tomographic bin combinations including bins 1, 2, 3 and 4, and $\theta \leq 16$ arcmin for tomographic bin combinations including bins 5 and 6.

I adopt this scheme for the rest of the paper, and perform the following simple test on the sensitivity to the choice of nonlinear correction: I fix all parameters except $\sigma_8$ to the best joint-fit *Planck*+WP and CFHTLenS cosmology, and obtain

[2]http://www.hep.anl.gov/cosmology/CosmicEmu/emu.html

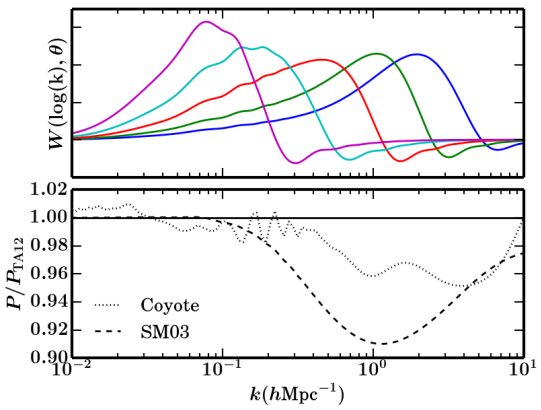


Figure 3.3: Top panel: the weight functions, $W(log_{10}(k), \theta)$ for $\xi_+(\theta)$, for the autocorrelation of the highest redshift CFHTLenS bin. The weight functions give the relative contribution to $\xi_+(\theta)$ as a function of $k$. The 5 lines are for the 5 $\theta$ bins used (with bin centres at 1.65, 3.58, 7.76, 16.80, 36.18 arcmin), with lower $\theta$ bins peaking at higher $k$. Bottom panel: The nonlinear matter power spectrum at z=0.5 predicted by Coyote and SM03, as a fraction of the TA12 prediction.

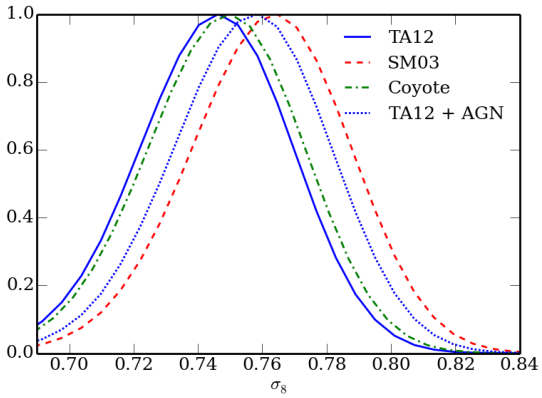


Figure 3.4: CFHTLenS $\sigma_8$ constraints in an otherwise fixed fiducial cosmology, with 3 different nonlinear power spectrum treatments. Also shown is the constraint using TA12 and a prescription for AGN feedback described in Section 3.3.3.

1d CFHTLenS constraints on $\sigma_8$, for each of TA12, SM03 and Coyote. Figure 3.4 shows the results of this test. Even after implementing the conservative $\theta$ cut, there is still a $0.7\sigma$ shift between SM03 and TA12, although the constraints from TA12 and Coyote are very similar for this slice of parameter space. Note that since I've fixed all other parameters, the errorbar on $\sigma_8$ will be smaller than when marginalising over e.g. $\Omega_m$, so in some sense this is a conservative test. Encouraged by this, I continue using TA12 for the rest of the paper, since it can be used consistently with non-zero neutrino mass.

### 3.3.3 Baryonic feedback

The matter power spectrum (and therefore the weak lensing convergence power spectrum) is also affected by baryonic feedback at $k > 1h$ Mpc$^{-1}$, as pointed out by White (2004) and Zhan & Knox (2004) who, using simple models of the

effect, reported several percent changes in the convergence power spectrum at $l > 1000$. Jing et al. (2006), Rudd et al. (2008), Guillet et al. (2010), Casarini et al. (2012) all confirmed the significance of baryonic feedback at $k > 1h\,\mathrm{Mpc}^{-1}$ by comparing hydrodynamical simulations to pure N-body dark matter ones. Schaye et al. (2010) performed the OverWhelmingly Large Simulations (OWLS) to investigate the effect of several different baryonic effects on the cosmic star formation history, while van Daalen et al. (2011) used OWLS to investigate the effect of baryons on the matter power spectrum. It has been argued (van Daalen et al. 2011; Semboloni et al. 2011) that the OWLS 'AGN' model, which accounts for the presence of black holes and AGN feedback in dark matter halos using the prescription described in Booth & Schaye (2009), is the most realistic of the different OWLS models, since it matches well both the observed optical and X-ray properties of galaxy groups (McCarthy et al. 2011). To test the effect of AGN feedback on the CFHTLenS constraints, I use the matter power spectra[3] derived by van Daalen et al. (2011) from the OWLS. Specifically, I use the 'AGN' spectrum which I call $P_\delta^{\mathrm{AGN}}$ and the 'DMONLY' spectrum $P_\delta^{\mathrm{DMONLY}}$, which is the power spectrum derived from the OWLS dark matter only simulation. I approximate the effect of AGN feedback by multiplying our varying TA12 power spectrum, $P_\delta^{\mathrm{TA12}}$ by the ratio of the 'AGN' power spectrum to the 'DMONLY' power spectrum

$$P_\delta = \frac{P_\delta^{\mathrm{AGN}}}{P_\delta^{\mathrm{DMONLY}}} P_\delta^{\mathrm{TA12}}\,. \tag{3.2}$$

I obtain a 1d constraint on $\sigma_8$ as before, shown by the dotted line labelled TA12 + AGN in Figure 3.4. Largely due to the fact that I have cut the smallest scales from the analysis, the shift from introducing AGN feedback is smaller than the shift arising from the use of different Halofit versions, which suggests that the effect of AGN feedback is probably not important here. Nevertheless, I also

[3] http://www.strw.leidenuniv.nl/VD11/

repeat the analysis of Section 3.3.1, introducing a new parameter $\alpha_{\rm AGN}$ given by

$$P_\delta = \left(1 + \alpha_{\rm AGN} \frac{(P_\delta^{\rm AGN} - P_\delta^{\rm DMONLY})}{P_\delta^{\rm DMONLY}}\right) P_\delta^{\rm TA12}\,. \tag{3.3}$$

Thus I allow the strength of the AGN feedback to vary by allowing $\alpha_{\rm AGN}$ to vary. The top right panel of Figure 3.5 shows the effect on the CFHTLenS alone contours when I allow $0 < \alpha_{\rm AGN} < 2$. I repeat the analysis of Section 3.3.1, but obtain only a small improvement in agreement between the two probes, with $\sigma_{\rm eq}$ =52% . In the joint fit, I allow $-3 < \alpha_{\rm AGN} < 3$, and find a preferred value of $\alpha = 0.78^{+1.5}_{-1.02}$,. The fact there is only weak preference for positive $\alpha_{\rm AGN}$ is consistent with this parameter not being very helpful in resolving the tension.

This is the first combined CMB and lensing analysis to constrain baryonic feedback and cosmology simultaneously, although I note that this is a very simplistic prescription for AGN feedback, let alone baryonic feedback as a whole. Harnois-Déraps et al. (2015) use three of the OWLS to construct a fitting function for the effect of baryonic feedback on the power spectrum, and use CFHTLenS to constrain this model while fixing the cosmology. Unlike this analysis, they extend the CFHTLenS data to sub-arcminute scales, and find indications of a preference for a universe with baryonic feedback. Eifler et al. (2015) show the importance of accounting for baryonic feedback for stage III and IV weak lensing experiments, and propose a PCA marginalisation approach that uses information from a range of hydrodynamical simulations, as a way of removing the bias with 3 or 4 nuisance parameters.

### 3.3.4 Sensitivity to the IA model

I follow HE13 by using the non-linear linear alignment model (henceforth NLA model, Bridle & King 2007) to account for intrinsic alignments. The NLA model is based on the linear alignment model (Catelan et al. 2001; Hirata & Seljak 2004), which assumes that galaxies are aligned with their haloes which are in

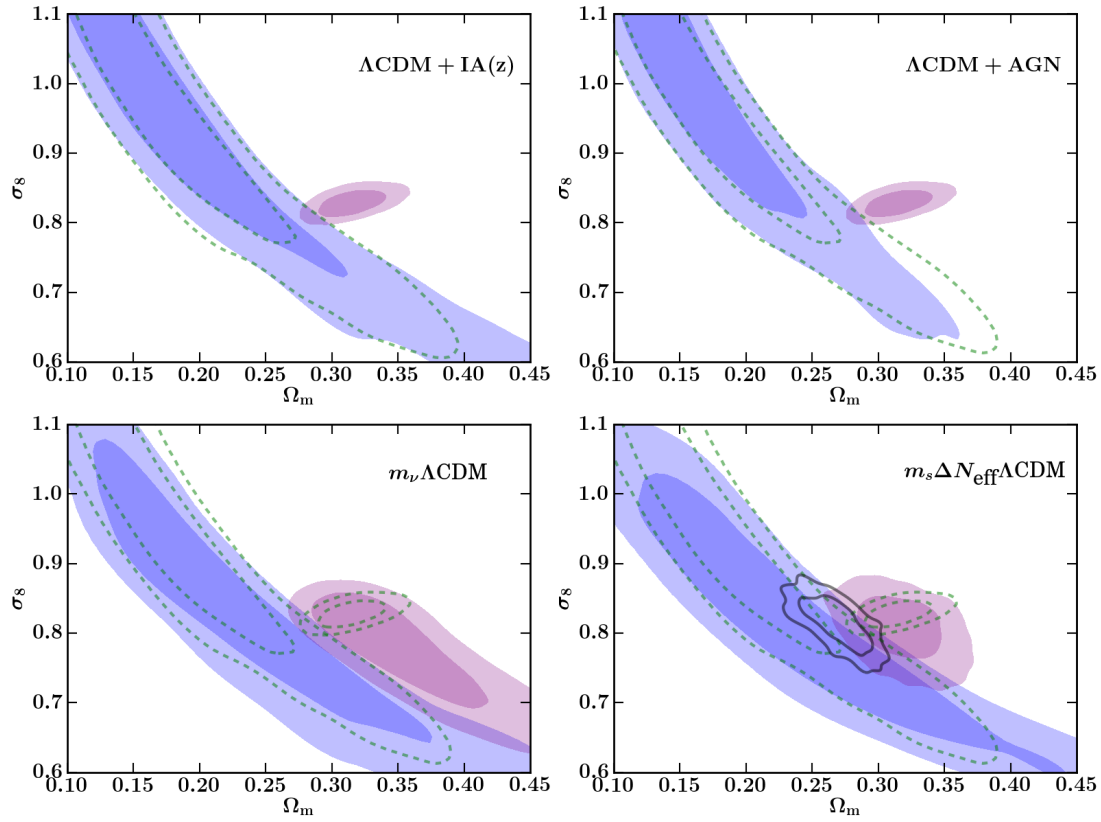


Figure 3.5: 68% and 95% confidence regions in the clustering amplitude $\sigma_8$ and matter density $\Omega_{\rm m}$ plane from *Planck*+WP alone and CFHTLenS alone. In all panels, dashed green contours represent the base ΛCDM constraints from Figure 3.2. **Top left**: CFHTLenS with extra IA redshift scaling parameter (filled blue contours) and *Planck*+WP (smaller purple contours). **Top right**: CFHTLenS marginalised over an AGN feedback parameter (filled blue contours) and *Planck*+WP (smaller purple contours). **Bottom left**: CFHTLenS (blue contours) and *Planck*+WP (smaller purple contours) allowing varying active neutrino mass. **Bottom right**: CFHTLenS (blue contours) and *Planck*+WP (smaller purple contours) allowing a massive sterile neutrino. The black contours are the joint fit.

turn are aligned with the local tidal gravitational field; for a given redshift the intrinsic galaxy ellipticity is taken to be proportional to the linear theory tidal field strength. In the linear alignment model, the intrinsic-intrinsic (II) and shear-intrinsic (GI) power spectra are given by

$$P_{\rm II}(k,z) = F^2(z)P_\delta(k,z), \quad P_{\rm GI}(k,z) = F(z)P_\delta(k,z), \tag{3.4}$$

where

$$F(z) = -AC_1\rho_{\rm crit}\frac{\Omega_{\rm m}}{D(z)}. \tag{3.5}$$

$\rho_{\rm crit}$ is the critical density at $z = 0$, $C_1 = 5 \times 10^{-14}h^{-2}M_{\odot}^{-1}{\rm Mpc}^3$, and $A$, the dimensionless amplitude, is the single free parameter.

In the NLA model, the linear matter power spectrum in equation 3.4 is replaced with the non-linear matter power spectrum. One of the main uncertainties of both of these alignment models is the redshift scaling - it may be that alignment was produced at high redshift during galaxy formation, but the strength of the signal is likely to have evolved over cosmic time. Hence I try a simple extension to the NLA model, by introducing a power law redshift scaling, $\alpha_{\rm IA}$, so that

$$F(z) = -AC_1(1+z)^{\alpha_{\rm IA}}\rho_{\rm crit}\frac{\Omega_{\rm m}}{D(z)}. \tag{3.6}$$

I repeat the analysis of Section 3.3.1, and obtain the marginalised constraints in the $\Omega_{\rm m}$-$\sigma_8$ plane shown in the top left panel of Figure 3.5. A small shift in the CFHTLenS contours is apparent when including the extra intrinsic alignment parameter, but by eye it does not appear significant in resolving the tension with *Planck*+WP. I find $\sigma_{\rm eq}$ =52% for this model, which supports this conclusion.

In agreement with HE13 I find that negative values of the intrinsic alignment amplitude parameter $A$ are slightly preferred for $\alpha_{\rm IA} = 0$. I allow a prior range of $-5 < \alpha_{\rm IA} < 5$ and find $\alpha_{\rm IA}$ to be unconstrained but preferred to be strongly negative for both CFHTLenS alone and for CFHTLenS + *Planck*+WP. This can be understood from the relatively large amount of power at low redshift in the CFHTLenS data - see HE13 Figure 2. The negative power law index allows more intrinsic alignment contribution at low redshift and very little at high redshift. An even more negative intrinsic alignment amplitude $A$ is preferred than for $\alpha_{\rm IA} = 0$, for both CFHTLenS alone and CFHTLenS + *Planck*+WP. This makes the contribution from the dominant intrinsic alignment term (GI) positive, to match the relative excess of power in the observations at low redshift.

### 3.3.5 A new CFHTLenS fitting function

HE13 presented the constraint $\sigma_8(\Omega_{\rm m}/0.27)^{0.46} = 0.774^{+0.032}_{-0.041}$ that has been used in combination with other datasets instead of running a full likelihood analysis. The HE13 analysis used the Smith et al. (2003) version of HALOFIT. Beutler et al. (2014b) showed a $\sim 1\sigma$ reduction in the Kilbinger et al. (2013) CFHTLenS constraint on $\sigma_8$ at $\Omega_{\rm m} = 0.3$ when using a newer HALOFIT version, however, that analysis used angular scales down to 0.9 arcmin in both $\xi_+$ and $\xi_-$, which are highly sensitive to the nonlinear modelling. From our more conservative analysis, I find

$$\sigma_8(\Omega_{\rm m}/0.27)^{0.48} = 0.768 \pm 0.037, \tag{3.7}$$

which is slightly lower than, but consistent with the HE13 result for e.g. $\Omega_m = 0.27$.

## 3.4 Discordance in extensions to ΛCDM

In this section I try the following extensions to ΛCDM: massive active neutrinos, a massive sterile neutrino, and primordial tensor modes, and quantify how much they resolve the tension between *Planck*+WP and CFHTLenS.

### 3.4.1 Discordance in $m_\nu$LCDM

We wish to know whether allowing a greater active neutrino mass alleviates the tension between *Planck*+WP and CFHTLenS. I allow the mass, $m_\nu$ of the massive neutrino eigenstate in the base ΛCDM model to vary, above a lower bound of 0.06 eV. I call this model $m_\nu$ΛCDM.

Line 5 of Table 3.1 summarises the consistency tests I performed for this model. $\sigma_{\rm eq}$ is 50% i.e. the 50% 7d confidence regions only just touch, which is only a small improvement over ΛCDM. Some insight into why this happens can be gained from the bottom left panel of Figure 3.5: the *Planck*+WP contours are ex-

tended along the same line of degeneracy as the CFHTLenS constraint. This can be explained as follows (drawing heavily on Section V of Howlett et al. (2012)): although increasing neutrino mass does reduce growth of structure, hence driving the *Planck*+WP contours to lower $\sigma_8$, light ($m_\nu$ well below 1 eV) neutrinos, are relativistic before/at recombination, so to preserve the position of the CMB acoustic peaks, $d_A(z_*)$ must remain constant. However, at late times, the massive neutrinos become non-relativistic, increasing the energy density relative to a model with massless neutrinos, and decreasing $d_A(z_*)$, unless $h$ also decreases. The degenerate combination $\Omega_m h^2$ is also well-constrained, so $\Omega_m$ must increase. I conclude that the datasets are still in tension, and discuss other related analyses in Section 3.5.1.

Principal component analysis gives a similar power law slope for this model, and I find the constraint

$$\sigma_8(\Omega_\mathrm{m}/0.27)^{0.46} = 0.753 \pm 0.039, \tag{3.8}$$

for CFHTLenS alone in the $m_\nu\Lambda$CDM model. This power law can be used to approximate the CFHTLenS constraints when a varying active neutrino mass is allowed.

### 3.4.2 A sterile neutrino: $m_\mathrm{s}^\mathrm{eff}\Delta N_\mathrm{eff}\Lambda$CDM

I add to the base model a sterile neutrino - an additional neutrino species with effective mass $m_\mathrm{s}^\mathrm{eff}$ and contribution to $N_\mathrm{eff}$ of $\Delta N_\mathrm{eff} = N_\mathrm{eff} - 3.046$, as proposed by Hamann & Hasenkamp (2013) and Battye & Moss (2014). The bottom right panel of Figure 3.5 shows constraints in the $\Omega_\mathrm{m}$ - $\sigma_8$ plane, and there is now better agreement between the two probes - the 68% 2d marginalised contours are now close to touching. I find $\sigma_\mathrm{eq}$ =31% for this model, a considerable improvement. I consider this agreement good enough to combine the measurements, and find $m_\mathrm{s}^\mathrm{eff} < 0.408$ eV(95%) and $\Delta N_\mathrm{eff} = 0.819^{+0.397}_{-0.455}$. The 1d marginalised pdfs are

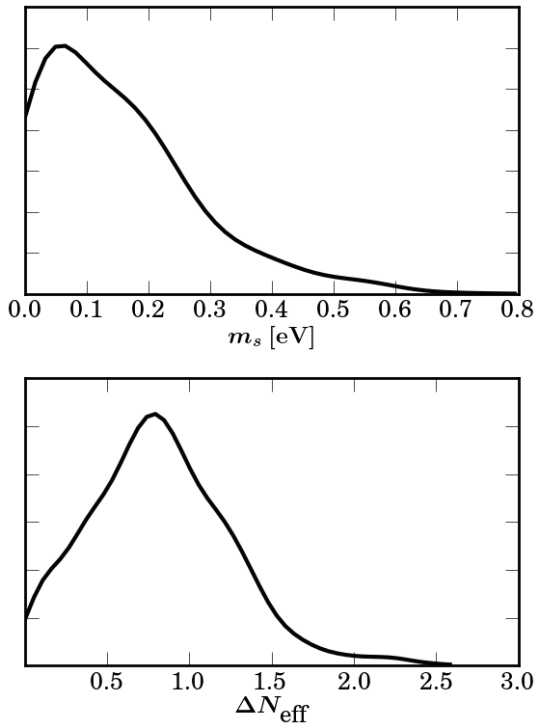


Figure 3.6: Constraints on sterile neutrino effective mass and number of extra neutrino species from combining *Planck*+WP and CFHTLenS.

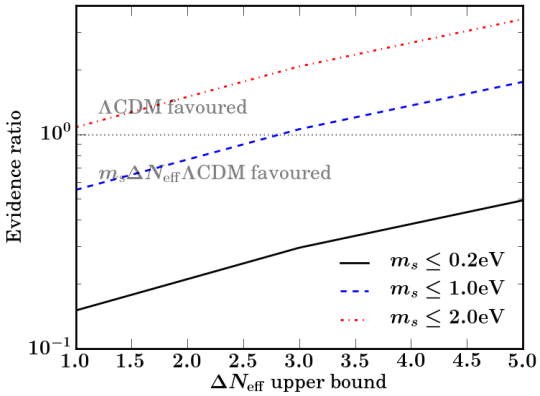


Figure 3.7: Evidence ratio as a function of the upper bound of the prior on $m_{\rm s}^{\rm eff}$ and $\Delta N_{\rm eff}$ (both of which are assumed to have a uniform prior with a lower bound of zero). The extended model is favoured when the evidence ratio is less than one.

shown in Figure 3.6, and the cosmological constraints are shown in Table 3.2.

Leistedt et al. (2014) used the Bayesian evidence ratio to assess whether extensions to ΛCDM were justified. The Bayesian evidence ratio for a model $M_0$ nested within model $M_1$ which has extra parameter(s) $p$ is given by

$$\frac{\mathrm{P}(d|M_0)}{\mathrm{P}(d|M_1)} = \frac{\mathrm{P}(d|M_1, p=0)}{\int dp \mathrm{P}(d|M_1,p)\mathrm{Pr}(p|M_1)} \tag{3.9}$$

where $P(d|M_1,p)$ is the likelihood of the data $d$ marginalised over all other parameters apart from $p$ and $Pr(p|M_1)$ is the normalised prior on $p$ (e.g. see Lewis & Bridle (2010), Trotta (2007) and references therein). The extended model $M_1$ is favoured if the ratio is less than one. The Jeffrey's scale (Jeffreys 1961) is often used to guide the interpretation of Baysian evidence. On this scale an evidence ratio of $\frac{1}{3}$ to $\frac{1}{10}$ would be considered substantial evidence for the extended model,

while a value less than $\frac{1}{10}$ would be considered strong evidence. If regions where the likelihood ($P(d|M_1, p)$) is very small are allowed by a wide prior ($Pr(p|M_1)$), the denominator can become very small, causing the extended model to be disfavoured. So the evidence ratio is very sensitive to the choice of prior.

To illustrate this, I compute the evidence ratio of $m_{\rm s}^{\rm eff}\Delta N_{\rm eff}\Lambda$CDM compared to $\Lambda$CDM, as a function of the priors on $m_{\rm s}^{\rm eff}$ and $\Delta N_{\rm eff}$, shown in Figure 3.7. Either model can be favoured, depending on the choice of prior. If the number of extra neutrino species is assumed to be less than 2.5 then the sterile neutrino model is favoured if an upper limit on the sterile neutrino mass of 1 eV is assumed. More stringently, if the number of extra species is assumed to be less than 2 and the mass less than 0.2 eV then the sterile neutrino model is around a factor of five more probable than $\Lambda$CDM. Conversely, if the prior range on the mass and number of neutrino species is large then the sterile neutrino model is disfavoured. For example, if the mass is restricted to be less than 2 eV and the number of extra species less than 5, then $\Lambda$CDM is a little over three times as probable as $m_{\rm s}^{\rm eff}\Delta N_{\rm eff}\Lambda$CDM. I note that no choice of priors considered here produces strong evidence according to the Jeffrey's scale.

Again, I provide a power law representation of the CFHTLenS constraint, finding

$$\sigma_8(\Omega_{\rm m}/0.27)^{0.47} = 0.750 \pm 0.037. \tag{3.10}$$

This is close to the result I found for the $m_\nu\Lambda$CDM, which is reasonable since low redshift probes like weak lensing are sensitive to the total neutrino mass, and not to $N_{\rm eff}$ (i.e. they do not care whether the neutrino mass eigenstate is active or sterile).

### 3.4.3 Primordial gravity waves

Inspired by the recent BICEP2 results (BICEP2 Collaboration et al. 2014) I investigate the effect of gravity waves on the tension between *Planck*+WP and

| *Model* | Base ΛCDM | $m_{\rm s}^{\rm eff}\Delta N_{\rm eff}$ΛCDM |
|---|---|---|
| *Data* | *Planck*+WP | *Planck*+WP CFHTLenS |
| $\Omega_{\rm m}$ | $0.315^{+0.016}_{-0.018}$ | $0.274^{+0.017}_{-0.017}$ |
| $\sigma_8$ | $0.829^{+0.012}_{-0.012}$ | $0.811^{+0.030}_{-0.028}$ |
| $h_0$ | $0.673^{+0.027}_{-0.025}$ | $0.741^{+0.020}_{-0.041}$ |
| $n_s$ | $0.960^{+0.007}_{-0.007}$ | $0.995^{+0.014}_{-0.014}$ |
| $\tau$ | $0.089^{+0.012}_{-0.014}$ | $0.099^{+0.017}_{-0.017}$ |
| $\Delta N_{\rm eff}$ | - | $0.819^{+0.397}_{-0.455}$ |
| $m_{\rm s}^{\rm eff}$ [eV] | - | $< 0.408$ (95%) |

Table 3.2: Cosmological parameter constraints in the $m_{\rm s}^{\rm eff}\Delta N_{\rm eff}$ΛCDM model. The values shown are means of the posterior distribution; errors are 68% confidence intervals unless specified. The *Planck*+WP base ΛCDM are included for easy reference.

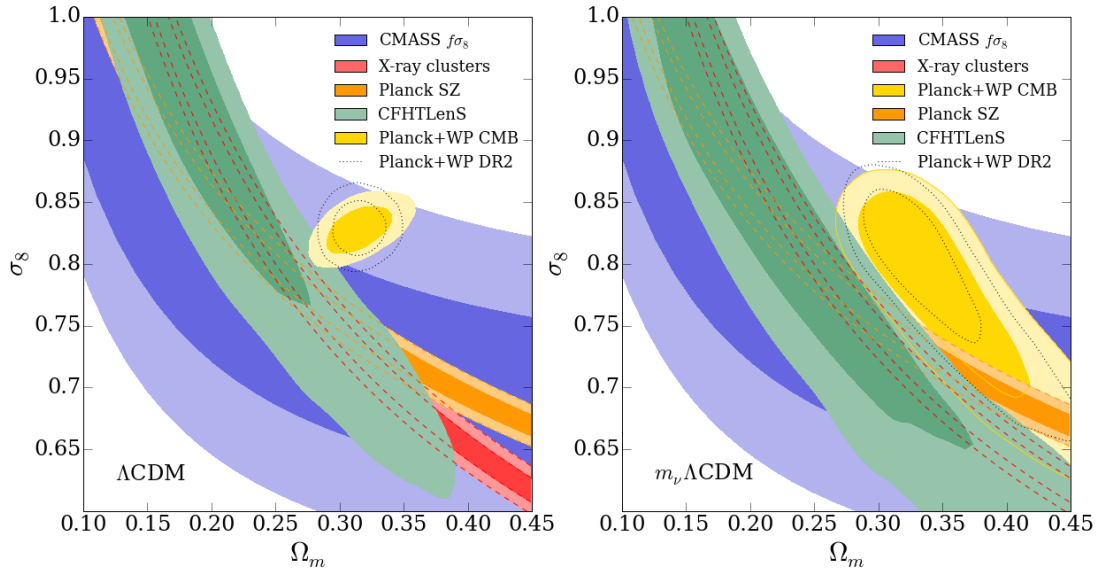


Figure 3.8: Comparison of constraints in the $\sigma_8$, $\Omega_{\rm m}$ plane in ΛCDM from CFHTLenS (this work; green), *Planck*+WP (yellow, Planck Collaboration et al. 2013c), *Planck* SZ cluster counts (orange, Planck Collaboration et al. 2013e), X-ray clusters (red, Vikhlinin et al. 2009), CMASS $f\sigma_8$ (blue, Beutler et al. 2014c) and *Planck* 2015 (grey dotted, TT + lowP, Planck Collaboration et al. 2015a). In the left panel, the contours are obtained assuming ΛCDM, while in the right panel, the CFHTLenS and *Planck*+WP constraints allow a varying active neutrino mass. Of note is the improved consistency of the *Planck*+WP contours with the CMASS $f\sigma_8$ and the *Planck* SZ contours when the neutrino mass is allowed to vary, driving the neutrino mass detections of Battye & Moss (2014) and Beutler et al. (2014b).

CFHTLenS. Although gravity waves are no longer required by the data (BICEP2/Keck and Planck Collaborations et al. 2015) I still consider their implications here. Qualitatively one might expect the agreement between *Planck*+WP and CFHTLenS to improve due to gravity waves: the increase of power at low multipoles in the CMB from tensors (Crittenden et al. 1993) will need to be compensated by a reduction in power from scalar modes; a reduction in scalar power would bring the *Planck*+WP contours closer to CFHTLenS. Meanwhile, the addition of tensor modes in the primordial power spectrum does not affect the matter power spectrum, which determines the shear-shear correlation function, and so has no effect on weak lensing. However, a detailed analysis is necessary to see how the values of the other cosmological parameters are affected by the change in shape of the CMB power spectrum due to the addition of tensors.

The original BICEP2 measurement of $r = 0.20^{+0.07}_{-0.05}$ (BICEP2 Collaboration et al. 2014) is not compatible with the *Planck*+WP data unless an additional modification is made to ΛCDM, because Planck Collaboration et al. (2013c) showed that when only $r$ is added to the base ΛCDM model, *Planck*+WP gives the constraint $r < 0.11$ (95% confidence). Therefore in this section I also consider the effect of adding a running spectral index of the primordial power spectrum, $\alpha_{run} = \mathrm{d}n_s/\mathrm{d}lnk$, which Planck Collaboration et al. (2013c) showed to relax the constraint on $r$ to $r < 0.26$ (95%), into agreement with BICEP2.

I repeat the investigation in $n$-dimensions described in Section 3.3.1, and find that the addition of gravity waves and running of the spectral index, in the $r\alpha_{run}$ΛCDM model, relaxes the tension between the datasets only slightly, with $\sigma_{\rm eq}$ =63% i.e. the 63% iso-likes from each dataset touch.

Therefore I conclude that gravity waves do not significantly resolve the tension between CFHTLenS and *Planck*+WP.

## 3.5 Discussion

In this Section I compare our results with those from other analyses, and speculate on alternative potential explanations for the discrepancy. I will refer to Figure 4.10, which shows a selection of other low-z probes of the growth of structure.

### 3.5.1 Comparison with other work

Several other authors have considered how to reconcile cosmology from the CMB and the amplitude of matter fluctuations measured by low-redshift probes. The most relevant to our work are by Planck Collaboration et al. (2013c), Battye & Moss (2014), Beutler et al. (2014b), Dvorkin et al. (2014), Leistedt et al. (2014), and Archidiacono et al. (2014). I discuss next the differences to this analysis.

The Planck Collaboration et al. (2013c) noted an approximately $2\sigma$ discrepancy between their Planck CMB analysis and the CFHTLenS analysis of Heymans et al. (2013) and noted that further work will be required to resolve the difference. They allow freedom in the effect of lensing on the primary anisotropies and find that a larger lensing amplitude is preferred when the *Planck* data is combined with smaller scale CMB measurements. Taken at face-value this suggests an increased $\sigma_8$ from low redshift data, unlike all the other low redshift data considered in the other papers I discuss below.

The tension between *Planck* Sunyaev–Zel'dovich (SZ) cluster counts and the primary anisotropies was discussed by the Planck Collaboration et al. (2013e). They discuss possible systematics in the SZ analysis and conclude that each is improbable, but that understanding the mass bias scaling relation is the key to further investigation. They find a $1.9\sigma$ preference for a non-zero active neutrino mass by combining *Planck*+WP with the *Planck* SZ constraints, marginalising over their preferred range in the hydrostatic mass bias ($0.7 < 1-b < 1.0$). Two recent analyses have attempted to constrain the mass bias by comparing the *Planck* mass

estimates ($M_{Planck}$) with weak-lensing mass estimates ($M_{WL}$). Using the ratio $< M_{Planck}/M_{WL} >$ as a proxy for the mass bias, von der Linden et al. (2014) find $< M_{Planck}/M_{WL} >= 0.688 \pm 0.072$ for 22 of the clusters in the *Planck* cosmology sample, and note that adopting this mass bias would substantially reduce the tension. Hoekstra et al. (2015) find $< M_{Planck}/M_{WL} >= 0.76 \pm 0.05(\mathrm{stat}) \pm 0.06(\mathrm{sys})$ for 37 clusters common between the Canadian Cluster Comparison Project and the *Planck* sample, and conclude that this does not resolve the tension.

Planck Collaboration et al. (2013d) used lensing of the CMB to measure the power spectrum of the gravitational potential at slightly higher redshift than that probed by CFHTLenS. This was combined with the constraints from the primary anisotropies and found to reduce the measured amplitude of fluctuations (Planck Collaboration et al. 2013c). One of the many extensions to ΛCDM investigated by the *Planck* team (Planck Collaboration et al. 2013c) was the mass of the active neutrino. When using the CMB lensing information, they found that this increased the upper limit on the neutrino mass relative to that from CMB primary anisotropies alone (the 95% upper limit increased from 0.66 eV to 0.85 eV), indicating some tension.

Battye & Moss (2014) found a preference for a non-zero active neutrino mass when combining CMB lensing, CFHTLenS and *Planck* SZ cluster counts (Planck Collaboration et al. 2013e) with the CMB. They use the correlation functions measured by Kilbinger et al. (2013), who performed a 2d cosmic shear analysis i.e. they did not use multiple redshift bins. They found similar but stronger preference for a non-zero sterile neutrino mass. They noted that both these joint fits come at the cost of a worse fit to the primary CMB data. Figure 4.10 shows an orange band corresponding to the SZ cluster counts prior from Planck Collaboration et al. (2013e), $\sigma_8(\Omega_\mathrm{m}/0.27)^{0.3} = 0.78 \pm 0.01(68\%)$. The shallower degeneracy direction of this prior as compared to the lensing constraint allows more overlap with the *Planck*+WP confidence regions with an active neutrino, explaining the significant detection of neutrino mass Battye & Moss (2014) claimed when combining this

prior with *Planck*+WP.

Hill & Spergel (2014) also used SZ information from *Planck*, constructing a thermal SZ map and cross-correlating with the *Planck* CMB lensing potential map. They constrain $\sigma_8(\Omega_{\rm m}/0.282)^{0.26} = 0.824 \pm 0.029$, a result consistent (within ΛCDM) with that from the *Planck* primary aniotropies, unlike the aforementioned SZ cluster counts.

Beutler et al. (2014b) investigate the constraints on the active neutrino mass using the Baryon Oscillation Spectroscopic Survey (BOSS, Schlegel et al. 2009), the CMB, and other low redshift measurements including a parameterised fit to the CFHTLenS cosmology constraints of Kilbinger et al. (2013). Their Figure 7 illustrates that the inclusion of a free active neutrino mass elongates the *Planck* contours in a direction parallel to the CFHTLenS constraints. They combine CMB constraints with those from the BOSS CMASS DR11 galaxy clustering results of Beutler et al. (2014c), which come from BAO, Alcock-Paczinski and growth measurements. The push towards a positive neutrino mass comes mostly from the growth constraint (shown as blue contours in Figure 4.10) since this is sensitive to the amplitude of clustering. They use various combinations of the data and find similar non-zero values for the neutrino mass to Battye & Moss (2014), and finally combine them all together to get a $\approx 3\sigma$ detection of the neutrino mass, with a similar result whether using WMAP or *Planck* temperature anisotropies.

Dvorkin et al. (2014) focus on the discrepancy between *Planck* and BICEP2, noting that extra relativistic species in the early universe can help alleviate the tension introduced into the *Planck* data by extra power from gravitational waves. They point out that the sterile neutrino can thus help alleviate the *Planck* vs. BICEP2 tension and additionally the CMB-low-z tension at the same time. They use local $H_0$, baryon acoustic oscillations and local X-ray cluster abundance measurements (Vikhlinin et al. 2009, shown as the red band in Figure 4.10) for low-redshift information, and obtain a $\approx 3\sigma$ sigma detection of the sterile neutrino

mass.

The cosmological constraints on sterile neutrinos are compared with those from short baseline neutrino oscillation experiments in Archidiacono et al. (2014). They use the CMB combined with low-redshift clustering measurements from the growth of structure obtained by Parkinson et al. (2012), *Planck* SZ and the parameterised fit to the CFHTLenS constraints of Kilbinger et al. (2013). They find a detection of non-zero sterile neutrino mass, and point out the significant inconsistency between its value and that found in the neutrino oscillation experiments.

However, the neutrino mass detections are disputed by Leistedt et al. (2014), who point out that they are driven by two highly constraining datasets from counting galaxy clusters (Planck Collaboration et al. 2013e; Vikhlinin et al. 2009). They describe some of the potential systematic effects in these two measurements. They use the same simple parameterised fit to the CFHTLenS constraints as Archidiacono et al. (2014) and Beutler et al. (2014b). Omitting the datasets in tension, they use each other low redshift probe one-at-a-time, and find only upper limits on the neutrino mass.

Other recent cosmic shear analyses have shown some variation in the preferred value of $\sigma_8$. Kitching et al. (2014) performed a '3D cosmic shear' analysis of CFHTLenS with conservative cuts on the scales considered ($k \leq 1\,\mathrm{hMpc}^{-1}$), leading to larger statistical errors, but probably less systemtic error due to uncertainty in the nonlinear matter power spectrum, and found constraints consistent with *Planck*+WP. Jee et al. (2013) use $\xi_{+/-}$ measurements from the Deep Lens Survey, and found $\sigma_8$ at $\Omega_m = 0.3$ to be $0.804 \pm 0.21$, significantly higher than the value of $0.73 \pm 0.035$ from this work. However, I note that their use of angular scales down to 0.3" in both $\xi_+$ and $\xi_-$, and the SM03 version of HALOFIT (which predicts less power at small scales than the version used in this work) are likely to contribute to this.

The *Planck* 2015 results (in particular Planck Collaboration et al. 2015a)

released since submission of this work, appear to have changed little of the above conclusions (as suggested by the grey dotted contours in Figure 4.10). The tension in $\sigma_8$ with a larger catalog of SZ clusters (Planck Collaboration et al. 2015d) remains, as does the uncertainty on the mass calibration. The preference for higher lensing smoothing in the CMB temperature power spectrum (suggesting a larger amplitude of fluctuations) also remains, as does the the lower amplitude preferred by the lensing reconstruction data (Planck Collaboration et al. 2015b). The combined constraint on the neutrino mass from the primary temperature anisotropies, LFI polarisation and CMB lensing is now $\Sigma m_\nu < 0.68$ eV (95%).

### 3.5.2 Other possible explanations

I have shown our results to be robust to uncertainties in the modelling of the nonlinear matter power spectrum (including AGN feedback) and intrinsic alignments. Two other weak-lensing systematics I have not considered in detail are photometric redshift errors and shape measurement errors. One can estimate how wrong these would have to be to account for the $\approx 20\%$ disparity (assuming the *Planck*+WP best-fit value of $\Omega_m$) between the CFHTLenS and *Planck*+WP best fit values of $\sigma_8$. As a rule of thumb, equation 24 from Huterer et al. (2006) tells us that the lensing power spectrum (at $l = 1000$ and assuming all source galaxies are at $z_s = 1$) has dependence

$$P^\kappa \propto \sigma_8^{2.9} z_s^{1.6}. \tag{3.11}$$

Hence to observe the same signal (i.e. setting $P^\kappa$ equal to a constant in equation 3.11), with a 20% higher $\sigma_8$, would require the redshifts to shift systematically by a fraction $\approx 1.2^{-1.8} = 0.72$ i.e. a systematic 30% error in photometric redshift, which would be very surprising in any one redshift bin, let alone all redshift bins with the same sign.

To estimate the effect of multiplicative bias on our results, note that $\xi_{+/-} \propto$

$(1+m)^2$, where $m$ is the multiplicative bias (see e.g. Heymans et al. (2006) for an introduction to shape measurement biases). The information in $\xi_{+/-}$ comes from a mixture of linear and nonlinear scales. On linear scales we have $\xi_{+/-}^{observed} \propto (1+m)^2 P_\delta \propto (1+m)^2\sigma_8^2$, whereas on nonlinear scales $\xi_{+/-} \propto (1+m)^2\sigma_8^3$. So an increase in $\sigma_8$ of 20% would require $(1+m) = 1.2^{-1} = 0.83$ (assuming all information comes from linear scales) and $(1+m) = 1.2^{-3/2} = 0.69$ (assuming all information comes from nonlinear scales). The multiplicative bias in the CFHTLenS shape measurements was calibrated using image simulations (Miller et al. 2013) and the average value of $(1+m)$ was found to be 0.94. It's clear then, that the value of the multiplicative bias estimated from simulations would have to be catastrophically wrong to produce such a significant shift in $\sigma_8$.

Spergel et al. (2013) reanalysed the *Planck* data, and claim that the 217GHz$\times$ 217 GHz detector set spectrum used in the *Planck* analysis is responsible for 'some' of the tension with other cosmological measurements. The latest version of Planck Collaboration et al. (2013c) does discuss a residual systematic in the 217 GHz $\times$ 217 GHz spectrum, but claim that this has an impact of less than half a standard deviation on cosmological parameters. The *Planck* 2015 releases will include a correction for this, but the *Planck* products used in this analysis do not.

Furthermore, the CMB constraints I use rely on the WMAP polarisation data primarily to constrain the optical depth to reionisation. The *Planck* satellite has measured the polarisation signal more precisely. A reduction in the optical depth to reionisation would be required to push the CMB contours towards those from CFHTLenS. This is because a lower optical depth increases the predicted CMB temperature anisotropy power spectrum on the majority of scales, and thus the underlying amplitude of scalar fluctuations must be reduced to retain a good fit to the observations. The Planck Collaboration et al. (2013c) noted that the

*Planck* temperature anisotropies alone tightly constrain the combination

$$\sigma_8 e^{-\tau} = 0.753 \pm 0.011 \tag{3.12}$$

which would require $\tau$ to be significantly smaller to make a significant impact on the discrepancy. Planck Collaboration et al. (2015a) did indeed find a lower value of $\tau$ of $0.078 \pm 0.019$ (down from $0.089 \pm 0.013$), however, this was accompanied by an upward shift in the overall calibration of the temperature data, which means that the value of $\sigma_8$ preferred by *Planck* has barely changed.

As noted by Archidiacono et al. (2014), the cosmology constraints on the sterile neutrino are not compatible with those from short baseline neutrino experiments. However, the cosmology constraints are relatively generic for other relativistic particles in the early universe.

Finally I note that other extensions of ΛCDM can be explored, such as the variation of the dark energy equation of state, a universe with non-zero curvature, or a deviation of the growth of structure from the GR prediction.

## 3.6 Conclusions

I have confirmed the tension between *Planck*+WP and CFHTLenS in the $\Omega_m$-$\sigma_8$ plane within the base ΛCDM cosmology, and shown its robustness to various weak lensing systematics. I find that considering the overlap in the full ΛCDM parameter space weakens this conclusion, since marginalising over some of the parameters makes contours tighter (the 68% contours lie at higher probability, and closer to the best fit point) in the remaining parameters.

I find that allowing massive active neutrinos does not significantly resolve the tension, because the slope of the CFHTLenS contours runs parallel to the effect of adding active neutrinos to the CMB. Other works include other datasets with a shallower slope than CFHTLenS, which intersect the CMB contours at high

active neutrino mass, thus leading to a detection of the neutrino mass. It was noted in Battye & Moss (2014) that the active neutrino mass detection comes at the cost of a decreased likelihood of the *Planck*+WP data. In this paper I have quantified the size of this decrease in terms of the full n-dimensional contours and used a more robust version of the cosmic shear data.

The addition of tensor modes, even with running of the spectral index also does not significantly affect the tension.

I have also added an extra, sterile species of neutrino, and find that the 31% confidence iso-likes in the 8 dimensional parameter space touch in this case. I find that the effective number of extra neutrino species ($\Delta N_{\rm eff}$) is favoured to be non-zero in the joint fit, at about the $2\sigma$ level. Although the $m_{\rm s}^{\rm eff}\Delta N_{\rm eff}\Lambda$CDM model does allow an acceptable joint fit, some tension remains between *Planck*+WP and CFHTLenS, since all points in the joint fit are on at least the 31% 8d iso-like of either the *Planck*+WP-only or CFHTLenS-only constraints (and at least the 68% 2d marginalised contour in the $\Omega_m - \sigma_8$ plane).

Therefore I am not completely satisfied by the amount which the flexible sterile neutrino model reduces the discrepancy, and believe that investigating other new physics, and other sources of systematic error in either experiment, may lead to a better resolution of the tension.

## Acknowledgements

Many thanks to Catherine Heymans, Richard Battye, Boris Leistedt, Fergus Simpson, Adam Amara, Anthony Lewis, Adam Moss, Tomasz Kacprzak, George Efstathiou, Ben Wandelt, John Beacom, Ofer Lahav, M. James Jee, J. Anthony Tyson and Michael D. Schneider for useful discussions. Thanks also to the non-author members of the core CosmoSIS team: Marc Paterno, Elise Jennings, Douglas Rudd, Alessandro Manzotti, Scott Dodelson, Saba Sehrish, James Kowalkowski.

## 3.A Confidence levels and the number of degrees of freedom

To parameterise the probability distribution of one or more model parameters, the 68% (95%) confidence intervals, defined as the contour (in the 2d case) of constant probability that encloses 68% (95%) of the probability distribution, is often used. In this paper I've used these contours (or 'iso-likelihood surfaces' in $> 2$ dimensions) to judge the consistency of the parameter constraints from two datasets. We've seen that when marginalising over several parameters, and reducing the 6+ dimensional parameter space to 2d, the percentile values of the just-overlapping surfaces/contours increase, giving the impression of greater discrepancy.

This phenomenon is illustrated by Figure 3.9, which shows samples from two two-dimensional gaussian pdfs whose 68% confidence regions touch in two dimensions (upper panel), but do not when the parameter in the $y$-direction is marginalised over (lower panel). This is related to the effect described in the table on page 815 Numerical Recipes in C (Press et al. 2007) (page 693 of the 2nd edition), which shows how the $\Delta\chi^2$ (the change in probability relative to the maximum probability point in parameter space) of the 68% confidence level varies with $\nu$, the number of degrees of freedom (analogous to the number of dimensions). They show that the $\Delta\chi^2$ of a given confidence level increases with $\nu$, or equivalently, for a given $\Delta\chi^2$, the confidence level increases as $\nu$ is reduced. This is consistent with Figure 3.9: $\nu$ is reduced from 2 to 1 by marginalising, the $\Delta\chi^2$ of the 68% level increases, so is found closer to the peak, and the constraint appears tighter. This tightening when reducing $\nu$ is consistent with the higher apparent significance of the tension in the 2d marginalised plots throughout this work, as compared to the quoted n-dimensional $\sigma_{eq}$ values.

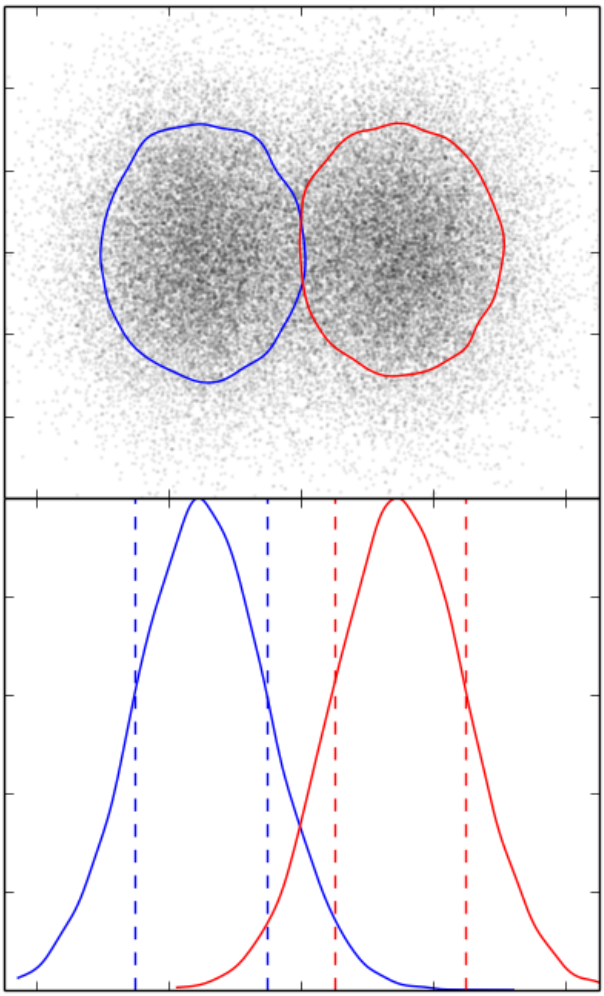

Figure 3.9: Top panel: Samples and 68% confidence regions for two 2d gaussian pdfs. Bottom panel: The pdfs marginalised in the $y$-direction, with 68% confidence levels as vertical dashed lines.

# Chapter 4

# Cosmology from Cosmic Shear with DES Science Verification Data

*This chapter is largely a reproduction of The Dark Energy Survey Collaboration et al. (2015), which as a DES collaboration cosmology paper, has a large number of co-authors (and rightly so). I led the analysis, working most closely with Joe Zuntz and Sarah Bridle.*

I present the first constraints on cosmology from the Dark Energy Survey (DES), using weak lensing measurements from the preliminary Science Verification (SV) data. I use 139 square degrees of SV data, which is less than 3% of the full DES survey area. Using cosmic shear 2-point measurements over three redshift bins I find $\sigma_8(\Omega_{\rm m}/0.3)^{0.5} = 0.81 \pm 0.06$ (68% confidence), after marginalising over 7 systematics parameters and 3 other cosmological parameters. I examine the robustness of the results to the choice of data vector and systematics assumed, and find them to be stable. About 20% of the error bar comes from marginalising over shear and photometric redshift calibration uncertainties. The current state-of-the-art cosmic

shear measurements from CFHTLenS are mildly discrepant with the cosmological constraints from *Planck* CMB data; these results are consistent with both datasets. The uncertainties are ∼30% larger than those from CFHTLenS when I carry out a comparable analysis of the two datasets, which I attribute largely to the lower number density of our shear catalogue. I investigate constraints on dark energy and find that, with this small fraction of the full survey, the DES SV constraints make negligible impact on the *Planck* constraints. The moderate disagreement between the CFHTLenS and *Planck* values of $\sigma_8(\Omega_\mathrm{m}/0.3)^{0.5}$ is present regardless of the value of $w$.

## 4.1 Introduction

The accelerated expansion of the Universe is the biggest mystery in modern cosmology. Many ongoing and future cosmology surveys are designed to shed new light on the potential causes of this acceleration using a range of techniques. Many of these surveys will probe the acceleration using the subtle gravitational distortion of galaxy images, known as cosmic shear. This method is particularly powerful because it is sensitive to both the expansion history of and the growth of structure in the Universe (Albrecht et al. 2006; Peacock & Schneider 2006; Weinberg et al. 2013). Measurement of both of these is important in trying to distinguish whether the acceleration is due to some substance in the Universe, dubbed dark energy, or whether General Relativity needs to be modified. Observations of cosmic shear offer the potential to elucidate the properties of dark energy and the nature of gravity. In addition, cosmic shear can constrain the amount and clustering of dark matter, which may help us to understand this mysterious constituent of the Universe and its role in galaxy formation.

Since the first detection of cosmic shear over a decade ago Bacon et al. (2000); Kaiser et al. (2000); Wittman et al. (2000); Van Waerbeke et al. (2000), a number

of subsequent surveys led to steadily improved measurements (Hoekstra et al. 2002; Hamana et al. 2003; Van Waerbeke et al. 2005; Jarvis et al. 2006; Semboloni et al. 2006; Massey et al. 2007; Hetterscheidt et al. 2007; Schrabback et al. 2010). More recently the Sloan Digital Sky Survey (SDSS) Stripe 82 region of 140 to 168 square degrees was analysed by Lin et al. (2012) and Huff et al. (2014). The recent Deep Lens Survey (DLS) cosmological constraints by Jee et al. (2013) used 20 square degrees of data taken with the Mosaic Imager on the Blanco telescope between 2000 and 2003. The Canada France Hawaii Telescope Lensing Survey (CFHTLenS, Heymans et al. (2012)) analysed 154 square degrees of data taken as part of the Canada France Hawaii Telescope Legacy Survey (CFHTLS) between 2003 and 2009. CFHTLenS cosmology analyses included Kilbinger et al. (2013) (hereafter K13), Heymans et al. (2013) (hereafter H13), Kitching et al. (2014) and Benjamin et al. (2013). H13 performed a six-redshift bin tomographic analysis, which is arguably the most constraining CFHTLenS result, since they marginalised over intrinsic alignments as well as cosmological parameters. The Kilo-Degree Survey (KiDS) have just released a weak lensing analysis of 100 square degrees of their survey and compare their cosmic shear measurements to predictions from CFHTLenS and *Planck* best-fit models (Kuijken et al. 2015).

Cosmic shear measures the integrated fluctuations in matter density along a line of sight to the observed galaxies, with a weight kernel that peaks approximately half way to these galaxies. This value can be compared with the clumpiness of the Universe at recombination observed in the temperature fluctuations of the Cosmic Microwave Background radiation (CMB), extrapolated to the present day using the parameters of ΛCDM derived from measurements of the CMB. The most recent measurements from the *Planck* satellite (Planck Collaboration et al. 2015a) are in tension with CFHTLenS and some other low-redshift measurements, which could point to new physics such as non-negligible neutrino masses or a modified growth history (Battye & Moss 2014; Beutler et al. 2014a). However, as noted by MacCrann et al. (2015), massive neutrinos are not a natural

explanation because they do not move the two sets of contours significantly closer together in the $(\Omega_{\rm m}, \sigma_8)$ plane.

Gravitational lensing of the CMB provides additional information on the clumpiness of the low redshift Universe. It probes slightly higher redshifts than cosmic shear ($z \lesssim 2$) and recent measurements have a constraining power comparable to that of current cosmic shear data (van Engelen et al. 2014; Story et al. 2014; Planck Collaboration et al. 2015c).

At present, three major ground-based cosmology surveys are in the process of taking high quality imaging data to measure cosmic shear: the KIlo-Degree Survey (KIDS)[1] which uses the VLT Survey Telescope (VST), the Hyper Suprime-Cam (HSC) survey[2] using the Subaru telescope, and the Dark Energy Survey (DES)[3] using the Blanco telescope. Furthermore, three new cosmology survey telescopes are under development for operation next decade, with designs tuned for cosmic shear measurements: the Large Synoptic Survey Telescope (LSST)[4], Euclid[5] and the Wide Field InfraRed Survey Telescope (WFIRST)[6].

Though one of the most cosmologically powerful techniques, cosmic shear is also among the most technically challenging. The lensing distortions are of order 2%, far smaller than the intrinsic ellipticities of typical galaxies. Therefore these distortions must be measured statistically, for example by averaging over an ensemble of galaxies within a patch of sky. To overcome statistical noise, millions of objects must be measured to high accuracy. The size and sky coverage of the next generation surveys will provide unprecedented statistical power.

Before the power of these data can be exploited, however, a number of practical difficulties must be overcome. The most significant of these fall broadly into four categories. (i) Shape measurements must be carried out in the presence

[1] http://kids.strw.leidenuniv.nl
[2] http://www.naoj.org/Projects/HSC/HSCProject.html
[3] http://www.darkenergysurvey.org
[4] http://www.lsst.org
[5] http://sci.esa.int/euclid
[6] http://wfirst.gsfc.nasa.gov

of noise, pixelisation, atmospheric distortion, and instrumental effects. These can be significantly larger than the shear signal itself. Even with perfect characterisation of these effects, biases can arise from e.g. imperfect knowledge of the intrinsic galaxy ellipticity distribution or morphology (see e.g. Jarvis et al. (2015)). (ii) To make useful cosmological inferences based on shear data one also needs accurate redshift information, but it is observationally infeasible to obtain spectroscopic redshifts for the large number of source galaxies. Instead one must rely on photometric redshift estimates (photo-$z$s), which are based on models of galaxy spectra, or spectroscopic training sets that may not be fully representative, and can therefore also suffer from biases (see e.g. Ma et al. (2006); Bridle & King (2007); Bernstein (2009); MacDonald & Bernstein (2010); Dahlen et al. (2013)). (iii) The cosmological lensing signal must be disentangled from intrinsic alignments (IAs). Systematic shape correlations can arise from tidal interactions between physically nearby galaxies during formation (Djorgovski 1987; Catelan et al. 2001; Crittenden et al. 2001). Even excluding such pairs of objects, correlations between the intrinsic shapes of foreground galaxies and the shear of background galaxies can contaminate the cosmic shear signal. For recent reviews of the field see Kirk et al. (2015), Joachimi et al. (2015) and Troxel & Ishak (2015). (iv) The density fluctuations in the matter distribution must be predicted with sufficient precision to allow interpretation of the data. On small scales this is sensitive to uncertain effects of baryonic feedback on the underlying matter, which are not yet fully understood from hydrodynamic simulations. Ignoring these effects can induce significant bias in estimates of cosmological parameters (van Daalen et al. 2011; Semboloni et al. 2011; Harnois-Déraps et al. 2015). For this reason cosmic shear studies commonly exclude the small scales where baryonic effects are expected to be strongest.

In this chapter I present the first cosmological constraints from the Dark Energy Survey, using the Science Verification data. A detailed description of the methods and tests of galaxy shape measurements is given in Jarvis et al. (2015)

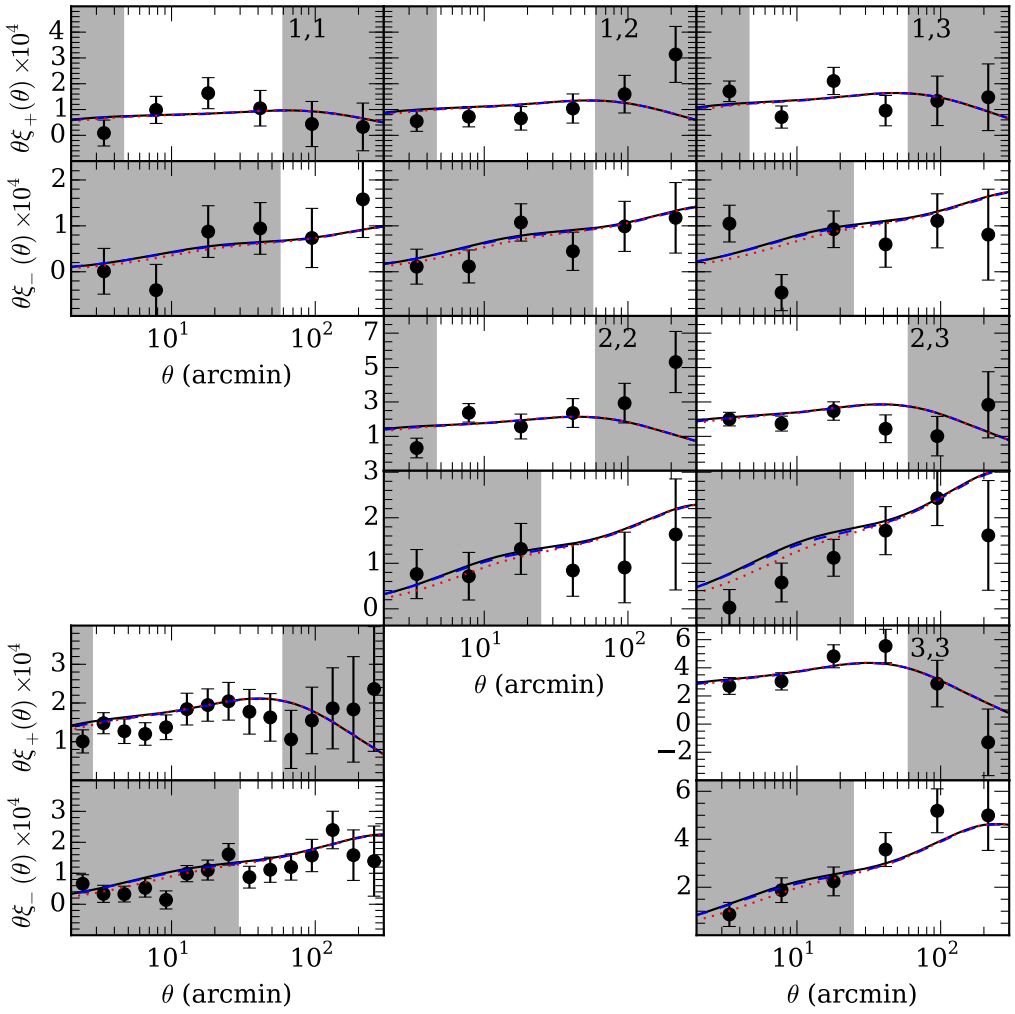


Figure 4.1: DES SV shear two-point correlation function $\xi_{+/-}$ measurements in each of the redshift bin pairings (from Becker et al. 2015a). The 3 redshift bins' ranges are $0.3 < z < 0.55$, $0.55 < z < 0.83$ and $0.83 < z < 1.3$, and each galaxy is assigned to a redshift bin according to the mean of its photometric redshift probability distribution (or excluded if this value is outside the above ranges). Alternating rows are $\xi_+$ and $\xi_-$, and the redshift bin combination is labelled in the upper right corner of each panel. The non-tomographic measurement is in the bottom left corner. The solid lines show the correlation functions computed for the best-fit *Planck* 2015 (TT + lowP) base $\Lambda$CDM cosmology, using HALOFIT (Smith et al. 2003; Takahashi et al. 2012) to model the non-linear matter power spectrum. The blue dashed lines (mostly obscured by the black lines) and red dotted lines assume the same cosmology but model nonlinear scales using FrankenEmu (Heitmann et al. 2014) (extended at high $k$ using the 'CEp' presciption from Harnois-Déraps et al. (2015)) and a prescription based on the OWLS 'AGN' simulation (Schaye et al. 2010) respectively. Points lying in grey regions are excluded from the analysis because they may be affected by either small-scale matter power spectrum uncertainty or large-scale additive shear bias, as explained in Section 4.4.2.

(hereafter J15); the photometric redshift measurements are described in Bonnett et al. (2015) (hereafter Bo15) and the cosmic shear two-point function estimates and covariances are described in Becker et al. (2015a) (hereafter Be15). I focus here on cosmological constraints and their robustness to systematic effects and choice of data, as quantified in the companion papers. I describe the data in Section 4.2 and present the main results in Section 4.3. In Section 4.4 I discuss the impact of the choice of scales and two point statistic and investigate the robustness of my main results to assumptions about systematics in Section 4.5. Finally, I combine and compare these constraints with those from other surveys in Section 4.6 and conclude in Section 4.7. More details on the intrinsic alignment models are given in Appendix 4.A.

## 4.2 DES SV Data

In this Section I overview some of the earlier work that provides essential ingredients for the cosmology analysis presented here.

### 4.2.1 The survey

The Dark Energy Survey (DES) is undertaking a five year programme of observations to image ∼5000 square degrees of the southern sky to ∼ 24th magnitude in the $grizY$ bands spanning 0.40-1.06 $\mu$m using the 570 megapixel imager DECam (Flaugher et al. 2015). The survey will consist of ∼10 interlaced passes of 90 s exposures in each of $griz$ and 45 s in $Y$ over the full area. The first weak lensing measurements from DES, using early commissioning data, were presented in Melchior et al. (2015). Science Verification data were taken between November 2012 and February 2013, including a contiguous region in the South Pole Telescope East (SPTE) field, of which I use the 139 square degrees presented in J15. A mass map of this field was presented in Vikram et al. (2015) and Chang et al. (2015). Significant improvements in instrument performance and image analysis

techniques have been made during and since the Science Verification period, so that one can expect the DES lensing results to exceed those presented here in quality as well as quantity.

### 4.2.2 Shear catalogues

The galaxy shape catalogue is discussed in detail in J15, and is produced using two independent shear pipelines, NGMIX (Sheldon 2014) and IM3SHAPE (Zuntz et al. 2013). Both shape measurement codes are based on model fitting techniques. Each object is fitted simultaneously to multiple reduced single epoch images. In addition to the intrinsic galaxy shape, the point spread function (PSF) and pixelisation are included in the model. The PSF is estimated separately on each exposure using the PSFEx package (Bertin 2011). The software measures the distortion kernel directly using bright stars. It then uses polynomial interpolation across the image plane to estimate the PSF at specific galaxy locations. J15 carried out an extensive set of tests of the shear measurements and found them to be sufficiently free of systematics for the analysis presented here, provided that a small multiplicative uncertainty on the ellipticities is introduced.

The raw number densities of the catalogues are 4.2 and 6.9 galaxies per square arcminute for IM3SHAPE and NGMIX respectively; weighted by signal-to-noise to get an effective number density one obtains 3.7 and 5.7 per square arcminute respectively[7]. The fiducial catalogue is NGMIX; in Section 4.5.1 I show the results using IM3SHAPE and the results ignoring the multiplicative bias uncertainty.

#### Blinding

To avoid experimenter bias the ellipticities that went into the 2-point functions used in this analysis were blinded by a constant scaling factor (between 0.9 and 1); this moved the contours in the $(\Omega_{\rm m}, \sigma_8)$ plane. Almost all adjustments to the

[7]The definition of effective density used here differs from previous definitions in the literature; see J15.

analysis were completed before the blinding factor was removed, so any tendency to tune the results to match previous data or theory expectations was negated. After unblinding, some changes were made to the analysis: the maximum angular scale used for $\xi_+$ was changed from 30 to 60 arcmin as a result of an improvement in the additive systematics detailed in J15. In particular, the shear difference correlation test in 8.6.2 of J15 significantly improved on large scales once a selection bias due to matching the two shear catalogs was accounted for. Additionally, a bug fix was applied to the weights in the IM3SHAPE catalogue.

### 4.2.3 Shear two-point function estimates

The first measurement of cosmic shear in DES SV is presented in Be15. The primary two-point estimators used in that paper are the real-space angular shear correlation functions $\xi_{+/-}$, defined as $\xi_{+/-}(\theta) = \langle\gamma_t\gamma_t\rangle(\theta) \pm \langle\gamma_\times\gamma_\times\rangle(\theta)$, where the angular brackets denote averaging over galaxy pairs separated by angle $\theta$ and $\gamma_{t,\times}$ are the tangential and cross shear components, measured relative to the separation vector. Our fiducial data vector, the real-space angular correlation functions measured in three tomographic bins, is shown in Figure 4.1. The redshift bins used span: (1) $0.3 < z < 0.55$, (2) $0.55 < z < 0.83$, and (3) $0.83 < z < 1.30$.

Be15 carry out a suite of systematics tests at the two-point level using $\xi_{+/-}$ estimates and find the shear measurements suitable for the analysis described in this paper. They also calculate PolSpice (Szapudi et al. 2000) pseudo-$C_\ell$ estimates of the convergence power spectrum and Fourier band power estimates derived from linear combinations of $\xi_{+/-}$ values (Becker & Rozo 2014). In Section 4.4.1 I compare cosmology constraints using my fiducial estimators, $\xi_{+/-}$, to constraints using these.

Be15 estimate covariances of the two-point functions using both 126 simulated mock surveys and the halo model. The halo model covariance was computed from the COSMOLIKE covariance module (Eifler et al. 2014). It neglects the exact sur-

vey mask by assuming a simple symmetric geometry, but unlike the mock covariance it does not suffer from statistical uncertainties due to the estimation process. The 126 simulated mock surveys were generated from 21 large N-body simulations and hence include halo-sample variance, and the correct survey geometry. Taylor et al. (2013) and Dodelson & Schneider (2013) explore the implications on parameter constraints of noise in the covariance matrix estimate due to having a finite number of independent simulated surveys. The fiducial data vector used in this analysis has 36 data points, hence one can expect the reported parameter errorbars to be accurate to $\sim 18\%$ (see Be15). Be15 use a Fisher matrix analysis to compare the errorbar on $\sigma_8(\Omega_\mathrm{m}/0.3)^{0.5}$ from the two covariance estimates, and find agreement within the noise expected from the finite number of simulations, with a larger errorbar when using the mock covariance. I believe the analytic halo model approach is a very promising one, which, with further validation (for example investigating the effect of not including the exact survey geometry), has the potential to relax the requirement of producing thousands of mock surveys for future, larger weak lensing datasets. For this study, I believe that the mock covariance, although noisy, is the more reliable and conservative option. I apply the correction factor to the inverse covariance described in Hartlap et al. (2007).

The analysis in this paper neglects the cosmology dependence of the covariance, which as outlined in Eifler et al. (2009), can substantially impact parameter constraints, depending on the depth and size of the survey. K13 find this effect to be small for CFHTLenS and since our data is shallower, I am confident that the cosmology-independent noise terms dominate our statistical error budget. However, I note that in regions of cosmological parameter space far from the fiducial cosmology assumed for the covariance i.e. in the extremes of the 'banana' in e.g. Figure 4.2, the reported uncertainties will be less reliable.

### 4.2.4 Photometric redshift estimates

The photometric redshifts used in this work are described in Bo15. They compare four methods: Skynet (Graff et al. 2014; Bonnett 2015), TPZ (Carrasco Kind & Brunner 2013), ANNz2 (Sadeh et al. 2015) and BPZ (Benítez 2000). These methods performed well amongst a more extensive list of methods tested in Sánchez et al. (2014). The first three are machine learning methods and are trained on a range of spectroscopic data; the fourth is a template-fitting method, empirically calibrated relative to simulation results from Chang et al. (2014) and Leistedt et al. (2015). The validation details are described in Bo15, including a suite of tests of the performance of these codes with respect to spectroscopic samples, simulation results, COSMOS photo-$z$s (Ilbert et al. 2009), and relative to each other. They conclude that the photometric redshift estimates of the $n(z)$ of the source galaxies are accurate to within an overall additive shift of the mean redshift of the $n(z)$ with an uncertainty of 0.05. The fiducial photometric redshift method is chosen to be Skynet, as it performed best in tests, but in Section 4.5.2 I show the impact of switching to the other methods.

## 4.3 Fiducial cosmological constraints

In this Section I present the headline DES SV cosmology results from the fiducial data vector, marginalising over a fiducial set of systematics and cosmology parameters. In the later sections I examine the robustness of the results to various changes of the data vector and modelling of systematics.

I evaluate the likelihood of the data from the two-point estimates and covariances presented in Be15 and the corresponding theoretical predictions, described in Section 4.4.1 assuming that the estimates are drawn from a multi-variate Gaussian distribution. Key results for this paper have been calculated with two separate pipelines: the CosmoSIS[8] (Zuntz et al. 2015) and CosmoLike (Eifler

[8] `https://bitbucket.org/joezuntz/cosmosis`

et al. 2014) frameworks. The constraints from these independent pipelines agree extremely well and thus are not shown separately. CosmoLike uses the Eisenstein & Hu (1998) prescription for the linear matter power spectrum $P_\delta(k, z)$, and CosmoSIS uses Camb (Lewis et al. 2000). For a vanilla ΛCDM cosmology ($\Omega_\mathrm{m} = 0.3$, $\sigma_8 = 0.8$, $n_s = 0.96$, $h = 0.7$), I find theory predictions using Camb and Eisenstein & Hu (1998) differ by at most 1% for the scales and redshifts I use. For the increased statistical power of future datasets, differences of this order will not be acceptable.

The fiducial data vector is the real-space shear–shear angular correlation function $\xi_\pm(\theta)$ measured in three redshift bins (hereafter bins 1, 2, 3, with ranges of $0.3 < z < 0.55$, $0.55 < z < 0.83$ and $0.83 < z < 1.3$, and galaxies assigned to bins according the mean of their photometric redshift probability distribution function) including cross-correlations, as shown in Figure 4.1. The data vector initially includes galaxy pairs with separations between 2 and 300 arcmin (although many of these pairs are excluded by the scale cuts described in Section 4.4.2). I focus mostly on placing constraints on the matter density of the Universe, $\Omega_\mathrm{m}$, and $\sigma_8$, defined as the rms mass density fluctuations in 8 Mpc/$h$ spheres at the present day, as predicted by linear theory.

I marginalise over wide flat priors $0.05 < \Omega_\mathrm{m} < 0.9$, $0.2 < \sigma_8 < 1.6$, $0.2 < h < 1$, $0.01 < \Omega_\mathrm{b} < 0.07$ and $0.7 < n_s < 1.3$, assuming a flat Universe, and thus I vary 5 cosmological parameters in total. The priors were chosen to be wider than the constraints in a variety of existing *Planck* chains. In practice the results are very similar to those with parameters other than $\Omega_\mathrm{m}$ and $\sigma_8$ fixed, due to the weak dependence of cosmic shear on the other parameters. Following Planck Collaboration et al. (2015a) I use a fixed neutrino mass of 0.06 eV.

I summarise our systematics treatments below:

**(i) Shear calibration:** For each redshift bin, I marginalise over a single free parameter to account for shear measurement uncertainties: the predicted data vector is modified to account for a potential unaccounted multiplicative bias as

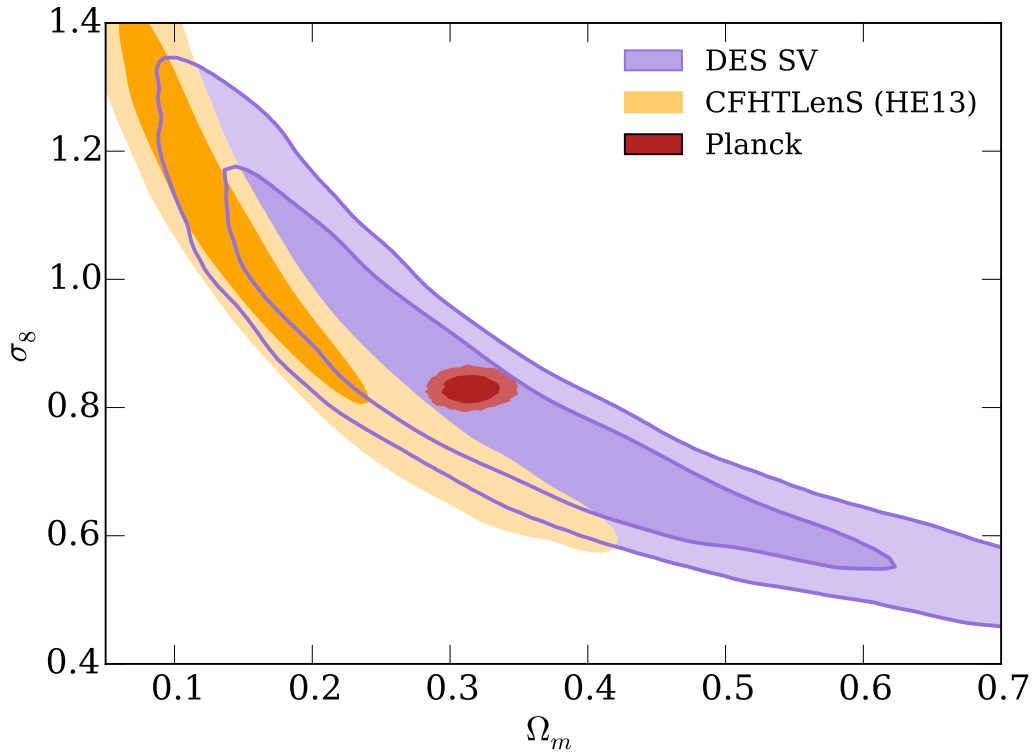


Figure 4.2: Constraints on the amplitude of fluctuations $\sigma_8$ and the matter density $\Omega_\mathrm{m}$ from DES SV cosmic shear (purple filled/outlined contours) compared with constraints from *Planck* (red filled contours) and CFHTLenS (orange filled, using the correlation functions and covariances presented in Heymans et al. (2013), and the 'original conservative scale cuts' described in Section 4.6.1). DES SV and CFHTLenS are marginalised over the same astrophysical systematics parameters and DES SV is additionally marginalised over uncertainties in photometric redshifts and shear calibration. *Planck* is marginalised over the 6 parameters of ΛCDM(the 5 I vary in our fiducial analysis plus $\tau$). The DES SV and CFHTLenS constraints are marginalised over wide flat priors on $n_s$, $\Omega_\mathrm{b}$ and $h$ (see text), assuming a flat universe. For each dataset, I show contours which encapsulate 68% and 95% of the probability, as is the case for subsequent contour plots.

$\xi^{ij} \rightarrow (1+m_i)(1+m_j)\xi^{ij}$. I place a separate Gaussian prior on each of the three $m_i$ parameters. Each is centered on 0 and of width 0.05, as advocated by J15. See Section 4.5.1 for more details.

**(ii) Photometric redshift calibration:** Similarly, I marginalise over one free parameter per redshift bin to describe photometric redshift calibration uncertainties. I allow for an independent shift of the estimated photometric redshift

distribution $n_i(z)$ in redshift bin $i$ i.e. $n_i(z) \rightarrow n_i(z - \delta z_i)$. I use independent Gaussian priors on each of the three $\delta z_i$ values of width 0.05 as recommended by Bo15. See Section 4.5.2 for more details.

**(iii) Intrinsic alignments:** I assume an unknown amplitude of the intrinsic alignment signal and marginalise over this single parameter, assuming the non-linear alignment model of Bridle & King (2007). See Section 4.5.3 for more details and tests on the sensitivity of the results to intrinsic alignment model choice.

**(iv) Matter power spectrum:** I use HALOFIT (Smith et al. 2003), with updates from Takahashi et al. (2012) to model the non-linear matter power spectrum, and refer to this prescription simply as 'HALOFIT' henceforth. The range of scales for the fiducial data vector is chosen to reduce the bias from theoretical uncertainties in the non-linear matter power spectrum to a level which is not significant given the statistical uncertainties (see Sections 4.4.2 and 4.5.4, and Table 4.2 for the minimum angular scale for each bin combination).

I thus marginalise over $3 + 3 + 1 = 7$ nuisance parameters characterising potential biases in the shear calibration, photometric redshift estimates and intrinsic alignments respectively.

Figure 4.2 shows the main DES SV cosmological constraints in the $\Omega_{\rm m} - \sigma_8$ plane, from the fiducial data vector and systematics treatment, compared to those from CFHTLenS and *Planck*. For the CFHTLenS constraints, I use the same six redshift bin data vector and covariance as H13, but apply the conservative cuts to small scales used as a consistency test in that work (for $\xi_+$ I exclude angles $< 3'$ for redshift bin combinations involving the lowest two redshift bins, and for $\xi_-$, I exclude angles $< 30'$ for bin combinations involving the lowest four redshift bins, and angles $< 16'$ for bin combinations involving the highest two redshift bins). In this plane, DES SV results are midway between the two datasets and are compatible with both. I discuss this further in Section 4.6.1.

Using the MCMC chains generated for Figure 4.2 I find the best fit power law $\sigma_8(\Omega_{\rm m}/0.3)^{\alpha}$ to describe the degeneracy direction in the $(\Omega_{\rm m}, \sigma_8)$ plane (I

| Model | $S_8 \equiv \sigma_8(\Omega_m/0.3)^{0.5}$ | Mean Error | |
|---|---|---|---|
| *Primary Results* | | | |
| Fiducial DES SV cosmic shear | $0.812^{+0.059}_{-0.060}$ | 0.059 | 0. |
| No photoz or shear systematics | $0.809^{+0.051}_{-0.040}$ | 0.046 | 0. |
| No systematics | $0.775^{+0.045}_{-0.041}$ | 0.043 | 0. |
| *Data Vector Choice* | | | |
| No tomography | $0.726^{+0.117}_{-0.137}$ | 0.127 | 0. |
| No tomography or systematics | $0.719^{+0.063}_{-0.053}$ | 0.058 | 0. |
| $\xi$-to-$C_\ell$ bandpowers, no tomo. or systematics | $0.744^{+0.075}_{-0.055}$ | 0.065 | 0. |
| PolSpice-$C_\ell$ bandpowers, no tomo. or systematics | $0.729^{+0.094}_{-0.058}$ | 0.076 | 0. |
| *Shape Measurement* | | | |
| Without shear bias marginalisation | $0.812^{+0.054}_{-0.054}$ | 0.054 | 0. |
| IM3SHAPE shears | $0.875^{+0.088}_{-0.075}$ | 0.082 | 0. |
| *Photometric Redshifts* | | | |
| Without photo-z bias marginalisation | $0.809^{+0.055}_{-0.054}$ | 0.054 | 0. |
| TPZ photo-zs | $0.814^{+0.059}_{-0.059}$ | 0.059 | 0. |
| ANNZ2 photo-zs | $0.827^{+0.060}_{-0.060}$ | 0.060 | 0. |
| BPZ photo-zs | $0.848^{+0.063}_{-0.064}$ | 0.063 | 0. |
| *Intrinsic Alignment Modelling* | | | |
| No IA modelling | $0.770^{+0.053}_{-0.053}$ | 0.053 | 0. |
| Linear alignment model | $0.799^{+0.063}_{-0.054}$ | 0.059 | 0. |
| Tidal alignment model | $0.810^{+0.061}_{-0.060}$ | 0.060 | 0. |
| Marginalised over redshift power law | $0.720^{+0.153}_{-0.153}$ | 0.153 | 0. |
| Marginalised over redshift power law with $A > 0$ | $0.808^{+0.058}_{-0.058}$ | 0.058 | 0. |
| *High-k power spectrum* | | | |
| Without small-scale cuts | $0.819^{+0.068}_{-0.062}$ | 0.065 | 0. |
| OWLS AGN $P(k)$ | $0.820^{+0.060}_{-0.061}$ | 0.061 | 0. |
| OWLS AGN $P(k)$ w/o small-scale cuts | $0.838^{+0.069}_{-0.059}$ | 0.064 | 0. |
| *Other lensing data* | | | |
| **CFHTLenS (H13) original conservative scales** | $0.710^{+0.040}_{-0.034}$ | 0.037 | 0. |
| CFHTLenS (H13) modified conservative scales | $0.692^{+0.044}_{-0.033}$ | 0.038 | 0. |
| CFHTLenS (H13) + DES SV | $0.744^{+0.035}_{-0.031}$ | 0.033 | 0. |
| CFHTLenS (K13) all scales | $0.738^{+0.055}_{-0.032}$ | 0.043 | 0. |
| CFHTLenS (K13) original conservative scales | $0.596^{+0.080}_{-0.073}$ | 0.077 | 0. |
| CFHTLenS (K13) modified conservative scales | $0.671^{+0.067}_{-0.061}$ | 0.064 | 0. |
| Planck Lensing | $0.820^{+0.100}_{-0.141}$ | 0.121 | 0. |
| *Planck 2015 Combination/Comparison* | | | |
| **Planck (TT+LowP)** | $0.850^{+0.024}_{-0.024}$ | 0.024 | −0 |
| Planck (TT+LowP)+DES SV | $0.848^{+0.022}_{-0.021}$ | 0.022 | −0 |
| Planck (TT+EE+TE+Low TT) | $0.861^{+0.020}_{-0.020}$ | 0.020 | 0. |
| Planck (TT+LowP+Lensing) | $0.825^{+0.017}_{-0.017}$ | 0.017 | 0. |
| Planck (TT+LowP+Lensing)+ext | $0.824^{+0.013}_{-0.013}$ | 0.013 | 0. |

Table 4.1: 68% confidence limits on $S_8 \equiv \sigma_8(\Omega_{\rm m}/0.3)^{0.5}$ in ΛCDM for various assumptions in the DES SV analysis, compared to CFHTLenS and *Planck* and combined with various datasets. In the first column the power law index from the fiducial case, 0.478, is rounded to 0.5 and used for all variants. The second column shows the symmetrised error bar on $S_8$ for ease of comparison between rows. In the third column I show the fitted power law index $\alpha$ for each variant, and in the final column I show the constraint

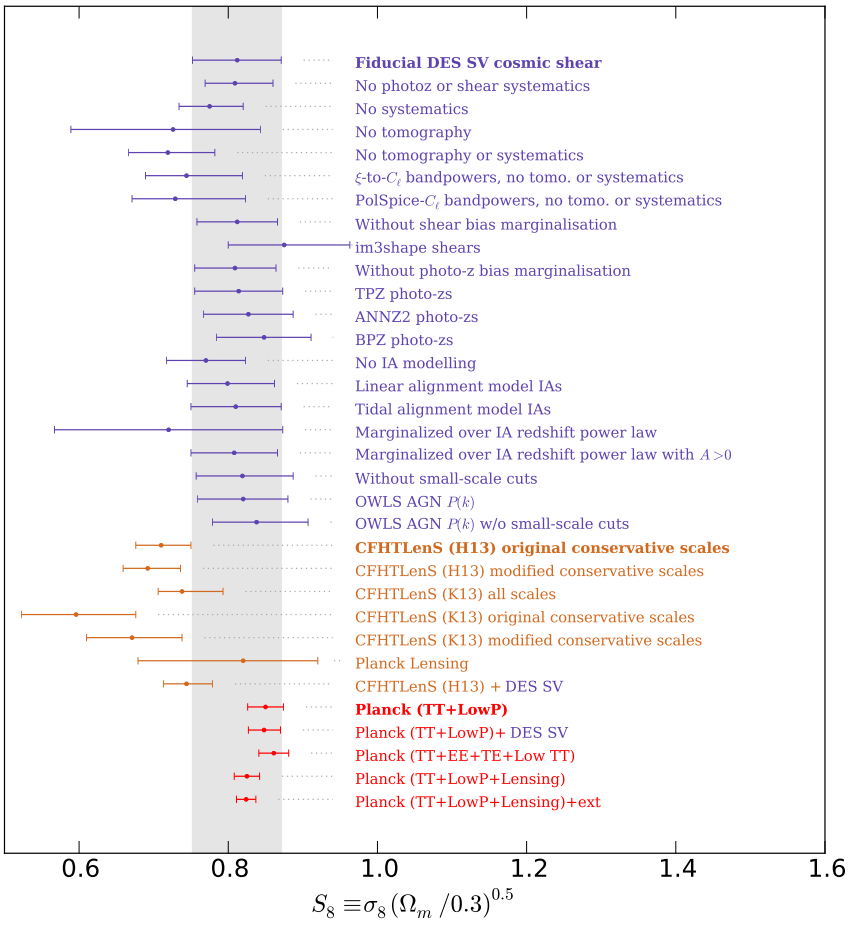


Figure 4.3: Graphical illustration of the 68% confidence limits on $S_8 \equiv \sigma_8(\Omega_\mathrm{m}/0.3)^{0.5}$ values given in Table 4.1, showing the robustness of our results (purple) and comparing with the CFHTLenS and *Planck* lensing results (orange) and *Planck* (red). The grey vertical band aligns with the fiducial constraints at the top of the plot. Note that *Planck* lensing in particular, and other non-DES lensing measurements optimally constrain a different quantity than shown above e.g. see the second and third columns of Table 4.1.

estimate $\alpha$ using the covariance of the samples in the chain in $\log\Omega_{\rm m} - \log\sigma_8$ space). I find $\alpha = 0.478$ and so use a fiducial value for $\alpha$ of 0.5 for the remainder of the paper [9]. I find a constraint perpendicular to the degeneracy direction of

$$S_8 \equiv \sigma_8(\Omega_{\rm m}/0.3)^{0.5} = 0.81 \pm 0.06 \quad (68\%). \tag{4.1}$$

Because of the strong degeneracy, the marginalised 1d constraints on either $\Omega_{\rm m}$ or $\sigma_8$ alone are weaker; I find $\Omega_{\rm m} = 0.36^{+0.09}_{-0.21}$ and $\sigma_8 = 0.81^{+0.16}_{-0.26}$. In Table 4.1 I also show other results which are discussed in the later sections, including variations of the DES SV analysis (see Sections 4.4.1 and 4.5) and combinations with CFHTLenS and *Planck* (see Section 4.6.1).

For comparison with other constraints I also investigated the impact of ignoring shear measurement and photometric redshift uncertainties and find that the central value of $S_8$ changes negligibly, and the error bar decreases by ∼20% (see Table 4.1 for details).

In Table 4.1 I also show results ignoring all systematics. This is the same as the "No photo-$z$ or shear systematics" case but additionally ignoring intrinsic alignments, so that only the other cosmological parameters are varied. The central value shifts down by 0.037 and the error bar is reduced by 27% compared to the fiducial case. Therefore the systematics contribute almost half (in quadrature) of the total error budget, and further effort will be needed to reduce systematic uncertainties if we are to realise a significant improvement in the constraints (from shear–shear correlations alone) with larger upcoming DES datasets.

[9] I would advise caution when using $S_8$ to characterise the DES SV constraints instead of a full likelihood analysis - $S_8$ is sensitive to the tails of the probability distribution, and also weakly depends on the priors used on the other cosmological parameters

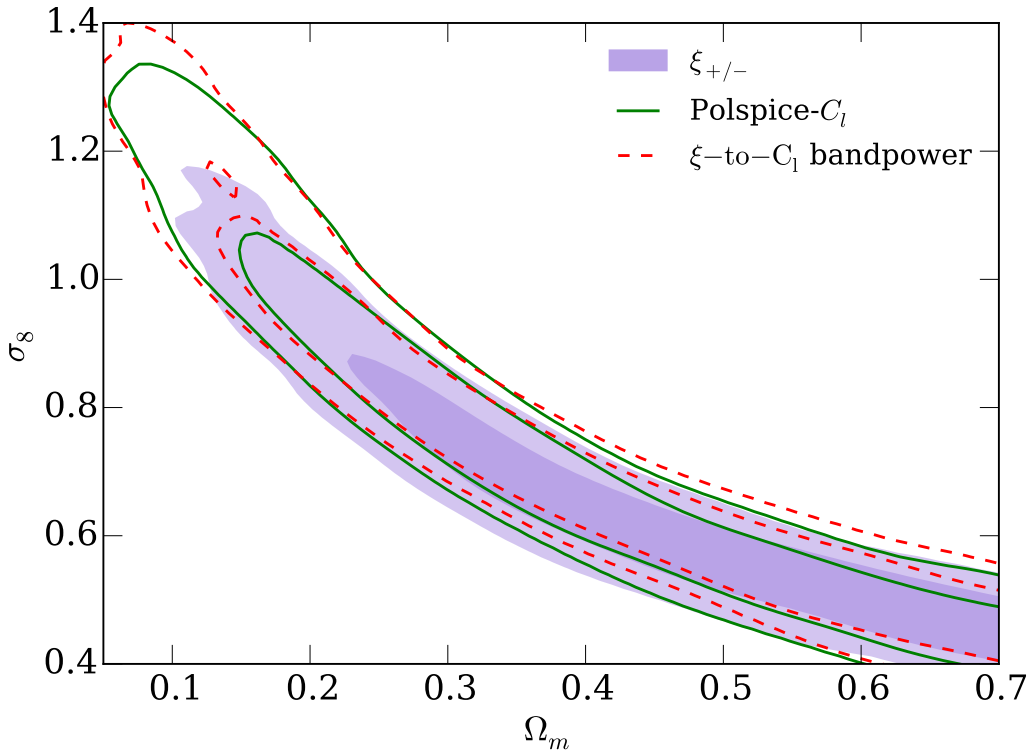


Figure 4.4: Comparison of constraints on $\sigma_8$ and $\Omega_\mathrm{m}$ for various choices of data vector: $\xi_\pm$ with no tomography or systematics (purple filled), $C_\ell^{ij}$ bandpowers (dashed red lines) and PolSpice-$C_\ell$ bandpowers (solid green lines) (both with no tomography or systematics). I do not show our fiducial constraints, or *Planck*, since I have not marginalised over systematics for the constraints shown here, so agreement is not necessary or meaningful (although Table 4.1 suggests there is reasonable agreement).

## 4.4 Choice of data vector and scales used

In this Section I consider the impact of the choice of two-point statistic on the cosmological constraints, and investigate how my fiducial estimators are affected by the choice of angular scales used.

### 4.4.1 Choice of two-point statistic

Be15 present results for a selection of two-point statistics – see that work, and references therein for more detailed description of the statistics and their estimators. For an overview of the theory presented here see Bartelmann & Schneider

(2001).

The statistics can all be described as weighted integrals over the weak lensing convergence power spectrum at angular wavenumber $\ell$, $C_\ell^{ij}$, of tomographic redshift bin $i$ and $j$, which can be related to the matter power spectrum, $P_\delta(k,z)$, by the Limber approximation

$$C_\ell^{ij} = \int_0^{\chi_{\rm h}} d\chi \frac{W_i(\chi)W_j(\chi)}{D_A^2(\chi)} P_\delta(k = l/D_A(\chi), \chi). \tag{4.2}$$

where $\chi$ is the comoving radial distance, $\chi_{\rm h}$ is the comoving distance of the horizon, and $D_A(\chi)$ the comoving angular diameter distance. I assume a flat universe ($D_A(\chi) = \chi$) hereafter. The lensing kernel $W_i$ is defined as an integral over the redshift distribution of source galaxies $n_i(\chi(z))$ in the $i^{\rm th}$ redshift bin:

$$W(\chi) = \int d\chi N(\chi_s) g(\chi, \chi_s) \tag{4.3}$$

where

$$g(\chi, \chi_s) = \begin{cases} \frac{3}{2} H_0^2 \Omega_m [1 + z(\chi)] D_A(\chi) \frac{D_A(\chi_s - \chi)}{D_A(\chi_s)} & \text{for } \chi < \chi_s \\ 0 \ \text{ otherwise.} \end{cases} \tag{4.4}$$

The fiducial statistics used here, the real space correlation functions, $\xi_{+/-}(\theta)$, are weighted integrals of the angular power spectra:

$$\xi_{+/-}^{ij}(\vartheta) = \frac{1}{2\pi} \int {\rm d}\ell \, \ell \, J_{0/4}(\ell\vartheta) \, C_\ell^{ij} \, , \tag{4.5}$$

where $J_{0/4}$ is the Bessel function of either $0^{\rm th}$ or $4^{\rm th}$ order. $\xi_{+/-}$ have the advantage of being straightforward to estimate from the data, whereas the $C_\ell^{ij}$s require more processing but are a step closer to the theoretical predictions. An advantage of using $C_\ell^{ij}$ is that the signal is split into two parts, E- and B-modes, the latter of which is expected to be very small for cosmic shear. The cosmic shear signal is

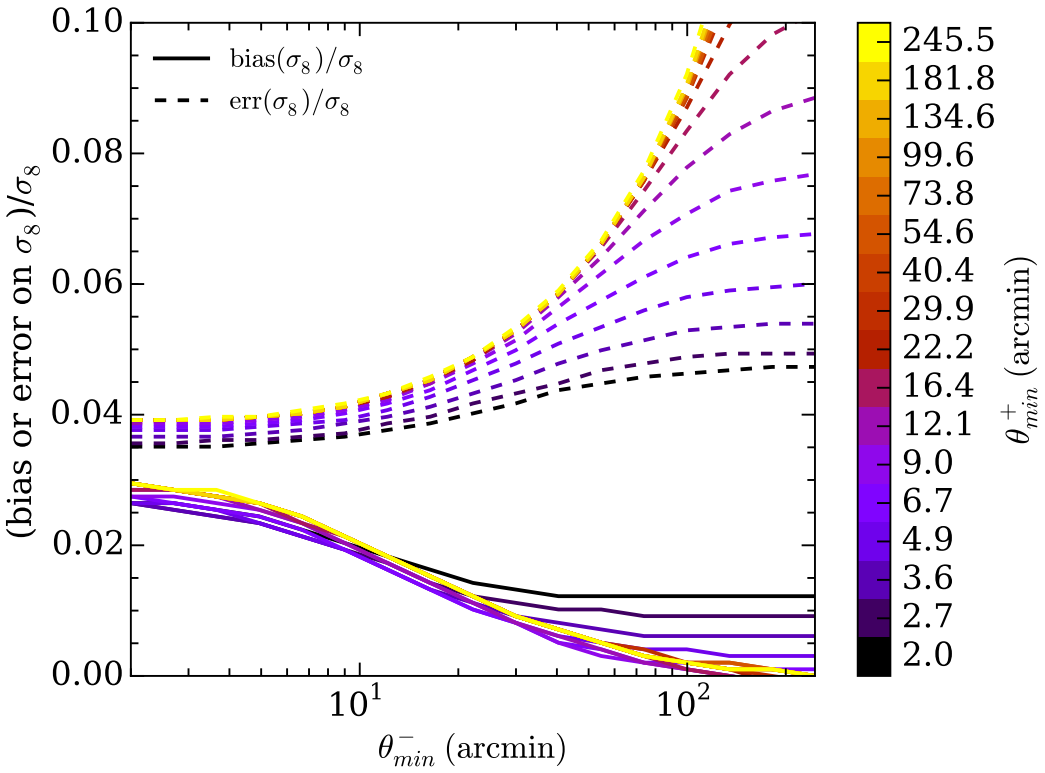


Figure 4.5: The fractional bias on $\sigma_8$ due to ignoring an OWLS AGN baryon model (solid lines) compared to the statistical uncertainty on $\sigma_8$ (dashed lines), as a function of minimum scale used for $\xi_-$ ($\theta^-_{\rm min}$, x-axis) or $\xi_+$ ($\theta^+_{\rm min}$, colours). Whereas the statistical error is minimised by using small scales, the bias is significant for $\theta^-_{\rm min} < 30'$ and $\theta^+_{\rm min} < 3'$.

concentrated in the E-mode because to first order the shear signal is the gradient of a scalar field. The B-mode can therefore be used as a test of systematics as discussed in J15 and Be15.

Be15 also implement the method of Becker & Rozo (2014) which uses linear combinations of $\xi_{+/-}(\theta)$ to estimate fourier space bandpowers of $C^{ij}_\ell$. Also presented are PolSpice (Szapudi et al. 2000) estimates of the $C^{ij}_\ell$s from pixelised shear maps using the pseudo-$C_\ell$ estimation process, which corrects the spherical harmonic transform values for the effect of the survey mask (see Hikage et al. 2011 for the first implementation for cosmic shear). For simplicity I do not perform a tomographic analysis using these estimators. To compare cosmological con-

straints with these different estimators I do not marginalise over any systematics, to enable a more conservative comparison between them. (Note that marginalising over intrinsic alignments inflates the errors of non-tomographic analyses as described in Section 4.5.3). Figure 4.4 shows constraints from the different estimators, and the three are in good agreement. A more detailed comparison can be made using the numbers in Table 4.1, which are shown graphically in Figure 4.3. The relevant lines for comparison are the "No tomography or systematics" line which uses the fiducial $\xi_{+/-}$ data vector, and the two $C_\ell$ bandpower lines. The uncertainties are similar between these methods and the $C_\ell$ constraints are qualitatively consistent with constraints based on the $\xi_{+/-}$ approach. Although I find the qualitative agreement between the constraints from the different estimators encouraging, I note that testing on survey simulations would be required to make a quantitative statement about the level of agreement.

### 4.4.2 Choice of scales

All the two-point statistics discussed thus far involve a mixing of physical scales: it is clear from Eq. 4.5 that $\xi_{+/-}$ at a given real space angular scale uses information from a range of angular wavenumbers $\ell$, while $C_\ell$ itself uses information from a range of physical scales $k$ in the matter power spectrum $P_\delta(k, z)$. In Section 4.5.4 I discuss some of the difficulties in producing an accurate theoretical estimate of $P_\delta(k, z)$ for high $k$ (small physical scales). In this work, I aim to null the effects of this theoretical uncertainty by cutting small angular scales from the data vector, since using scales where the theoretical prediction is inaccurate can bias the derived cosmological constraints, mostly due to unknown baryonic effects on clustering.

Figure 4.5 demonstrates the impact of errors in the matter power spectrum prediction on estimates of $\sigma_8$ from a non-tomographic analysis. In this figure I estimate the potential bias on $\sigma_8$ as that which would arise from ignoring the

presence of baryonic effects; as a specific model for these effects I use the OWLS AGN simulation (Schaye et al. 2010). See Section 4.5.4 for more details, in particular Eq. 4.9 for the implementation of the AGN model. For a given angular scale $\xi_-$ is more affected than $\xi_+$: for example the fractional bias when using all scales in $\xi_-$, but none in $\xi_+$ ($\theta^-_{\rm min} = 2', \theta^+_{\rm min} = 245.5'$) is $\approx 0.03$ whereas the bias when using all scales in $\xi_+$, but none in $\xi_-$ ($\theta^+_{\rm min} = 2', \theta^-_{\rm min} = 245.5$) is $\approx 0.015$. For the non-tomographic case, I use a minimum angular scale of 3 arcminutes for $\xi_+$, and 30 arcminutes for $\xi_-$, because on these angular scales the bias is $< 25\%$ of the statistical uncertainty on $\sigma_8$ (with no other parameters marginalised).

For the tomographic case, I now need to choose a minimum scale for $\xi_+$ and $\xi_-$ for each of the redshift bin combinations - i.e. 12 parameters. Hence a procedure analagous to that based on Figure 5 is non-trivial. I instead use a more general (but probably non-optimal) prescription in which I cut angular bins that change significantly when I change the model for the non-linear matter power spectrum. I remove data points where the theoretical prediction changes by more than 5% when the nonlinear matter power spectrum is switched from the fiducial to either that predicted from the FrankenEmu[10] code (based on the Coyote Universe Simulations described in Heitmann et al. (2014), and extended at high $k$ using the 'CEp' prescription from Harnois-Déraps et al. (2015)), or to the OWLS AGN model (the baryonic model used in Figure 5). I believe 5% is a reasonable (but again, probably not optimal) choice, since on these nonlinear scales, the signal is proportional to $\sigma_8^3$, so a 5% prediction error would result in a $\sigma_8$ error of order 0.05/3 i.e. well below the statistical uncertainties. The inferred biases for the non-tomographic $\xi_{+/-}$ shown in Figure 4.5 suggest similar angular cuts. The results of these cuts are summarised in Table 4.2. I demonstrate the effectiveness of these cuts in producing robust constraints, and discuss other methods of dealing with non-linear scales in Section 4.5.4.

I limit the large scales in $\xi_+$ to $< 60$ arcmin, since the large scales in $\xi_+$

[10]http://www.hep.anl.gov/cosmology/CosmicEmu/emu.html

| Redshift bin combination | $\theta_{min}(\xi_+)$ | $\theta_{min}(\xi_-)$ |
|---|---|---|
| (1,1) | 4.6 | 56.5 |
| (1,2) | 4.6 | 56.5 |
| (1,3) | 4.6 | 24.5 |
| (2,2) | 4.6 | 24.5 |
| (2,3) | 2.0 | 24.5 |
| (3,3) | 2.0 | 24.5 |

Table 4.2: Scale cuts for tomographic shear two-point functions $\xi_{+/-}$ using the prescription described in the text.

are highly correlated, and I have verified that little is gained in signal-to-noise by including larger scales. Furthermore, including these larger scales would also increase the number of data points, increasing the noise in the covariance matrix, and degrading the parameter constraints.

## 4.5 Robustness to systematics

I now examine the robustness of the fiducial constraints to assumptions made about the main systematic uncertainties for cosmic shear. In each subsection I consider the impact of ignoring the systematic in question, and examine alternative prescriptions for the input data or modelling.

### 4.5.1 Shear calibration

The measurement of galaxy shapes at the accuracy required for cosmic shear is a notoriously hard problem. The raw shapes in the two catalogues are explicitly corrected for known sources of systematic bias. This involves either calibration using image simulations in the case of IM3SHAPE or sensitivity corrections in the case of NGMIX (see J15). They rely on a number of assumptions and one cannot be completely certain the final catalogues carry no residual bias. It is therefore important that the model includes the possibility of error in our shape measurements. As in Jee et al. (2013) I marginalise over shear measurement

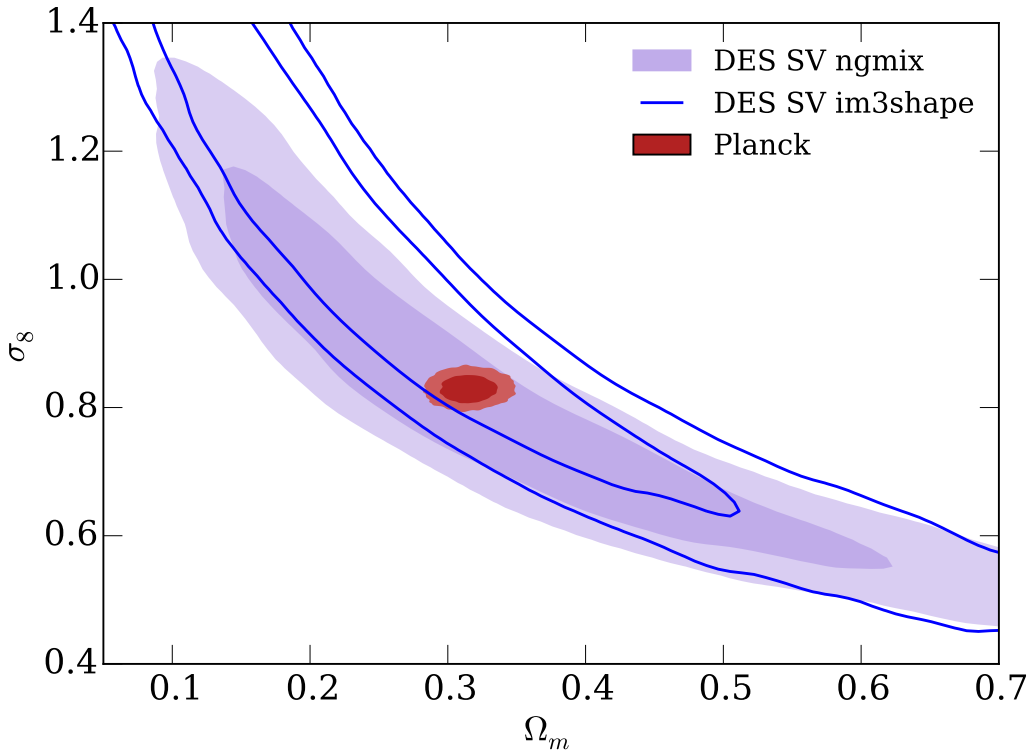


Figure 4.6: Robustness to assumptions about shear measurement. Shaded purple (fiducial case): NGMIX, with one shear multiplicative bias parameter m for each of the 3 tomographic redshift bins, with an independent Gaussian prior on each $m_i$ with $\sigma = 0.05$. Solid blue lines: IM3SHAPE with the same assumptions. *Planck* is shown in red.

uncertainties in parameter estimation.

J15 estimate the systematic uncertainty on the shear calibration by comparing the two shape measurement codes to image simulations, and to each other. Following that discussion I include a multiplicative uncertainty which is independent in each of the three redshift bins. I thus introduce three free parameters $m_i$ ($i = 1, 2, 3$). The predicted data are transformed as

$$\xi^{i,j}_{\pm\mathrm{pred}} = (1 + m_i)(1 + m_j)\xi^{i,j}_{\pm\mathrm{true}} \tag{4.6}$$

for redshift bins $i, j$.

As discussed in J15, I use a Gaussian prior on the $m_i$ parameters of width

0.05, compared to a 0.06 uniform prior used by Jee et al. (2013). I note that since the $m_i$ are independent, the effective prior on the mean multiplicative bias for the whole sample is less than 0.05. No systematic shear calibration uncertainties were propagated by CFHTLenS in H13 or earlier work (although K13 did investigate the statistical uncertainty on the shear calibration arising from having a limited calibration sample). If I neglect this uncertainty and assume that the shape measurement has no errors (fixing $m_i = 0$) then the uncertainty on $S_8$ is reduced by 9% and the central value is unchanged (see the "Without shear bias marginalisation" row in Table 4.1 and Figure 4.3 for more details).

Figure 4.6 shows the result of interchanging the two shear measurement codes, swapping NGMIX (fiducial) to IM3SHAPE. The IM3SHAPE constraints are weaker, because the shapes are measured from a single imaging band (r-band) instead of simultaneously fitting to three bands (r, i, z) as in NGMIX, and IM3SHAPE retains fewer galaxies after quality cuts (in particular the IM3SHAPE catalogue contains around half as many galaxies as NGMIX in the highest redshift bin). The preferred value of $S_8$ is shifted about $1\sigma$ higher for IM3SHAPE than NGMIX and the error bar is increased by 38% (see the "IM3SHAPE shears" row in Table 4.1 and Figure 4.3). While one does not expect the constraints from the two shear codes to be identical, since they come from different data selections, the two codes do share many of the same galaxies, and of course probe a common volume. I estimate the significance of the shift using the mock DES SV simulations detailed in Be15. Carefully taking into account the overlapping galaxy samples, correlated shape noise and photon noise, and of course the common area, I create an NGMIX and an IM3SHAPE realisation of the signal for each mock survey. I then compute the difference in the best-fit $\sigma_8$s (keeping all other parameters fixed to fiducial values for computational reasons) for the two signals, and compute the standard deviation of this difference over the 126 mock realisations. I find this difference has a standard deviation of 0.028, compared with the difference in this statistic (the best-fit $\sigma_8$ with all other parameters fixed) on the data of 0.046. I conclude

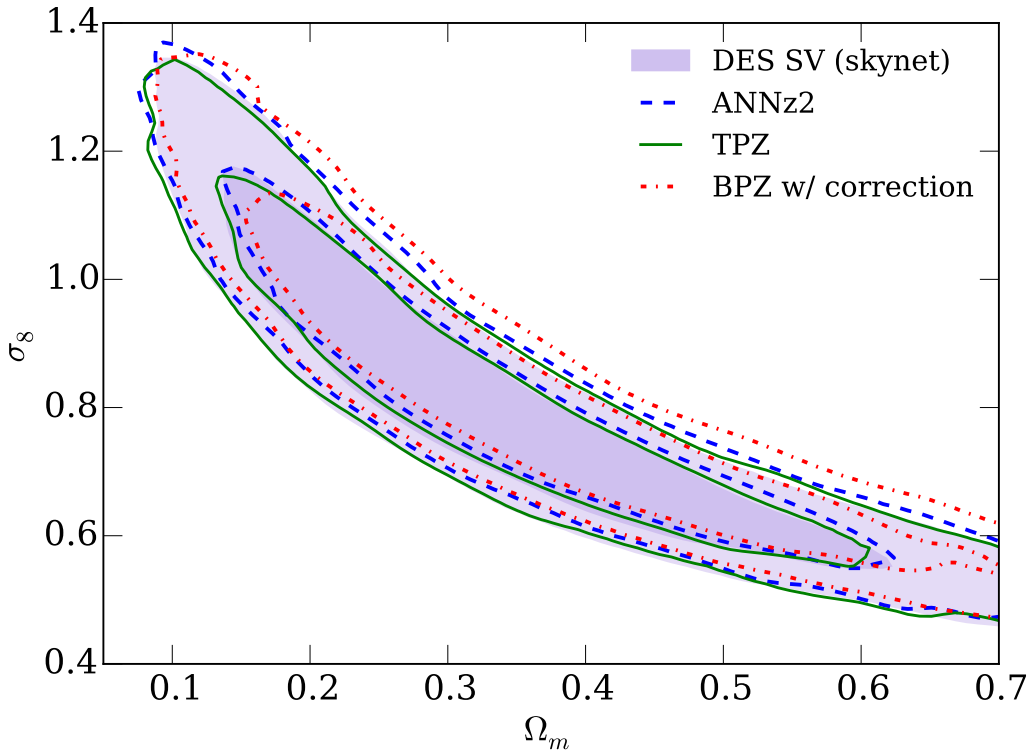


Figure 4.7: Results using different photo-$z$ codes. Purple filled contours: fiducial case (SkyNet). Blue dashed lines: ANNz2. Green solid lines: TPZ. Red dash-dotted lines: BPZ w/ correction.

that although this shift is not particularly significant, it could be an indication of shape measurement biases in either catalogue. The decreased statistical errors of future DES analyses will provide more stringent tests on shear code consistency.

### 4.5.2 Photometric redshift biases

In this subsection I investigate the robustness of the constraints to errors in the photometric redshifts. As motivated by Bo15, for the fiducial model I marginalise with a Gaussian prior of width 0.05 over three independent photometric redshift calibration bias parameters $\delta z_i$ $(i = 1, 2, 3)$ where

$$n_i^{\rm pred}(z) = n_i^{\rm meas}(z - \delta z_i) \tag{4.7}$$

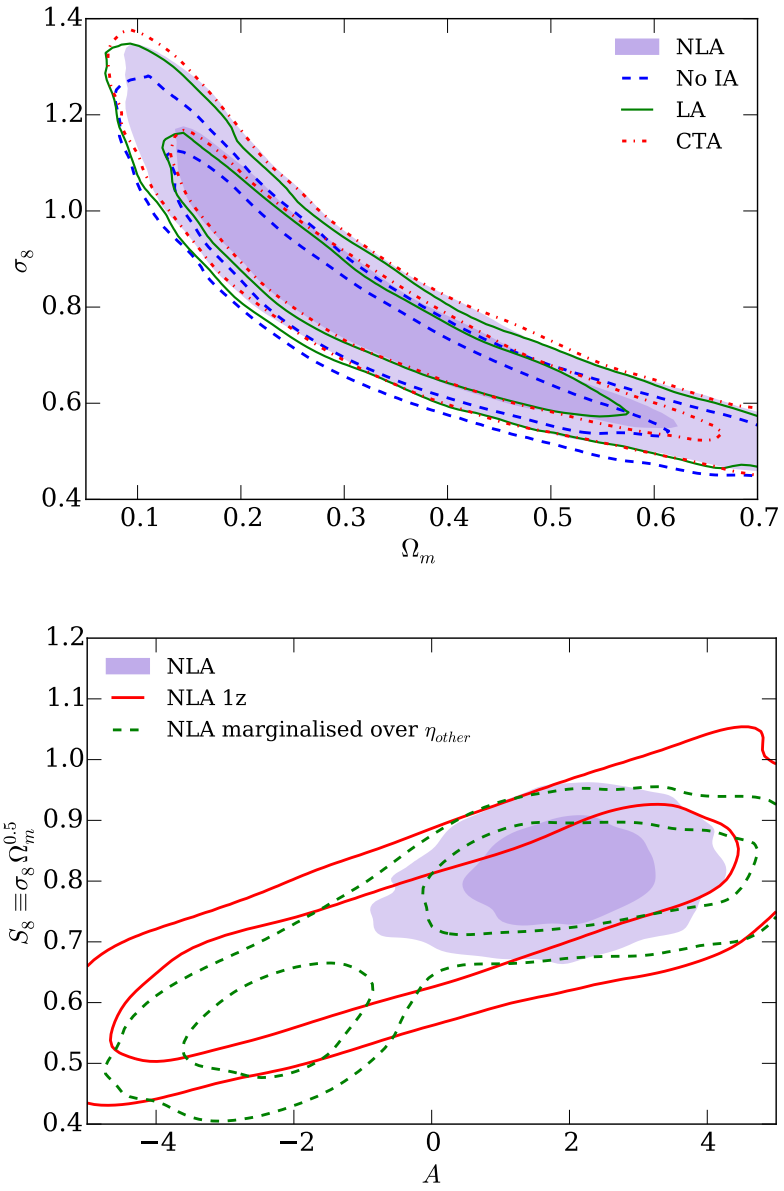


Figure 4.8: Top panel: Constraints on the clustering amplitude $\sigma_8$ and the matter density $\Omega_\mathrm{m}$ from DES SV alone. The purple shaded contour shows the constraints when our fiducial NLA model of intrinsic alignments is assumed, the green filled lines shows constraints when the LA model is used, the dot-dashed red lines the CTA model and the blue dashed lines shows constraints when IAs are ignored. Bottom panel: Constraints on $\sigma_8\Omega_\mathrm{m}^{0.5}$ and the intrinsic alignment amplitude $A$ from DES alone. The purple shaded contour shows the constraints when our fiducial NLA model of intrinsic alignments is assumed with three tomographic bins, the red lines shows constraints, again using our fiducial NLA model, but using only a single redshift bin and the green dashed contour shows our fiducial NLA model, with three tomographic bins, but marginalised over an additional power law in redshift, where the power law index is a free parameter. Note that the treatment of IAs in both panels assumes a prior range for the amplitude $A = [-5, 5]$.

for redshift bin $i$, where $n_i^{\rm meas}(z)$ is the measured photometric redshift probability distribution and $n_i^{\rm pred}(z)$ is the redshift distribution used in predicting the shear two-point functions (i.e. the model for the true $n_i(z)$ assuming the given $\delta z_i$). This model is discussed further in Bo15 where it is shown to be a reasonably good model for the uncertainties at the current level of accuracy required.

If I neglect photometric redshift calibration uncertainties then the error on $S_8$ is reduced by $\sim$10% and its value shifts down by $\sim$10% of the fiducial error bar (see the row labelled "Without photo-z bias marginalisation" in Table 4.1 and Figure 4.3).

In Figure 4.7 I show the impact of switching between the four photometric redshift estimation codes described in Bo15. There is excellent agreement between the codes, although as detailed in Bo15, the machine learning codes are not independent - Skynet, ANNZ2, TPZ are trained on the same spectroscopic data, while an empirical calibration is performed on the template fitting method BPZ using simulation results. As quantified in Table 4.1 and illustrated in Figure 4.3, the constraint on $S_8$ moved by less than two thirds of the error bar when switching between photometric redshift codes, with the biggest departure occurring for BPZ, which moves to higher $S_8$. A more detailed analysis and validation of the photo-zs using relevant weak lensing estimators and metrics is performed in Bo15 for galaxies in the shear catalogues.

### 4.5.3 Intrinsic alignments

In this subsection I investigate the effect of assumptions made about galaxy intrinsic alignments (IAs), by repeating the cosmological analysis with (i) no intrinsic alignments, (ii) a simpler, linear, intrinsic alignment model, (iii) a more complete tidal alignment model, and (iv) adding a free power law redshift evolution. I also show constraints on the amplitude of intrinsic alignments and show the benefit of using tomography. I use the same data vector and likelihood calculation for

all models.

It was realised early in the study of weak gravitational lensing (Heavens et al. 2000; Croft & Metzler 2000; Catelan et al. 2001; Crittenden et al. 2001) that the unlensed shapes of physically close galaxies may align during galaxy formation due to the influence of the same large-scale gravitational field. This type of correlation was dubbed "Intrinsic-Intrinsic", or II. Hirata & Seljak (2004) then demonstrated that a similar effect can give rise to long-range IA correlations as background galaxies are lensed by the same structures that correlate with the intrinsic shapes of foreground galaxies. This gives rise to a "Gravitational-Intrinsic", or GI, correlation. The total measured cosmic shear signal is the sum of the pure lensing contribution and the IA terms:

$$C^{ij}_{\rm obs}(\ell) = C^{ij}_{\rm GG}(\ell) + C^{ij}_{\rm GI}(\ell) + C^{ij}_{\rm IG}(\ell) + C^{ij}_{\rm II}(\ell). \tag{4.8}$$

Neglecting this effect can lead to significantly biased cosmological constraints (Heavens et al. 2000; Bridle & King 2007; Joachimi et al. 2011; Kirk et al. 2012; Krause et al. 2015).

I treat IAs in the "tidal alignment" paradigm, which assumes that intrinsic galaxy shapes are linearly related to the tidal field (Catelan et al. 2001), and thus that the additional $C^{ij}(\ell)$ terms above are integrals over the 3D matter power spectra. It has been shown to accurately describe red/elliptical galaxy alignments (Joachimi et al. 2011; Blazek et al. 2011). More details of all the IA models considered in this paper can be found in Appendix 4.A. Within the tidal alignment paradigm, the leading-order correlations define the linear alignment (LA) model. As the fiducial model, I use the "non-linear linear alignment" (NLA) model, an ansatz introduced by Bridle & King (2007), in which the non-linear matter power spectrum, $P^{\rm nl}_\delta(k,z)$, is used in place of the linear matter power spectrum, $P^{\rm lin}_\delta(k,z)$, in the LA model predictions for the II and GI terms. Although it does not provide a fully consistent treatment of non-linear contributions to IA, the

NLA model attempts to include the contribution of non-linear structure growth to the tidal field, and it has been shown to provide a better fit to data at quasi-linear scales than the LA model (Bridle & King 2007; Singh et al. 2015).

I also consider a new model, described in Blazek et al. (2015a), which includes all terms that contribute at next-to-leading order in the tidal alignment scenario, while simultaneously smoothing the tidal field (e.g. at the Lagrangian radius of the host halo). The effects of weighting by the source galaxy density can be larger than the correction from the non-linear evolution of dark matter density. This more complete tidal alignment model (denoted the "CTA model" below) is described in more detail in Appendix 4.A.

The top panel of Figure 4.8 shows cosmological constraints for the fiducial (NLA), LA, and CTA models, as well as the case in which IAs are ignored. These constraints include marginalization over a free IA amplitude parameter, $A$, with a flat prior over the range [-5,5]. As shown by the values in Table 4.1 and illustrated in Figure 4.3, cosmological parameters are robust to the choice of IA model. The largest departure from the fiducial model happens when IAs are ignored entirely. This decreases the best-fit $S_8$ by roughly two thirds of the $1\sigma$ uncertainty. Results for all IA models retain the other choices of our fiducial analysis, including cuts on scale and the choice of cosmological and other nuisance parameters that are marginalised.

The NLA model assumes a particular evolution with redshift, based on the principle that the alignment of galaxy shapes is laid down at some early epoch of galaxy formation and retains that level of alignment afterwards.[11] I test for more general redshift evolution through the inclusion of a free power-law in $(1 + z)$, $\eta_{\rm other}$, which is varied within the (flat) prior range [-5,5] and marginalised over, in addition to the IA amplitude free parameter, $A$. Details of these terms and of our IA models are explained in more detail in Appendix 4.A.

[11] See Kirk et al. (2012) and Blazek et al. (2015a) for further discussion of the treatment of non-linear density evolution in the NLA and similar models.

The fiducial constraints rely on the data's ability to constrain the free IA amplitude parameter $A$. This is possible with three-bin tomography because the cosmic shear and IA terms evolve differently with redshift, meaning they contribute with different weight to the observed signal from each bin pair. In the right panel of Figure 4.8 I show constraints on $S_8$ and the IA amplitude, $A$, for the NLA model with three-bin tomography as well as after marginalising over the redshift power law $\eta_{\rm other}$. I also show the constraints from an analysis of the fiducial NLA model (no redshift power law) without tomography.

This figure clearly demonstrates the need for redshift information to constrain the IA contribution. Using three tomographic bins and the NLA model I obtain a constraint on the IA amplitude which is consistent with $A = 1$, although the contours are wide enough that it is also consistent with zero IAs. As soon as the redshift information is reduced, either by using only a single tomographic bin, or by marginalising over an additional power law in redshift, the constraints on the IA amplitude degrade markedly, becoming nearly as broad as the prior range in each case. The constraints on cosmology are also significantly degraded, an effect which is almost entirely due to the degeneracy between the lensing amplitude and the (now largely unconstrained) IA amplitude. The constraints on $S_8$ are considerably stronger if I ignore IAs in the case without tomography.

The use of the free power law in redshift substantially reduces the best-fit value of $S_8$ as well as greatly increasing the errors, as shown in Table 4.1 and Figure 4.3. This is driven by the preference of this model for low values of $\sigma_8$ and $\Omega_m$ when sampling at the negative end of the prior range in $A$. Motivated by astrophysical arguments and observational evidence that red galaxies exhibit radial alignment with overdensities (i.e. $A > 0$) while blue galaxies are weakly aligned (e.g. Singh et al. 2015; Joachimi et al. 2011; Mandelbaum et al. 2011b), I repeat the analysis restricting $A > 0$. As expected, imposing this lower bound significantly improves constraints when flexible redshift evolution of IA is allowed (see Table 4.1 and Figure 4.3). While allowing for mildly negative $A$ within the tidal alignment

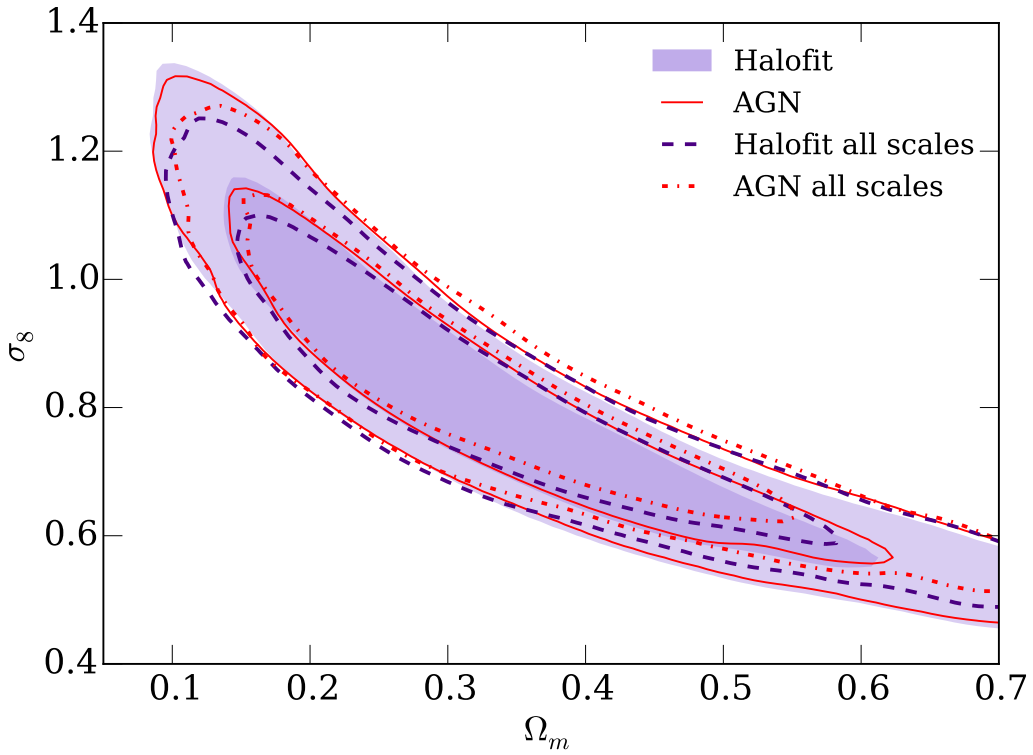


Figure 4.9: The effect of AGN feedback on cosmological constraints. The purple shaded region and the red solid lines the our fiducial matter power spectrum (HALOFIT) and the OWLS AGN model respectively. Blue dashed and red dot-dashed lines use a more aggressive data vector, using scales down to 2 arcmin in $\xi_+$ and $\xi_-$, again with the fiducial matter power spectrum (HALOFIT) and the OWLS AGN model respectively.

paradigm may partially account for potential non-zero alignments of blue and mixed-population source galaxies, a more sophisticated treatment (e.g. including "tidal torquing" of spiral galaxy angular momenta) should be included in the analysis of future weak lensing measurements with increased statistical power.

### 4.5.4 Matter power spectrum uncertainty

Along with IAs, the main theoretical uncertainty in cosmic shear is the prediction of how matter clusters on non-linear scales. For the scales which these measurements are most sensitive to, simulations are required to predict the matter power spectrum $P_\delta(k, z)$.

Under the assumption that only gravity affects the matter clustering, Heitmann et al. (2014) used the Coyote Universe simulations to achieve an accuracy in $P_\delta(k, z)$ of 1% at $k \sim 1\,\mathrm{Mpc}^{-1}$ and $z < 1$, and 5% for $k < 10\,\mathrm{Mpc}^{-1}$ and $z < 4$, a level of error which would have little impact on the results described in this paper. For use in parameter estimation, they released the emulator code FrankenEmu to predict the matter power spectrum given a set of input cosmological parameters. For the range of scales used in this work, I find very close agreement between HALOFIT and FrankenEmu, as demonstrated in Figure 4.1. I use HALOFIT for the fiducial analysis. However, these codes are based on gravity-only (often referred to as 'dark matter-only') simulations which do not tell the whole story. Baryonic effects on the power spectrum due to active galactic nuclei (AGN), gas cooling, and supernovae could be of order 10% at $k = 1\ \mathrm{Mpc}^{-1}$ (van Daalen et al. 2011). To predict these effects accurately requires hydrodynamic simulations, which are not only more computationally expensive, but are also sensitive to poorly understood physical processes operating well below the resolution scales of the simulations. The effect of baryonic feedback on the matter power spectrum at small scales is therefore sensitive to 'sub-grid' physics. See Jing et al. (2006) and Rudd et al. (2008) for early applications of hydrodynamic simulations in this context, and Vogelsberger et al. (2014) and Schaye et al. (2015) for the current state of the art.

As discussed in Section 4.4.2, in this paper I reduce the impact of non-linearities and baryonic feedback by excluding small angular scales from the data vector. To get an idea of the magnitude of these effects, I have analysed the power spectra from van Daalen et al. (2011) which are based on the OWLS simulations (a suite of hydrodynamic simulations which include various different baryonic scenarios). For a given baryonic scenario, I follow Kitching et al. (2014) and MacCrann et al. (2015) by modulating the fiducial matter power spectrum

$P(k, z)$ (from CAMB and HALOFIT) as follows:

$$P(k, z) \rightarrow \frac{P_{\rm baryonic}(k, z)}{P_{\rm DMONLY}} P(k, z) \tag{4.9}$$

where $P_{\rm baryonic}(k, z)$ is the OWLS power spectrum for a particular baryonic scenario, and $P_{\rm DMONLY}$ is the power spectrum from the OWLS 'DMONLY' simulation, which does not include any baryonic effects. I assume this somewhat ad-hoc approach of applying a cosmology-independent correction to the cosmology-dependent fiducial matter power spectrum is sufficient for estimating the order of the biases in the constraints expected from ignoring baryonic effects. McCarthy et al. (2011) find that of the OWLS models, the AGN model best matches observed properties of galaxy groups, both in the X-ray and the optical. Furthermore Semboloni et al. (2011), Zentner et al. (2013), and Eifler et al. (2015) examine the impact of various baryonic scenarios on cosmic shear measurements, and find that the AGN model causes the largest deviation from the pure dark matter scenario, substantially suppressing power on scales from $k = 0.3\,h/\mathrm{Mpc}$ to $k = 50\,h/\mathrm{Mpc}$. Of the hydrodynamic simulations I have investigated, the OWLS AGN feedback model is the one that affects the results most significantly, and so I focus on this model here.

Figure 4.9 shows the constraints resulting when performing the modulation above on the matter power spectrum, using the AGN model as the baryonic prescription. The purple shaded region and red solid lines, which have small scales removed as described in Section 4.4.2, are very similar to each other, indicating that my choice of scale cuts is conservative, and suggesting that the results are robust to baryonic effects on the power spectrum. The blue dashed and red dot-dashed lines show the constraints when not cutting any small scales from the data vector (i.e. using down to 2 arcminutes in both $\xi_+$ and $\xi_-$). Here more of a shift in the constraints is apparent. This is quantified in Table 4.1 and illustrated in Figure 4.3. When I use all scales down to 2 arcminutes, the inclusion of the AGN

model causes an increase in $S_8$ of 20% of the errorbar (compare the "Without small-scale cuts" line in Table 4.1 with the "OWLS AGN $P(k)$ w/o small-scale cuts" line). However, with my fiducial cuts to small scales the increase is only 13% of the error bar (compare the "OWLS AGN $P(k)$" line in Table 4.1 with the "Fiducial" line). I note that although the contours in Figure 4.9 do appear to tighten slightly along the degeneracy direction when including small scales, the errorbar on $S_8$ increases slightly. This could be due to the theoretical model being a poor fit at small scales, or the noisiness of the covariance matrix.

To take advantage of the small scale information in future weak lensing analyses, more advanced methods of accounting for baryonic effects will be required. Eifler et al. (2015) propose a PCA marginalisation approach that uses information from a range of hydrodynamic simulations, while Zentner et al. (2013) and Mead et al. (2015) propose modified halo model approaches to modelling baryonic effects. Even with more advanced approaches to baryonic effects, future cosmic shear studies will have to overcome other systematics that affect small angular scales, such as the shape measurement selection biases explored in Hartlap et al. (2011).

## 4.6 Other data

In this Section I compare the DES SV cosmic shear constraints with other recent cosmological data. I first compare these constraints to those from CFHTLenS. I then compare and combine with the Cosmic Microwave Background (CMB) constraints from *Planck* (Planck Collaboration et al. 2015a), primarily using the TT + lowP dataset throughout (which I refer to simply as "Planck" in most figures). I also compare to another *Planck* data combination which used high-$\ell$ TT, TE and EE data and low-$\ell$ polarisation data.

*Planck* also measured gravitational lensing of the CMB, which probes a very similar quantity to cosmic shear, but weighted to higher redshifts ($z \sim 2$); I refer

to this as "Planck lensing" when comparing constraints. I discuss additional datasets and present constraints on the dark energy equation of state. See Planck Collaboration et al. (2015a) and Lahav & Liddle (2014) for a broad review of current cosmological constraints.

### 4.6.1 Comparisons

A comparison of DES SV constraints to those from other observables is shown in Figure 4.10. The observables shown are described below. Constraints on $S_8$ from these comparisons are also shown in Table 4.1 and Figure 4.3.

#### Other lensing data

CFHTLenS remains the most powerful current cosmic shear survey, with 154 square degrees of data in the $u$, $g$, $r$, $i$, and $z$ bands. Table 4.1 summarises the constraints from the non-tomographic analysis of K13 and the tomographic analysis of H13 that I have computed using the same parameter estimation pipeline as the DES SV data (starting from the published correlation functions and covariance matrices).

I investigate the effect of the scale cuts used for the CFHTLenS analysis so that I can make a more fair comparison to DES SV. In Table 4.1 and Fig 4.3 I show constraints using scale cuts that were used in both H13 and K13 to test the robustness of the results, labelled "original conservative scales" (H13 exclude angles $< 3'$ for redshift bin combinations involving the lowest two redshift bins from $\xi_+$; and angles $< 30'$ for bin combinations involving the lowest four redshift bins, and angles $< 16'$ for bin combinations involving the highest two redshift bins from $\xi_-$. K13 exclude angles $< 17'$ from $\xi_+$ and $< 53'$ from $\xi_-$). Finally, I show the CFHTLenS results using minimum scales selected using the approach described in Section 4.4.2, which I refer to as "modified conservative scales" in Table 4.1 and Fig 4.3.

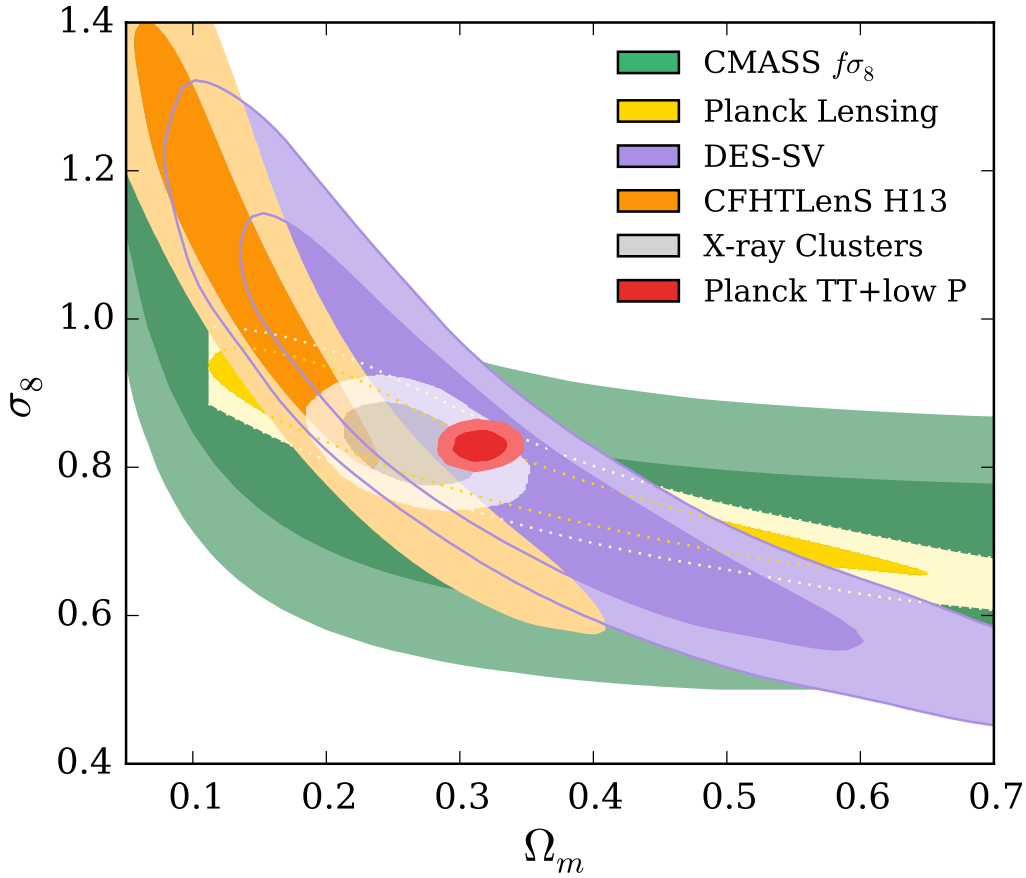


Figure 4.10: Joint constraints from a selection of recent datasets on the total matter density $\Omega_m$ and amplitude of matter fluctuations $\sigma_8$. From highest layer to lowest layer: *Planck* TT + lowP (red); X-ray cluster mass counts (Mantz et al. 2015, white/grey shading); DES SV (purple); CFHTLenS (H13, orange); *Planck* CMB lensing (yellow); CMASS $f\sigma_8$ (Chuang et al. 2013, green).

I show constraints from H13, with my scale cuts, on $(\Omega_m, \sigma_8)$ as orange contours in Figure 4.10. The DES SV constraints are consistent with H13, but have a higher amplitude and larger uncertainties.

The values in Table 4.1 show that my prescription for selecting which scales to use gives similar results to the prescription in H13 (compare the "CFHTLenS (H13) original conservative scales" line to the "CFHTLenS (H13) modified conservative scales" line). The K13 results show some sensitivity to switching from using all scales to cutting small scales (possibly because of the apparent lack of

power in the large scale points that K13 used but H13 did not), with a lower amplitude preferred when excluding small scales (though see also Kitching et al. (2014) which prefers higher amplitudes). The uncertainties increase by $\sim 50\%$ for the "modified conservative scales" case ($\theta_{min}(\xi_+) = 3.5'$ and $\theta_{min}(\xi_-) = 28'$) compared to using all scales.

The most comparable lines in Table 4.1 show that the DES SV tomographic uncertainties are $\sim 20\%$ larger than those from CFHTLenS (compare "No photoz or shear systematics" with "CFHTLenS (H13) modified conservative scales"). The main differences between the two datasets are (i) the DES SV imaging data are shallower and have a larger average PSF than CFHTLenS (ii) DES SV are more conservative in the selection of source galaxies (see J15) (iii) DES SV covers a larger area of sky ($139\,\mathrm{deg}^2$ square degrees compared to 75% of $154\mathrm{deg}^2$ $\sim 115\,\mathrm{deg}^2$; Heymans et al. (2012)) although DES SV is contiguous instead of four independent patches. The upshot of the different depths and galaxy selection are that CFHTLenS has an effective source density of $\sim 11$ per arcmin$^2$ while DES SV has an effective density of 6.8 and 4.1 galaxies per arcmin$^2$ for NGMIX and IM3SHAPE respectively, using the H13 definition. While the extra redshift resolution in the 6-redshift-bin H13 analysis may contribute to their better constraining power (particularly on intrinsic alignments), I expect the main contribution comes from their increased number density of galaxies. Given the size of the errors, DES-SV does not yet have the constraining power required to resolve the apparent discrepancy in the $(\Omega_\mathrm{m}, \sigma_8)$ plane between CFHTLenS and *Planck* (MacCrann et al. 2015; Leistedt et al. 2014; Battye & Moss 2014), and is consistent with both.

I also show in Table 4.1 and Figure 4.3 the result of combining CFHTLenS and DES SV constraints, which is is straightforward since the surveys do not overlap on the sky. As expected, the joint constraints lie between the two individual constraints. Although judging agreement between multi-dimensional contours is non-trivial, by the simple metric of difference in best-fit $S_8$ divided by the lensing

error bar on $S_8$, the tension between CFHTLenS and *Planck* is somewhat reduced by combining CFHTLenS with DES SV.

DES SV constraints are also in good agreement with those from *Planck* lensing (Planck Collaboration et al. 2015c), which are shown as yellow contours in Figure 4.10. The *Planck* lensing measurement constrains a flatter degeneracy direction in $(\Omega_m, \sigma_8)$ because it probes higher redshifts than galaxy lensing, as discussed in Planck Collaboration et al. (2015c), Pan et al. (2014), and Jain & Seljak (1997). This means that the constraints it imposes on $\sigma_8(\Omega_m/0.3)^{0.5}$ are rather weak, as shown in Table 4.1 and Figure 4.3, but the constraints with the best fitting combination $\sigma_8(\Omega_m/0.3)^{0.24}$ are much stronger (also shown in Table 4.1).

**Non-lensing data**

Figure 4.10 clearly shows that DES SV agrees well with *Planck* on marginalising into the $(\Omega_\mathrm{m}, \sigma_8)$ plane in ΛCDM. Table 4.1 shows that this is true for both the *Planck* TT + lowP and the TT+TE+EE+lowP variant of the *Planck* data. Since the DES-SV constraints show very little constraining power on any of the other ΛCDM parameters varied, agreement of the multi-dimensional contours with *Planck* seems likely. Since submission of this paper, Raveri 2015 used a Bayesian data concordance test to judge agreement between the constraints from different datasets, including *Planck* and CFHTLenS. They apply 'ultra-conservative' cuts to the CFHTLenS data, resulting in much enlarged contours in the $\Omega_\mathrm{m}$ - $\sigma_8$ plane, which appear to be in agreement with *Planck*, however their data concordance test still suggests disagreement between the two datasets. A natural question is whether the converse situation is also be possible - where 2d marginalised contours disagree, but a data concordance test will not show tension. It is clear that caution must be exercised when judging agreement based on 2d marginalised contours.

At the time of writing, the *Planck* 2015 likelihood code has not been released, but chains derived from it are publicly available. As I therefore cannot calculate

likelihoods for general parameter choices, I must instead combine *Planck* with DES SV data using importance sampling: each sample in the *Planck* chain is given an additional weight according to their likelihood under DES SV data. Since the *Planck* chains do not, of course, include the DES-SV nuisance parameters I also generate a sample of each of those from the priors to append to each *Planck* sample. In this approach one must then *not* apply the nuisance parameter priors again when computing the posteriors during sampling, since that would count the prior twice. As usual in importance sampling for a finite number of samples this procedure is only valid when the distributions are broadly in agreement, as in this case. Table 4.1 shows that the *Planck* uncertainties on $S_8$ are reduced by 10% on combining with DES SV, and the central value moves down by about 10% of the error bar. This can be compared to the combination of *Planck* with *Planck* lensing, which brings $S_8$ down further and tightens the errorbar further.

Galaxy cluster counts are a long-standing probe of the matter density and the amplitude of fluctuations (see Mantz et al. 2015 for a recent review). The constraints from the Sunyayev–Zel'dovich effect measured by *Planck* (Planck Collaboration et al. 2015d) are at the lower end of the amplitudes allowed by the DES SV cosmic shear constraints and are in some tension with those from the *Planck* TT+ lowP primordial constraints, depending on the choice of mass calibration used. X-ray cluster counts also rely on a mass calibration to constrain cosmology and tend to fall at the lower end of the normalisation range (see e.g. Vikhlinin et al. 2009). Finally, optical and X-ray surveys can use lensing to measure cluster masses and abundances; there are several ongoing analyses in DES to place constraints on the cluster mass calibration. Figure 4.10 includes a constraint in white from an analysis of X-ray clusters with masses calibrated using weak lensing from Mantz et al. (2015). This is clearly in good agreement with the DES SV results presented here.

Spectroscopic large-scale structure measurements with anisotropic clustering, such as the CMASS data presented in Chuang et al. (2013), can be used to

constrain the growth rate of fluctuations, and are shown in green in Figure 4.10. There is a broad region of overlap between that data and DES SV.

The *Planck* 2015 data release contains chains that have been importance sampled with large scale structure data from 6dFGS, SDSS-MGS and BOSS-LOWZ (Beutler et al. 2011; Ross et al. 2015; Anderson et al. 2014), supernova data from the Joint Likelihood Analysis (Betoule et al. 2014), and a re-analysis of the Riess et al. (2011) HST Cepheid data by Efstathiou (2014b). In Table 4.1 and Figure 4.3 I refer to this combination as 'ext'. *Planck* alone measures $\sigma_8(\Omega_\mathrm{m}/0.3)^{0.5} = 0.850 \pm 0.024$, while *Planck*+ext measures $\sigma_8(\Omega_\mathrm{m}/0.3)^{0.5} = 0.824 \pm 0.013$.

Figure 4.11 shows the DES SV, CFHTLenS and *Planck* data points translated onto the matter power spectrum assuming a ΛCDM cosmology. This uses the method described in MacCrann et al. (2015) which follows Tegmark & Zaldarriaga (2002) in translating the central $\theta$ and $\ell$ values of the measurements into wavenumber values $k$. The wavenumber of the point is the median of the window function of the $P(k)$ integral used to predict the observable ($\xi_+$ or $C_\ell$). The height of the point is given by the ratio of the observed to predicted observable, multiplied by the theory power spectrum at that wavenumber. For simplicity I use the non-tomographic results from each of DES SV and CFHTLenS (K13). The results are therefore cosmology-dependent, and I use the *Planck* best fit cosmology for the version shown here. The CFHTLenS results are below the *Planck* best fit at almost all scales (see also discussion in MacCrann et al. 2015). The DES results agree relatively well with *Planck* up to the maximum wavenumber probed by *Planck* and then drop towards the CFHTLenS results.

### 4.6.2 Dark Energy

The DES SV data is only 3% of the total area of the full DES survey, so I do not expect to be able to significantly constrain dark energy with this data. Nonetheless, I have recomputed the fiducial DES SV constraints for the second

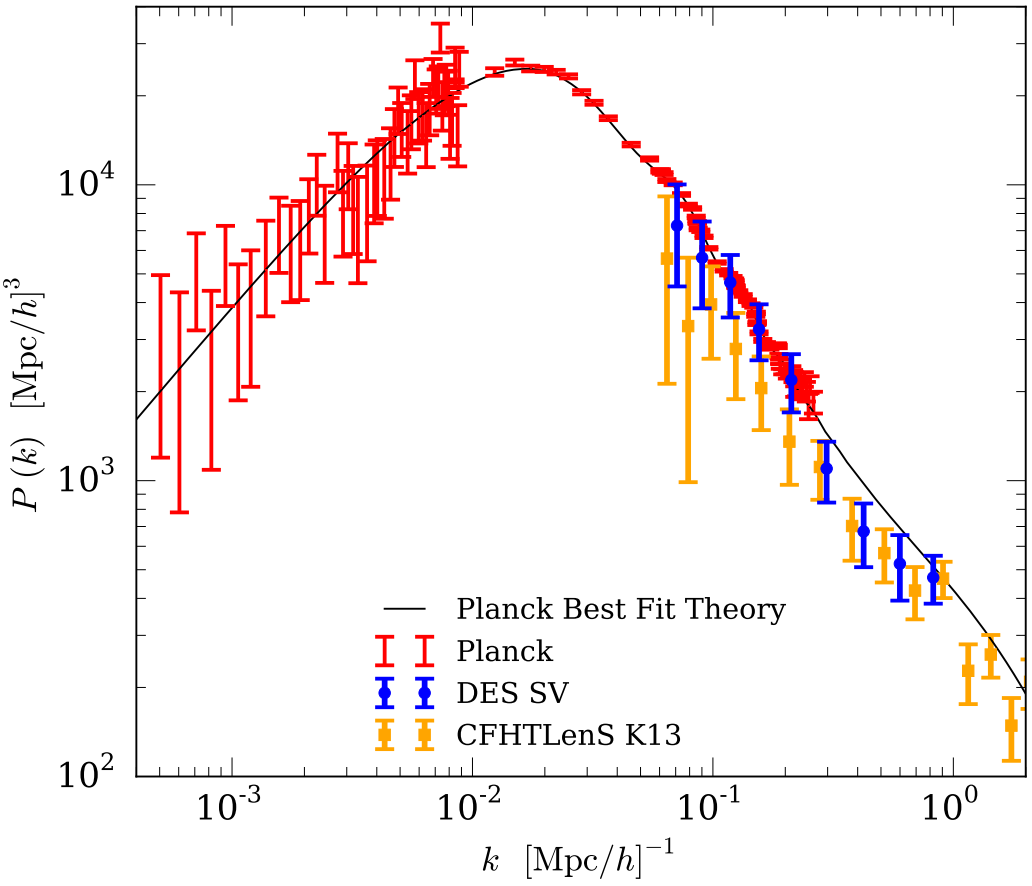


Figure 4.11: Non-tomographic DES SV (blue circles), CFHTLenS K13 (orange squares) and *Planck* (red bars) data points projected onto the matter power spectrum (black line). This projection is cosmology-dependent and assumes the *Planck* best fit cosmology in ΛCDM. The *Planck* error bars change size abruptly because the $C_\ell$s are binned in larger $\ell$ bins above $\ell = 50$.

simplest dark energy model, $w$CDM, which has a free (but constant with redshift) equation of state parameter $w$, in addition to the other cosmological and fiducial nuisance parameters (see Section 3). The purple contours in Figure 4.12 show constraints on $w$ versus the main cosmic shear parameter $S_8$; I find DES SV has a slight preference for lower values of $w$, with $w < -0.68$ at 95% confidence. There is a small positive correlation between $w$ and $S_8$, but the constraints on $S_8$ are generally robust to variation in $w$.

The *Planck* constraints (the red contours in Figure 4.12) agree well with the

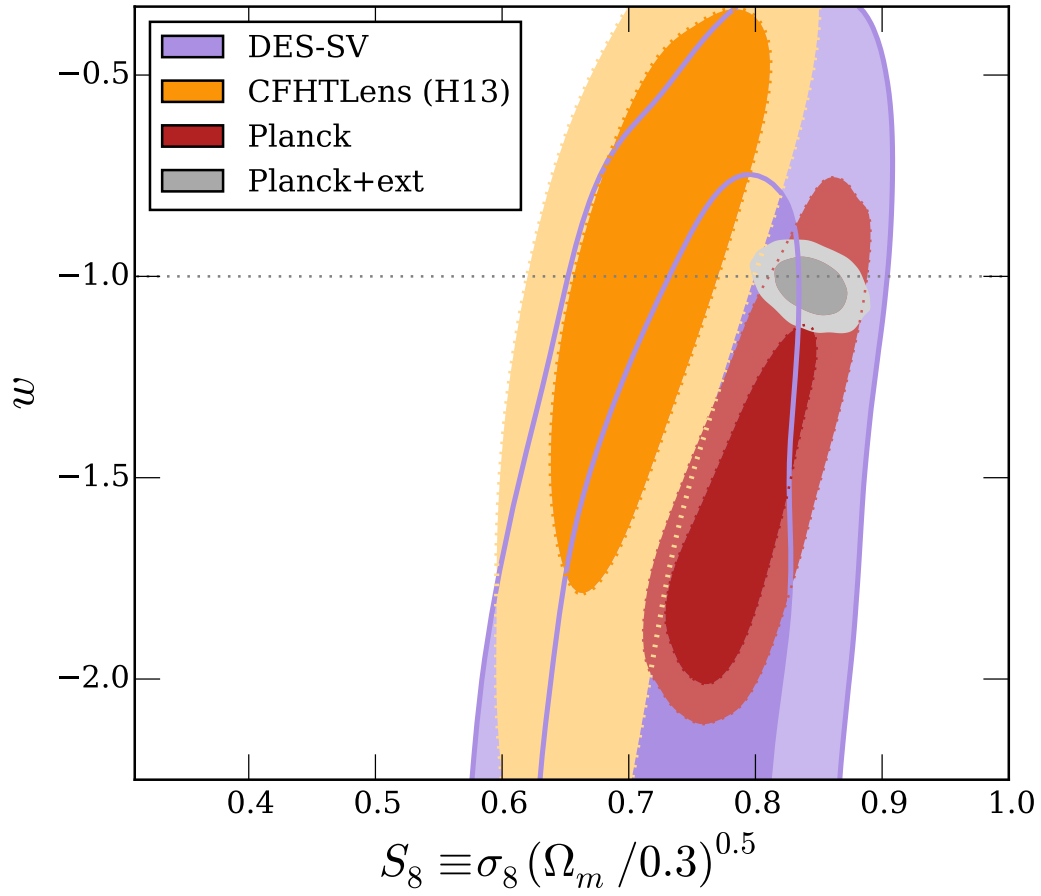


Figure 4.12: Constraints on the dark energy equation of state $w$ and $S_8 \equiv \sigma_8(\Omega_m/0.3)^{0.5}$, from DES SV (purple), *Planck* (red), CFHTLenS (orange), and *Planck*+ext (grey). DES SV is consistent with *Planck* at $w = -1$. The constraints on $S_8$ from DES SV alone are also generally robust to variation in $w$.

DES SV constraints: combining DES SV with *Planck* gives negligibly different results to *Planck* alone. This is also the case when combining with the *Planck*+ext results shown in grey. Planck Collaboration et al. (2015a) discuss that while *Planck* CMB temperature data alone do not strongly constrain w, they do appear to show close to a $2\sigma$ preference for $w < -1$. However, they attribute it partly to a parameter volume effect, and note that the values of other cosmological parameters in much of the $w < -1$ region are ruled out by other datasets (such as those used in the 'ext' combination).

*Planck* CMB data combined with CFHTLenS also show a preference for $w < -1$ (Planck Collaboration et al. 2015a). The CFHTLenS constraints (orange contours) in Figure 4.12 show a similar degeneracy direction to the DES SV results, although with a preference for slightly higher values of $w$ and lower $S_8$. The tension between *Planck* and CFHTLenS in ΛCDM is visible at $w = -1$, and interestingly, is not fully resolved at any value of $w$ in Figure 4.12. This casts doubt on the validity of combining the two datasets in $w$CDM.

## 4.7 Conclusions

I have presented the first constraints on cosmology from the Dark Energy Survey. Using 139 square degrees of Science Verification data I have constrained the matter density of the Universe $\Omega_\mathrm{m}$ and the amplitude of fluctuations $\sigma_8$, and find that the tightest constraints are placed on the degenerate combination $S_8 \equiv \sigma_8(\Omega_\mathrm{m}/0.3)^{0.5}$, which is measured to 7% accuracy as $S_8 = 0.81 \pm 0.06$.

DES SV alone places weak constraints on the dark energy equation of state: $w < -0.68$ (95%). These do not significantly change constraints on $w$ compared to *Planck* alone, and the cosmological constant remains within marginalised DES SV+*Planck* contours.

The state of the art in cosmic shear, CFHTLenS, gives rise to some tension when compared with the most powerful dataset in cosmology, *Planck* (Planck Collaboration et al. 2015a). DES SV constraints are in agreement with both *Planck* and CFHTLenS results, and cannot rule either out due to larger uncertainties caused by a smaller effective number density of galaxies and my propagation of uncertainties in the two most significant lensing systematics into the constraints.

I have investigated the sensitivity of my results to variation in a wide range of aspects of the analysis, and found the fiducial constraints to be remarkably robust. The results are stable to switching to our alternative shear catalogue, IM3SHAPE, or to any of the alternative photometric redshift catalogues, TPZ,

ANNZ2 and BPZ. Nonetheless, to account for any residual systematic error I marginalise over 5% uncertainties on shear and photometric redshift calibration in each of three redshift bins in my fiducial analysis; this inflates the error bar by 9%.

The results are also robust to the choice of data vector: constraints from Fourier space $C_\ell$ are consistent with those from real space $\xi_{+/-}(\theta)$. As expected, a 2D analysis is less powerful than one split into redshift bins; the biggest benefit of tomography comes from its constraints on intrinsic alignments.

In the future, DES will be an excellent tool for learning about the nature of IAs. In this current analysis I only aim to show that the details of IA modelling do not affect the cosmological conclusions drawn from the SV dataset. I investigated four alternatives to my fiducial intrinsic alignment model and found the results to be stable, even when including an additional free parameter adding redshift dependence. Similarly, the similarity in parameter constraints when using the NLA and CTA models, as well as the minor shift when compared with the LA and no IA cases, is consistent with the results of Krause et al. (2015), who forecast the effects of IA contamination for each of these models for the full DES survey.

The DES SV results are also robust to astrophysical systematics in the matter power spectrum predictions. I chose to use only scales where the effect of baryons on the matter power spectrum predictions are expected to be relatively small, however, the results are relatively insensitive to the inclusion of small angular scales and to the effects of baryonic feedback as implemented in the OWLS hydrodynamic simulations. The fiducial results are shifted by only 14% of the error bar when the OWLS AGN model is included.

In the analysis of future DES data from Year One and beyond I aim to be more sophisticated in several ways. Greater statistical power will allow more precise constraints on astrophysical systematics, and algorithmic improvements will reduce nuisance parameter priors. Forthcoming Dark Energy Survey data will provide much more powerful cosmological tests, such as constraints on neutrino

masses, modified gravity, and of course dark energy.

## Acknowledgements

I am grateful for the extraordinary contributions of my CTIO colleagues and the DECam Construction, Commissioning and Science Verification teams in achieving the excellent instrument and telescope conditions that have made this work possible. The success of this project also relies critically on the expertise and dedication of the DES Data Management group.

I am very grateful to Iain Murray for advice on importance sampling. I thank Catherine Heymans, Martin Kilbinger, Antony Lewis and Adam Moss for helpful discussion.

## 4.A Intrinsic alignment models

Here I briefly describe the fiducial, NLA, model of intrinsic alignments (IAs), as well as the other models I compare against in Section 4.5.3.

The observed cosmic shear power spectrum is the sum of the effect due to gravitational lensing, GG, the IA auto-correlation, II, and the gravitational-intrinsic cross-terms:

$$C^{ij}_{\rm obs}(\ell) = C^{ij}_{\rm GG}(\ell) + C^{ij}_{\rm GI}(\ell) + C^{ij}_{\rm IG}(\ell) + C^{ij}_{\rm II}(\ell). \tag{4.10}$$

When I quote results for "No IAs" I am simply ignoring the three IA terms on the right hand side of this equation.

Each of these contributions can be written as integrals over appropriate win-

dow functions and power spectra,

$$C^{ij}_{\rm GG}(\ell) = \int_0^{\chi_{\rm h}} d\chi \frac{W_i(\chi)W_j(\chi)}{D_A^2(\chi)} P_\delta(k = l/D_A(\chi), \chi), \tag{4.11}$$

$$C^{ij}_{\rm II}(\ell) = \int_0^{\chi_{\rm h}} d\chi \frac{N_i(\chi)N_j(\chi)}{D_A^2(\chi)} P_{\rm II}(k = l/D_A(\chi), \chi), \tag{4.12}$$

$$C^{ij}_{\rm GI}(\ell) = \int_0^{\chi_{\rm h}} d\chi \frac{N_i(\chi)W_j(\chi)}{D_A^2(\chi)} P_{\delta{\rm I}}(k = l/D_A(\chi), \chi), \tag{4.13}$$

where $W_i(\chi)$ is the lensing kernel, $N_i(\chi)$ is the radial distribution of the galaxies in tomographic bin $i$ and I have assumed the Limber approximation. The details of any chosen IA model are encoded in the auto- and cross-power spectra, $P_{\rm II}$ and $P_{\delta{\rm I}}$.

Within the tidal alignment paradigm of IAs (see Troxel & Ishak (2015); Joachimi et al. (2015) for general reviews of IAs), the leading-order correlations define the linear alignment (LA) model (Catelan et al. 2001; Hirata & Seljak 2004, 2010). In the LA model predictions for the II and GI terms give

$$P_{\rm II}(k,z) = F^2(z)P_{\delta\delta}(k,z), \quad P_{\delta{\rm I}}(k,z) = F(z)P_{\delta\delta}(k,z), \tag{4.14}$$

where

$$F(z) = -AC_1\rho_{\rm crit}\frac{\Omega_{\rm m}}{D(z)}. \tag{4.15}$$

$\rho_{\rm crit}$ is the critical density at $z = 0$, $C_1 = 5\times10^{-14}h^{-2}M_\odot^{-1}{\rm Mpc}^3$ is a normalisation amplitude (Brown et al. 2002; Bridle & King 2007), and $A$, the dimensionless amplitude, is the single free parameter. $D(z)$ is the growth function. In the case where redshift dependence for IA is included, the amplitude is

$$F(z,\eta_{\rm other}) = -AC_1\rho_{\rm crit}\frac{\Omega_{\rm m}}{D(z)}\left(\frac{1+z}{1+z_0}\right)^{\eta_{\rm other}}. \tag{4.16}$$

In the LA alignment paradigm galaxy intrinsic alignments are sourced at the epoch of galaxy formation and do not undergo subsequent evolution, as such they

are unaffected by non-linear clustering at late times, and the $P_{\delta\delta}(k,z)$ that enter equation 4.14 are linear matter power spectra. My fiducial model, the non-linear alignment (NLA) model, simply replaces the linear power spectra with their non-linear equivalents, $P^{\rm nl}_{\delta\delta}$, wherever they occur, increasing the power of IAs on small scales. This simple ansatz has no physical motivation under the LA paradigm, but it has been shown to agree better with data (Bridle & King 2007; Singh et al. 2015). The non-linear power spectra are calculated using the Takahashi et al. (2012) version of the HALOFIT formalism (Smith et al. 2003).

I also consider a model called the complete tidal alignment (CTA) model (Blazek et al. 2015a). This model includes all terms that contribute at next-to-leading order in the tidal alignment scenario, while also smoothing the tidal field. The equivalent II and GI terms

$$\begin{aligned} P_{\delta I}(k,z) = \quad & F_{\rm CTA}(z)\left[P_{\rm NL}(k,z) + \frac{58}{105}b_1\sigma_S^2 P_{\rm lin} + b_1 P_{0|0\mathcal{E}}\right], \\ P_{II}(k,z) = \quad & F^2_{\rm CTA}(z)[P_{\rm NL}(k,z) + \frac{116}{105}b_1\sigma_S^2 P_{\rm lin} \\ & + 2b_1 P_{0|0\mathcal{E}} + b_1^2 P_{0\mathcal{E}|0\mathcal{E}}], \end{aligned} \tag{4.17}$$

where $b_1$ is the linear bias of the source sample (approximated to be $b_1 = 1$ for this sample), $\sigma_S^2$ is the variance of the density field, smoothed in Fourier space at a comoving scale of $k = 1\ h^{-1}$Mpc, corresponding to roughly the Lagrangian radius of a dark matter halo. $P_{0|0\mathcal{E}}$ and $P_{0\mathcal{E}|0\mathcal{E}}$ are $\mathcal{O}(P^2_{\rm lin})$ terms that arise from weighting the intrinsic shape field by the source density. The amplitude of the CTA model is given by

$$F_{\rm CTA} = -AC_1\rho_{\rm crit}\Omega_{\rm m}(1+z)\left(1+\frac{58}{105}b_1\sigma_S^2\right)^{-1}. \tag{4.18}$$

# Chapter 5

# Cosmic Shear: Exploring the Small Scales

Cosmic shear is sensitive to fluctuations in the cosmological density field over a wide range of scales, and to exploit this sensitivity we need to be able to model these fluctuations over a wide range of scales, as well as any other contributions to the cosmic shear signal. In this chapter I explore some of the difficulties in interpreting the small scales in cosmic shear measurements. Having introduced the dominant source of theoretical uncertainty for small scale measurements, the effect of baryonic physics, I also discuss some of the other systematic effects that make inference from small scales difficult. I estimate two of these, the lensing bias and the blend-exclusion bias, using image simulations. I perform a re-analysis of the DES-SV cosmic shear measurements, now including smaller scales, and marginalising over the Mead et al. (2015) halo model. I also forecast how much other systematic effects may bias inference about baryonic effects from future datasets.

## 5.1 Introduction

The high galaxy number densities of typical weak lensing datasets, and the subsequent large number of galaxy pairs with ∼arcminute angular separation, makes shear two-point correlations a powerful probe of the density field on $\lesssim 1\,\mathrm{Mpc}$ physical scales, where density fluctuations are highly nonlinear. The shear two-point signal depends on the matter power spectrum, $P_\delta(k)$, so it is this that we need to be able to predict from theory, given a set of cosmological parameters, if we are to infer anything about those cosmological parameters.

For $k \gtrsim 0.1\,h\mathrm{Mpc}^{-1}$, n-body simulations are used to predict the nonlinear matter clustering, under the assumption that gravity is the only force we need to consider. Epic computational demands come from the requirements for the simulations to be large enough to include the effects of large-scale power and subdue sampling variance, and sufficiently high resolution to reach the large $k$ required to make predictions of e.g. the small scale cosmic shear signal (see e.g. Heitmann et al. 2010 for discussion of the simulation requirements for matter power spectrum prediction). In order to make predictions for a range of different cosmological models, we require the simulations to be re-run with a range of different cosmological models i.e. a suite of simulations is required. The most advanced example of this sort of suite is the Extended Coyote Universe simulations (Heitmann et al. 2014), which were used to build a matter power spectrum emulator accurate to 5% up to $k = 10h\mathrm{Mpc}^{-1}$ and $z = 4$. These types of simulations are often called 'dark matter only' simulations, although 'gravity-only' would perhaps be more appropriate since they do have $\Omega_b > 0$, but do not include the effects of non-gravitational physics on matter clustering.

White (2004) and Zhan & Knox (2004) first identified the potential of baryonic physics to contaminate the cosmic shear signal, using simple theoretical models to predict several percent changes in the shear power spectrum at $l \gtrsim 1000$. Jing et al. (2006); Rudd et al. (2008); Guillet et al. (2010); Casarini et al. (2012)

used *hydrodynamic simulations* to account for the many complex baryonic processes such as active galactic nuclei (AGN) feedback, gas cooling and supernovae feedback which affect the matter power spectrum. Hydrodynamic simulations incorporate gas physics by including fluid dynamics as well as gravity, and are subsequently more expensive than gravity-only simulations. To fully simulate the relevant baryonic physical processes would require far higher resolution than can currently be achieved for the large volumes required for cosmology, so they are added using 'sub-grid' prescriptions. Since we have incomplete understanding of these physical processes (hence the need to simulate them!), these sub-grid prescriptions need to be calibrated against observables. For example in the state-of-the-art EAGLE simulations (Schaye et al. 2015; Crain et al. 2015), stellar and AGN feedback efficiency is calibrated to reproduce the observed $z \sim 0$ galaxy stellar mass function (GSMF). While this guarantees that the feedback implementation is accurate in its effect on the $z \sim 0$ GSMF, it does not guarantee the feedback implementation is accurate in its effect on e.g. the $z \sim 1$ GSMF or the nonlinear matter power spectrum. My point is that although hydrodynamic simulations can give us indications of the size and scale-dependence of baryonic effects on the matter power spectrum, they are not yet sufficiently advanced enough to make predictions at the level of accuracy required for precision cosmology.

Various works (including Chapters 3 and 4 of this thesis) have made use of the Overwhelmingly Large Simulations (OWLS, Schaye et al. 2010), a suite of hydrodynamic simulations incorporating various different baryonic physics scenarios. van Daalen et al. (2011) measure matter power spectra from the different OWLS simulations which Semboloni et al. (2011) propagate to the shear power spectrum and correlation functions, finding biases as large as $10 - 20\%$ for $\xi_+(\theta = 1')$ and $\xi_-(\theta = 10')$.

In Chapter 4, I used the matter power spectra from van Daalen et al. (2011) to calculate a set of small scale cuts to apply to the measured shear correlation functions, that would reduce any bias due to baryons to below the level of the

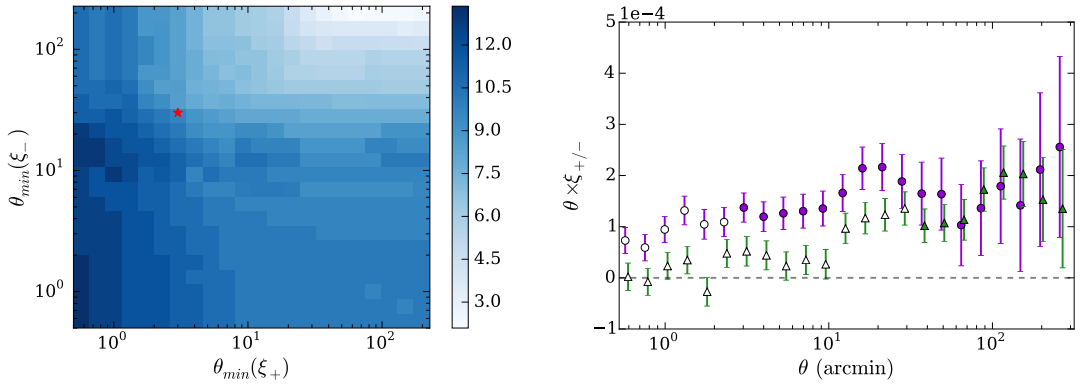


Figure 5.1: Left panel: $S/N$of the DES-SV non-tomographic correlation functions $\xi_{+/-}$, as a function of the minimum scale use in $\xi_{+/-}$, $\theta_{min}(\xi_{+/-})$. Right panel: DES-SV shear correlation functions, open points indicate scales below the minimum scales used in the DES15 analysis.

statistical errors. This chapter is motivated by the significant signal-to-noise that this procedure in some sense wastes. Figure 5.1 demonstrates this waste; the left panel shows the total $S/N$ of the DES-SV non-tomographic measurement, as a function of $\theta_{\rm min}(\xi_{+/-})$, the minimum scale used in $\xi_{+/-}(\theta)$. The red star marks the minimum scales used in DES15, and it's clear that more $S/N$ (from $\sim 8$ up to $\sim 13$) can be gained by reducing these minimum scales. The right panel shows the non-tomographic measurement, with $\xi_+$ represented as purple circles and $\xi_-$ as green triangles. Open symbols mark scales not used in the DES15 analysis. The covariance at these small scales is dominated by diagonal shape noise, so the open points are only weakly correlated, implying again, that there is a lot of $S/N$ to be gained by using the small scales.

Even if astrophysical effects mean we cannot infer cosmological parameters from the small scale cosmic shear signal, one hopes we can learn about the astrophysical effects themselves. Therefore it is tempting to try and exploit the extra $S/N$ by including the small scales, and attempting to model or parameterise the effects of baryons. In §5.4 I overview some methods for modeling or parameterising the effect of baryons on the matter power spectrum. Although baryonic effects may be the largest, there are several additional systematic effects that I

did not describe in detail in Chapter 2 that arise on small scales, which I will start this chapter by describing. Firstly, the observed (two-point) cosmic shear signal is usually considered to be sensitive only to second order correlations in the underlying density field (and hence can be written as an integral over the matter power spectrum). In §5.2, I describe the corrections at third order in the density field that become significant on small scales. Meanwhile, the removal of blended objects during shape measurement can introduce a selection bias on the cosmic shear signal at small scales (Hartlap et al. 2011); I investigate this effect using image simulations in §5.3. One such systematic that I do not consider further here is intrinsic alignments, for which the successful large-scale models such as the (nonlinear-)linear alignment model are likely to break down. Blazek et al. (2015b) systematically include nonlinear corrections (at one-loop order) to the linear alignment model, producing a model that provides a good fit in the mildly nonlinear regime. Halo model-based intrinsic alignment models (see e.g. Schneider & Bridle 2010) are likely to be more successful in the fully nonlinear 1-halo regime.

In §5.5 I describe DES-SV shear two-point function measurements which are extended to smaller scales with respect to the analysis in DES15. In §5.6 I use these measurements to constrain the Mead et al. (2015) halo model, working under the assumption that with the limited statistical power of DES-SV, considering only the dominant small-scale systematic effect, baryonic effects, is reasonable. Finally, I show forecasts for the power of DES Year 5 data to constrain the Mead et al. (2015) model, potentially allowing us to learn about the effect of baryonic physics on dark matter halos from cosmic shear.

## 5.2 Reduced-shear and lensing bias

In this section I consider two contributions to the observed cosmic shear signal that arise from third-order correlations of the convergence or equivaliently third

order in the gravitational potential, $\Psi$ (usually only the second-order correlations are considered, see §1.6.1). Krause & Hirata (2010) investigate corrections up to $O(\Psi^4)$, and although the $O(\Psi^4)$ terms will be non-negligible for future surveys, the $O(\Psi^3)$ terms are around an order of magnitude larger, and so I only consider the latter here. The observable in cosmic shear is the two-point correlation of the observed ellipticity, $< \epsilon^{obs}\epsilon^{obs} >$. It is usually assumed that this is an unbiased estimate of the two-point correlation of the shear $< \gamma\gamma >$. Ignoring intrinsic alignments, I describe below two $O(\Psi^3)$ reasons why this is not quite correct.

1. Firstly, the ellipticity that we measure is actually an estimate of the *reduced shear*, $g$, which is related to the shear via

$$g = \frac{\gamma}{1-\kappa} \approx \gamma(1+\kappa). \tag{5.1}$$

   This requires a 'reduced shear' correction to the predicted signal, which is derived in Appendix 5.A, following Shapiro (2009).

2. Secondly, we only observe the shear at the position of galaxies, so when we compute a two-point correlation function, using e.g. the estimator in equation 1.88, we are effectively computing the correlation function of the galaxy density-weighted reduced shear, $g^{obs}$, given by

$$g_{\rm obs} = (1+\delta_{\rm obs})g \tag{5.2}$$

   where $\delta_{\rm obs}$ is the observed galaxy overdensity at a particular point in space. An observed galaxy overdensity at $(\boldsymbol{\theta}, \chi)$ can arise from two effects. Firstly there could be an overdensity in the galaxy number at $(\boldsymbol{\theta}, \chi)$ e.g. if there is a cluster there. Secondly, there could be a change in the number density of galaxies that we can observe, due to lensing magnification e.g. if there is a cluster at $(\boldsymbol{\theta}, \chi' < \chi)$. The first leads to the 'source-lens clustering' (Bernardeau 1998; Hamana et al. 2002) which is zero in the Limber limit

(see Appendix 5.A). The second effect produces what is known as *lensing bias* (or sometimes 'magnification bias'), and I derive an expression for it Appendix 5.A, following Schmidt et al. (2009).

### 5.2.1 The reduced-shear correction

From Appendix 5.A, the reduced-shear correction to the projected shear power spectrum for tomographic bin pairs $i$ and $j$ is given by

$$\delta_{red}C_{ij}^{\kappa}(l) = \ 2\int \frac{d^2l'}{(2\pi)^2}\cos(2\phi_{l'} - 2\phi_l)\ B_{ij}(\vec{l'}, \vec{l} - \vec{l'}, -\vec{l}). \tag{5.3}$$

where

$$B_{ij}(\vec{l_1}, \vec{l_2}, \vec{l_3}) = \ \frac{1}{2}\int \frac{d\chi}{\chi^4}W_i(\chi)W_j(\chi)[W_i(\chi) + W_j(\chi)]B_{\delta}(\vec{k_1}, \vec{k_2}, \vec{k_3}; \chi) \tag{5.4}$$

and $B_{\delta}(\vec{k_1}, \vec{k_2}, \vec{k_3}; \chi)$ is the matter bispectrum. I use the fitting formula for the matter bispectrum from Scoccimarro & Couchman (2001). Figure 5.2 shows the effect of reduced shear on the shear power spectrum. The fractional bias is $\sim 1\%$ at $l$ of a few hundred, and $\sim 10\%$ at $l$ of $10^4$.

Figure 5.3 shows the effect of the reduced shear on the shear correlation functions $\xi_{+/-}$, which at 1 arcmin is $\sim 2\%$ for $\xi_+$ and $\sim 8\%$ for $\xi_-$. Hence the reduced shear correction, although not as large as the effect of baryons in the OWLS AGN model, is non-negligible for small-scale cosmic shear measurements.

### 5.2.2 The lensing-bias

In Appendix 5.A I derive (drawing heavily on Schmidt et al. 2009) the lensing-bias correction to the shear power spectrum, which for a pair of redshift bins $i$ and $j$ is

$$\delta_{\rm lensing}C_{ij}^{\kappa}(l) = \int \frac{d^2l'}{(2\pi)^2}\cos(2\phi_{l'} - 2\phi_l)B_{ij}^{q}(\vec{l'}, \vec{l} - \vec{l'}, -\vec{l}) \tag{5.5}$$

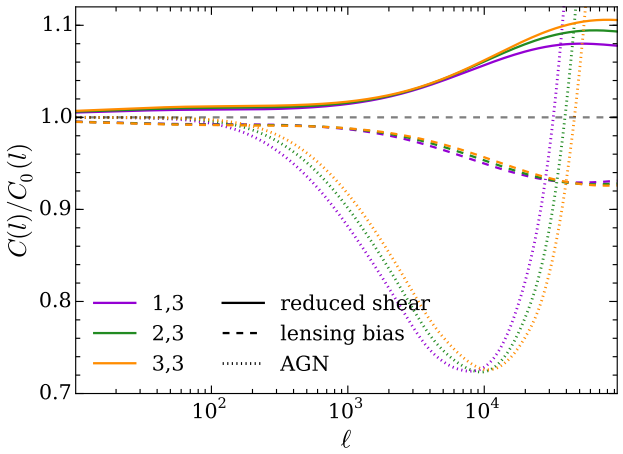


Figure 5.2: The fractional difference in the shear power spectrum from reduced-shear (solid lines) and lensing-bias (dashed lines) are compared to the contribution from the OWLS AGN model (dotted lines). I used the DES-SV tomographic redshift distributions, and for clarity only show the correlations with the highest redshift bin.

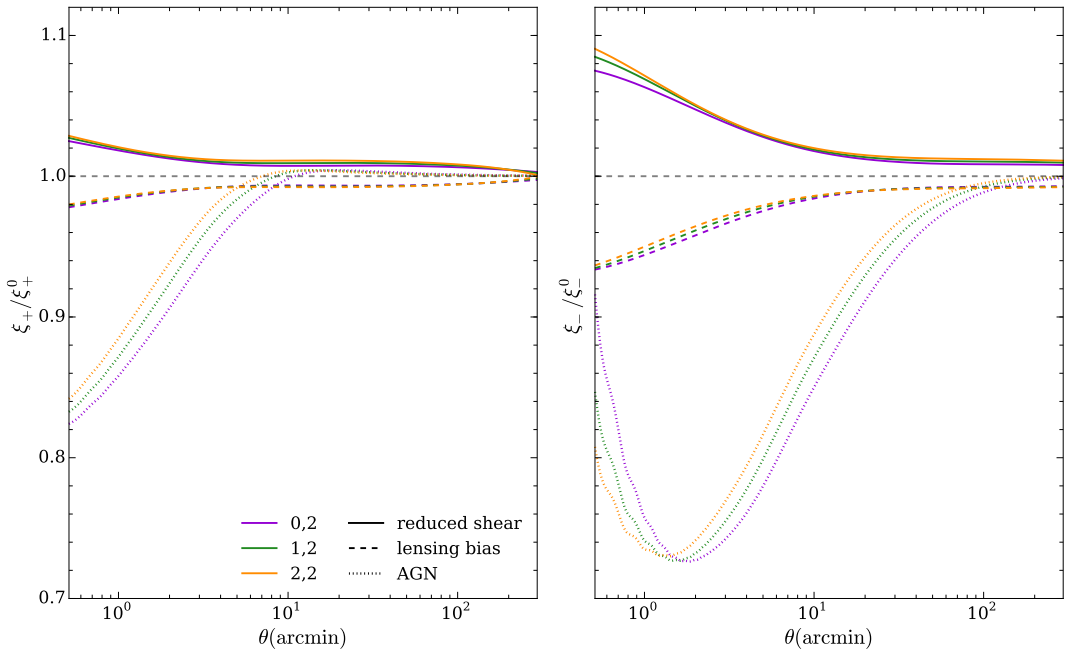


Figure 5.3: The fractional difference in the projected shear power spectrum from reduced-shear (solid lines) and lensing-bias (dashed lines) are compared to the contribution from the OWLS AGN model (dotted lines). I used the DES-SV tomographic redshift distributions, and for clarity only show the correlations with the highest redshift bin.

where

$$B^q_{ij}(\vec{l_1},\vec{l_2},\vec{l_3}) = \frac{1}{2}\int \frac{d\chi}{\chi^4} W_i(\chi)W_j(\chi)[q_i W_i(\chi) + q_j W_j(\chi)] B_\delta(\vec{l_1}/\chi, \vec{l_2}/\chi, \vec{l_3}/\chi; \chi). \tag{5.6}$$

The quantity $q_i$ is given by

$$q_i = 2\beta_f + \beta_r - 2 \tag{5.7}$$

where

$$\beta_f \equiv \int dr \int df \frac{\partial \epsilon(f,r)}{\partial(\ln(f))} \Phi(f,r) \tag{5.8}$$

$$\beta_r \equiv \int dr \int df \frac{\partial \epsilon(f,r)}{\partial(\ln(r))} \Phi(f,r). \tag{5.9}$$

$\epsilon(f,r)$ is the survey selection function in galaxy flux, $f$, and size, $r$; $\Phi(f,r)$ is the true galaxy distribution in flux and size. I make use of the Balrog simulations (Suchyta et al. 2016) to estimate $\epsilon(f,r)$ and $\Phi(f,r)$. Balrog is a method for simulating observed galaxy catalogs, by injecting simulated objects with known properties into real survey images. The resulting 'simulated' images therefore contain many of the important properties of the real data, including observational systematics that would be otherwise difficult to simulate, as well as a small[1] number of extra injected objects. The properties (both morphology and multi-band fluxes) of the inserted objects are based on COSMOS observations, which also have accurate redshifts. By running the same catalog creation software (in this case SExtractor) on these simulated images as is run on the real data, and then repeating the injection and catalog creation process many times over, we can estimate the mapping from the true properties of a galaxy to the properties estimated by SExtractor in our galaxy catalogs. For example, we can estimate the probability of detecting a galaxy with a particular true flux and size, or more

[1] small enough that we need not consider any interaction between the injected objects

generally, the survey selection function as defined above, $\epsilon(f, r)$. I estimate $\Phi(f, r)$ and $\epsilon(f, r)$ as follows:

1. I start with the SV NGMIX shape catalog (that used in The Dark Energy Survey Collaboration et al. (2015)), and the Balrog catalog used in Suchyta et al. (2016), the latter of which contains both 'observed' fluxes and sizes i.e. those estimated by SEXTRACTOR, as well as true fluxes, sizes (those used when drawing the simulated objects into the DES images) and redshifts. Note that the observed sizes are PSF-convolved.

2. For a given redshift bin of the SV ngmix data, I reweight the Balrog data to have the same redshift distribution. Then I compute $\Phi(f, r)$ using weighted kernel-density-estimation (KDE) in the true flux and size of these weighted Balrog objects. For the highest redshift SV bin, this is shown in the left panel of Figure 5.4.

3. I then reweight the Balrog data to have the same observed flux and size distribution as the NGMIX shape catalog, for that particular redshift bin. For the observed flux and size I use the $i-$band SEXTRACTOR quantities MAG_AUTO and FLUX_RADIUS to do this and make use of the HEP_ML package [2] to perfrom Gradient Boosting[3] reweighting. With this new set of weights, I again use weighted KDE to estimate $\Phi^{obs}(f, r)$, given by

$$\Phi^{obs}(f, r) = \epsilon(f, r)\Phi(f, r). \tag{5.10}$$

   This is shown in the middle panel of Figure 5.4, and as expected is shifted to larger flux and size than $\Phi(f, r)$, since brighter, larger objects are weighted more heavily in shape measurement.

[2] https://github.com/arogozhnikov/hep_ml
[3] https://en.wikipedia.org/wiki/Gradient_boosting

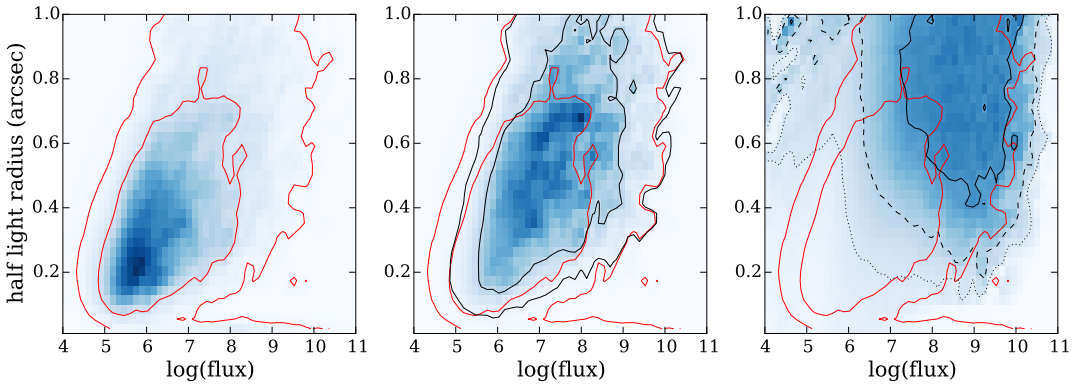


Figure 5.4: Flux-size distribution and selection function for the highest SV redshift bin. Left panel: The 'true' (i.e. pre-selection) distribution of log(flux) and half-light-radius, $\Phi(f, r)$, from the redshift-weighted Balrog truth catalog. Middle panel: The log(flux)-size distribution of observed SV galaxies $\Phi_{obs}(f, r)$, estimated by reweighting the Balrog catalogs to have the same *observed* flux and size distribution as the SV data. Right panel: The selection function $\epsilon(f, r) = \Phi_{obs}(f, r)/\Phi(f, r)$. For a reference I show the original flux-size distribution, $\Phi(f, r)$ as the red contours in each panel (the contours contain 95% and 68% of the probability).

4. I then estimate $\eta(f, r)$ as $\Phi^{obs}(f, r)/\Phi(f, r)$. This is shown in the right panel of Figure 5.4, and can become noisy in regions where $\Phi(f, r)$ is small, however, the smoothing from using KDE helps with this, and these regions do not contribute significantly to the integrals in 5.9.

Having estimated $\Phi(f, r)$ and $\epsilon(f, r)$, the expressions in 5.9 can be calculated and substituted into 5.7. I find $q_1 = -0.98, q_2 = -0.79, q_3 = -0.64$. I use these $q$ values to estimate the lensing-bias contribution to the shear power spectra (Figure 5.2, dashed lines), and the shear correlation functions (Figure 5.3, dashed lines). The lensing-bias correction has the same scale dependence and similar magnitude to the reduced-shear correction, but the negative values of $q_i$ make it negative, partially cancelling out the reduced-shear correction.

## 5.3 Blend exclusion bias: Estimates using BCC-UFig

As discussed in §2.1, accurately measuring the shape of a galaxy with a close neighbour is difficult. We categorise objects as *blended* if they overlap at a particular isophotal level, for example SExtractor identifies objects by first finding groups of contiguous pixels above some detection threshold, and then deciding how many objects to split these pixels into (this decision is part of the *deblending* process). If that number of objects is more than one, then these objects will be flagged as blended objects. Shape or photometry estimates (required for photo-z estimation) from these objects should be used with caution. Indeed in the DES-SV analyses, we excluded any objects that SExtractor judged to be blended.

Hartlap et al. (2011) realised that this exclusion of blended of objects produces a selection bias by the following mechanism: Blended objects are more likely to be in crowded regions of the sky (e.g. along the same line-of-sight as a cluster), and these crowded regions will have higher convergence than average (e.g. because of the aforementioned cluster). Therefore by excluding blended objects, we're undersampling the higher convergence regions of the sky, compared to the less-crowded, lower convergence regions. Thus we'll underestimate the shear two-point signal, especially on small scales, where sensitivity to those crowded, high convergence regions is highest. I'll call this effect *blend-exclusion bias*. Hartlap et al. (2011) estimated the magnitude of this effect by starting with a mock weak lensing catalog (produced from ray-traced N-body simulations), and cutting out galaxies based on various criteria, for example, they apply what they call the "FIX" criterion, where if a pair of galaxies is separated by less than some angle $\theta_{\rm FIX}$, they exclude one of those galaxies. For $\theta_{\rm FIX} = 2''(5'')$, they find a $-1(-2)\%$ bias in $\xi_+(\theta = 1\,\mathrm{arcmin})$, and a $-2(-7)\%$ bias in $\xi_-(\theta = 1\,\mathrm{arcmin})$.

These sorts of criteria give a useful indication of the expected bias, however,

on real data, the criteria we use for deciding whether to use a galaxy are often not so well defined. As I explained above, in DES-SV we used SExtractor to decide whether a galaxy is blended, and the behavior of SExtractor is dependent on the details of our images, for example the PSF, the noise levels, and the distribution of galaxy fluxes and sizes. These details are not captured in the approach taken by Hartlap et al. (2011), since they do not simulate survey images. The approach I take uses the BCC-UFig image simulations (Chang et al. 2015), which allows me to investigate the behavior of the same selections we use on the real data. The BCC-UFig simulations are images produced by starting with a cosmological mock galaxy simulation (the Blind Cosmology Challenge (BCC), Busha et al. 2013), with lensing information from ray-tracing, and using this as input to an image generator (the Ultra Fast Image Generator (UFIG), Bergé et al. 2013) which produces images with properties like noise levels, PSF properties, and galaxy flux and size distributions well-matched to DES data via an iterative approach. The BCC-UFig catalogs are then produced by running SExtractor on these simulated images.

I estimate the size of the selection bias as follows:

1. I start with the DES-SV shape catalogs, split into 3 redshift bins, and reweight the BCC-UFig catalog to have the same observed magnitude, size and redshift distribution. I again use the $i-$band SExtractor quantities MAG_AUTO and FLUX_RADIUS to match the magnitude and size distributions since I have these for both the SV data, and the BCC-UFig catalogs. I call this reweighted catalog the 'full' UFIG catalog.

2. I measure the shear correlation functions $\xi_{+/-}(\theta)$ from the full UFIG catalog, using the true input shears to the simulation. I use the true input shears, since the aim here is to isolate the selection bias, rather than study any other shape measurement biases. I call this signal $\xi^{\rm full}_{+/-}(\theta)$.

3. I then impose a cut on the SExtractor flag value in the full UFIG cat-

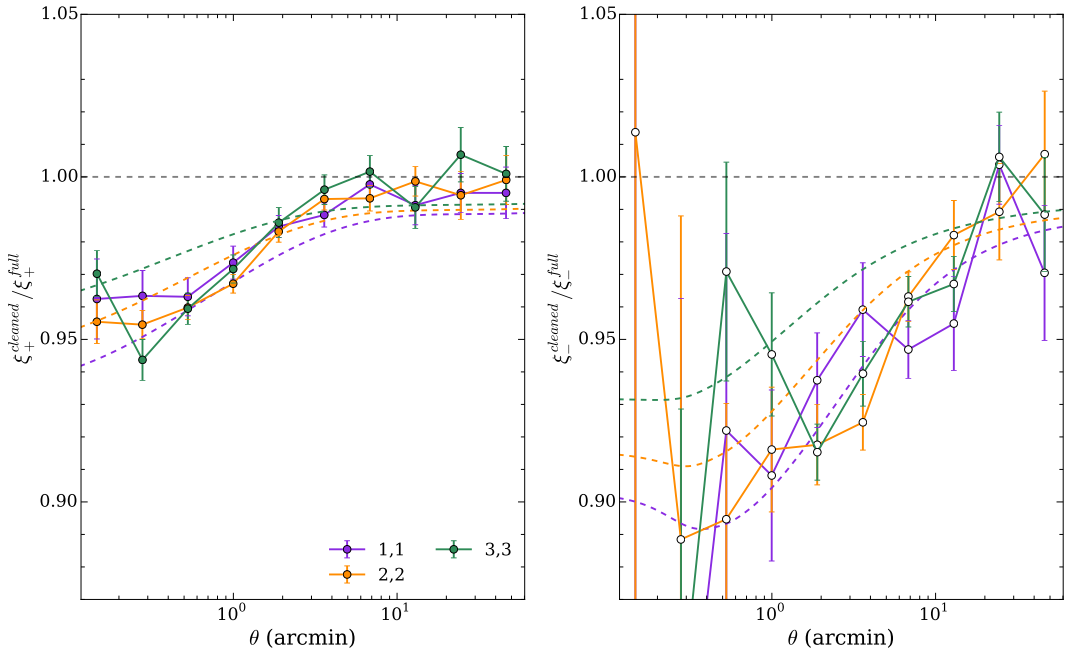


Figure 5.5: A measurement of blend-exclusion bias using BCC-UFig. The ratio of the shear correlation functions estimated from the BCC-UFig simulations after removing SExtractor blends, to the correlation functions using the full galaxy sample. The two samples were weighted to have the same redshift distributions, and the true input shears to the simulations were used to calculate $\xi_{+/-}$, in order to isolate the selection effect. The dashed lines shows the prediction of the toy model described in §5.3

alog that removes blended objects or those with bright, close neighbours (around 15% of the objects). This is the same cut that we applied to the DES-SV shape catalogs. I reweight the resulting catalog to have the same redshift distribution as the full UFIG catalog, and call this the 'cleaned' UFIG catalog. I measure the shear correlation functions from the cleaned UFIG catalog, and call this signal $\xi_{+/-}^{\rm cleaned}(\theta)$. Then the fractional bias is $\xi_{+/-}^{\rm cleaned}(\theta)/\xi_{+/-}^{\rm full}(\theta) - 1$.

The ratio $\xi_{+/-}^{\rm cleaned}(\theta)/\xi_{+/-}^{\rm full}(\theta)$ is plotted in Figure 5.5. I show only redshift auto-correlations for clarity, but there is no clear redshift dependence of the bias anyway. For $\xi_+$, the bias reaches $\sim 3\%$ at 1 arcmin, while for $\xi_-$, the bias reaches this level at 10-20 arcmin. Thus the effect is of the same order as found in Hartlap et al. (2011) and is similar in magnitude and scale-dependence to the reduced

shear and lensing-bias effects.

This similarity is perhaps not surprising, since this blend-exclusion bias can be thought of as a form of source-lens clustering. Motivated by this similarity, I formulate a toy model for the blend-exclusion bias. In this toy model, I assume the probability of a galaxy at $\boldsymbol{\theta}$ being blended depends only on the amount of light from neighbours in that area of sky. This can be quantified as the excess flux density (above the mean flux density), which I will call $\kappa_{\rm flux}(\boldsymbol{\theta})$. Consider the contribution to $\kappa_{\rm flux}(\boldsymbol{\theta})$ from a comoving volume element $dV$ at comoving distance $\chi$. The contribution to the excess flux in area element $d\Omega$ is

$$\Delta\kappa_{\rm flux}(\boldsymbol{\theta},\chi)d\chi\, d\Omega = \frac{\delta_L(\boldsymbol{\theta},\chi)}{4\pi d_L(\chi)^2}dV \tag{5.11}$$

where $d_L(\chi)$ is the luminosity distance. $\delta_L(\theta,\chi)$ is the comoving volume luminosity overdensity at $(\theta,\chi)$, given by

$$\delta_L(\boldsymbol{\theta},\chi) = \frac{L(\boldsymbol{\theta},\chi) - \bar{L}(\chi)}{\bar{L}(\chi)} \tag{5.12}$$

where $L(\boldsymbol{\theta},\chi)$ is the luminosity density at $(\boldsymbol{\theta},\chi)$ and $\bar{L}(\chi)$ is the mean luminosity density at comoving distance $\chi$. The comoving volume element can be replaced using $dV = \chi^2 d\chi\, d\Omega$, yielding

$$\Delta\kappa_{\rm flux}(\boldsymbol{\theta},\chi)d\chi = \frac{\delta_L(\boldsymbol{\theta},\chi)}{4\pi d_L(\chi)^2}\chi^2 d\chi\,. \tag{5.13}$$

I make the assumption that the luminosity overdensity $\delta_L(\theta,\chi)$ is proportional to the matter overdensity $\delta(\theta,\chi)$. This would be the case if galaxies did not evolve with redshfit, and had luminosity-independent bias (hence I call this a toy model!). Then

$$\Delta\kappa_{\rm flux}(\boldsymbol{\theta},\chi)d\chi \propto \frac{\chi^2\delta(\boldsymbol{\theta},\chi)}{d_L(\chi)^2}d\chi \tag{5.14}$$

and

$$\kappa_{\rm flux}(\boldsymbol{\theta}) \propto \int d\chi \, \frac{\chi^2 \delta(\boldsymbol{\theta}, \chi)}{d_L(\chi)^2}. \tag{5.15}$$

I assume that the observed galaxy overdensity (i.e. the fractional excess in galaxy number density) due to blending is proportional to the excess flux density $\kappa_{\rm flux}(\boldsymbol{\theta})$, so using equation 5.15,

$$\delta^{\rm blend}_{\rm obs}(\boldsymbol{\theta}) = \alpha \int d\chi \, \frac{\chi^2 \delta(\boldsymbol{\theta}, \chi)}{d_L(\chi)^2} d\chi \tag{5.16}$$

where $\alpha$ is a constant of proportionality, which we expect to be negative, since an excess in flux density should lead to more blending, and so a negative $\delta^{\rm blend}_{\rm obs}$.

Like the convergence, $\delta^{\rm blend}_{\rm obs}(\boldsymbol{\theta})$ is a projection in $\chi$ of the matter overdensity, $\delta$, but with a kernel

$$W'(\chi) = \frac{\alpha \chi^2}{d_L^2(\chi)} = \frac{\alpha \chi^2}{(1+z(\chi))^2 D_A^2(\chi)} \tag{5.17}$$

instead of the lensing kernel (c.f. equation 1.59). So the effect on the shear power spectrum can be calculated in exactly the same way as the reduced shear correction, but replacing the lensing kernels $[W_i(\chi) + W_j(\chi)]$ in equations 5.3 and 5.4, with $2W'(\chi)$.

The dashed lines Figure 5.5 show the prediction of this toy model, with $\alpha = -0.1$ showing qualitative agreement with the measurement from BCC-UFig.

## 5.4 Modelling baryonic effects on the matter power spectrum

We know from hydrodynamic simulations that baryonic physics can have a significant effect on the matter power spectrum at small scales. However, as I've described in §5.1, given the uncertainty in what sub-grid prescriptions to add to the simulations (as well as the uncertainties due to different results from differ-

ent implementations of the same sub-grid prescriptions!), the magnitude, scale-dependence and redshift dependence of the effect is very uncertain. So in order to extract any information from the small scales, a model or nuisance parameterisation, that is sufficiently flexible to describe the baryonic effects, is required. Judging how flexible is 'sufficiently' flexible is always a challenge when assessing the suitability of a nuisance parameterisation. The fact that a nuisance parameterisation is required means that we lack knowledge about the physical process. However, deciding on a parameterisation, and priors on the nuisance parameters, requires assumptions (presumably based on some knowledge) about the same physical process.

In the case of baryonic effects on the matter power spectrum, hydrodynamic simulations arguably provide a level of knowledge sufficient to justify a nuisance parameterisation or modeling approach. The proposal of Eifler et al. (2015) makes this assumption; they propose using PCA to identify modes with the most variance between multiple simulations with different baryonic treatments. These modes can either be projected out of the analysis (this is really just a cleverer way of cutting small scales), or some number of them marginalised over as nuisance parameters.

Another approach is to use a theoretical model for the matter power spectrum, with some physically motivated free parameters to account for possible baryonic effects. Zentner et al. (2008) showed that the effect of baryons on the matter power spectrum could be qualitatively reproduced in the halo model framework. The halo model (Seljak 2000; Peacock & Smith 2000) is an analytic model for the matter distribution in the Universe, that, given its simplicity, is extremely successful at reproducing the matter power spectrum, even on nonlinear scales. The model assumes that all matter is contained in spherical halos. The halo radial density profile is assumed to only depend on the mass of the halo. The statistical properties of the matter field are then set by three inputs: (i) the relation between the halo density profile and mass (ii) the number density of

halos of a given mass, and (iii) the large scale distribution of halos, which just depends on the (analytic) linear matter power spectrum. The halo density profile is usually the *NFW* profile (Navarro et al. 1996), which has one free parameter, the concentration. Input (i) is then the 'concentration-mass relation'. Input (ii) is the halo mass function, the fraction of halos in a given mass range. Both the concentration-mass relation and the halo mass function can be calibrated using N-body simulations.

Mead et al. (2015) use the halo model as a basis for which to tackle the problem of predicting the nonlinear matter power spectrum. They firstly implement various adjustments to the basic halo model I've described which are required to accurately predict the dark matter-only matter power spectrum. With these adjustments, they achieve a 5% matter power spectrum accuracy for $k \leq 10h\text{Mpc}^{-1}$, $z \leq 2$, which they judge by comparison with the Coyote Universe simulations. They further extend this halo model to account for baryonic effects. Since baryonic physics are likely to change the internal structure of halos, but have a lesser effect on their positions or total masses, they propose two extra nuisance parameters to allow for the former: $A$, a constant in the concentration-mass relation (i.e. increasing $A$ makes halos of a given mass more concentrated), and $\eta_0$, which they descriptively call the 'halo bloating parameter', because it allows bloating in the halo profile. They test this parameterisation by fitting the model to three of the OWLS simulations, and in all cases achieve similar accuracy in the matter power spectrum as for the dark matter only case (at the cost of these two extra nuisance parameters). I'll refer to this extended halo model as the 'Mead+15' model. In §5.6, I fit the Mead+15 model to small-scale cosmic shear measurements from DES-SV.

## 5.5 Small-scale extended DES SV shear correlation functions

In this section I extend the DES-SV shear correlation function measurements to smaller scales. Figure 5.6 shows measurements of the shear correlation functions $\xi_{+/-}$ in 10 angular bins between 0.5 and 120 arcminutes for the tomographic case (12 top-right panels), and 20 angular bins between 0.5 and 120 arcminutes for the non-tomographic case (2 bottom-right panels). There is a significant signal at scales down to an 0.5 arcminutes, particularly for the highest redshift bin, and for the non-tomographic measurements. At scales less than a few arcminutes, diagonal shape-noise is the dominant contribution to the covariance, so the data points are only weakly correlated.

For the Chapter 4 analysis I used a covariance matrix calculated from 126 mock survey simulations, as described in Becker et al. (2015b). In Becker et al. (2015b) we discuss the limitations on the accuracy of the parameter constraints that can be achieved when the number of simulation realisations is not much greater than the number of data points in the data vector. The extended tomographic data vector that I have measured has 120 data points, so this requirement is clearly not satisfied. I therefore use the following approach. A jackknife covariance (see e.g. Norberg et al. 2009; Friedrich et al. 2016) reliably captures the noise properties of the data on scales much smaller than the size of the jackknife patches. I compute a jackknife covariance matrix using 250 jackknife patches. The area of the DES-SV data is $139\,\mathrm{deg}^2$, so the patches typically have size $\sim 40$ arcminutes.

Meanwhile, on large scales, the weak lensing convergence field (and therefore shear fields) is well described by Gaussian statistics, so a simple approximation to the cosmic shear covariance can be obtained by generating many Gaussian random fields with the expected shear power spectrum, and computing a sample covariance matrix using the same method as on the mocks. Since generation of

the Gaussian realisations is very fast, the covariance uncertainty due to having a finite number of realisations can be made negligible. On smaller scales, the convergence field is sensitive to nonlinearities in the density field, and the Gaussian approximation is no-longer a good approximation. However, Taruya et al. (2002) and Takahashi et al. (2011) demonstrate that lognormal statistics provide a good description of the convergence field, while Hilbert et al. (2011) demonstrate that a covariance matrix obtained under the lognormal approximation is very effective, resulting in very accurate confidence intervals on cosmological parameters, even when using sub-arcminute scales.

For the non-tomographic data vector described above, Figure 5.7 show a comparison of the correlation matrices from the three methods I've mentioned, the 126 mock surveys, the jackknife method, and the lognormal realisations. The jackknife method captures the small scale features accurately, but is not valid on large scales, comparable to the jackknife patch size. The lognormal realisations are able to reproduce the large scale features seen in the noisy mock covariance - strong off diagonals in the $\xi_+$ covariance, as well as weaker off diagonal terms in the $\xi_+, \xi_-$ cross covariance.

For the parameter estimation in §5.6, I use a composite covariance: jackknife on scales less than 5', lognormal otherwise. I have checked that the results are not very sensitive to using purely the lognormal covariance. I have also verified that the composite covariance agrees well with the mock covariance on the smaller data vector used in Chapter 4.

## 5.6 Halo-model constraints from small-scale cosmic shear

In this section I present constraints on the Mead+15 halo model (described in §5.4), using the shear correlation function measurements from §5.5.

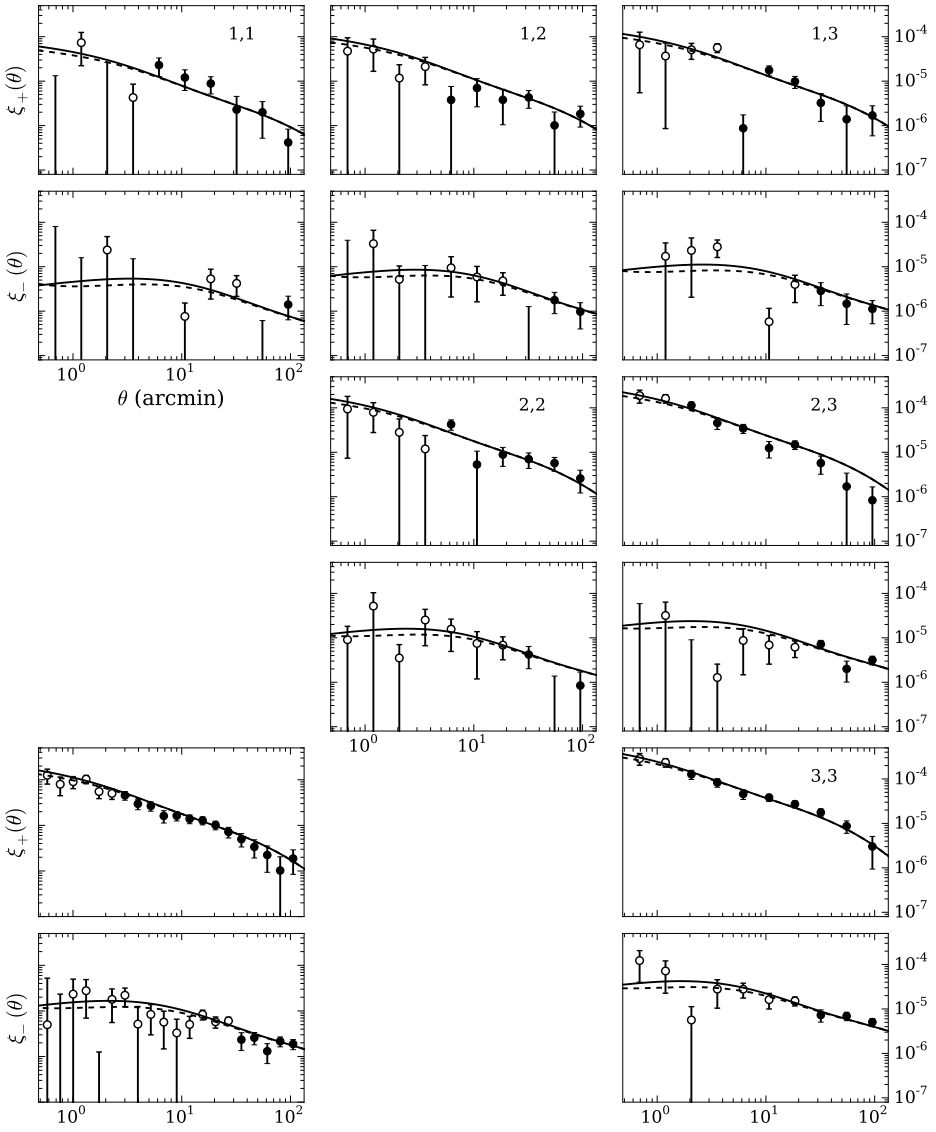


Figure 5.6: Shear correlation functions, $\xi_{+/-}$ from DES-SV data, now using a data vector extended to smaller scales than in DES15 (open symbols indicate these smaller scales). The two bottom-left panel show the non-tomographic measurement. The other panels show the tomographic measurement, with the bin pairing in the upper right corner of each $\xi_+$ panel, and the corresponding $\xi_-$ measurement in the panel below.

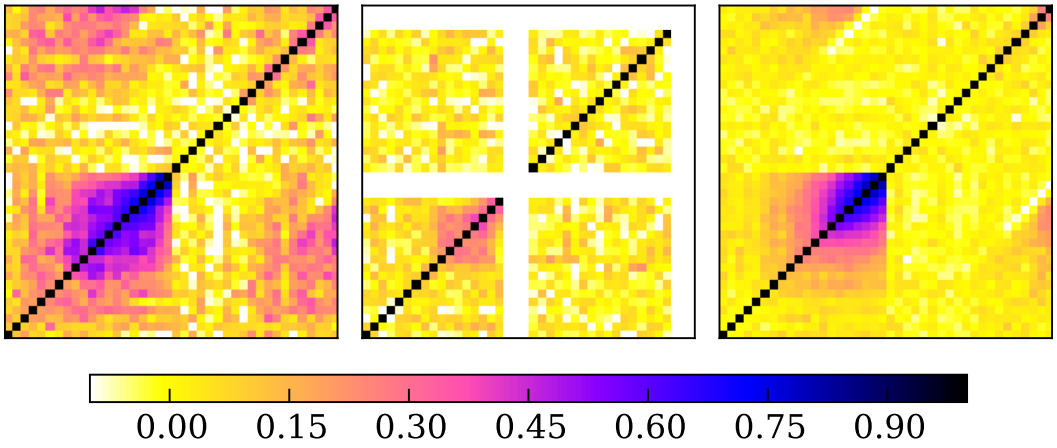


Figure 5.7: A comparison of covariance matrix estimation methods. Shown are correlation matrices estimated via 126 mock surveys (left panel), jackknife resampling (middle panel), and 1000 lognormal realisations (right panel).

I restrict this study to the sensitivity of cosmic shear to the baryonic effects, and therefore fix the cosmological model to the Planck 2015 best-fit ΛCDM model. As well as varying the Mead+15 halo model parameters $A$ and $\eta_0$, I marginalise over the same 7 (3 for the non-tomographic case) nuisance parameters as used in the DES15 analysis - an intrinsic alignment amplitude, a shear calibration uncertainty parameter per redshift bin, and a photo-$z$ uncertainty parameter per redshift bin. Figure 5.8 shows the constraints on $A$ and $\eta_0$ from DES-SV cosmic shear, for three different data vectors. The purple contour uses the same non-tomographic measurements as in DES15, but without making any scale cuts (i.e. 15 angular bins from 2 to 300 arcminutes). The green contour is from the extended non-tomographic measurement (20 angular bins between 0.5 and 120 arcminutes), while the orange outlined contour is from the extended tomographic measurement (3 redshift bins, 10 angular bins between 0.5 and 120 arcminutes). The black markers indicate the best-fit halo model parameters for four different OWLS simulations, as calculated by Mead et al. (2015). The plus is the 'REF' simulation, which contains star formation, chemical enrichment, supernovae feedback, and

gas cooling. The cross is the 'AGN' simulation which includes AGN feedback in addition to the effects in 'REF'. The triangle is the DBLIM simulation, which is again similar to REF, but incorporates a top-heavy stellar initial mass function, and additional supernova wind velocity. The circle indicates the the fit to the Coyote Universe simulations i.e. no baryonic effects. While the SV constraints are not powerful enough to significantly favour or disfavour any of the scenarios, there is preference for low $A$, and high $\eta_0$, as in the AGN simulation.

Figure 5.9 shows forecasted DES Year 1 (Y1) constraints on the halo model parameters. I perform the forecast by using a 'simulated' data vector predicted from theory, and running an MCMC chain as in a real data analysis. For the simulated data vector I use the halo model parameters corresponding to the no baryons case. The size of the contours indicates whether the Y5 data will have the statistical power to rule out other baryonic scenarios. For the green filled contours, I apply the reduced shear correction from equation 5.3 to the simulated data vector, for the orange outline contours I apply the lensing bias correction from equation 5.53, while the data vector for the purple contours includes neither correction. When I fit the simulated data vectors, I include neither of these corrections, so the shift between the contours illustrates the importance of these corrections. The observed shifts in the contours due to these corrections are small compared to the difference between the baryonic models in this parameter space. For the Y1 covariance matrix, I simply rescaled the SV covariance by the ratio of the SV area to the expected Y1 area. Even when including the same levels of systematic errors as we used in SV[4], the upper panel of Figure 5.9 demonstrates that the DES Y1 cosmic shear measurements have the potential to rule out certain baryonic scenarios, such as the AGN model. This potential will be increased if improvements in the quality of shape measurements and photometric redshifts allow a reduction in the priors on systematic errors, as indicated by the bottom panel, for which I did not marginalize over the systematics nuisance parameters.

[4]which would be disastrous for the cosmology constraints by the way!

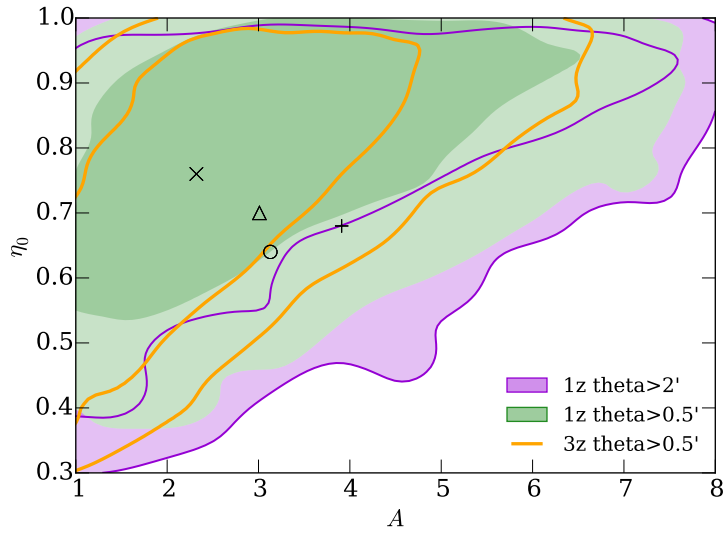


Figure 5.8: DES-SV cosmic shear constraints on the two nuisance parameters of the Mead+15 halo model. The data vector has been extended to small scales than the original analysis (Chapter 4, The Dark Energy Survey Collaboration et al. 2015). The purple and green contours are non-tomographic and use angular scales $2' < \theta < 300'$ and $0.5' < \theta < 120'$ respectively. The orange contour is tomographic (3 redshift bins), and uses angular scales $0.5' < \theta < 120'$. The black markers show the best-fit parameters for several different OWLS simulations, as estimated by Mead et al. (2015). The plus is 'REF', the cross is 'AGN', the triangle is 'DBLIM' and the circle is dark matter-only (see Schaye et al. 2010; Mead et al. 2015 for descriptions of the OWLS simulation names).

## 5.7 Discussion

The small scales of cosmic shear measurements are rich in both signal-to-noise, and difficult-to-model systematic uncertainties. Baryonic effects present the largest systematic uncertainty, with $10-20\%$ deviations from the dark matter-only case on arcminute scales predicted by some hydrodynamic simulations. The prospects for gaining useful cosmological information from the small scales of cosmic shear do not look bright given these uncertainties. However, small scale cosmic shear measurements do still provide unique observational constraints on the small-scale matter clustering, from which can be inferred the relative likelihood of different baryonic scenarios. Information from future DES data, which has the potential to differentiate between baryonic scenarios, could be fed back into future hydro-

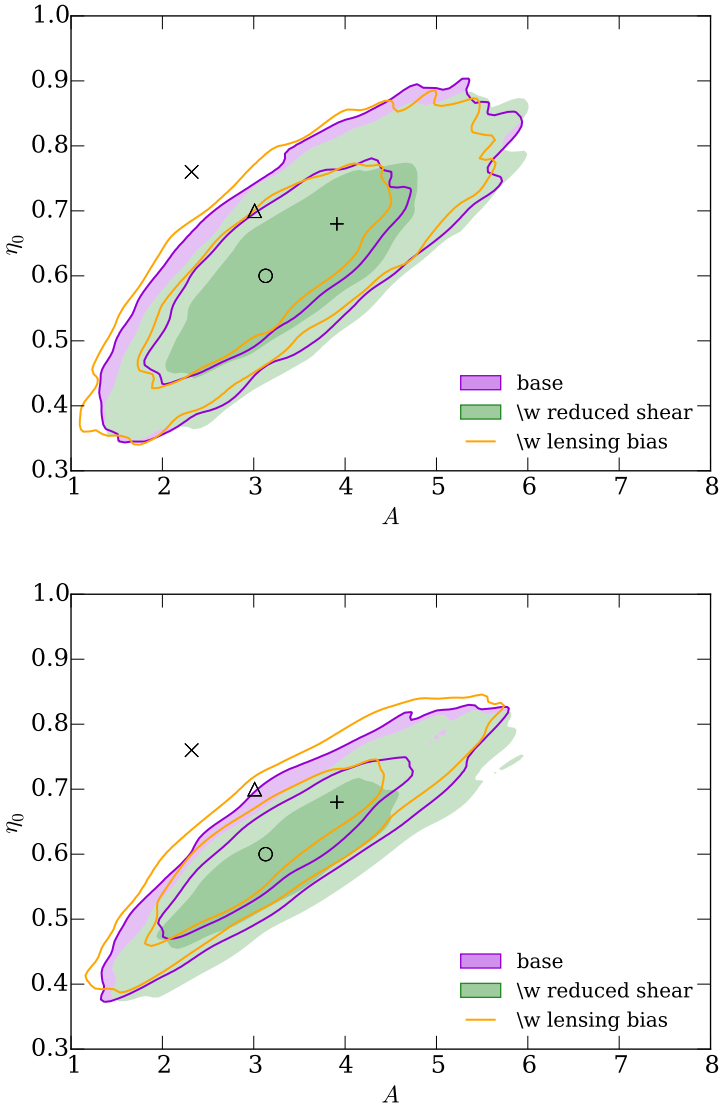


Figure 5.9: Expected constraints on the Mead+15 model from DES Year 1, with (upper panel) and without (lower panel) marginalising over the same 7 nuisance parameters used in DES15. I assume the same tomographic data vector as I used in the SV small-scale analysis i.e. three redshift bins, and 10 angular bins between $0.5' < \theta < 120'$. For the green (orange) contours, I include a correction to the simulated data vector for reduced shear (lensing bias). When fitting the simulated data vector, I do not include either correction, hence the difference between the contours demonstrates the importance of these corrections. The black markers are described in the text, and in the caption to Figure 5.8.

dynamic simulations, which in turn will hopefully improve our ability to model the small scale clustering. In order to make robust conclusions about baryonic physics from small scale cosmic shear, other non-negligible systematics should be accounted for, such as the reduced shear correction and lensing bias. I've shown how these terms can be modeled, and that they are sub-dominant, but not negligible compared to the theoretical uncertainty due to baryonic physics. Intrinsic alignments on nonlinear scales will also have to be accounted for, which will require advances in theoretical modeling or simulation of the phenomenon, since most of the popular modeling approaches used today are valid only on linear or mildly nonlinear scales.

## 5.A Third order corrections to shear-shear correlations

In cosmic shear, we attempt to measure the two-point correlation of the shear, possibly between two different redshift bins $i$ and $j$

$$\xi_{i,j} = \langle \gamma_i(\vec{x})\gamma_j(\vec{x'})\rangle. \tag{5.18}$$

Contributions to shear-shear two-point correlation at third order in the density field arise from two effects

1. We observe the *reduced shear*,

$$g(\vec{x}) = \frac{\gamma(\vec{x})}{1-\kappa(\vec{x})} \approx (1+\kappa(\vec{x}))\gamma(\vec{x}). \tag{5.19}$$

2. We can only estimate the shear at positions of galaxies. So any statistic (e.g. mean shear or $\xi_{+/-}$) estimated from the measured shears will effectively be

using the galaxy number-density weighted reduced shear:

$$g^{obs}(\vec{x}) = (1 + \delta_{\rm obs}(\vec{x}))g(\vec{x})) \tag{5.20}$$

$$= (1 + \delta_{\rm obs}(\vec{x}))(1 + \kappa(\vec{x}))\gamma(\vec{x}) \tag{5.21}$$

where $\delta_{\rm obs}(\vec{x})$ is the observed overdensity in galaxy number at position $\vec{x}$. This observed overdensity can be due to a true change in the number density of galaxies (for example due to the presence of a cluster), or due to a change in the *observable* number density due to lensing magnification (for example due to the presence of a cluster at lower redshift). The first effect leads to *source-lens clustering* (Bernardeau 1998; Hamana et al. 2002) and the second leads to *lensing-bias* (Schmidt et al. 2009).

We start with the expression from Schmidt et al. (2009) for the expectation of the standard $\xi_{+/-}$ estimator (and using the substitution in 5.21)

$$\langle \xi_{ij}^{\rm obs} \rangle = \left\langle \frac{(1 + \delta_{\rm obs}(\vec{x})(1 + \kappa(\vec{x}))\gamma_i(\vec{x})(1 + \delta_{\rm obs}(\vec{x'}))(1 + \kappa(\vec{x'}))\gamma_j(\vec{x'})}{1 + 2\overline{\delta_{\rm obs}} + \widehat{\delta_{\rm obs}\delta_{\rm obs}}} \right\rangle \tag{5.22}$$

where $\overline{\delta_{\rm obs}}$ is the mean observed galaxy overdensity across the survey (negligible for a wide survey), $\widehat{\delta_{\rm obs}\delta_{\rm obs}}$ is a mean product of overdensities smoothed over the bin width ($\xi_{gg}(\theta)$ in the limit of an infinite survey and narrow bin). The terms up to third order in $\gamma$, $\kappa$ or $\delta$ are

$$\begin{aligned} \langle \xi_{ij}^{obs} \rangle =& \langle \gamma_i(\vec{x})\gamma_j(\vec{x'}) \rangle \\ &+ \langle \kappa(\vec{x})\gamma_i(\vec{x})\gamma_j(\vec{x'}) \rangle + \langle \gamma_i(\vec{x})\kappa(\vec{x'})\gamma_j(\vec{x'}) \rangle \\ &+ \langle \delta_{\rm obs}(\vec{x})\gamma_i(\vec{x})\gamma_j(\vec{x'}) \rangle + \langle \gamma_i(\vec{x})\delta_{\rm obs}(\vec{x'})\gamma_j(\vec{x'}) \rangle. \end{aligned} \tag{5.23}$$

The first line is the 'true' shear-shear signal. The second line is the reduced shear contribution, which is only zero if the convergence $\kappa$ is not correlated with the shear at a given point on the sky, which is not likely. The third line is the

source-lens clustering (including 'lensing bias', since magnification contributes to $\delta_{\rm obs}$). This would be zero if there was no correlation between the source galaxy overdensity and the shear at a given point on the sky e.g. if source galaxies were randomly distributed.

It's more convenient to compute these term in Fourier space, as

$$\langle \gamma_i^{obs}(\vec{l},\chi)\gamma_j^{obs,*}(\vec{l''},\chi')\rangle = \ \langle \gamma_i(\vec{l},\chi)\gamma_j^*(\vec{l''},\chi')\rangle + \ R_{ij} + R_{ji} + S_{ij} + S_{ji} \tag{5.24}$$

where

$$R_{ij} = \langle (\kappa_i\gamma_i)(\vec{l},\chi)\gamma_j^*(\vec{l''},\chi'))\rangle \tag{5.25}$$

$$R_{ji} = \langle \gamma_i(\vec{l},\chi)(\kappa_j\gamma_j)^*(\vec{l''},\chi')\rangle \tag{5.26}$$

$$S_{ij} = \langle (\delta_{{\rm obs},i}\gamma_i)(\vec{l},\chi)\gamma_j^*(\vec{l''},\chi'))\rangle \tag{5.27}$$

$$S_{ji} = \langle \gamma_i(\vec{l},\chi)(\delta_{{\rm obs},j}\gamma_j)^*(\vec{l''},\chi')\rangle \tag{5.28}$$

and subscripts $i$ and $j$ denote shears/overdensities/convergences taken from redshift bins $i$ and $j$. In Fourier space, the multiplicative adjustments to the shear become convolutions i.e.

$$(\kappa\gamma)(\vec{l}) = \int \frac{d^2l'}{(2\pi)^2}\gamma(\vec{l'})\kappa(\vec{l}-\vec{l'}) \tag{5.29}$$

$$(\delta_{\rm obs}\gamma)(\vec{l}) = \int \frac{d^2l'}{(2\pi)^2}\gamma(\vec{l'})\delta_{\rm obs}(\vec{l}-\vec{l'}). \tag{5.30}$$

So

$$R_{ij} = \int \frac{d^2l'}{(2\pi)^2} \langle \gamma_i(\vec{l'}, \chi) \kappa_i(\vec{l} - \vec{l'}, \chi) \gamma_j^*(\vec{l''}, \chi') \rangle \tag{5.31}$$

$$R_{ji} = \int \frac{d^2l'}{(2\pi)^2} \langle \gamma_i(\vec{l}, \chi) \gamma_j^*(\vec{l'}, \chi') \kappa_j(\vec{l''} - \vec{l'}, \chi') \rangle \tag{5.32}$$

$$S_{ij} = \int \frac{d^2l'}{(2\pi)^2} \langle \delta_{\mathrm{obs},i}(\vec{l'}, \chi) \gamma_i(\vec{l} - \vec{l'}, \chi) \gamma_j^*(\vec{l''}, \chi') \rangle \tag{5.33}$$

$$S_{ji} = \int \frac{d^2l'}{(2\pi)^2} \langle \gamma_i(\vec{l}, \chi) \gamma_j^*(\vec{l'}, \chi') \delta_{\mathrm{obs},j}^*(\vec{l''} - \vec{l'}, \chi') \rangle. \tag{5.34}$$

We use the following:

$$\gamma_i(\vec{l}) = e^{2i\phi_l} \kappa_i(\vec{l}) \tag{5.35}$$

$$\kappa_i^*(\vec{l}) = \kappa_i(-\vec{l}) \tag{5.36}$$

$$\delta_{\mathrm{obs},i}^*(\vec{l}) = \delta_{\mathrm{obs},i}(-\vec{l}) \tag{5.37}$$

where $\phi_l$ is the angle made by $\vec{l}$ with the $x$-axis, to obtain

$$R_{ij} = \int \frac{d^2l'}{(2\pi)^2} e^{2i(\phi_{l'} - \phi_{l''})} \langle \kappa_i(\vec{l'}, \chi) \kappa_i(\vec{l} - \vec{l'}, \chi) \kappa_j(-\vec{l''}, \chi') \rangle \tag{5.38}$$

$$R_{ji} = \int \frac{d^2l'}{(2\pi)^2} e^{2i(\phi_l - \phi_{l'})} \langle \kappa_i(\vec{l}, \chi) \kappa_j(-\vec{l'}, \chi') \kappa_j(l' - \vec{l''}, \chi') \rangle \tag{5.39}$$

$$S_{ij} = \int \frac{d^2l'}{(2\pi)^2} e^{2i(\phi_{l'} - \phi_{l''})} \langle \kappa_i(\vec{l'}, \chi) \delta_{\mathrm{obs},i}(\vec{l} - \vec{l'}, \chi) \kappa_j(-\vec{l''}, \chi') \rangle \tag{5.40}$$

$$S_{ji} = \int \frac{d^2l'}{(2\pi)^2} e^{2i(\phi_l - \phi_{l'})} \langle \kappa_i(\vec{l}, \chi) \kappa_j(-\vec{l'}, \chi') \delta_{\mathrm{obs},j}(\vec{l'} - \vec{l''}, \chi') \rangle. \tag{5.41}$$

We can write the reduced shear terms $R_{ij}$ and $R_{ji}$ in terms of the convergence bispectrum, $B_{(\kappa_1,\kappa_2,\kappa_3)}(\vec{l_1}, \vec{l_2}, \vec{l_3})$ defined as

$$\langle \kappa_i(\vec{l_1}) \kappa_j(\vec{l_2}) \kappa_k, (\vec{l_3}) \rangle = \ (2\pi)^2 \delta_D(\vec{l_1} + \vec{l_2} + \vec{l_3}) B_{(\kappa_1,\kappa_2,\kappa_3)}(\vec{l_1}, \vec{l_2}, \vec{l_3}). \tag{5.42}$$

This can be related to the matter bispectrum using the Limber approximation

$$B_{(\kappa_1,\kappa_2,\kappa_3)}(\vec{l_1},\vec{l_2},\vec{l_3}) = \int \frac{d\chi}{\chi^4} W_1(\chi)W_2(\chi)W_3(\chi)B_\delta(\vec{k_1},\vec{k_2},\vec{k_3};\chi) \tag{5.43}$$

where $W_i(\chi)$ is the lensing kernel for redshift bin $i$ and $\vec{k_1} = \vec{l_1}/\chi$ etc. Note the $\delta_D(\vec{l_1}+\vec{l_2}+\vec{l_3})$ enforces a triangle configuration of the three vectors. So $R_{ij}$ and $R_{ji}$ become

$$R_{ij} = \int \frac{d^2l'}{(2\pi)^2} e^{2i(\phi_{l'}-\phi_{l''})}(2\pi)^2 B_{(\kappa_i,\kappa_i,\kappa_j)}(\vec{l'},\vec{l}-\vec{l'},-\vec{l}) \tag{5.44}$$

$$R_{ji} = \int \frac{d^2l'}{(2\pi)^2} e^{2i(\phi_l-\phi_{l'})}(2\pi)^2 B_{(\kappa_i,\kappa_j,\kappa_j)}(\vec{l},-\vec{l'},l'\vec{-}l). \tag{5.45}$$

We can write the LHS of 5.24 as

$$\langle\gamma_i(\vec{l})\gamma_j^*(\vec{l''})\rangle = \ (2\pi)^2\delta^D(\vec{l}-\vec{l''})C_{ij}^\kappa(l), \tag{5.46}$$

so the change in $C_{ij}^\kappa(l)$ due to reduced shear is

$$\begin{aligned}\delta_{red}C_{ij}^\kappa(l) &= [R_{ij}+R_{ji}]/(2\pi)^2 \\ &= \int \frac{d^2l'}{(2\pi)^2} e^{2i(\phi_{l'}-\phi_l)}\ B_{(\kappa_i,\kappa_i,\kappa_j)}(\vec{l'},\vec{l}-\vec{l'},-\vec{l}) \\ &+ e^{2i(\phi_l-\phi_{l'})}B_{(\kappa_i,\kappa_j,\kappa_j)}(\vec{l},-\vec{l'},\vec{l'}-\vec{l}).\end{aligned} \tag{5.47}$$

If this isn't a sufficiently final-looking result for your tastes, we can get to equation 13 of Shapiro (2009) by taking the real part, assuming some symmetry properties of the convergence bispectrum ($B(\vec{l_1},\vec{l_2},\vec{l_3}) = B(-\vec{l_1},-\vec{l_2},-\vec{l_3})$ and $B(\vec{l_1},\vec{l_2},\vec{l_3}) = B(\vec{l_3},\vec{l_1},\vec{l_2})$) and defining the '2-redshift convergence bispectrum'

$$B_{ij}(\vec{l_1},\vec{l_2},\vec{l_3}) = \ \frac{1}{2}\int \frac{d\chi}{\chi^4} W_i(\chi)W_j(\chi)[W_i(\chi)+W_j(\chi)]B_\delta(\vec{k_1},\vec{k_2},\vec{k_3};\chi), \tag{5.48}$$

which in my notation is equal to

$$\frac{1}{2}[B_{(\kappa_i,\kappa_i,\kappa_j)}(\vec{l_1},\vec{l_2},\vec{l_3}) + B_{(\kappa_i,\kappa_j,\kappa_j)}(\vec{l_1},\vec{l_2},\vec{l_3})]. \tag{5.49}$$

Substituting into equation 5.47

$$\delta_{red}C^{\kappa}_{ij}(l) = \ 2\int \frac{d^2l'}{(2\pi)^2}\cos(2\phi_{l'} - 2\phi_l)\ B_{ij}(\vec{l'},\vec{l}-\vec{l'},-\vec{l}). \tag{5.50}$$

Now let's move on to the $S_{ij}$ and $S_{ji}$ terms. Various things can cause a galaxy overdensity $\delta_{obs}$, but we're concerned with ones that are correlated with the density field. These arise from two sources. The first and most obvious one is if the source galaxies trace the density field e.g. with some linear bias $b_g$

$$\delta_{\mathrm{obs},i}(\vec{l},\chi) = N_i(\chi)b_g(\chi)\delta(\vec{l},\chi). \tag{5.51}$$

Then we have

$$S_{ij} = \int \frac{d^2l'}{(2\pi)^2}e^{2i(\phi_{l'}-\phi_{l''})}\langle\kappa_i(\vec{l'},\chi)b_g(\chi)N_i(\chi)\delta(\vec{l}-\vec{l'},\chi)\kappa_j(-\vec{l''},\chi')\rangle. \tag{5.52}$$

In the Limber approximation (in which we assume density fluctuations at different radial distance are uncorrelated), this term goes to zero, by the following argument: $\kappa_i(\vec{l'},\chi)$ only depends on the density field for radial distances less than $\chi$, and so is uncorrelated with $\delta(\vec{l}-\vec{l'},\chi)$. $\kappa_j(-\vec{l''},\chi')$ gets contributions from density fluctuations all along the line of sight. Those produced by fluctuations at $\chi'! = \chi$ will be uncorrelated with $\delta(\vec{l}-\vec{l'},\chi)$, so for $\chi'! = \chi$, $\delta(\vec{l}-\vec{l'},\chi)$ is correlated with neither $\kappa_i(\vec{l'},\chi)$ or $\kappa_j(\vec{l'},\chi')$. The contribution to $\kappa_j(-\vec{l''},\chi')$ produced by fluctuations at $\chi' = \chi$ will be correlated with $\delta(\vec{l}-\vec{l'},\chi)$, but uncorrelated with $\kappa_i(\vec{l'},\chi)$. In both these cases, one of the variables in the 3-point correlator is uncorrelated with the other two, and since all variables have zero mean, the 3-point correlation is zero. Hence for $\delta_{\mathrm{obs}}(\chi)$ satisfying $\langle\delta_{\mathrm{obs}}(\chi)\delta(\chi')\rangle = \delta^D(\chi-\chi')\langle\delta_{\mathrm{obs}}(\chi)\delta(\chi')\rangle$,

$S_{ij} = S_{ji} = 0$. This is the source-lens clustering term which is zero in the Limber approximation (see Valageas 2014 for a treatment beyond the Limber approximation).

From Schmidt et al. (2009), the lensing-bias produces an observed galaxy overdensity $\delta_{\mathrm{obs},i}(\vec{\theta},\chi) = q_i\kappa_i(\vec{\theta},\chi)$ (to first order in $\kappa$), where $q$ is a constant that depends on the survey selection function. In this case, $S_{ij} = q_i R_{ij}$, and we get the same result as in the reduced-shear case, but for the $q_i$ prefactors

$$\begin{aligned}\delta_{\mathrm{lensing}}C^{\kappa}_{ij}(l) &= [q_i R_{ij} + q_j R_{ji}]/(2\pi)^2 \\ &= \int \frac{d^2l'}{(2\pi)^2}\cos(2\phi_{l'} - 2\phi_l)B^q_{ij}(\vec{l'}, \vec{l} - \vec{l'}, -\vec{l})\end{aligned} \tag{5.53}$$

where

$$B^q_{ij}(\vec{l_1},\vec{l_2},\vec{l_3}) = \frac{1}{2}\int \frac{d\chi}{\chi^4}W_i(\chi)W_j(\chi)[q_iW_i(\chi) + q_jW_j(\chi)]B_\delta(\vec{l_1}/\chi,\vec{l_2}/\chi,\vec{l_3}/\chi;\chi). \tag{5.54}$$

This is a generalisation for tomography of the result of Schmidt et al. (2009), who did not consider multiple redshift bins. Schmidt et al. (2009) show that the factor q has contributions from three effects. Let $f$, $r$ and $\vec{\theta}$ denote the observed flux, size and position of a galaxy, and $f_g$, $r_g$ and $\vec{\theta_g}$ the corresponding intrinsic (*unlensed*) quantities. To first order in $\kappa$, the observed and intrinsic properties are related via

$$\vec{\theta} = \vec{\theta_g} + \delta\vec{\theta},\ f = Af_g,\ r = \sqrt{A}r_g,\ d^2\vec{\theta} = Ad^2\vec{\theta_g} \tag{5.55}$$

where $A = 1 + 2\kappa$. The first contribution to the observed galaxy overdensity comes from the change in the observed area element - a small patch of unlensed sky of area $\delta\theta^2$ has area $A\delta\theta^2$ due to lensing, and so $\delta_{\mathrm{obs}}$ is reduced by a factor $A$. The second and third contributions come from the effect of magnification on the observed galaxies fluxes and sizes. In positive convergence regions, the mag-

nification produces larger brighter galaxies, which are more likely to be detected and have well-measured shapes. Schmidt et al. (2009) show that the observed galaxy overdensity can be written as

$$\delta_{\rm obs}(\vec{\theta},\chi) = q\kappa(\vec{\theta},\chi) = (2\beta_f + \beta_r - 2)\kappa(\vec{\theta},\chi) \tag{5.56}$$

where

$$\beta_f \equiv \int dr \int df \frac{\partial\epsilon(f,r)}{\partial(\ln(f))}\Phi(f,r) \tag{5.57}$$

$$\beta_r \equiv \int dr \int df \frac{\partial\epsilon(f,r)}{\partial(\ln(r))}\Phi(f,r). \tag{5.58}$$

$\epsilon(f,r)$ is the selection function (i.e. accounts for the exclusion of faint, small galaxies) and $\Phi(f,r)$ is the true galaxy distribution in flux and size. These functions are normalised such that $\int df \int dr\epsilon(f,r)\Phi(f,r) = 1$. Hence if $\epsilon(f,r)$ is an increasing function of flux and size, $\beta_f$ and $\beta_r$ will be positive, since we'll observe a higher galaxy number density due to the magnification when $\kappa$ is positive.

# Chapter 6

# Concluding Remarks

Weak gravitational lensing provides a wealth of information about the matter distribution and the geometry of the Universe. Its power arises from its sensitivity to the perturbations of the total matter, rather than relying on e.g. galaxy or cluster positions to trace the perturbations. This information undoubtedly contains the signatures of exciting new fundamental physics, like dark energy and neutrino physics. The challenge is extracting unbiased measurements of weak lensing statistics, and also modelling the aforementioned signatures on these weak lensing statistics.

## 6.1 Summary

In Chapter 2 I detailed some of the challenges to obtaining cosmology from weak lensing, often in the context of recent work on the Dark Energy Survey. I identified four key sources of systematic uncertainties. The first of these is estimating the shear which, despite many advances in the last two decades, is still a notoriously difficult problem. As well as the generic problem of fitting a nonlinear function to noisy data, shape measurement is complicated by many other potential sources of bias, like the model bias, which arises when an insufficiently flexible model is used, or selection biases due to the fact that galaxies which are rounder or aligned

with the PSF are easier to measure.

The second systematic barrier I identified was galaxy intrinsic alignments, the contamination of weak lensing signals due to galaxies having non-randomly oriented intrinsic ellipticities. I presented current observational constraints and modelling approaches. Although useful, the direct intrinsic alignment measurements that exist are not directly applicable to cosmic shear analyses, since the galaxies used in the former do not span the full range of galaxy types, redshifts and luminosities of the galaxies used in the latter. Direct intrinsic alignment measurements will hopefully provide useful priors on physically motivated, flexible models, which incorporate nuisance parameters that can be marginalised over in a weak lensing cosmology analysis.

Next I discussed photometric redshift estimation. DES will provide imaging, and therefore shear estimates for a spectacular number of galaxies. However, their usefulness for cosmological inference is limited if we don't have accurate redshift information. Multi-band imaging surveys like DES have to use photometric redshifts, where several broad-band magnitudes (5 for DES) are used as a very coarse measurement of the spectral energy distribution (SED) for each galaxy. As a statistical problem, this has analogous challenges to shape measurement: Template fitting methods require a reliable model (i.e. template set) for unbiased inference of redshift information from the wide-band magnitudes. Also, just as in shape measurement, high-quality galaxy images are required for calibration or testing methods, for photo-$z$ estimation a large quantity of galaxies with high quality (i.e. spectroscopic or similar) redshifts are required. Obtaining a sufficient volume of representative spectroscopic data presents a huge observational challenge.

Finally I identified the theoretical uncertainty in prediction of the matter power spectrum on small scales, primarily due to baryonic (i.e. non-gravitational) physics. I covered this in Chapter 5, overviewing the usefulness of hydrodynamic simulations, and possible approaches to mitigating baryonic effects, through mod-

elling or marginalising over a suitable nuisance parameterisation. I also consider how inference from small scales is further complicated by other systematic effects like higher order shear terms, and observational effects like blending.

In Chapters 3 & 4 I attempted to account for some of the systematic effects when performing cosmological analyses on two weak lensing datasets. In Chapter 3 I performed a joint analysis of CFHTLenS weak lensing and *Planck* CMB data, with a view to explaining the tension between the two datasets in the clustering amplitude at low redshift. The tension has been viewed as disfavouring the ΛCDM model, but of course this conclusion depends on a certain set of assumptions about systematic effects present in the two datasets. I looked at various extensions to the treatment of systematics in the CFHTLenS data such as intrinsic alignments and baryonic effects, neither of which looked likely to be solely responsible for the tension. The tension can be resolved by extending the ΛCDM model, however, I think an analysis which realistically and simultaneously accounts for all the systematic effects I've mentioned would be required to make any conclusions about extensions to ΛCDM. I think we still are some way from being able to model all of the systematic effects I've mentioned to the level of realism required to do this, but progress is being made, which I'll allude to below.

In Chapter 4 I applied some of the same tools to a cosmic shear analysis of DES Science Verification (SV) data. Although a similar sized dataset, this presented new challenges, although it may just be that I was more aware of the possible sources of biases because I was involved in the whole pipeline (from observing, to shape measurement, to signal and covariance estimation). By marginalising over additional nuisance parameters, I attempted to produce constraints that were more robust to shape measurement and photometric redshift uncertainties than my CFHTLenS analysis, and I also used more advanced intrinsic alignment models, and was more systematic about the exclusion of small scales. Due partly to the limited statistical power, the resulting cosmological constraints are consistent with both *Planck* and CFHTLenS; future DES datasets will have the statistical

power to get off the fence.

I extended the DES SV cosmic shear measurements to smaller scales in Chapter 5, and used the Mead et al. (2015) model, a modified halo model prescription to model the effects of baryons on small scales. I use a simple DES Year 5 forecast to demonstrate that future DES data will have the power to differentiate between baryonic scenarios, at least the more extreme ones.

## 6.2 Future work

Significant portions of Stage III weak lensing surveys like DES, KiDS and HSC have already been observed, so the data volume required to propel weak lensing into the precision cosmology regime already exists. Over the next few years I will continue working on the aforementioned systematic effects, which require improvements before robust inference of fundamental physics like dark energy and neutrinos is possible. The techniques developed for these datasets will be applicable to the next generation of ambitious surveys like Euclid, LSST and WFIRST.

One aspect of these surveys that I will keenly exploit are cross-correlation techniques. An idealised cosmic shear analysis requires only shear estimates at a large number of random points on the sky and in redshift. While galaxy surveys do not provide exactly this, they are an incredibly rich source of other information. The cross correlation of the angular positions of weak lensing source galaxies with the positions of a smaller sample of galaxies with higher quality redshifts will be an important tool in constraining photo-$z$ uncertainty. Combining shear-shear correlations with the galaxy clustering and galaxy position-shear correlations will also be key in constraining intrinsic alignments. The parameter estimation pipeline I developed for the CFHTLenS and DES SV cosmic shear analyses is part of the CosmoSIS framework (Zuntz et al. 2015). I am currently working to extend this framework to include the tools required for a '3×2-point' i.e. shear-shear,

position-shear and position-position correlations analysis, which we plan to apply to DES data. The extra information from using large-scale structure tracers will produce better constraints on photometric redshift biases and intrinsic alignments in particular. The cost is that we will also have to model galaxy bias, but Joachimi & Bridle (2010) show that significant gains in constraints on intrinsic alignments (and therefore cosmology) can be achieved even when allowing extremely flexible models for galaxy bias. I will test these analysis tools (which include real-space and Fourier space two-point estimators of the signal, as well as the theoretical predictions for modelling the signal) on DES mock survey simulations. Cross correlating galaxy imaging survey data with CMB lensing data from increasingly wide, high-resolution CMB experiments (e.g. van Engelen et al. 2014, Story et al. 2014) will also be fruitful for mitigating systematics, as well as for the high redshift information CMB lensing provides.

With the extra statistical power provided by future datasets, more advanced modelling of astrophysical systematics will be required. For intrinsic alignments, the use of the linear alignment model (or nonlinear extensions) has been attractive, since it has only one free parameter (or possibly two or three if luminosity and/or redshift scaling is included), it is physically motivated, and it fits observations fairly successfully. However, there is no reason to believe it should be a good description of the majority of weak lensing source galaxies, which are disc-dominated. I am currently working on more advanced intrinsic alignment modelling for mixed galaxy populations, that includes aspects of tidal alignment (see §2.2.1) and tidal torque theory (see §2.2.1), and allows for interactions between tidally aligned and tidally torqued galaxies. As well as applying this model to data, I would like to compare it to measurements on hydrodynamic simulations; IA measurements by Chisari et al. (2015) on the Horizon-AGN simulations (Dubois et al. 2014) show clear dependence on galaxy type. In particular they observe a tendency for disc galaxies to have tangential alignment with respect to overdensities (with the opposite true for ellipticals), which would not be described

by the simple tidal-torque model of e.g. Mackey et al. (2002) that I presented in §2.2.1.

Hydrodynamic simulations will also play a part in our understanding of the other main theoretical uncertainty faced by weak lensing, the effects of baryonic physics on the small-scale matter clustering. In the next few years, more accurate, larger hydrodynamic simulations will provide sterner tests of physically motivated models like the Mead et al. (2015) halo model I used in Chapter 5. I look forward to applying these kinds of modelling approaches to future DES data, which will have the statistical power to be informative about the effect of baryonic physics on the matter clustering, even if cosmological inference is not possible from the small scale cosmic shear signal.

Realistic simulations will also be crucial in improving shear estimation to the level required for future weak lensing datasets. Since shear is estimated from images, it is images that must be simulated, with all the noise, atmospheric distortion and instrumental effects that make measuring galaxy shapes such a tricky, nonlinear process. Promising approaches include Chang et al. (2014), who attempt to model the 'transfer function' of the Dark Energy Survey, simulating DES-like images starting from simulated mock galaxy catalogs; and the atmosphere and telescope modelling of PHOSIM[1] which is being used to simulate images for LSST. Tools like GALSIM (Rowe et al. 2015) a software package for simulating galaxy images, including real HST galaxy profiles, have and will continue to be extremely useful. As part of the IM3SHAPE team, I am contributing to the ongoing effort to produce more realistic image simulations for shear calibration; we hope to include effects such as multiple exposures, blending and more realistic galaxy selection in the calibration of future DES shear catalogs.

Realising the potential of cosmic shear will require a broad program of advances in simulations, theoretical modelling and understanding of our instruments and data reduction software. Some of the approaches I have described here can

[1] `http://www.lsst.org/scientists/simulations/phosim`

provide some of the gains required. The gains will become increasingly marginal as higher order effects become more important. The task of reducing systematic uncertainties to below the requirements of the vast future datasets is an incredibly challenging one, and whether it can be done remains to be seen. It is the scale of this task, and the potential scientific reward at the end of it that makes weak lensing such a stimulating and exciting topic to work on.

# References


Aad, G., Abajyan, T., Abbott, B., et al., 2012, Physics Letters B, 716, 1, arXiv:1207.7214

Abazajian, K. N., Arnold, K., Austermann, J., et al., 2015, Astroparticle Physics, 63, 66, arXiv:1309.5383

Abbott, B. P., Abbott, R., Abbott, T. D., et al., 2016, Phys. Rev. Lett., 116, 061102

Albrecht, A., Bernstein, G., Cahn, R., et al., 2006, ArXiv Astrophysics e-prints, astro-ph/0609591

Albrecht, A., Steinhardt, P. J., 1982, Phys. Rev. Lett., 48, 1220

Allen, S. W., Evrard, A. E., Mantz, A. B., 2011, ARA&A, 49, 409, arXiv:1103.4829

Amanullah, R., Lidman, C., Rubin, D., et al., 2010, ApJ, 716, 712, arXiv:1004.1711

Amara, A., Réfrégier, A., 2008, MNRAS, 391, 228, arXiv:0710.5171

Anderson, L., Aubourg, É., Bailey, S., et al., 2014, MNRAS, 441, 24, arXiv:1312.4877

Archidiacono, M., Fornengo, N., Gariazzo, S., Giunti, C., Hannestad, S., Laveder, M., 2014, ArXiv e-prints, arXiv:1404.1794

Asgari, M., Heymans, C., Blake, C., Harnois-Deraps, J., Schneider, P., Van Waerbeke, L., 2016, ArXiv e-prints, arXiv:1601.00115

Bacon, D. J., Refregier, A., Clowe, D., Ellis, R. S., 2001, MNRAS, 325, 1065, astro-ph/0007023

Bacon, D. J., Refregier, A. R., Ellis, R. S., 2000, MNRAS, 318, 625, astro-ph/0003008

Bartelmann, M., Schneider, P., 2001, Phys. Rep., 340, 291, astro-ph/9912508

Battye, R. A., Moss, A., 2014, Physical Review Letters, 112, 5, 051303, arXiv:1308.5870

Becker, M. R., Rozo, E., 2014, arXiv:astro-ph/1412.3851, arXiv:1412.3851

Becker, M. R., Troxel, M. A., MacCrann, N., et al., 2015a, ArXiv e-prints, arXiv:1507.05598

Becker, M. R., Troxel, M. A., MacCrann, N., et al., 2015b, ArXiv e-prints, arXiv:1507.05598

Benítez, N., 2000, ApJ, 536, 571, astro-ph/9811189

Benjamin, J., Van Waerbeke, L., Heymans, C., et al., 2013, MNRAS, 431, 1547, arXiv:1212.3327

Bennett, C. L., Halpern, M., Hinshaw, G., et al., 1997, in American Astronomical Society Meeting Abstracts, vol. 29 of *Bulletin of the American Astronomical Society*, 1353

Bennett, C. L., Halpern, M., Hinshaw, G., et al., 2003, ApJS, 148, 1, astro-ph/0302207

Bennett, C. L., Larson, D., Weiland, J. L., et al., 2013, ApJS, 208, 20, arXiv:1212.5225

Bergé, J., Gamper, L., Réfrégier, A., Amara, A., 2013, Astronomy and Computing, 1, 23, arXiv:1209.1200

Beringer, J., Arguin, J.-F., Barnett, R. M., et al., 2012, Phys. Rev. D, 86, 1, 010001

Bernardeau, F., 1998, A&A, 338, 375, astro-ph/9712115

Bernstein, G. M., 2009, ApJ, 695, 652, arXiv:0808.3400

Bernstein, G. M., 2010, MNRAS, 406, 2793, arXiv:1001.2333

Bernstein, G. M., Armstrong, R., 2014a, MNRAS, 438, 1880, arXiv:1304.1843

Bernstein, G. M., Armstrong, R., 2014b, MNRAS, 438, 1880, arXiv:1304.1843

Bernstein, G. M., Jarvis, M., 2002, AJ, 123, 583, astro-ph/0107431

Bertin, E., 2011, in Astronomical Data Analysis Software and Systems XX, edited by Evans, I. N., Accomazzi, A., Mink, D. J., Rots, A. H., vol. 442 of *Astronomical Society of the Pacific Conference Series*, 435

Betoule, M., Kessler, R., Guy, J., et al., 2014, A&A, 568, A22, arXiv:1401.4064

Beutler, F., Blake, C., Colless, M., et al., 2011, MNRAS, 416, 3017, arXiv:1106.3366

Beutler, F., Blake, C., Colless, M., et al., 2012, MNRAS, 423, 3430, arXiv:1204.4725

Beutler, F., Saito, S., Brownstein, J. R., et al., 2014a, MNRAS, 444, 3501, arXiv:1403.4599

Beutler, F., Saito, S., Brownstein, J. R., et al., 2014b, ArXiv e-prints, arXiv:1403.4599

Beutler, F., Saito, S., Seo, H.-J., et al., 2014c, MNRAS, 443, 1065, arXiv:1312.4611

Bianchi, D., Guzzo, L., Branchini, E., et al., 2012, MNRAS, 427, 2420, arXiv:1203.1545

BICEP2 Collaboration, Ade, P. A. R., Aikin, R. W., et al., 2014, ArXiv e-prints, arXiv:1403.4302

BICEP2/Keck and Planck Collaborations, :, Ade, P. A. R., et al., 2015, ArXiv e-prints, arXiv:1502.00612

Blake, C., Brough, S., Colless, M., et al., 2012, MNRAS, 425, 405, arXiv:1204.3674

Blazek, J., McQuinn, M., Seljak, U., 2011, J. Cosmology Astropart. Phys., 5, 010, arXiv:1101.4017

Blazek, J., Vlah, Z., Seljak, U., 2015a, ArXiv e-prints, arXiv:1504.02510

Blazek, J., Vlah, Z., Seljak, U., 2015b, J. Cosmology Astropart. Phys., 8, 015, arXiv:1504.02510

Bolzonella, M., Miralles, J.-M., Pelló, R., 2000, A&A, 363, 476, astro-ph/0003380

Bond, J. R., Efstathiou, G., Tegmark, M., 1997, MNRAS, 291, L33, astro-ph/9702100

Bonnett, C., 2015, MNRAS, 449, 1, 1043, "http://mnras.oxfordjournals.org/content/449/1/1043.full.pdf+html"

Bonnett, C., Troxel, M. A., Hartley, W., et al., 2015, ArXiv e-prints, arXiv:1507.05909

Booth, C. M., Schaye, J., 2009, MNRAS, 398, 53, arXiv:0904.2572

Bridle, S., King, L., 2007, New Journal of Physics, 9, 444, arXiv:0705.0166

Bridle, S., Shawe-Taylor, J., Amara, A., et al., 2009, Annals of Applied Statistics, 3, 6, arXiv:0802.1214

Bridle, S. L., Kneib, J.-P., Bardeau, S., Gull, S. F., 2002, in The Shapes of Galaxies and their Dark Halos, edited by Natarajan, P., 38–46

Brown, M. L., Taylor, A. N., Hambly, N. C., Dye, S., 2002, MNRAS, 333, 501, astro-ph/0009499

Busca, N. G., Delubac, T., Rich, J., et al., 2013, A&A, 552, A96, arXiv:1211.2616

Busha, M. T., Wechsler, R. H., Becker, M. R., Erickson, B., Evrard, A. E., 2013, in American Astronomical Society Meeting Abstracts #221, vol. 221 of *American Astronomical Society Meeting Abstracts*, 341.07

Cannon, R., Drinkwater, M., Edge, A., et al., 2006, MNRAS, 372, 425, astro-ph/0607631

Carrasco Kind, M., Brunner, R. J., 2013, MNRAS, 432, 1483, arXiv:1303.7269

Casarini, L., Bonometto, S. A., Borgani, S., et al., 2012, A&A, 542, A126, arXiv:1203.5251

Castro, P. G., Heavens, A. F., Kitching, T. D., 2005, Phys. Rev. D, 72, 2, 023516, astro-ph/0503479

Catelan, P., Kamionkowski, M., Blandford, R. D., 2001, MNRAS, 320, L7, astro-ph/0005470

Chang, C., Busha, M. T., Wechsler, R. H., et al., 2014, ArXiv e-prints, arXiv:1411.0032

Chang, C., Busha, M. T., Wechsler, R. H., et al., 2015, ApJ, 801, 73, arXiv:1411.0032

Chevallier, M., Polarski, D., 2001, International Journal of Modern Physics D, 10, 213, gr-qc/0009008

Chisari, N., Codis, S., Laigle, C., et al., 2015, MNRAS, 454, 2736, arXiv:1507.07843

Choi, A., Heymans, C., Blake, C., et al., 2015, ArXiv e-prints, arXiv:1512.03626

Chuang, C.-H., Prada, F., Beutler, F., et al., 2013, ArXiv e-prints, arXiv:1312.4889

Clowe, D., Bradač, M., Gonzalez, A. H., et al., 2006, ApJ, 648, L109, astro-ph/0608407

Cole, S., Percival, W. J., Peacock, J. A., et al., 2005, MNRAS, 362, 505, astro-ph/0501174

Colless, M., Dalton, G., Maddox, S., et al., 2001, MNRAS, 328, 1039, astro-ph/0106498

Collister, A. A., Lahav, O., 2004, PASP, 116, 345, astro-ph/0311058

Crain, R. A., Schaye, J., Bower, R. G., et al., 2015, MNRAS, 450, 1937, arXiv:1501.01311

Crittenden, R., Bond, J. R., Davis, R. L., Efstathiou, G., Steinhardt, P. J., 1993, Physical Review Letters, 71, 324, astro-ph/9303014

Crittenden, R. G., Natarajan, P., Pen, U.-L., Theuns, T., 2001, ApJ, 559, 552, astro-ph/0009052

Croft, R. A. C., Metzler, C. A., 2000, ApJ, 545, 561, astro-ph/0005384

Cunha, C. E., Huterer, D., Busha, M. T., Wechsler, R. H., 2012, MNRAS, 423, 909, arXiv:1109.5691

Dahlen, T., Mobasher, B., Faber, S. M., et al., 2013, ApJ, 775, 93, arXiv:1308.5353

Dawson, K. S., Schlegel, D. J., Ahn, C. P., et al., 2013, AJ, 145, 10, arXiv:1208.0022

Dawson, W. A., Schneider, M. D., Tyson, J. A., Jee, M. J., 2014, ArXiv e-prints, arXiv:1406.1506

de Bernardis, P., Ade, P. A. R., Bock, J. J., et al., 2000, Nature, 404, 955, astro-ph/0004404

de Vaucouleurs, G., 1953, MNRAS, 113, 134

Delubac, T., Bautista, J. E., Busca, N. G., et al., 2015, A&A, 574, A59, arXiv:1404.1801

Djorgovski, S. G., 1987, in Nearly Normal Galaxies. From the Planck Time to the Present, edited by Faber, S. M., 227–233

Dodelson, S., Schneider, M. D., 2013, Phys. Rev. D, 88, 6, 063537, arXiv:1304.2593

Drinkwater, M. J., Jurek, R. J., Blake, C., et al., 2010, MNRAS, 401, 1429, arXiv:0911.4246

Dubois, Y., Pichon, C., Welker, C., et al., 2014, MNRAS, 444, 1453,

arXiv:1402.1165

Dvorkin, C., Wyman, M., Rudd, D. H., Hu, W., 2014, ArXiv e-prints, arXiv:1403.8049

Efstathiou, G., 2014a, MNRAS, 440, 1138, arXiv:1311.3461

Efstathiou, G., 2014b, MNRAS, 440, 1138, arXiv:1311.3461

Efstathiou, G., Bond, J. R., 1999, MNRAS, 304, 75, astro-ph/9807103

Eifler, T., Krause, E., Dodelson, S., Zentner, A. R., Hearin, A. P., Gnedin, N. Y., 2015, MNRAS, 454, 2451, arXiv:1405.7423

Eifler, T., Krause, E., Schneider, P., Honscheid, K., 2014, MNRAS, 440, 1379, arXiv:1302.2401

Eifler, T., Schneider, P., Hartlap, J., 2009, A&A, 502, 721, arXiv:0810.4254

Einstein, A., 1915, Sitzungsberichte der Königlich Preußischen Akademie der Wissenschaften (Berlin), Seite 844-847.

Eisenstein, D. J., Hu, W., 1998, ApJ, 496, 605, astro-ph/9709112

Eisenstein, D. J., Weinberg, D. H., Agol, E., et al., 2011, AJ, 142, 72, arXiv:1101.1529

Eisenstein, D. J., Zehavi, I., Hogg, D. W., et al., 2005, ApJ, 633, 560, astro-ph/0501171

Erben, T., Hildebrandt, H., Miller, L., et al., 2013, MNRAS, 433, 2545, arXiv:1210.8156

Flaugher, B., Diehl, H. T., Honscheid, K., et al., 2015, ArXiv e-prints, arXiv:1504.02900

Font-Ribera, A., Kirkby, D., Busca, N., et al., 2014, J. Cosmology Astropart. Phys., 5, 027, arXiv:1311.1767

Friedrich, O., Seitz, S., Eifler, T. F., Gruen, D., 2016, MNRAS, 456, 2662, arXiv:1508.00895

Fu, L., Semboloni, E., Hoekstra, H., et al., 2008, A&A, 479, 9, arXiv:0712.0884

Fukuda, Y., Hayakawa, T., Ichihara, E., et al., 1998, Physical Review Letters, 81, 1158, hep-ex/9805021

Graff, P., Feroz, F., Hobson, M. P., Lasenby, A., 2014, MNRAS, 441, 1741, arXiv:1309.0790

Guillet, T., Teyssier, R., Colombi, S., 2010, MNRAS, 405, 525, arXiv:0905.2615

Guth, A. H., 1981, Phys. Rev. D, 23, 347

Guzik, J., Seljak, U., 2002, MNRAS, 335, 311, astro-ph/0201448

Hamana, T., Colombi, S. T., Thion, A., Devriendt, J. E. G. T., Mellier, Y., Bernardeau, F., 2002, MNRAS, 330, 365, astro-ph/0012200

Hamana, T., Miyazaki, S., Shimasaku, K., et al., 2003, ApJ, 597, 98, astro-ph/0210450

Hamann, J., Hasenkamp, J., 2013, J. Cosmology Astropart. Phys., 10, 044, arXiv:1308.3255

Hambly, N. C., MacGillivray, H. T., Read, M. A., et al., 2001, MNRAS, 326, 1279, astro-ph/0108286

Hamilton, A. J. S., 1998, in The Evolving Universe, edited by Hamilton, D., vol. 231 of *Astrophysics and Space Science Library*, 185, astro-ph/9708102

Hanany, S., Ade, P., Balbi, A., et al., 2000, ApJ, 545, L5, astro-ph/0005123

Harnois-Déraps, J., van Waerbeke, L., Viola, M., Heymans, C., 2015, MNRAS, 450, 1212, arXiv:1407.4301

Hartlap, J., Hilbert, S., Schneider, P., Hildebrandt, H., 2011, Astronomy & Astrophysics, 528, A51, arXiv:1010.0010

Hartlap, J., Simon, P., Schneider, P., 2007, A&A, 464, 399, astro-ph/0608064

Hawley, D. L., Peebles, P. J. E., 1975, AJ, 80, 477

Heavens, A., 2003, MNRAS, 343, 1327, astro-ph/0304151

Heavens, A., Refregier, A., Heymans, C., 2000, MNRAS, 319, 649, astro-ph/0005269

Heitmann, K., Lawrence, E., Kwan, J., Habib, S., Higdon, D., 2014, ApJ, 780, 111, arXiv:1304.7849

Heitmann, K., White, M., Wagner, C., Habib, S., Higdon, D., 2010, ApJ, 715, 104, arXiv:0812.1052

Henrion, M., Mortlock, D. J., Hand, D. J., Gandy, A., 2011, MNRAS, 412, 2286, arXiv:1011.5770

Hetterscheidt, M., Simon, P., Schirmer, M., et al., 2007, A&A, 468, 859, astro-ph/0606571

Heymans, C., Grocutt, E., Heavens, A., et al., 2013, MNRAS, 432, 2433, arXiv:1303.1808

Heymans, C., Van Waerbeke, L., Bacon, D., et al., 2006, MNRAS, 368, 1323, astro-ph/0506112

Heymans, C., Van Waerbeke, L., Miller, L., et al., 2012, MNRAS, 427, 146, arXiv:1210.0032

Hikage, C., Takada, M., Hamana, T., Spergel, D., 2011, MNRAS, 412, 65, arXiv:1004.3542

Hilbert, S., Hartlap, J., Schneider, P., 2011, A&A, 536, A85, arXiv:1105.3980

Hildebrandt, H., Erben, T., Kuijken, K., et al., 2012, MNRAS, 421, 2355, arXiv:1111.4434

Hill, J. C., Spergel, D. N., 2014, J. Cosmology Astropart. Phys., 2, 030, arXiv:1312.4525

Hirata, C., Seljak, U., 2003, MNRAS, 343, 459, astro-ph/0301054

Hirata, C. M., Mandelbaum, R., Ishak, M., et al., 2007, MNRAS, 381, 1197, astro-ph/0701671

Hirata, C. M., Mandelbaum, R., Seljak, U., et al., 2004, MNRAS, 353, 529, astro-ph/0403255

Hirata, C. M., Seljak, U., 2004, Phys. Rev. D, 70, 6, 063526, astro-ph/0406275

Hirata, C. M., Seljak, U., 2010, ArXiv Astrophysics e-prints, arXiv:astro-ph/0406275

Hoekstra, H., Franx, M., Kuijken, K., Squires, G., 1998, New A Rev., 42, 137, astro-ph/9711096

Hoekstra, H., Herbonnet, R., Muzzin, A., et al., 2015, MNRAS, 449, 685, arXiv:1502.01883

Hoekstra, H., Yee, H. K. C., Gladders, M. D., Barrientos, L. F., Hall, P. B., Infante, L., 2002, ApJ, 572, 55, astro-ph/0202285

Hogg, D. W., Lang, D., 2013, PASP, 125, 719, arXiv:1210.6563

Howlett, C., Lewis, A., Hall, A., Challinor, A., 2012, J. Cosmology Astropart. Phys., 4, 027, arXiv:1201.3654

Howlett, C., Ross, A. J., Samushia, L., Percival, W. J., Manera, M., 2015, MNRAS, 449, 848, arXiv:1409.3238

Hu, W., 1999, ApJ, 522, L21, astro-ph/9904153

Hu, W., Jain, B., 2004, Phys. Rev. D, 70, 4, 043009, astro-ph/0312395

Hubble, E., 1929, Proceedings of the National Academy of Science, 15, 168

Huff, E. M., Eifler, T., Hirata, C. M., Mandelbaum, R., Schlegel, D., Seljak, U., 2014, MNRAS, 440, 1322

Hui, L., Zhang, J., 2002, ArXiv Astrophysics e-prints, astro-ph/0205512

Huterer, D., Takada, M., Bernstein, G., Jain, B., 2006, MNRAS, 366, 101, astro-ph/0506030

IceCube Collaboration, 2013, Science, 342, 1242856, arXiv:1311.5238

Ilbert, O., Capak, P., Salvato, M., et al., 2009, ApJ, 690, 1236, arXiv:0809.2101

Jain, B., Seljak, U., 1997, ApJ, 484, 560, astro-ph/9611077

Jarvis, M., Jain, B., 2004, ArXiv Astrophysics e-prints, astro-ph/0412234

Jarvis, M., Jain, B., Bernstein, G., Dolney, D., 2006, ApJ, 644, 71, astro-ph/0502243

Jarvis, M., Sheldon, E., Zuntz, J., et al., 2015, ArXiv e-prints, arXiv:1507.05603

Jee, M. J., Tyson, J. A., Hilbert, S., Schneider, M. D., Schmidt, S., Wittman, D., 2015, ArXiv e-prints, arXiv:1510.03962

Jee, M. J., Tyson, J. A., Schneider, M. D., Wittman, D., Schmidt, S., Hilbert, S., 2013, ApJ, 765, 74, arXiv:1210.2732

Jeffreys, H., 1961, Theory of Probability, Oxford, Oxford, England, 3rd edn.

Jing, Y. P., Zhang, P., Lin, W. P., Gao, L., Springel, V., 2006, ApJ, 640, L119, astro-ph/0512426

Joachimi, B., Bridle, S. L., 2010, A&A, 523, A1, arXiv:0911.2454

Joachimi, B., Cacciato, M., Kitching, T. D., et al., 2015, ArXiv e-prints, arXiv:1504.05456

Joachimi, B., Mandelbaum, R., Abdalla, F. B., Bridle, S. L., 2011, A&A, 527, A26, arXiv:1008.3491

Joachimi, B., Schneider, P., 2010, ArXiv e-prints, arXiv:1009.2024

Kacprzak, T., Bridle, S., Rowe, B., et al., 2013, ArXiv e-prints, arXiv:1308.4663

Kacprzak, T., Zuntz, J., Rowe, B., et al., 2012, MNRAS, 427, 2711, arXiv:1203.5049

Kaiser, N., 1987, MNRAS, 227, 1

Kaiser, N., 1992, ApJ, 388, 272

Kaiser, N., 2000, ApJ, 537, 555, astro-ph/9904003

Kaiser, N., Squires, G., Broadhurst, T., 1995, ApJ, 449, 460, astro-ph/9411005

Kaiser, N., Wilson, G., Luppino, G. A., 2000, ArXiv Astrophysics e-prints, astro-ph/0003338

Kazin, E. A., Koda, J., Blake, C., et al., 2014, MNRAS, 441, 3524, arXiv:1401.0358

Kiessling, A., Cacciato, M., Joachimi, B., et al., 2015, Space Sci. Rev., 193, 67, arXiv:1504.05546

Kilbinger, M., 2015, Reports on Progress in Physics, 78, 8, 086901, arXiv:1411.0115

Kilbinger, M., Benabed, K., Guy, J., et al., 2009, A&A, 497, 677, arXiv:0810.5129

Kilbinger, M., Fu, L., Heymans, C., et al., 2013, MNRAS, 430, 2200, arXiv:1212.3338

King, L. J., Schneider, P., 2003, A&A, 398, 23, astro-ph/0209474

Kirk, D., Brown, M. L., Hoekstra, H., et al., 2015, Space Sci. Rev., 193, 139, arXiv:1504.05465

Kirk, D., Rassat, A., Host, O., Bridle, S., 2012, MNRAS, 424, 1647, arXiv:1112.4752

Kitching, T. D., Heavens, A. F., Alsing, J., et al., 2014, ArXiv e-prints, arXiv:1401.6842

Koekemoer, A. M., Aussel, H., Calzetti, D., et al., 2007, ApJS, 172, 196, astro-ph/0703095

Komatsu, E., Smith, K. M., Dunkley, J., et al., 2011, ApJS, 192, 18, arXiv:1001.4538

Kowalski, M., Rubin, D., Aldering, G., et al., 2008, ApJ, 686, 749-778, arXiv:0804.4142

Krause, E., Eifler, T., Blazek, J., 2015, ArXiv e-prints, arXiv:1506.08730

Krause, E., Hirata, C. M., 2010, A&A, 523, A28, arXiv:0910.3786

Kuijken, K., 1999, A&A, 352, 355, astro-ph/9904418

Kuijken, K., Heymans, C., Hildebrandt, H., et al., 2015, ArXiv e-prints, arXiv:1507.00738

Lahav, O., Liddle, A. R., 2014, ArXiv e-prints, arXiv:1401.1389

Lee, J., Pen, U.-L., 2001, ApJ, 555, 106, astro-ph/0008135

Leistedt, B., Peiris, H. V., Elsner, F., et al., 2015, ArXiv e-prints, arXiv:1507.05647

Leistedt, B., Peiris, H. V., Verde, L., 2014, Physical Review Letters, 113, 4, 041301, arXiv:1404.5950

Lewis, A., 2009, MNRAS, 398, 471, arXiv:0901.0649

Lewis, A., Bridle, S., 2010, Parameter estimation using Monte Carlo sampling, 57

Lewis, A., Challinor, A., Lasenby, A., 2000, ApJ, 538, 473, astro-ph/9911177

Lima, M., Cunha, C. E., Oyaizu, H., Frieman, J., Lin, H., Sheldon, E. S., 2008, MNRAS, 390, 118, arXiv:0801.3822

Limber, D. N., 1954, ApJ, 119, 655

Lin, H., Dodelson, S., Seo, H.-J., et al., 2012, ApJ, 761, 15, arXiv:1111.6622

Linde, A. D., 1982, Physics Letters B, 108, 389

Linder, E. V., 2003, Physical Review Letters, 90, 9, 091301, astro-ph/0208512

Lobashev, V. M., Aseev, V. N., Belesev, A. I., et al., 1999, Physics Letters B, 460, 227

Luppino, G. A., Kaiser, N., 1997, ApJ, 475, 20, astro-ph/9601194

Ma, Z., Hu, W., Huterer, D., 2006, ApJ, 636, 21, astro-ph/0506614

MacCrann, N., Zuntz, J., Bridle, S., Jain, B., Becker, M. R., 2015, MNRAS, 451, 2877, arXiv:1408.4742

MacDonald, C. J., Bernstein, G., 2010, PASP, 122, 485, arXiv:1002.0008

Mackey, J., White, M., Kamionkowski, M., 2002, MNRAS, 332, 788, astro-ph/0106364

Mandelbaum, R., Blake, C., Bridle, S., et al., 2011a, MNRAS, 410, 844, arXiv:0911.5347

Mandelbaum, R., Blake, C., Bridle, S., et al., 2011b, MNRAS, 410, 844, arXiv:0911.5347

Mandelbaum, R., Rowe, B., Bosch, J., et al., 2014, ApJS, 212, 5, arXiv:1308.4982

Mandelbaum, R., Slosar, A., Baldauf, T., et al., 2013, MNRAS, 432, 1544, arXiv:1207.1120

Mantz, A. B., von der Linden, A., Allen, S. W., et al., 2015, MNRAS, 446, 2205, arXiv:1407.4516

Massey, R., Rhodes, J., Leauthaud, A., et al., 2007, ApJS, 172, 239, astro-ph/0701480

McCarthy, I. G., Schaye, J., Bower, R. G., et al., 2011, MNRAS, 412, 1965, arXiv:1008.4799

Mead, A., Peacock, J., Heymans, C., Joudaki, S., Heavens, A., 2015, ArXiv e-prints, arXiv:1505.07833

Melchior, P., Böhnert, A., Lombardi, M., Bartelmann, M., 2010, A&A, 510, A75, arXiv:0906.5092

Melchior, P., Suchyta, E., Huff, E., et al., 2015, MNRAS, 449, 2219, arXiv:1405.4285

Meszaros, P., 1974, A&A, 37, 225

Miller, L., Heymans, C., Kitching, T. D., et al., 2013, MNRAS, 429, 2858, arXiv:1210.8201

Miller, L., Kitching, T. D., Heymans, C., Heavens, A. F., van Waerbeke, L., 2007, MNRAS, 382, 315, arXiv:0708.2340

Navarro, J. F., Frenk, C. S., White, S. D. M., 1996, ApJ, 462, 563, astro-ph/9508025

Newman, J. A., 2008, ApJ, 684, 88-101, arXiv:0805.1409

Norberg, P., Baugh, C. M., Gaztañaga, E., Croton, D. J., 2009, MNRAS, 396, 19, arXiv:0810.1885

Oka, A., Saito, S., Nishimichi, T., Taruya, A., Yamamoto, K., 2014, MNRAS, 439, 2515, arXiv:1310.2820

Okumura, T., Seljak, U., Desjacques, V., 2012, J. Cosmology Astropart. Phys., 11, 014, arXiv:1206.4070

Oort, J. H., 1932, Bull. Astron. Inst. Netherlands, 6, 249

Padmanabhan, T., 1993, Structure Formation in the Universe, Cambridge University Press

Palanque-Delabrouille, N., Yèche, C., Baur, J., et al., 2015, J. Cosmology Astropart. Phys., 11, 011, arXiv:1506.05976

Pan, Z., Knox, L., White, M., 2014, MNRAS, 445, 2941, arXiv:1406.5459

Parkinson, D., Riemer-Sørensen, S., Blake, C., et al., 2012, Phys. Rev. D, 86, 10, 103518, arXiv:1210.2130

Paulin-Henriksson, S., Amara, A., Voigt, L., Refregier, A., Bridle, S. L., 2008, A&A, 484, 67, arXiv:0711.4886

Peacock, J., Schneider, P., 2006, The Messenger, 125, 48

Peacock, J. A., 2003, ArXiv Astrophysics e-prints, astro-ph/0309240

Peacock, J. A., Dodds, S. J., 1996, MNRAS, 280, L19, astro-ph/9603031

Peacock, J. A., Smith, R. E., 2000, MNRAS, 318, 1144, astro-ph/0005010

Percival, W. J., Reid, B. A., Eisenstein, D. J., et al., 2010, MNRAS, 401, 2148, arXiv:0907.1660

Perlmutter, S., Aldering, G., Goldhaber, G., et al., 1999, ApJ, 517, 565, astro-ph/9812133

Planck Collaboration, Ade, P. A. R., Aghanim, N., et al., 2013a, ArXiv e-prints, arXiv:1303.5062

Planck Collaboration, Ade, P. A. R., Aghanim, N., et al., 2013b, ArXiv e-prints, arXiv:1303.5075

Planck Collaboration, Ade, P. A. R., Aghanim, N., et al., 2013c, ArXiv e-prints, arXiv:1303.5076

Planck Collaboration, Ade, P. A. R., Aghanim, N., et al., 2013d, ArXiv e-prints, arXiv:1303.5077

Planck Collaboration, Ade, P. A. R., Aghanim, N., et al., 2013e, ArXiv e-prints, arXiv:1303.5080

Planck Collaboration, Ade, P. A. R., Aghanim, N., et al., 2015a, ArXiv e-prints, arXiv:1502.01589

Planck Collaboration, Ade, P. A. R., Aghanim, N., et al., 2015b, ArXiv e-prints, arXiv:1502.01591

Planck Collaboration, Ade, P. A. R., Aghanim, N., et al., 2015c, ArXiv e-prints, arXiv:1502.01591

Planck Collaboration, Ade, P. A. R., Aghanim, N., et al., 2015d, ArXiv e-prints, arXiv:1502.01597

Planck Collaboration, Aghanim, N., Arnaud, M., et al., 2015e, ArXiv e-prints, arXiv:1507.02704

Press, W. H., Teukolsky, S. A., Vetterling, W. T., Flannery, B. P., 2007, Numerical Recipes 3rd Edition: The Art of Scientific Computing, Cambridge University Press, New York, NY, USA, 3rd edn.

Refregier, A., Kacprzak, T., Amara, A., Bridle, S., Rowe, B., 2012, MNRAS, 425, 1951, arXiv:1203.5050

Reid, B. A., Seo, H.-J., Leauthaud, A., Tinker, J. L., White, M., 2014, MNRAS, 444, 476, arXiv:1404.3742

Rhodes, J., Refregier, A., Collins, N. R., Gardner, J. P., Groth, E. J., Hill, R. S., 2004, ApJ, 605, 29, astro-ph/0312283

Rhodes, J., Refregier, A., Groth, E. J., 2000, ApJ, 536, 79, astro-ph/9905090

Riess, A. G., Filippenko, A. V., Challis, P., et al., 1998, AJ, 116, 1009, astro-ph/9805201

Riess, A. G., Macri, L., Casertano, S., et al., 2011, ApJ, 730, 119, arXiv:1103.2976

Ross, A. J., Samushia, L., Howlett, C., Percival, W. J., Burden, A., Manera, M., 2015, MNRAS, 449, 835, arXiv:1409.3242

Rowe, B., 2010, MNRAS, 404, 350, arXiv:0904.3056

Rowe, B., Jarvis, M., Mandelbaum, R., et al., 2015, Astronomy and Computing, 10, 0, 121 , ISSN 2213-1337

Rozo, E., Rykoff, E. S., Abate, A., et al., 2015, ArXiv e-prints, arXiv:1507.05460

Rozo, E., Wechsler, R. H., Rykoff, E. S., et al., 2010, ApJ, 708, 645, arXiv:0902.3702

Rubin, V. C., 1983, Scientific American, 248, 96

Rudd, D. H., Zentner, A. R., Kravtsov, A. V., 2008, ApJ, 672, 19, astro-ph/0703741

Sadeh, I., Abdalla, F. B., Lahav, O., 2015, ArXiv e-prints, arXiv:1507.00490

Samushia, L., Reid, B. A., White, M., et al., 2014, MNRAS, 439, 3504, arXiv:1312.4899

Sánchez, C., Carrasco Kind, M., Lin, H., et al., 2014, MNRAS, 445, 1482, arXiv:1406.4407

Schaye, J., Crain, R. A., Bower, R. G., et al., 2015, MNRAS, 446, 521, arXiv:1407.7040

Schaye, J., Dalla Vecchia, C., Booth, C. M., et al., 2010, MNRAS, 402, 1536,

arXiv:0909.5196

Schlegel, D., White, M., Eisenstein, D., 2009, in astro2010: The Astronomy and Astrophysics Decadal Survey, vol. 2010 of *Astronomy*, 314, arXiv:0902.4680

Schmidt, F., Rozo, E., Dodelson, S., Hui, L., Sheldon, E., 2009, ApJ, 702, 593, arXiv:0904.4703

Schneider, M. D., Bridle, S., 2010, MNRAS, 402, 2127, arXiv:0903.3870

Schneider, P., van Waerbeke, L., Kilbinger, M., Mellier, Y., 2002a, A&A, 396, 1, astro-ph/0206182

Schneider, P., van Waerbeke, L., Mellier, Y., 2002b, A&A, 389, 729, astro-ph/0112441

Schrabback, T., Hartlap, J., Joachimi, B., et al., 2010, A&A, 516, A63, arXiv:0911.0053

Scoccimarro, R., Couchman, H. M. P., 2001, MNRAS, 325, 1312, astro-ph/0009427

Seljak, U., 2000, MNRAS, 318, 203, astro-ph/0001493

Semboloni, E., Hoekstra, H., Schaye, J., van Daalen, M. P., McCarthy, I. G., 2011, MNRAS, 417, 2020, arXiv:1105.1075

Semboloni, E., Mellier, Y., van Waerbeke, L., et al., 2006, A&A, 452, 51, astro-ph/0511090

Sérsic, J. L., 1963, Boletin de la Asociacion Argentina de Astronomia La Plata Argentina, 6, 41

Shapiro, C., 2009, ApJ, 696, 775, arXiv:0812.0769

Sheldon, E. S., 2014, MNRAS, 444, L25, arXiv:1403.7669

Singh, S., Mandelbaum, R., More, S., 2015, MNRAS, 450, 2195, arXiv:1411.1755

Slipher, V. M., 1917, Proceedings of the American Philosophical Society, 56, 403

Slosar, A., Iršič, V., Kirkby, D., et al., 2013, J. Cosmology Astropart. Phys., 4, 026, arXiv:1301.3459

Smith, R. E., Peacock, J. A., Jenkins, A., et al., 2003, MNRAS, 341, 1311, astro-ph/0207664

Smoot, G. F., Bennett, C. L., Kogut, A., et al., 1992, ApJ, 396, L1

Spergel, D., Flauger, R., Hlozek, R., 2013, ArXiv e-prints, arXiv:1312.3313

Story, K. T., Hanson, D., Ade, P. A. R., et al., 2014, ArXiv e-prints, arXiv:1412.4760

Suchyta, E., Huff, E. M., Aleksić, J., et al., 2016, MNRAS, 457, 786, arXiv:1507.08336

Szapudi, I., Prunet, S., Pogosyan, D., Szalay, A. S., Bond, J. R., 2000, ArXiv Astrophysics e-prints, astro-ph/0010256

Takahashi, R., Oguri, M., Sato, M., Hamana, T., 2011, ApJ, 742, 15, arXiv:1106.3823

Takahashi, R., Sato, M., Nishimichi, T., Taruya, A., Oguri, M., 2012, ApJ, 761, 152, arXiv:1208.2701

Taruya, A., Takada, M., Hamana, T., Kayo, I., Futamase, T., 2002, ApJ, 571, 638, astro-ph/0202090

Taylor, A., Joachimi, B., Kitching, T., 2013, MNRAS, 432, 1928, arXiv:1212.4359

Tegmark, M., Zaldarriaga, M., 2002, Phys. Rev. D, 66, 10, 103508, astro-ph/0207047

The Dark Energy Survey Collaboration, Abbott, T., Abdalla, F. B., et al., 2015, ArXiv e-prints, arXiv:1507.05552

Tinker, J., Kravtsov, A. V., Klypin, A., et al., 2008, ApJ, 688, 709-728, arXiv:0803.2706

Trotta, R., 2007, MNRAS, 378, 72, astro-ph/0504022

Troxel, M. A., Ishak, M., 2015, Phys. Rep., 558, 1, arXiv:1407.6990

Valageas, P., 2014, A&A, 561, A53, arXiv:1306.6151

van Daalen, M. P., Schaye, J., Booth, C. M., Dalla Vecchia, C., 2011, MNRAS, 415, 3649, arXiv:1104.1174

van Engelen, A., Sherwin, B. D., Sehgal, N., et al., 2014, ArXiv e-prints, arXiv:1412.0626

Van Waerbeke, L., Mellier, Y., Erben, T., et al., 2000, A&A, 358, 30, astro-ph/0002500

Van Waerbeke, L., Mellier, Y., Hoekstra, H., 2005, A&A, 429, 75, astro-ph/0406468

Vikhlinin, A., Kravtsov, A. V., Burenin, R. A., et al., 2009, ApJ, 692, 1060, arXiv:0812.2720

Vikram, V., Chang, C., Jain, B., et al., 2015, ArXiv e-prints, arXiv:1504.03002

Vogelsberger, M., Genel, S., Springel, V., et al., 2014, MNRAS, 444, 1518, arXiv:1405.2921

Voigt, L. M., Bridle, S. L., 2010, MNRAS, 404, 458, arXiv:0905.4801

von der Linden, A., Mantz, A., Allen, S. W., et al., 2014, MNRAS, 443, 1973, arXiv:1402.2670

Weinberg, D. H., Davé, R., Katz, N., Kollmeier, J. A., 2003, in The Emergence of Cosmic Structure, edited by Holt, S. H., Reynolds, C. S., vol. 666 of *American Institute of Physics Conference Series*, 157–169, astro-ph/0301186

Weinberg, D. H., Mortonson, M. J., Eisenstein, D. J., Hirata, C., Riess, A. G., Rozo, E., 2013, Phys. Rep., 530, 87, arXiv:1201.2434

Weinheimer, C., Degenddag, B., Bleile, A., et al., 1999, Physics Letters B, 460, 219

White, M., 2004, Astroparticle Physics, 22, 211, astro-ph/0405593

White, M., Reid, B., Chuang, C.-H., et al., 2015, MNRAS, 447, 234, arXiv:1408.5435

White, S. D. M., 1984, ApJ, 286, 38

Wittman, D. M., Tyson, J. A., Kirkman, D., Dell'Antonio, I., Bernstein, G., 2000, Nature, 405, 143, astro-ph/0003014

Yoo, J., Seljak, U., 2012, Phys. Rev. D, 86, 8, 083504, arXiv:1207.2471

Yoo, J., Tinker, J. L., Weinberg, D. H., Zheng, Z., Katz, N., Davé, R., 2006, ApJ, 652, 26, astro-ph/0511580

Zaldarriaga, M., Spergel, D. N., Seljak, U., 1997, ApJ, 488, 1, astro-ph/9702157

Zentner, A. R., Rudd, D. H., Hu, W., 2008, Phys. Rev. D, 77, 4, 043507, arXiv:0709.4029

Zentner, A. R., Semboloni, E., Dodelson, S., Eifler, T., Krause, E., Hearin, A. P., 2013, Phys. Rev. D, 87, 4, 043509, arXiv:1212.1177

Zhan, H., Knox, L., 2004, ApJ, 616, L75, astro-ph/0409198

Zhang, J., 2008, MNRAS, 383, 113, astro-ph/0612146

Zuntz, J., Kacprzak, T., Voigt, L., Hirsch, M., Rowe, B., Bridle, S., 2013, MNRAS, 434, 1604, arXiv:1302.0183

Zuntz, J., Paterno, M., Jennings, E., et al., 2015, Astronomy and Computing,

12, 0, 45 , ISSN 2213-1337

Zwicky, F., 1937, ApJ, 86, 217